Star Formation in the Orion A Molecular Cloud

INAUGURAL-DISSERTATION

zur
Erlangung des Doktorgrades
der Mathematisch-Naturwissenschaftlichen Fakultät
der Universität zu Köln

vorgelegt von

Sümeyye Suri
aus Ankara, Türkei
Köln, 2019

Berichterstatter: Prof. Dr. Peter Schilke
Prof. Dr. Stefanie Walch-Gassner

Tag der mündlichen Prüfung: 18. Januar 2019

For my family

I think a life or a time looks simple
when you leave out the details,
the way a planet looks smooth, from orbit.

— Ursula K. Le Guin

ABSTRACT

Stars are found to form along and at junctions of filaments within molecular clouds. Filaments are elongated structures that have higher densities compared to their diffuse surroundings. Their first sightings date back to photographic plate observations of Barnard (1910). With the advances in astronomical instrumentation, observatories such as the *Herschel* Space Observatory were able to produce high sensitivity images of molecular clouds throughout the Galaxy. These images revealed that molecular clouds are pervaded with filaments on all scales. Furthermore, the filaments observed with *Herschel* in all molecular clouds are found to have common physical properties such as their width, bringing up an important question: "Can the properties of filamentary structure be universal?"

In this thesis, I focused on the most nearby high-mass star forming region, the Orion A molecular cloud, and investigated the properties of its filamentary structure. Orion A is one of the most studied regions in the Galaxy and its filamentary nature was first presented with a large scale ^{13}CO map in a study by Bally et al. (1987). Throughout this I made use of two large scale mapping surveys; the CARMA-NRO Orion Survey (Kong et al. 2018) and the C^+ Square Degree Project. I also made use of the *Herschel* column density and temperature maps of the region (Stutz & Kainulainen 2015).

In order to study the properties of the filaments, I first employed a structure detection algorithm, Discrete Persistent Structures Extractor (`DisPerSE`, Sousbie 2011), and investigated its performance on synthetic datasets. I found that in cases of low dynamic range and high levels of noise, `DisPerSE` can create artificial networks of filaments. Moreover, I developed a python based package, the Filament Characterization Package (`FilChaP`), that takes 2-dimensional (2D) or 3-dimensional (3D) datasets and `DisPerSE` filaments, and returns filament properties. `FilChaP` calculates filament length, width, skewness, kurtosis and curvature and is freely available for the community at `https://github.com/astrosuri/filchap`.

Using `FilChaP`, I have investigated filament properties in different tracers (^{12}CO, ^{13}CO, C^{18}O, [C II] and dust column density). I found that filaments seen in C^{18}O emission have a common width of $\sim$0.1 pc. The filament widths are independent from their central column densities, line masses and velocity dispersions. The majority of the dense cores are formed along the most gravitationally unstable filaments. I also found that the filaments are highly substructured and these substructures contribute to the turbulent velocity dispersion that provides support to the filaments and keeps them at a relatively constant width.

This study revealed that, when calculating filament properties, it is important to separate structures along the line of sight by their velocities. In cases of filament widths

calculated on the $C^{18}O$ integrated emission and dust column density maps, I found deviations from those filament widths calculated using the $C^{18}O$ datacube. These deviations are purely caused by the fact that integrated emission and column density maps cannot distinguish nearby structures or structures along the same line-of-sight at different velocities. Finally, I have looked at the [C II] emission that mainly outlines the stellar feedback in the region. By comparing the radial profiles of $C^{18}O$, ^{13}CO, dust column density and [C II] , I found that [C II] emission almost always surrounds the emission from the dense gas indicating a chemical layering of different species that is typical for clumpy photo-dissociation regions.

ZUSAMMENFASSUNG

Sterne entstehen üblicherweise in Molekülwolken entlang oder an Knotenpunkten von Filamenten. Filamente sind ausgedehnte Strukturen, die verglichen mit ihrer diffusen Umgebung höhere Dichten haben. Ihre erstmalige Sichtung gab es schon zu Zeiten photographischer Plattenbeobachtung Barnard (1910). Doch mit dem Fortschritt astronomischer Instrumente, konnten Observatorien wie das *Herschel* Weltraumobservatorium Bilder höherer Sensitivität von Molekülwolken überall in der Galaxie aufnehmen. Diese Aufnahmen enthüllten, dass Molekülwolken durchzogen sind von Filamenten in allen Größenordnungen. Des Weiteren ergab sich, dass die mit Herschel beobachteten Filamente gemeinsame Eigenschaften wie beispielsweise deren Breite hatten. Dies warf eine wichtige Frage auf: "Könnten die Eigenschaften filamentärer Strukturen universell sein?"

In meiner Dissertation beschäftige ich mich mit der uns am nächsten liegenden Sternentstehungsregion massereicher Sterne, der Molekülwolke Orion A, und bestimmte die Eigenschaften ihrer Filamente. Orion A ist die meist untersuchteste Region unserer Galaxie und ihre filamentären Strukturen wurden erstmals in einer large-scale ^{13}CO Karte von Bally et al. (1987) dargestellt. Grundlage meiner Arbeit waren zwei large-scale surveys: Das CARMA-NRO Orion Survey (Kong et al. 2018) und das C$^+$ Square Degree Project. Ebenfalls verwendete ich *Herschel* Säulendichte und Temperatur Karten (Stutz & Kainulainen 2015). Um die Eigenschaften der Filamente zu bestimmen, nutzte ich zunächst einen Struktur-Ermittlungs Algorithmus, Discrete Persistent Structures Extractor (`DisPerSE`, Sousbie 2011), und testete dessen Performance (Leistungsfähigkeit) an synthetischen Daten. Im Falle eines low dynamic range und starkem Rauschen, konnte Disperse ungewollt artifizielle Netzwerke filamentärer Strukturen erstellen. Zudem entwickelte ich einen Python basierten Code, Filament Characterization Package (`FilChaP`), welcher aus einem 2-dimensionalen (2D) oder 3-dimensionalen (3D) Datensatzes und `DisPerSE` Filamenten, die Filament Eigenschaften ermittelt. `FilChaP` bestimmt die Filament Länge, Breite, Neigung, Wölbung und Krümmung und ist für die Community frei verfügbar auf `https://github.com/astrosuri/filchap`.

Mit `FilChaP` habe ich die Charakteristika der Filamente für verschiedene Tracer (^{12}CO, ^{13}CO, C^{18}O, [C II] und Staub Säulendichte) bestimmt, mit folgenden Ergebnissen: Filamente in C^{18}O Emission haben eine uniforme Breite von $\sim$0.1 pc, welche unabhängig von ihrer zentralen Säulendichte , Masse pro Länge oder Geschwindigkeitsdispersion ist. Die Mehrzahl der dichten Kerne entstehen entlang der gravitativ instabilen Filamente. Auch wiesen die Filamente viele Substrukturen auf, welche Turbulenzen erzeugen und somit für eine realtiv konstante Filamentbreite sorgen.

Diese Arbeit zeigte, dass beim Berechnen der Filament Eigenschaften, Strukturen entlang der Blickrichtung nach ihren Geschwindigkeiten sortiert werden sollten. Filamentbreiten, die mittels $C^{18}O$ integrierten Emissions und Säulendichten Karten bestimmt wurden, zeigten Abweichungen zu denen, die durch $C^{18}O$ Daten ermittelt wurden. Diese Abweichungen wurden lediglich verursacht, da die integrierten Emissions und Säulendichten Karten nicht zwischen nahen Strukturen und Strukturen entlang der gleichen Blickrichtung mit anderen Geschwindigkeiten unterscheiden. Im letzten Teil betrachte ich die [C II] Emission, welche stellares Feedback aufzeigt. Beim Vergleich der radialen Profile von $C^{18}O$, ^{13}CO, Staub Säulendichte und [C II] ergab sich, dass die [C II] Emission nahezu immer die Emission des dichten Gases umgab. Dies deutet auf chemische Schichten verschiedener Spezien hin, was typische für klumpige Photodissoziation Regionen ist.

CONTENTS

Part I

UNDERSTANDING THE STAR FORMATION PROCESS

The following two chapters intend to provide a motivation and an up-to-date, yet, perhaps incomplete, astrophysical background for the reader.

1 MOTIVATION

We wonder. As mankind, what makes us special is the ability to wonder, ask questions and assess the answers that we find. We live on a planet that orbits around a G-type, or in other words an average, star. But we know more than that. We know that there are other planets in our Solar System. Our Solar System is at a distance of approximately 8 kpc[1] from the center of our Galaxy, the Milky Way (see Figure 1.1). We also know, that the Milky Way harbours at least 100 billion stars and is a spiral galaxy that belongs with a group of other nearby galaxies called the Local Group. The Local Group extends about 6 Mpc and belongs to a super galaxy cluster named the Virgo Supercluster with a diameter of 33 Mpc. We observed other superclusters in the Universe too, and we know that they are the largest gravitationally bound structures. In retrospect, we have uncovered unimaginable scales around us and with the advancing technology we are able to study scales ranging orders of magnitudes: from the birthplaces of individual stars in our own Galaxy to clusters of galaxies at distances of tens of megaparsecs away from us.

As cliché as it may sound, stars are indeed the building blocks of galaxies. Understanding the detailed physics of how stars form is one of the many steps in the quest of understanding our Universe. Especially high-mass stars, those stars with masses at least 8 times the mass of our Sun ($M_{\odot}$) play an important role. Through stellar feedback processes such as stellar winds and radiation pressure in earlier stages of their evolution and supernova (SN) explosions at the end of their lifetimes, the high-mass stars affect the dynamics and composition of the Interstellar Medium (ISM) of our Galaxy. The SN explosions may even disrupt the birthplaces of stars, the molecular clouds. Therefore, formation and evolution of stars alter the ISM dynamically and chemically, and hence, affect the evolution of galaxies.

Within the past decade, stars are found to be form along dense and elongated structures called the *filaments* in molecular clouds (Molinari et al. 2010; Schneider et al. 2012). The *Herschel* space observatory showed that indeed all the observed molecular clouds are pervaded by filamentary networks (André et al. 2010). As filamentary structures are observed even in non-star forming clouds, they are thought to be the precursors of star formation. Therefore, it is vital to study the properties of the filamentary structure of molecular clouds, in order to be able to understand the processes that lead to formation of stars.

1 Parsec (pc) is a unit of length that is equal to 3.26 light years, or 30 trillion kilometers. A kiloparsec (kpc) is a thousand parsecs and a megaparsec (Mpc) is a million parsecs.

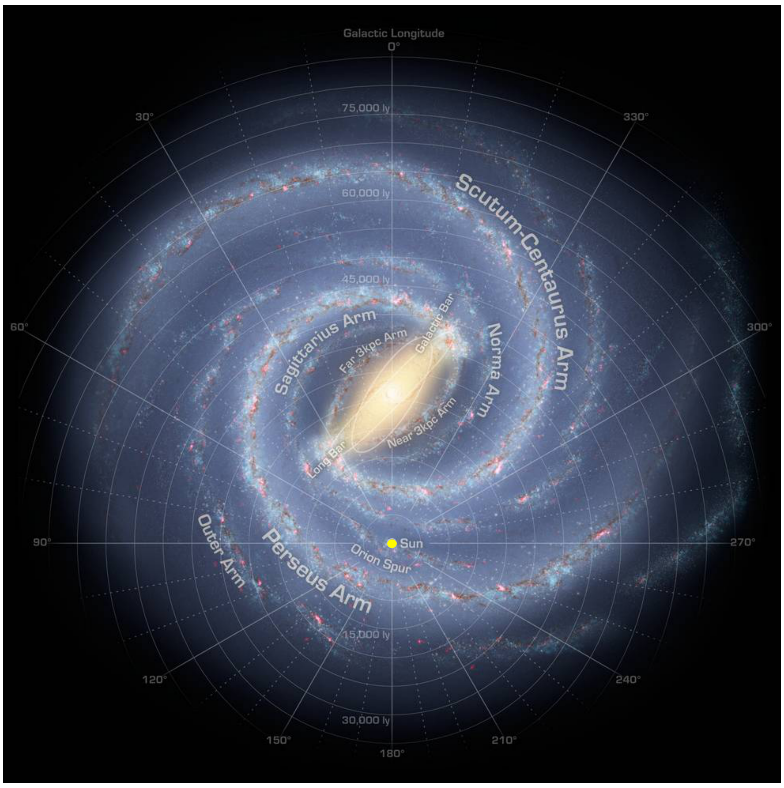

Figure 1.1: Artist's impression of the Milky Way. Our Sun is located at distance of about 8 kpc from the center. Credits: NASA/JPL-Caltech/R. Hurt (SSC/Caltech).

This thesis is aimed at studying the filamentary structure of the most nearby cloud that actively forms high-mass stars: the Orion A molecular cloud. With its wide range of star formation activities and proximity of only 388 pc (Kounkel et al. 2017), the Orion A molecular cloud is perhaps one of the best laboratories to study the role of filaments in the process of star formation.

In the following, I give a brief description of how this thesis is organized. In Chapter 2, I give a detailed introduction to the properties of the ISM (Section 2.1), description of observations of molecular clouds (Section 2.2), low and high-mass star formation (Section 2.3), the filamentary structure (Section 2.3), properties of the Orion A molecular cloud (Section 2.5) and an insight on the observational astronomy (Section 2.6).

In this work I use observational datasets from two large-scale Orion surveys: the CARMA-NRO Orion Survey and the C^{+} Square Degree Project. Hence, in Chapter 3, I give the technical details of these observations.

Chapter 4 and 5 are dedicated to two softwares that are used in this thesis: `DisPerSE`[2] and `FilChaP`[3]. `DisPerSE` is an open source software that I employed for filament identi-

2 Discrete Persistent Structures Extractor (DisPerSE), Sousbie (2011).
3 Filament Characterization Package (FilChaP), Suri et al. 2018, submitted to A&A.

fication. `FilChaP` on the other hand has been developed for automated characterization of filament properties throughout this work. Furthermore, in Chapter 6 I describe how the filament identification was performed on the CARMA-NRO datasets.

In Chapter 7, I apply `FilChaP` on the $C^{18}O$ data cube from the CARMA-NRO Orion Project, and present the distribution of filament widths as seen in $C^{18}O$ emission (Section 7.1). In this chapter, I present a filament stability analysis that is closely related to fragmentation and formation of new stars (Section 7.2). I also discuss the role of substructure and turbulence in keeping filaments at what seems to be a constant width (Section 7.3).

In Chapter 8, I present a comparison of filament properties in different tracers: ^{13}CO, $C^{18}O$, dust column density and [C II] emission. In Section 8.1, I discuss the general morphology of these tracers. In Section 8.2, I give the results of calculated filament properties in each tracer and discuss their differences. In Section 8.2.3, I discuss the possibility of the less dense filaments being affected by the strong UV radiation and resembling clumpy photo-dissociation regions.

Finally, in Chapter 9 and Chapter 10, I present the conclusions of this work and future possibilities.

2 INTRODUCTION

In the Galaxy, everything between the stars is called the Interstellar Medium (ISM). The ISM is composed of dust grains, the interstellar radiation field, cosmic rays, magnetic fields, molecules and atoms. In the following few sections, I elaborate on how the stars form within their cold ($\sim$10 K) and dense ($\sim$10^4 cm^{-3}) natal clouds and how the signatures of this process can be observed.

2.1 PROPERTIES OF THE INTERSTELLAR MEDIUM

The majority of the gas within the ISM is in the form of the two most abundant elements in the Universe, hydrogen and helium. While hydrogen accounts for 70% of the gas mass and helium is 28%, a small fraction (2%) of the gas mass is in heavier elements. While 60% of the hydrogen is in the form of atomic hydrogen (H I)[1], 20% of it is in the molecular form (H_2) and 20% is ionized hydrogen (H II). The ISMis often referred to be *multi-phased*. The term multi-phase ISMimplies the co-existence of gas at different temperatures, densities, hence having a variety of distinguishable chemical and thermal states. As explained in the recent review by Klessen & Glover (2016), these states are:

- Warm Neutral Medium (WNM): Warm and diffuse atomic gas with temperatures of 10^4 K and densities of 0.2–0.5 cm^{-3}.
- Cold Neutral Medium (CNM): Cold and dense atomic gas with temperatures of 100 K and densities of 20–50 cm^{-3}. The existence of CNM and WNM, the two-phased ISMmodel, was first suggested by Field et al. (1969).
- Hot Ionized Medium (HIM): Hot, ionized state of gas created through blast waves from energetic explosions of supernovae, first suggested by McKee & Ostriker (1977). The HIM reaches temperatures of 10^6 K and densities of 10^{-2} cm^{-3}. As these temperatures are close to the temperatures in the Sun's corona, the HIM is sometimes referred as *Coronal Gas*.
- Warm Ionized Medium (WIM): Ionized gas with temperatures of 10^4 K but densities similar to WNM. The origin of this medium is the regions of ionized hydrogen known as H II regions, and this is the reason for high temperatures and relatively high densities.

1 Throughout this work the roman numerals are used to indicate the emission from certain species as the following: the ionized hydrogen as species is denoted as H^+ whereas its emission is denoted as H II. The roman numeral II is used for the singly ionized atom and I denotes a neutral atom.

- Molecular Gas: Cold and dense phase of the ISMwith temperatures of 10 K and densities larger than 10^2 cm^{-3}. Molecular gas is observed in the form of molecular clouds that harbour star formation throughout the ISM.

In addition to the atomic and molecular species that accounts for the 99% of the mass of the ISM, dust grains which account for the remaining 1% also play an important role in the process of star formation. Dust grains absorb and scatter photons at wavelengths smaller than their sizes (1 μm - 1 nm, Mathis et al. 1977), therefore, can be accounted for absorption in the UV and optical regime of the electromagnetic spectrum. They process and reemit the absorbed starlight at far-infrared wavelengths. Dust grains are mainly carbonaceous (Mathis et al. 1977) or are made of silicates (Draine & Lee 1984). The infrared emission from the dust mostly correlates with the emission from the dense gas, as dust surfaces act as a catalysts for H_2 formation. Furthermore, the dust grains shield molecules from ionizing radiation and by reemitting the absorbed photons they contribute to the cooling in the ISM.

2.2 MOLECULAR CLOUDS

Molecular clouds so as the name goes are composed predominantly of molecular gas. Therefore, the fact that the molecular clouds exist suggests conversion of majorly atomic gas to molecular gas. There are two main theories of molecular cloud formation, formation via cloud-cloud collision and formation via converging flows (also known as colliding flows).

The cloud-cloud collision theory was first suggested by Oort (1954). The idea is very similar to the coagulation of dust particles that form larger dust particles, planetesimals and eventually planets in solar systems. In the case of molecular cloud formation, it is the discrete self-shielded smaller masses of molecular clouds that coagulate and form larger clouds. However, this theory was discarded for the formation of higher mass molecular clouds (10^6 $M_\odot$) because acquiring such masses require a timescale of 100 Myr which is much larger than the lifetime of these clouds (Blitz & Shu 1980).

The colliding flow theory suggests that instead of being discrete and isolated objects, molecular clouds are stagnation points of interacting turbulent flows. In this scenario, dense gas with low temperatures is produced via thermal instabilities at the shock-front, allowing molecular gas (H_2 and CO) to form. For further reading, I refer to Hennebelle & Pérault (2000), and for a more recent review; Klessen & Glover (2016) and the references therein. This scenario helps us think molecular clouds as the densest locations of the multi-phase ISM, embedded in a much lower density gas.

Larson (1981) showed that there are common properties of the observed molecular clouds. He compiled a number of observations towards different molecular clouds that yielded what is now known as the "Larson's Relations": the size–linewidth and the

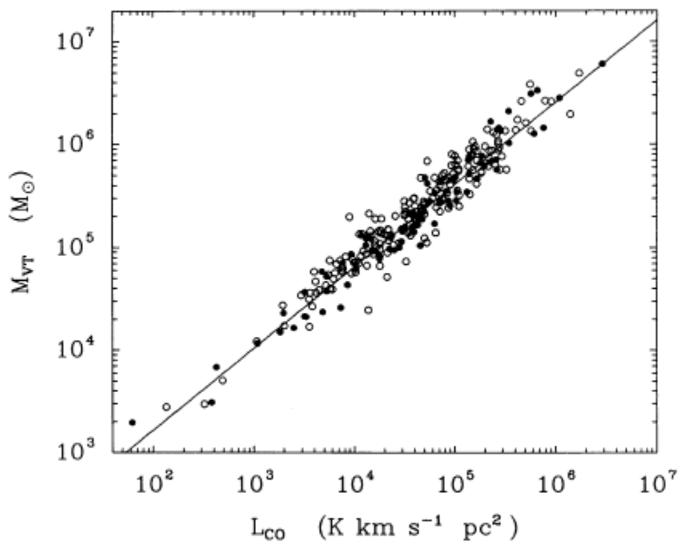

Figure 2.1: Size–linewidth relation derived in Solomon et al. (1987).

mass–linewidth relations. The size–linewidth relation suggests that the observed size of a molecular cloud is related to the linewidth of the observed emission with:

$$\sigma \simeq 1.1 \text{ km s}^{-1} \left(\frac{L}{1 \text{ pc}}\right)^{0.38}, \tag{2.1}$$

where σ is the linewidth and L is the size of the cloud. The mass–linewidth relation is similar, the correlation of the mass of a cloud and the linewidth of the observed tracer is given with:

$$\sigma \simeq 0.43 \text{ km s}^{-1} \left(\frac{M}{1\ M_\odot}\right)^{0.2}, \tag{2.2}$$

where M is the mass of the cloud. Later Solomon et al. (1987) used 273 cloud samples and found the scaling index to be 0.5, instead of 0.38. Figure 2.1 shows the scaling relation presented in Solomon et al. (1987). The size–linewidth relation is accepted as a proof of turbulence in molecular clouds. For a detailed read, I refer to the review by McKee & Ostriker (2007). More recently, Larson's size-linewidth relation was revisited (e.g. Heyer et al. 2009; Ballesteros-Paredes et al. 2011). The authors found that the size-linewidth relations is also dependent on the gas surface density, Σ, following a relation: $\sigma \propto L^{1/2}\Sigma^{1/2}$. Additional physical properties of molecular clouds are presented in Table 2.1.

2.3 STAR FORMATION

Star formation process progresses differently based on the initial stellar mass. With this idea in mind, let us first take a look at the most generic view of the star formation. In order to explain the scales involved, I will use three different definitions; molecular clouds, clumps, prestellar cores as given in Table 2.1. Turbulent compression within molecular clouds cause formation of higher density clumps, which then fragment to condensations of bound cores. The first stage of star formation is the isothermal collapse of the cores. These cores are initially in a balanced state with turbulent, magnetic and thermal pressure supporting against gravitational collapse (e.g. Shu et al. 1987). Due to turbulent motions and local instabilities, the cores start to collapse. The collapse is at first isothermal because the energy can still be radiated away through atomic excitation. This isothermal phase is followed by the formation of a central "protostar" with high densities, the protostar is therefore no longer transparent to the radiation. The following evolution of the protostar is often regarded as *early stages of star formation* and can be observationally distinguished stage by stage.

2.3.1 *Low-mass star formation*

Firstly, the youngest protostar, a Class 0 object, goes through the main accretion phase. It is embedded within an envelope where it constantly gains mass through an accretion disk. To conserve its angular momentum, the protostar radiates away its excess energy by bipolar outflows. The Class 0 objects can be observed through their collimated outflows in, for example, CO or SiO emission lines in the millimeter regime, or dust emission from the envelope in sub-millimeter continuum emission. During the ClassI phase the evolved accreting protostar becomes visible in the infrared regime. The mass of the protostar becomes larger than the mass of the infalling envelope and the temperature rises to a few hundred Kelvins. The next phase, the Class II object no longer accretes, the envelope is dissipated and the object is now a pre-main sequence star. The Class II and Class III objects (Classical and weak T Tauri stars) are distinguished by the existence of a protoplanetary disk. Once the central temperature of the pre-main-sequence star is high enough to ignite hydrogen fusion, it no longer contracts, and is supported by the radiation pressure. The main sequence object is then called a *star*. Illustrations of protostellar evolution of low-mass stars and their corresponding Spectral Energy Distributions (SEDs) are given in Figure 2.2 and 2.3, respectively (Credit: Persson, Magnus Vilhelm (2014): Current view of protostellar evolution and SEDs of the different protostellar evolutionary stages).

Table 2.1: Properties of molecular clouds, clumps and cores taken from Klessen & Glover (2016)

	Molecular Clouds	Clumps	Cores
Size (pc)	2 – 20	0.1–2	$\leq$0.1
Mean Density (H_2 cm^{-3})	10^2–10^3	10^3–10^5	$\geq 10^5$
Mass ($M_\odot$)	10^2–10^6	10–10^3	0.1–10
Temperature (K)	10–30	10-20	7–12
Linewidth (km s^{-1})	1–10	0.5–3	0.2–0.5
Turbulent Mach number	5–50	2–15	0–2
Column Density (g cm^{-2})	0.03	0.03–1.0	0.3–3
Crossing time (Myr)	2–10	≤ 1	0.1–0.5
Free-fall time (Myr)	0.3–3	0.1–1	$\leq$0.1
Examples	Orion, Perseus	L1641, L1709	B68, L1544

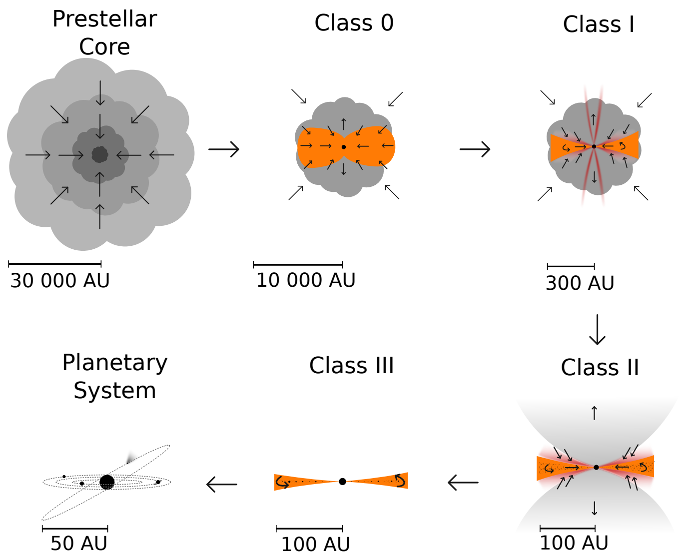

Figure 2.2: Evolutionary stages of a protostar (Credit: Magnus Vilhelm Persson, doi: https://doi.org/10.6084/m9.figshare.654555.v7).

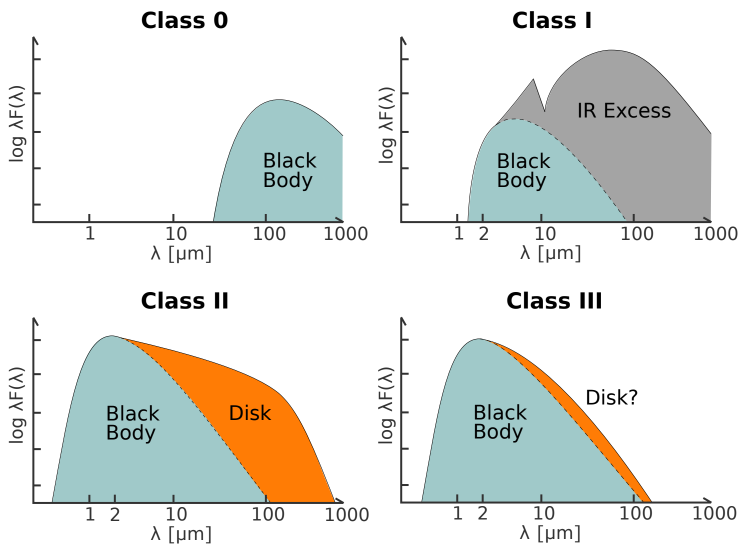

Figure 2.3: SEDs of protostars at different evolutionary stages (Credit: Magnus Vilhelm Persson, doi: https://doi.org/10.6084/m9.figshare.1121574.v2).

2.3.2 *High-mass star formation*

The formation and evolution of high-mass stars are known to differentiate from that low-mass stars, mainly because of the different time scales involved and energies involved. The Kelvin-Helmholz timescale or the thermal timescale of stars indicated the time that is needed for the star to radiate away its gravitational potential energy. It is given as the following:

$$\tau_{KH} = \frac{GM^2}{2RL}, \tag{2.3}$$

where G is the gravitational constant, M is the stellar mass, R is the radius of the star and L is the luminosity. In this context, the Kelvin-Helmholz timescale represents the phase of gravitational contraction, that lasts until the protostar ignites hydrogen burning. For high-mass stars, the τ_{KH} is much longer than the free-fall time scale of the envelope given by:

$$\tau_{ff} = \left(\frac{3\pi}{32G\rho}\right)^2, \tag{2.4}$$

where ρ is the density. This means, that the high-mass protostar starts nuclear fusion while it is still in the accretion phase. Figure 2.4 illustrates the high-mass star formation processes. The main observational difference between the low-mass and high-mass star

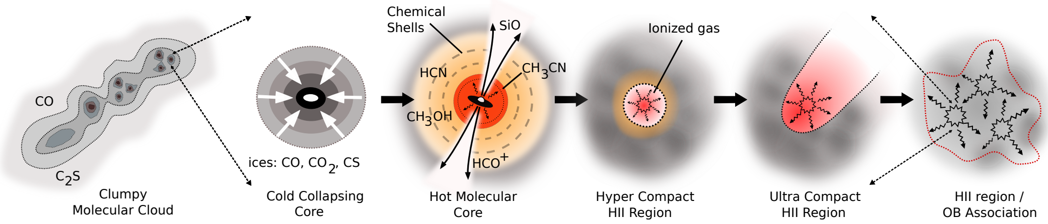

Figure 2.4: Illustration of formation and evolutionary sequence of high-mass stars (Credit: Cormac Purcell).

formation is that the high-mass stars are able to produce enough UV photons to ionize hydrogen in their immediate surroundings. Firstly, the density and temperature of the prestellar core increase due to the collapse, at this stage a Hot Molecular Core (HMC) is formed. The embedded protostar heats up the core to a few hundred Kelvins (Kurtz et al. 2000). The HMCs show rich chemistry of e.g long hydrocarbon chains, and complex organic molecules that are also present on the Earth (e.g. Schilke et al. 2001). The HMC can be observed in the infrared and sub-millimeter regime. When the accreting protostostar is able to ionize its surroundings, a Hyper Compact H II (HCH II) and then Ultra Compact H II (UCH II) regions form. These two stages are distinguished by their electron densities, the HCH II regions have electron densities of about 10^7 to 10^9 cm^{-3}, whereas for UCH II regions these values are around 10^5 to 10^6 cm^{-3}. The HCH II regions are also smaller in size by an order of magnitude (Kurtz 2005). This stage is followed by the formation of a classical H II region where high-mass stars and OB-associations are often observed.

2.3.3 *Photo-dissociation regions*

The far-ultraviolet radiation (5.6 eV $<$ hν $<$ 13.6 eV) from the high-mass stars or the interstellar radiation field can produce a so called photo-dissociation region or photon-dominated region (PDR) (Hollenbach & Tielens 1999). PDRs are the transition regions where chemical layering between the molecular, atomic and ionized species in molecular clouds can be observed. An illustration of a PDR is given in Figure 2.5. Close to the radiation front, ionized and atomic species are observed while further outside the gas is in neutral and molecular form. In this case the important transition regions are $H^+/H/H_2$, $C^+/C/CO$ and O/O_2.

PDRs are often observed around the high-mass stars where H II regions are present. Surrounding the H II region, lower energy photons escape into the cloud and dissociate CO and O_2 and ionize, for example, the carbon atom. [C II] fine structure line is, therefore, a good tracer of PDRs.

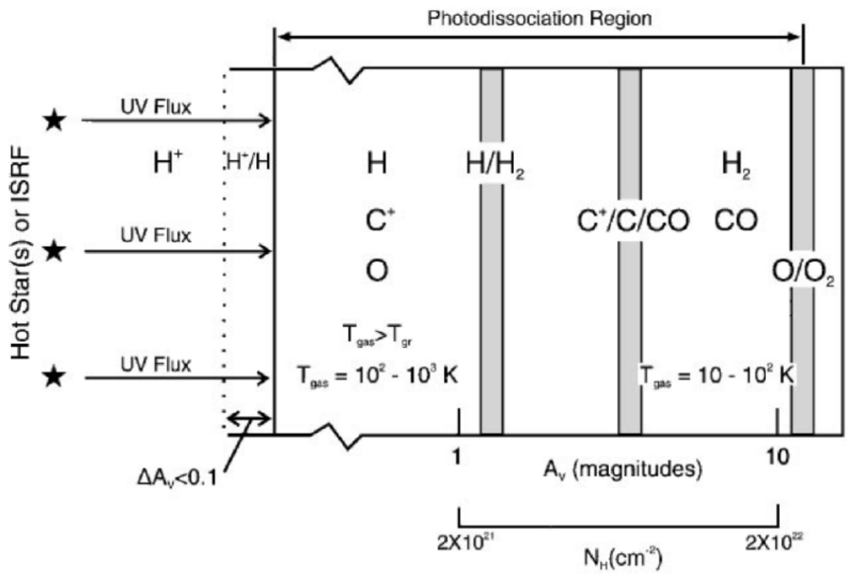

Figure 2.5: Illustration of of a photo-dissociation region (Credit: Hailey-Dunsheath 2009).

2.3.4 *The initial mass function*

For a group of stars, the distribution of masses at which a star starts hydrogen burning is usually described as the Initial Mass Function (IMF). The IMF was first characterized by (Salpeter 1955) with a power-law. The function has the following form:

$$\xi(m)\Delta(m) = \xi_0 \left(\frac{m}{M_\odot}\right)^{-2.35} \left(\frac{\Delta m}{M_\odot}\right), \tag{2.5}$$

where $M_\odot$ is the mass of the Sun and $\xi(m)\Delta(m)$ is the number of stars with masses between m and $m + \Delta(m)$. The index -2.35 indicates a sharp decline in the number of stars as one moves towards higher and higher stellar masses. Later, (Kroupa 2001) introduced a second power law with a less steep index towards the low mass end of the function, and (Chabrier 2003) re-defined the function as a log-normal distribution. Although the number of high-mass stars are much less compared to the low-mass stars as seen from the IMF, they are vital sources of thermal, kinetic and radiative energy in the ISM through stellar winds and UV radiation. At the end of their lives they explode as SN, and this process can disrupt embedding molecular clouds. The SN explosions are also sources of nucleosynthesis where elements heavier than iron are produced.

A mass distribution similar to the IMF has also been observed for the masses of dense cores within molecular clouds (Lada et al. 2007). The Core Mass Function (CMF) has a similar shape to the IMF but is shifted towards the higher masses. The similarity and differences in these two functions suggest that (1) the initial masses of the cores are relevant for the final mass of the stars, (2) since the cores tend to have higher masses,

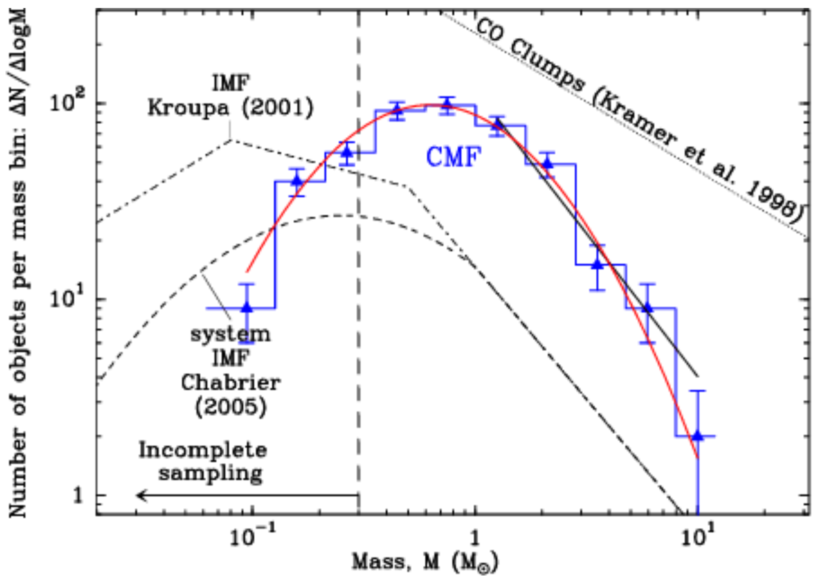

Figure 2.6: Comparison of the IMF and CMF presented in Könyves et al. (2010).

only a fraction of this mass seems to be turned into stars (Matzner & McKee 2000). Figure 2.6 is an example of the observed CMFs compared to the Kroupa and Chabrier IMFs (Könyves et al. 2010).

2.4 FILAMENTARY STRUCTURE

Over the past decade, the *Herschel* Space Observatory revealed that the locations of dense clumps are coincident with filamentary structures within molecular clouds. Filaments are simply elongated, high-contrast structures. Although, Herschel has revealed that filaments are prevalent in *all* of the observed molecular clouds, the existence of these structures have been known for over a century. For example, Barnard (1910) describes the filamentary structures in his photographic plate observations towards Ophiuchus as the existence of vacant, dark and elongated lanes.

More recently, science highlights of *Herschel* Gould Belt Survey (HGBS) revealed extraordinary images of detailed filamentary structures of the Aquila and Polaris molecular clouds (André et al. 2010; Molinari et al. 2010). Figure 2.7 shows a composite 3-color image of the Aquila (Eagle) nebula that is constructed from 70, 160 and 500 μm images of *Herschel*'s PACS and SPIRE receivers. Later, Arzoumanian et al. (2011) analyzed the properties of 3 HGBS clouds including $\sim$ 90 filaments spanning an order of magnitude in column density. The analysis yielded a narrow filament width distribution with a median of 0.1$\pm$0.03 pc. As the distribution of filament widths appeared to have a very little dispersion around this median value, the question was whether there is a "universal" filament width that is perhaps set by the underlying physical processes.

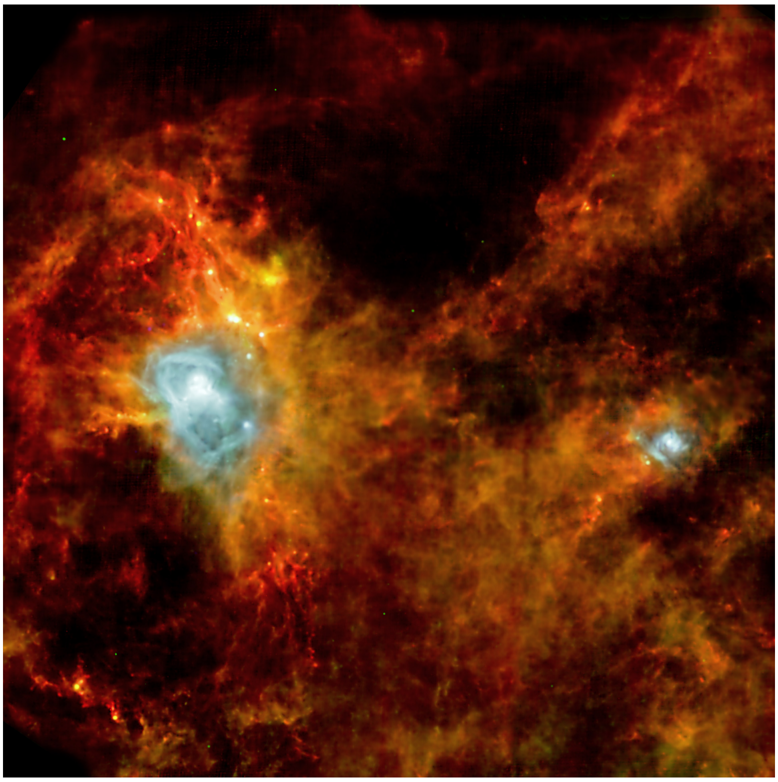

Figure 2.7: 3-color composite image of the Aquila (Eagle) nebula observed with *Herschel*. The red, green and blue colors represent 500 (SPIRE), 160 (PACS) and 70 (PACS) observations (image credit: http://www.esa.int/Our_Activities/Space_Science/Herschel/Inside_the_dark_heart_of_the_Eagle).

The interest in filament properties have significantly increased with the observations of the Rosetta molecular cloud revealing that the majority of the stars and star clusters reside within the identified filaments (Schneider et al. 2012). Therefore, a tremendous observational and theoretical effort has since been devoted to understand the properties of filaments and how they are tied to the process of star formation.

2.4.1 *Formation of filaments*

Filaments are prominent structures throughout the Universe; they are found in large scale simulations of the Universe as the *Cosmic Web* spanning kpc scales, but they are also found in nanometer scales in muscle cells called the *actin filaments*. Here, we are concerned with the filaments of sizes of a fraction of a parsec, within molecular clouds in the Galaxy, and there are comprehensive theories about how these filaments form.

The formation of the cosmic web structure happens purely due to gravitational collapse as in the early Universe the gravitational potential of the dark matter haloes dominate. The gravitational collapse of tri-axil matter naturally forms structures with large aspect ratios, as the matter first collapses along the short axis (Lin et al. 1965; McKee & Ostriker 2007). In molecular scales, gravity is not the only dominant force. In fact in a number of studies, filaments were found to form as a result of supersonic turbulence regardless of the existence of the gravity (e.g. Ballesteros-Paredes et al. 1999; Padoan et al. 2001; Krumholz et al. 2007; Gómez & Vázquez-Semadeni 2014; Smith et al. 2014b). While Pudritz & Kevlahan (2013) argued filaments form at the intersection of colliding flows, Hennebelle (2013) suggested turbulent shear may also stretch structures into an elongated form.

2.4.2 *Filament widths*

Let us take a closer look at how the filament widths are calculated in the aforementioned studies. As the observations do not have a real third dimension, the observers do not know the real 3-d orientation of molecular clouds. What we do know, is a projected image of the observed structure on the plane of the sky. Thus, we are only able to calculate the width of a filament assuming it has a very little extension along the line of sight. With this idea in mind, Arzoumanian et al. (2011) calculates slices perpendicular to the filament spines. Each of these slices along the filaments yield a radial column density profile. The assumption here is that the width of these profiles is a good representation of the width of the filaments. Arzoumanian et al. (2011) average all the perpendicular slices along a single filament to obtain an averaged column density profile that represents the entire filament[2]. An example column density profile and the resulting distribution of filament widths of 90 filaments in this study is shown in Figure 2.8 left and right panels respectively.

Arzoumanian et al. (2011) uses Gaussian and Plummer-like functions to estimate the width of the average column density profiles. The Plummer-like function takes the following form:

$$\Sigma_p(r) = A_p \frac{\rho_c R_{flat}}{\left[1 + \left(\frac{r}{R_{flat}}\right)^2\right]^{\left(\frac{p-1}{2}\right)}}, \tag{2.6}$$

where ρ_c is the central density, R_{flat} is the radius within which the density is uniform, p is the power law index at large radii, and A_p is a finite constant that is related to the filament's inclination compared to the plane of the sky. As we cannot estimate the inclination, it is often assumed to be zero. Plummer-like functions are employed to describe the column density of a homogeneous cylinder with an inner flat portion. Previously, Ostriker (1964) showed that for an isothermal and homogeneous cylinder the

2 In Chapter 5 I study how well an averaged profile can represent an entire filament.

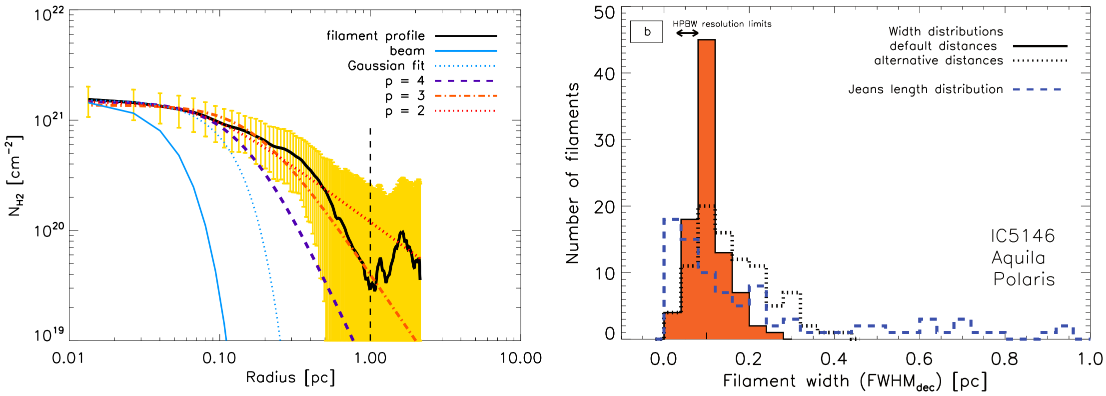

Figure 2.8: *Left:* An averaged column density profile from Arzoumanian et al. (2011), their Figure 5. The profile is overlaid with the beam of the observations (cyan solid line), Gaussian fit (cyan dotted line), and three Plummer-like fits with power law indices of 4 (purple dashed line), 3 (red dot-dashed line) and 2 (dotted red line). The dispersion around the averaged profile is shown with yellow errobars. *Right:* Distribution of filament widths obtained from 3 different molecular clouds in Arzoumanian et al. (2011), their Figure 6.

power-law index of the Plummer-like function takes a value of 4. When Arzoumanian et al. (2011) fitted the power-law index as a free parameter, they obtained a value of 2; which was attributed to these filaments being non-isothermal.

As the studied filaments spanned orders of magnitudes in column density, the fact that the higher column density filaments still have an approximately constant width brought up the question: "How do the high column density filaments sustain their width without shrinking?". The authors suggested that filaments may be constantly accreting from their surroundings, hence, the higher column density filaments do not narrow down as a consequence of gravitational collapse. Clarke et al. (2017) suggests that formation of substructure within the filaments may lessen the effects of gravity, thus, quenching gravitational collapse.

2.4.3 *Fibers and substructure*

All evidence from studies within the last decade point to a dynamic star formation scenario where most of the mass is gathered in dense filaments which then fragment into star forming cores. There has been substantial effort from both observational and theoretical side to understand and explain the substructure of filaments. Hacar et al. (2013) investigated the filamentary structure of the low mass star forming region Taurus in $C^{18}O$ emission. They found the 10 pc long main filament is composed of many smaller fibers that have lengths of 0.5 pc and are coherent in velocity. They found that these fibers belong to distinct groups in terms of the similarities in their kinematics and chemical compositions. Therefore, they suggest a hierarchical core formation scenario as follows; first the gas is accumulated in the main filament that fragments into bundles. The bundles fragment into velocity coherent fibers which then further fragment into cores. Following up on the work by Hacar et al. (2013), Tafalla & Hacar (2015) studied the distribution and properties of dense cores in the Taurus region. Together with the analysis of Hacar et al. (2013), they refer the hierarchical core formation scenario as *fray and fragment*. From the theoretical side this idea was challenged by the simulations of **?**. The authors found that the fibers in their simulated molecular cloud existed before fragmentation of the main filaments. The simulations showed that as the cloud collapses, the fibers are swept together into a large scale filament by large-scale flows of gas. The authors referred the opposing scenario as *fray and gather* (Smith et al. 2016).

As mentioned earlier, the observed data has 3-dimensions, position-position-velocity (PPV). The velocity information comes along because of the movement of each observed particle along the line of sight. The real 3-dimensional space, however, has dimensions: position-position-position (PPP) to which observers have no access to. Therefore the real 3-dimensional structure of fibers identified in PPV space can only be assessed in synthetic datacubes. Smith et al. (2016) showed that the network of fibers in their simulated cloud overlap along a sightline which causes then the observed narrow fibers as distinct velocity components in $C^{18}O$. Clarke et al. (2018), however, has showed that the fibers identified in PPV correspond to sub-filaments identified in PPP only 50% of the time. Because of the projection effects, the fibers may seem velocity coherent and distinct in PPV space, but in PPP they do not always translate to continuous and distinct structures. Figure 2.9 shows velocities of each point along a single sub-filament identified in PPP. This filament shows at least 3 different velocity coherent structures that in PPV may appear as 3 distinct fibers, whereas in reality they are one single sub-filament.

2.5 THE ORION A MOLECULAR CLOUD

The main subject of interest for this thesis is the Orion A molecular cloud. The Orion A molecular cloud is a part of the Orion Giant Molecular Cloud complex at a distance of approximately 388 pc (Kounkel et al. 2017). It is the closest region where high-mass stars are actively being formed. It also already encompasses a high-mass star cluster called the Trapezium cluster, which baths the region in ionizing UV radiation. This young star cluster was discovered by Galileo Galilei in 1617. The brightest star in the cluster is named Θ^1 Orionis C, and it is an O-type star with a mass 40 times than that of the Sun.

Due to its proximity, Orion A has been observed continuously at all wavelengths. As seen in the optical regime, the molecular cloud lies below the belt of the infamous winter sky constellation Orion, also known as the Hunter, and can be spotted with bare eyes on a clear night. The Trapezium stars emit ionizing UV radiation that consequently

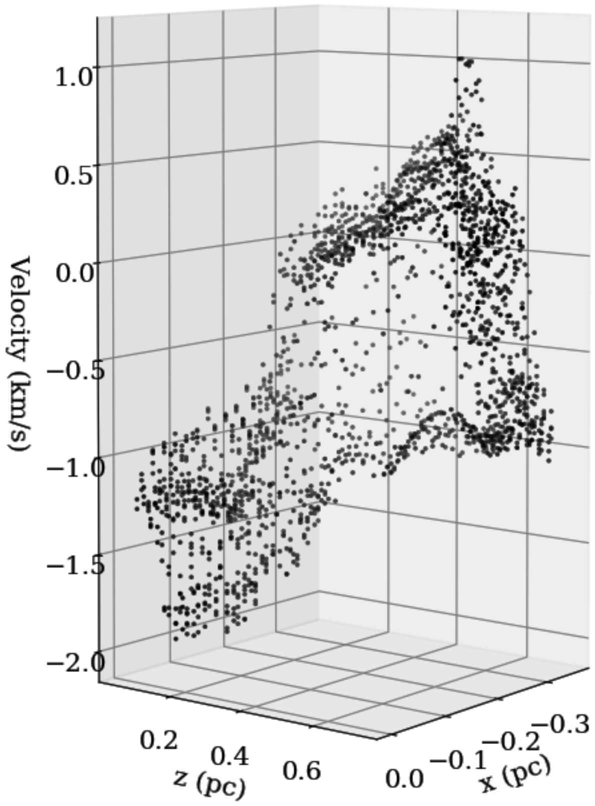

Figure 2.9: Velocities along a single PPP sub-filament (Clarke et al. 2018). When looked at in PPV this single sub-filament can be identified as multiple velocity coherent fibers.

formed the first observed H II region, known as M42. The ionizing radiation also creates a PDR between the molecular gas and the H II region. The Orion Bar is the most studied PDR in the ISM. The winds from the Trapezium stars form an expanding bubble called the Orion Veil Bubble. A part of the bubble was also observed in high energy X-rays (Yamauchi et al. 1996, later observed also with the Chandra Observatory). The first large scale molecular line observations towards the cloud were done by Bally et al. (1987), allowing for the first time to see the dense filamentary gas distribution of ^{13}CO line emission over 2 square degrees. Bally et al. (1987) named the northern portion of the cloud the integral shaped filament (ISF), which is how it is referred up to this date. These observations revealed that the ISF is highly filamentary. Quoting Bally et al. (1987); *"..the observations unraveled that in addition to the two or three larger ones, the Orion A molecular cloud is composed of many smaller filaments"*.

More recently, Hacar et al. (2018) studied dense gas emission (N_2H^+) in the northern portion of the ISF with Atacama Large-millimeter Array (ALMA). These observations confirmed the existence of many dense and narrow filaments (with widths of 0.03 pc) in the northern ISF.

A comprehensive image of the Orion A cloud was published in Meingast et al. (2016), as a part of the Vienna Survey in Orion (VISION) project. Figure 2.10 shows the beautiful near-infrared map of Orion A using the Visible and Infrared Survey Telescope for Astronomy (VISTA, Emerson et al. 2006) within the frame work of the VISION project. The upper panel of this image is a histogram with the number of publications throughout the cloud. The region that has been studied the most is the OMC-1 region. Here, I should mention that the individual star forming regions in Orion A use a common nomenclature throughout the ISF. These regions are referred as: Orion Molecular Cloud X (OMC-X), where X is a number denoting the region. The center of the ISF hosting the Trapezium cluster and the the Orion Bar is named OMC-1, along with OMC-2 and OMC-3 in the north. OMC-2 and OMC-3 regions host intermediate mass protostars that have been studied thoroughly (e.g. Takahashi et al. 2008, 2012). The OMC-3 region lays adjacent to the NGC1977 star forming region in the north. The NGC1977 region also has an expanding bubble powered by a B0 star (42 Ori). A PDR at the intersection between the NGC1977 bubble and the OMC-3 region is recently observed in [C II] emission (Pabst et al. submitted; Kabanovic, S. PhD thesis). Additionally, OMC-4 lays about 10 arcmin south of the Trapezium cluster and harbours dense cores that form a V-shaped structure that is prominent in dust emission (Johnstone & Bally 2006). About 30 arcmin south of the Trapezium cluster, the NGC1980 region harbours a high-mass binary system with spectral types O9 and B1 (Johnstone & Bally 2006). Behind the NGC1980 cluster, Johnstone & Bally (2006) identified a cluster of sub-millimeter cores which they named OMC-5. L1641-N is also an embedded cluster and an active star forming region in the southern ISF which harbours many mid-infrared sources and Herbig-Haro (HH) flows (Ali & Noriega-Crespo 2004; Reipurth

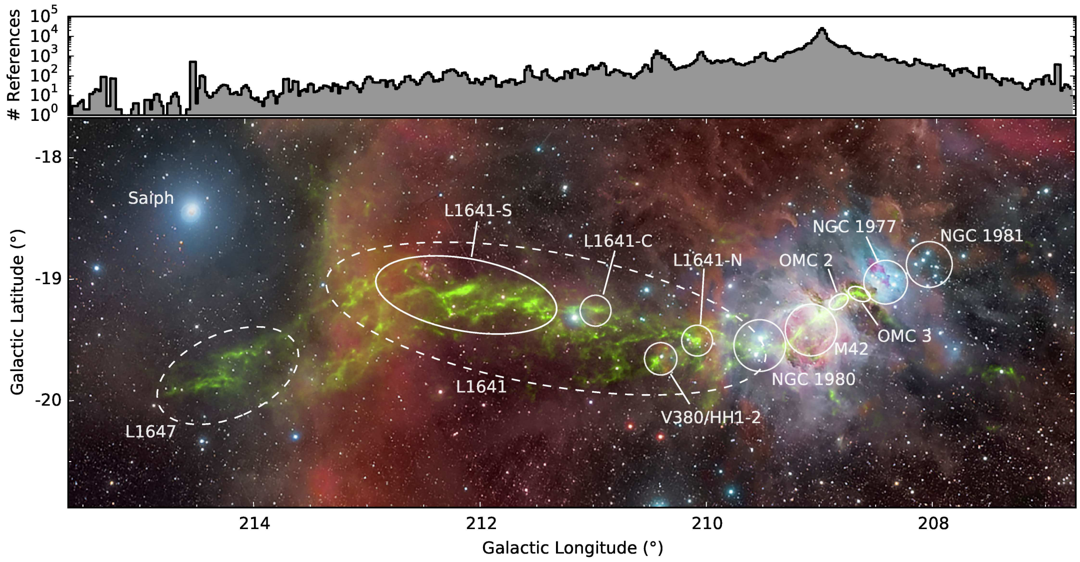

Figure 2.10: The Orion A molecular cloud as seen in near infrared in VISION survey (Meingast et al. 2016). The upper panel indicated the number of publications regarding each region throughout the cloud.

et al. 1998). For a detailed study of the southern L1641 region, different clumps and mass distributions, I refer to Polychroni et al. (2013).

2.6 AN OBSERVATIONAL VIEW

We live in the age of advanced telescopes and high quality receivers with which we can look for answers to our almost "too specific" astrophysical questions. These telescopes and receivers are designed to receive emission at certain wavelengths. Particular wavelengths carry information on physical processes in the Universe which lead to absorption and emission of light. Except for the analysis of meteorites, cosmic rays and space experiments where material can actually be collected, all we know about the Universe is based on the information we receive through electromagnetic radiation. However, the Earth's atmosphere is not transparent to all wavelengths of the electromagnetic spectrum. Figure 2.11 is a sketch showing which wavelengths can be observed and how. As one can see, not all the light is transmitted to the Earth's surface, some of it is scattered or absorbed by the atmosphere. Therefore, for the wavelengths that cannot be observed with ground-based telescopes there are air-borne observatories, space telescopes (or satellites) and space-shuttle missions. The visible (also known as optical) light can be observed both with space and ground-based telescopes. Some of the widely used optical telescopes are Keck and Gemini ground-based telescopes, along with the Hubble Space Telescope (HST).

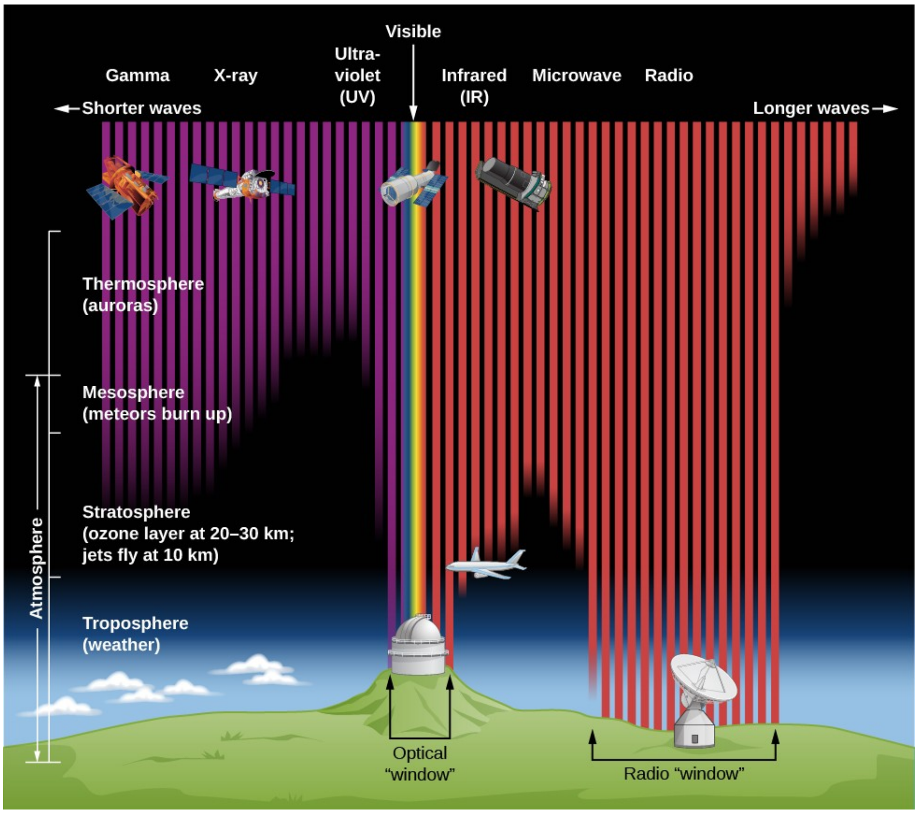

Figure 2.11: Transmission of different wavelengths through the Earth's atmosphere. Figure credit: https://courses.lumenlearning.com/astronomy/chapter/the-electromagnetic-spectrum/

The atmosphere becomes opaque as one moves towards higher energy radiation (or shorter wavelengths; $E = h\, c/\lambda$). However, there are (and have been) space telescopes that operate at orbits above the Earth's atmosphere and observe UV-radiation, X-rays and gamma rays. For example Galaxy Evolution Explorer (GALEX) space telescope operated in the UV-regime. Some of the X-ray telescopes are; Chandra, The Roentgen Satellite (ROSAT), and The X-ray Multi-Mirror Mission (XMM-Newton), while Fermi and International Gamma-Ray Astrophysics Laboratory (INTEGRAL) operate in gamma-rays. In addition to these satellites, there have been balloon-borne experiments and space shuttle launches that gave us the opportunity to observe this high energy part of the electromagnetic spectrum.

The atmosphere is more transparent to longer wavelengths, therefore, infrared (partially) and radio waves can be observed from the ground. Observatories such as Gemini and Subaru can observe in the near-infrared regime from the ground. Satellites such as *Spitzer* and *Herschel* observed infrared emission from outside of the atmosphere, while the Stratospheric Observatory for Infrared Astronomy (SOFIA) telescope mounted on an airplane that flies at high altitudes providing observations of this regime.

Far-infrared and sub-millimeter emission can also be observed from the ground with radio telescopes such as the James-Clerk-Maxwell Telescope (JCMT), Institut de Radioastronomie Millimétrique (IRAM) 30 m telescope and the Nobeyama Radio Observatory (NRO) 45 m telescope. Longer wavelengths in the radio regime can be observed with, for example, the Effelsberg and the Green Bank Telescope (GBT).

2.6.1 *Observations of molecular clouds*

This particular thesis is focused on disentangling the properties of the Orion A molecular cloud and for this purpose, I would like to explain how the molecular clouds can be observed. As mentioned in Section 2.2, the molecular clouds are made mostly of molecules which can be observed in absorption and emission. In addition, molecular clouds can also be observed through line emission of atoms and of course, dust emission.

2.6.1.1 *Molecular line emission*

In order for a molecule to be observed, it either has to absorb or emit photons from a certain quantum mechanical state. These states are discrete and can be excited by collisions, photons and radiative (de)excitation. If the (de)excitation yields absorption or emission of a photon, then, this photon can be observed at a frequency that is proportional to the energy difference between the transition states ($\Delta E = h\nu$).

Unfortunately, the most abundant molecule in the Universe, H_2, cannot be used to study the molecular clouds, and the reason is as follows: molecular clouds are often cold (10 – 20 K), and hence, only the low energy states of molecules can be excited. The transitions between the lowest energy states are called the rotational transitions, and are followed by higher energy transitions allowed in vibrational and electronic states. The H_2 is a symmetric molecule and lacks a permanent electric dipole moment. Its electric quadrapole transitions, although observable, are very weak and require high energies to excite. Therefore H_2 cannot be used to trace the cold gas, but can be observed towards PDRs.

The rotational transitions can be observed in the sub-millimeter and millimeter regime, while the vibrational transitions are observed in infrared and the electronic transitions are observed in the optical regime. The rotational levels of the abundant molecules can be used to probe properties of clouds. CO (carbon monoxide[3]) is the second most abundant molecule in the ISM, because of its low excitation energy it is often observed instead of H_2 to trace the molecular gas. However, there is a portion of

3 Throughout this thesis the main carbon-monoxide isotope $^{12}C^{16}O$ is denoted as CO. The isotopologues $^{13}C^{16}O$ and $^{12}C^{18}O$ are denoted as ^{13}CO and $C^{18}O$, respectively.

the molecular gas that cannot be observed in CO, called the CO-dark gas. For a more in depth discussion on the CO-dark gas, I refer to Smith et al. (2014).

Although CO is abundant in all molecular clouds, it cannot be used to study all densities. As we know, from filaments to clumps and cores the density inside a molecular cloud increases. How far inside a molecular cloud we can see is measured by the optical depth, and in order to understand it, one must also understand the radiative transfer. The radiative transfer equation describes the propagation of radiation in the ISMand it is as follows:

$$I_\nu(\tau_\nu) = I_\nu(0)e^{-\tau_\nu} + \int_0^{\tau_\nu} e^{(\tau_\nu - \tau')} S_\nu \mathrm{d}\tau', \tag{2.7}$$

where $I_\nu(\tau_\nu)$ is the observed intensity that equals to the optical depth attenuated intensity of the observed source, plus the sum of the emission from the medium that is attenuated by the optical depth at each point. The term S_ν is called the source term and it depends on the characteristics of the medium. When the optical depth is large ($\tau >> 1$) the emission is called optically thick, whereas, when the optical depth is significantly small ($\tau << 1$) the emission is optically thin. Because CO is abundant, the emission from the CO molecules can be absorbed by the molecular gas and is radiated away only at the surface of the cloud. Therefore, CO is optically thick and through the CO emission seeing deeper into the cloud is not possible. The less abundant isotopologues ^{13}CO and C^{18}O are often used to trace denser regions in molecular clouds.

2.6.1.2 *Fine Structure Line Emission*

In this work I make use of ionized Carbon observations to trace the transition regions between the molecular gas and the atomic gas called PDRs. Throughout this work the ionized Carbon species is denoted as C^+, while the emission caused by the forbidden transitions from these species is denoted as [C II]. These transitions are called "forbidden" because in laboratory conditions no emission from these transitions can be measured due to collisional de-excitation. They are collisionally de-excited because the corresponding transitions are electric dipole forbidden and, hence, are either electric quadrapole or magnetic dipole which are very weak. In space however, where the densities are much lower, it is more likely that the atoms would emit a photon that corresponds to a forbidden transition line, than to be collisionally de-excited.

Fine structure states are energy levels that split from the main energy levels of an atom. The fine structure line splitting is caused by the interaction of the orbital momentum of an electron around the nucleus and its spin. This split was first observed for the Hydrogen atom by Michelson & Morley (1887) and later, Sommerfeld (1916) expanded the classical Bohr model to include relativistic corrections and introduced the "fine-structure constant" to characterize the amount of splitting between the energy levels.

In order to understand the fine structure transitions, we have to look at how exactly the orbital angular momentum and the spin angular momentum couple to one another. The total angular momentum of an atom (J) is the vectorial sum of total spin angular momentum of its electrons (S) and their total orbital angular momentum (L):

$$\mathbf{J} = \mathbf{L} + \mathbf{S} \tag{2.8}$$

Therefore J can have the values between $L+S$ and $L-S$ and this is known as the spin-orbit coupling that causes the fine structure energy levels. The notation to descrive these energy levels is simply: ${}^{2S+1}L_J$. For electron shells $S, P, D, F, ...$ L takes the values 0, 1, 2, 3, ...

Now we can look at the electron configuration of the Carbon ion specifically: $1s^2 2s^2 2p^1$ (for a thorough discussion, I refer to Draine 2011). The electron that is responsible for the fine structure splitting is the electron in the last shell (p-shell). As this electron is in the p-shell, the angular momentum $L = 1$. The spin angular momentum is $S = 1/2$, yielding $J = 1/2$ and $J = 3/2$. Therefore the fine structure transition of C^+ in the ground state is:

$$^2P_{3/2} \rightarrow {}^2P_{1/2}$$

This transition takes place in the infrared regime and can be observed at 1.9 THz.

2.6.1.3 *Dust continuum emission*

While the interstellar dust can be observed in extinction of starlight in the near-infrared regime, it can also be observed in emission in the far-infrared/sub-millimeter regimes as the dust continuum emission. The observed dust continuum emission in the far-infrared/sub-millimeter regimes is simply thermal radiation from the dust grains as a result of heating by the absorbed starlight. Cox & Mezger (1989) suggests that one quarter of the observed emission from a spiral galaxy originates from thermal dust emission.

The dust emission is, given a uniform dust temperature (T_{dust}) can be approximated as a modified blackbody function. Hence, the intensity at frequency ν is then given by:

$$I_\nu = B_\nu(T_d)(1 - e^{-\tau_\nu}), \tag{2.9}$$

where τ_ν is the optical depth as a function of the given frequency and $B_\nu(T_d)$ is the Planck function:

$$B_\nu(T_d) = \frac{2h\nu^3}{c^2} \frac{1}{e^{h\nu/kT_d} - 1}, \tag{2.10}$$

where h is the Planck constant, k is the Boltzmann constant and c is the speed of light. The optical depth is given by:

$$\tau_\nu = \int_{los} \kappa_\nu \rho dl, \tag{2.11}$$

where κ_ν is the absorption coefficient at the given frequency. The frequency dependent dust opacity is defined as:

$$\left[\frac{\kappa_\nu}{\mathrm{cm}^2\ \mathrm{g}^{-1}}\right] = \kappa_0 \left[\frac{\nu}{1000\ \mathrm{GHz}}\right]^\beta, \tag{2.12}$$

where β is the dust emissivity index. The dust emissivity index is depends on the properties of the dust grains such as the sizes and composition, but in the star forming regions it is found to be between 1 and 2 (Walker et al. 1990). The exact value of the coefficient κ_0 is not known, however at 1000 GHz, it is taken as 0.1 cm^2 g^{-1} (Beckwith et al. 1990). Assuming a gas-to-dust ratio (or can also be calculated as shown in Sánchez-Monge 2011) that is often taken as 110 (Sodroski et al. 1997), one can calculate the total volume density:

$$n_{\mathrm{H}_2} = \frac{1}{\mu m_H} \frac{X_{\mathrm{gd}}}{(4/3)\pi R^3}, \tag{2.13}$$

where μ is the mean molecular mass of the hydrogen atom, m_H is the mass of the hydrogen atom, X_{gd} is the gas-to-dust ratio and R is the radius of the cloud. Then, integrating over the line-of-sight the total column density can be calculated:

$$N_{\mathrm{H}_2} = \int_{los} n_{\mathrm{H}_2} dl, \tag{2.14}$$

as given in Sánchez-Monge (2011) this equation can be rewritten in practical units as the following:

$$\left[\frac{N_{\mathrm{H}_2}}{\mathrm{cm}^{-2}}\right] = 2.21 \times 10^{24} \left[\frac{X_{\mathrm{gd}}}{\mathrm{M}_\odot}\right] \left[\frac{\mu}{2.3}\right]^{-1} \left[\frac{\Theta_\mathrm{S}}{\mathrm{arcsec}}\right]^{-3} \left[\frac{D}{\mathrm{kpc}}\right]^{-3}, \tag{2.15}$$

where Θ_S is the beamsize of the observations and D is the distance to the observed object.

2.6.2 *Radio Astronomy and Radio Interferometry*

As most of this work is based on sub-millimeter observations, I will discuss further about radio astronomy and radio interferometry in this section. The radio sky is much more quieter than the visible sky because the emission from the Sun does not play an important role in longer wavelengths. Therefore, the radio observations can be carried out also during day time. One of the limitations of radio observations, on the other hand, is the water vapor in the atmosphere absorbing the emission at shorter radio wavelengths. Because of this reason, most radio telescopes that operate at shorter wavelengths are placed at dry regions and a few kilometers up in the mountains.

Radio telescopes consist of a large dish that is a parabolic reflector, a mount and the electronics that amplify the incoming signal and send it to the receiver on the back-end of the telescope. By the receiver, the signal is converted from power to digital signal which can then be analyzed using a computer. The Fourier transform of a single dish antenna's aperture, gives us the beam pattern that is composed of the "main-beam" (or "main-lobe") and the "side-lobes" as illustrated in Figure 2.12.

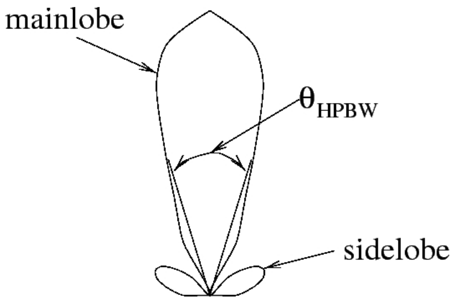

Figure 2.12: Beam pattern of a single dish telescope. Credit: http://gmrt.ncra.tifr.res.in/gmrt_hpage/Users/doc/WEBLF/LFRA/node29.html

The main-beam is the primary maximum response of the antenna, however, some of the emission is lost through the side-lobes. The width of the main-beam where its response drops to half of its maximum is called Half Power Beam Width (HPBW). HPBW is proportional to λ/D, where λ is the wavelength of the incoming radiation and D is the diameter of the telescope. Therefore, the resolution of a single-dish telescope depends on the observed wavelength and the size of the antenna. In order to achieve a higher angular resolution in the sky, the telescope size must be increased. However, building large telescopes is technically non-trivial and very expensive. Therefore, we use interferometers instead, which are composed of smaller sized telescopes but act as one large telescope. Figure 2.13 shows a simple sketch of a two-element interferometer.

The antenna pairs separated by the baseline d receive the signal which is then cross-correlated for each pair. The recorded phase difference between the antenna-pairs can be corrected when the data is calibrated (see Chapter 3). The correlated signal from an antenna pair is called a "visibility" and it is simply the Fourier transform of the observed emission from the source. The Fourier transform of the sky-plane ($xy - plane$) is called the $uv - plane$, and each visibility that comes from an antenna pair corresponds to a point in the $uv - plane$. In order to obtain a good map, the $uv - plane$ has to be sampled with as many baselines to prevent the loss of emission due to the gaps between the telescopes.

Instead of the diameter of a single telescope, the angular resolution of an interferometer depends on the longest baseline between the antenna pairs; the longer the baseline, the smaller scales can be resolved. Although, the baselines can be increased to improve the resolution, they can never be zero. This introduces the non-zero baseline problem. Because of the gaps between the antennas, an interferometer filters out the large scale extended emission. Therefore, interferometric observations are almost always combined with single dish observations to account for emission on all the observable size scales.

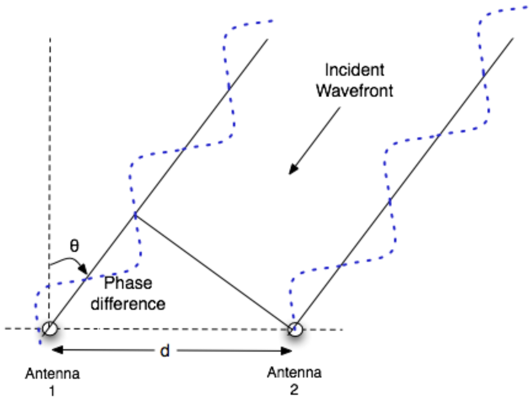

Figure 2.13: A simple interferometer. Credit: https://en.wikipedia.org/wiki/File:PhaseInterferometry.png

Part II

OBSERVATIONS AND TOOLS

The goal of the following chapters is to acquaint the reader with the astrophysical observations that are used for this work (see Chapter 3), present the analysis tools that I used and developed. One of the two major tools that I used is `DisPerSE`; an open source software for structure identification (see Chapter 4). The latter is `FilChaP`, a python-based tool for the analysis of the filaments that I developed and made publicly available (see Chapter 5). The tests on `FilChaP` and its functionalities are published in Suri et al. (2019) which can be found in Appendix B. Figures 4, A1, A2, A3 and A4 from Suri et al. (2019) are reproduced in this part of the thesis with permission ©ESO. I note, however, because the publication of the article superseded the submission of the thesis, some figures slightly deviate in the refereed and published version of Suri et al. (2019) from the ones presented in this part of the thesis.

3 OBSERVATIONS

In this chapter, I elaborate on the acquisition, preparation and highlights of the science data that is utilized in this thesis work. The majority of this work is based on the data observed within the framework of the CARMA-NRO Orion Survey (Kong et al. 2018), where we combined a set of interferometric data (see Section 3.1.1) and a set of single dish data (see Section 3.1.2). In the CARMA-NRO Orion Project, I have contributed to the observations at Combined Array for Research in Millimeter-wave Astronomy (CARMA), and was responsible for the data reduction between 2014-2015 while the data acquisition still continued. Additionally, I have contributed to the earlier efforts to combine interferometric and single dish data. I am also a part of the C^+ Square Degree Project, and made use of [C II] emission data that is further explained in Section 3.2. I, additionally, used the *Herschel* dust column density and temperature maps from Stutz & Kainulainen (2015). For the details on the derivation on the dust column density and temperature maps I refer to the corresponding paper.

3.1 THE CARMA–NRO ORION SURVEY

3.1.1 *CARMA Observations*

CARMA[1], was a 23-element interferometer in California, USA (see Figure 3.1). It composed of 6 antennas with a size of 10.4 meters, 9 antennas with a size of 6.1 meters and 8 antennas with a size of 3.5 meters. The array operated at frequencies 30 – 250 GHz, or wavelengths 1 cm – 1 mm. With the longest baselines at 230 GHz, the array could reach a 0.15 arcsec angular resolution; at the distance of Orion A, this translates to a spatial resolution of 0.003 pc $\approx$ 620 AU. The array alternated between different configurations for varying baselines, that are listed below from the longest baseline with the most extended to shortest baseline with the most compact configurations:

- A configuration (extended): 0.25 – 2 km
- B configuration: 100 m – 1 km
- C configuration: 30 – 350 m
- D configuration: 11 – 150 m
- E configuration (compact): 8 – 6 m

1 CARMA has shut down in April 2015.

Figure 3.1: The CARMA interferometer. (Credit: J. Kauffmann)

The CARMA Orion Key Project (PI: Dr. John Carpenter, the project was later named CARMA-NRO Orion Survey) was granted approximately 1500 hours of observing time at CARMA and the observations took place between 2013–2015. A 2 square degree area towards the Orion A molecular cloud was divided into subfields of 6 arcmin x 6 arcmin with a total number of subfields 181. Each subfield was observed at 3 different hour angles in order to obtain a good *uv* coverage. Furthermore, each of these subfields was observed using 126 pointings with hexagonal Nyquist sampling, with each pointing observed approximately for 15 seconds. The observations were done in the two most compact configurations of that array; CARMA D and E configurations. The CARMA D and E configurations provided minimum and maximum baselines of: 11–150 m and 8–66 m, as listed above. This in angular scales translates to 4.5 – 62 arcsec with D configuration at 110.2 GHz, and 10–85.5 arcsec with the E array. The two configurations were chosen such that the observed spatial scales have an overlap, therefore they can be combined together, resulting in a final angular scale coverage from 4.5 to 85.5 arcsec.

The array receivers were tuned to observe ^{12}CO(1–0), ^{13}CO(1–0), C^{18}O(1–0), CS(2–1), CN(1–0), SO(2–1) and 3 mm continuum emission simultaneously. The CO isotopologues towards the same region was also mapped using the NRO 45m telescope, and then, combined with the interferometric dataset. The final rms and spectral resolution for the combined datasets are shown in Table 3.1. As the rest of the interferometric data are yet

Table 3.1: Specifics of the CARMA Observations

Transition	Frequency [GHz]	Velocity Resolution [km s^{-1}]	rms [K]
^{12}CO(1–0)	115.27	0.25	0.86
^{13}CO(1–0)	110.201	0.22	0.64
C^{18}O(1–0)	109.782	0.22	0.47
CS(2–1)	97.981	0.08	–
CN(1–0)	113.490	0.07	–
SO(2–1)	109.252	0.26	–
continuum	101 & 111.8	–	–
continuum	102 & 110.8	–	–

to be combined with single dish data, they have no final rms values, and the indicated velocity resolutions correspond to velocity resolution in the initial correlator setup.

3.1.1.1 *Calibration*

Data reduction is a crucial step in order to deduce the source fluxes. There are features of the telescopes, receivers and the atmosphere that affect the observed flux, therefore need to be eliminated when preparing for the version of the data that is scientifically acceptable. In order to calibrate the data, 3 different calibrators are used, namely: flux, gain/phase and bandpass calibrators. These calibrators are often selected to be point like sources, often bright quasars, in order to ensure that all the baselines detect the same amount of flux, in a relatively short amount of time.

The calibration of the data during and after data acquisition was performed using Multichannel Image Reconstruction, Image Analysis and Display (miriad) radio interferometry data reduction software (Sault et al. 1995) using a customized bash script that was developed and optimized for CARMA by Dr. John Carpenter.

The *bandpass calibration* is used to calibrate the receiver response for each frequency window. This is usually done by looking at a bright quasar with no bright spectral lines. Alternatively, during recent Atacama Large Millimeter/submillimeter Array (ALMA) observations, planets and satellites for which the spectral lines can be modeled in detail are also being used. In the case of our CARMA observations the observed quasars were primarily 3C84 and also, 0423–013 and 0532+075.

The *gain/phase calibration* helps correct for the phase variations over time. It is desirable that the observed, preferentially, quasar is close to the object of interest for the observations. This prevents large atmospheric changes when moved from the calibrator to source. For the gain calibration we observed quasar 0532+075 every 20 minutes.

Figure 3.2: The NRO 45 m telescope. Credit: NRO

Within the observed period of 20 minutes the phase variations in the atmosphere are not large, and therefore, can be tracked, in order to perform calibration.

The *flux calibration* is used to calibrate the absolute flux scale of the observed sources. This is done by looking at a bright object with a well-know flux, and therefore, having corrections for amplitude over time. Flux calibration during the CARMA observations were done using Uranus, Mars and when both not observable 3C84.

3.1.2 *NRO45m observations*

The NRO 45m telescope (NRO45m, see Figure 3.2) is a single radio antenna located in Nobeyama, Japan. The 45 meter dish telescope observes at a wavelength regime between 20 GHz ($\sim$1 cm) and 115 GHz (3 mm). This gives the telescope an angular resolution of 15 arcsec at 115 GHz.

The NRO45m observations of ^{12}CO, ^{13}CO and C^{18}O were taken in two steps with two different receivers. Between 2007 and 2009 the The 25-Beam Array Receiver System (BEARS) receiver was used (Sunada et al. 2000). These observations are well described in Shimajiri et al. (2014). More recently, to extend the single dish map in order to match the CARMA coverage, the new dual-polarization 4-beam receiver, the Four beam Receiver System on 45m-Telescope (FOREST), Minamidani et al. 2016, was used. The FOREST observations took place between 2014 and 2017, and the process is described in Kong et al. (2018).

The BEARS receiver observations took in separate parts, as the simultaneous observations of all the CO isotopologues with the given bandwidth (32 MHz, Sorai et al. 2000) were not possible. Therefore the ^{12}CO observations took place first, between 2007 and 2009 (Shimajiri et al. 2011). The ^{13}CO and C^{18}O observations took place between 2013 and 2014 (Shimajiri et al. 2014, 2015). The CO isotopologues were observed with an original velocity resolution of the receiver; 0.1 km s^{-1} . The resulting maps, however, were convolved to 0.3 km s^{-1} to reach an rms level of 0.7 K in ^{13}CO and 0.2 K in C^{18}O, and to 1.0 km s^{-1} for ^{12}CO to reach an rms level of 0.94 K. The resolution of these observations are 0.03 pc with an effective beamsize of 15 arcsec at 115 GHz.

During the FOREST observations, all three CO isotopologues were observed simultaneously Spectral Analysis Machine for the 45m telescope until December 2016. As the receiver settings were changed after, the observations of ^{13}CO and C^{18}O were carried out separately. For these observations the Spectral Analysis Machine for the 45m telescope (SAM45) which allowed for larger bandwidth (63MHz) and resolution (0.04 km s^{-1}) compared to BEARS observations. The final effective beamsize of the NRO45m observations is 22 arcsec, resulting in an spatial resolution of 0.04 pc.

3.1.3 *Joint imaging of the CARMA and NRO45m data*

Although the interferometers provide us with a unique, detailed look of the observed region, they are not perfect instruments. The fact that the shortest spacing between the elements of an interferometric array can never be zero means that an interferometer can never 100% recover the information on the extended structures in the observed region. In order to account for the missing flux caused by the gaps between the antennas, the interferometric data is often combined with a single dish (SD) data. The combination allows for recovering the information on large scales (with the SD) and on scales that are well resolved (with the interferometer). For the CARMA-NRO Orion Survey, `miriad` is utilized for this task. The combination and joint imaging of the data is explained thoroughly in Kong et al. (2018). The survey team has followed the milestones set by Koda et al. (2011), and a schematic explanation on the process is given in Figure 3.3. Going along this scheme, following the arrows, the data combination process starts with having the data from both observatories. we start with the data from both observatories. For the interferometer, we follow the standard data reduction explained above, and obtained calibrated visibilites. For the single dish data, we followed the standard data reduction and obtain a datacube (image) for each molecular line. This datacube was then Fourier transformed and sampled with a gaussian distribution of visibilities to produce visibilities for the single-dish data. The single-dish visibilities are then combined with the interferometer visibilities to finally produce the final image.

Below I explain the critical steps of the data combination process in more detail:

- **Flux Scaling Factor**: In order to combine the NRO45m data with the interferometric data in the *uv*-plane, our team first investigated the *flux scaling factor* between

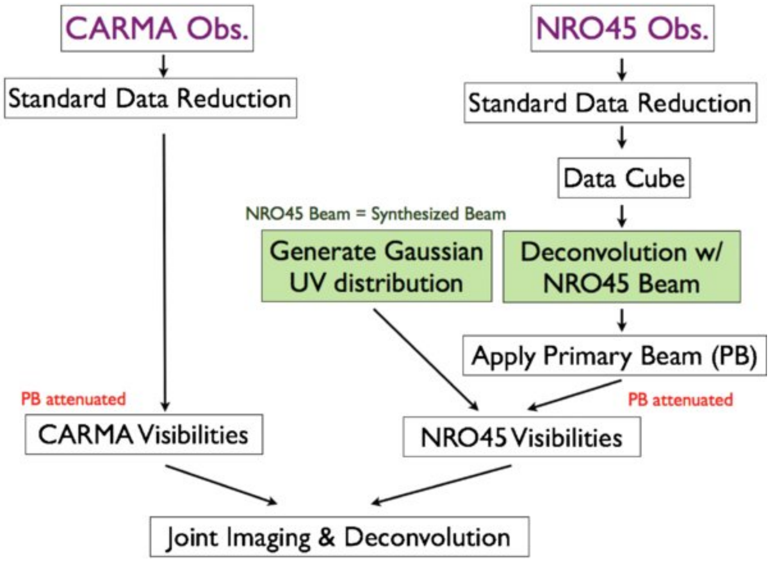

Figure 3.3: Flow chart of how CARMA and NRO45m data was combined (taken from Koda et al. (2011), Figure 4).

the CARMA image, and visibilities created from the NRO45m data. The flux scaling factor is the comparison between the fluxes observed by the interferometer and the single dish telescope. As a first step, the NRO45m data is regridded to the same pixel size as CARMA (both in velocity and spatial pixels), and deconvolved with the NRO45m beam. The deconvolution of the NRO45m map is done by using the `demos` task within miriad. During this task a dummy primary beam response to each de-mosaicked pointing is added. This is simply because, the imaging task `invert` that will be used in the next step will correct for the primary beam response. Then, using the task `uvmodel` the NRO45m pointings visibility distribution that mimicks the CARMA visibility distribution is created. The entire *uv* domain that the CARMA spans is (0–17 kλ), but for the combination a common range of visibilities from the both telescopes is selected (3–6 kλ). The common range of visibility sets are, then, transferred from the Fourier domain back to the image domain using the `invert` task. Finally the flux scaling factor between the two maps (CARMA and NRO45m visiblities) are calculated. These flux scale ratios in the common range of visibilities ($F_{\mathrm{CARMA}}\,/\,F_{\mathrm{NRO45m}}$) are; 1.6 for ^{12}CO and 1.5 for ^{13}CO and C^{18}O (see Kong et al. (2018) for a detailed discussion).

- **Joint imaging and deconvolution**: Once the flux scaling between the two maps is determined, the datasets can be combined, once again in the *uv* domain. For this, the flux scale corrected NRO45m image is deconvolved and transferred back to the Fourier space as described above. A random set of NRO45m baselines were generated using the task `hkuvrandom`. Then, the `uvmodel` task is used to generate

Table 3.2: Properties of the combined maps.

Transition	Beam [arcsec]	PA [deg]	ΔV [km s^{-1}]	σ_K [K]
^{12}CO(1–0)	10×8	-13	0.25	0.86
^{13}CO(1–0)	8×6	10	0.22	0.64
C^{18}O(1–0)	10×8	-0.4	0.22	0.47

visibilities for each pointing. The newly created NRO45m visibilities and the existing CARMA visibilities are transformed back to the image domain together using the `invert` task as a combined dirty cube. Each channel of the dirty cube is then cleaned (deconvolved) using `mossdi2` task until the stopping intensity threshold (3 times the rms noise) is reached.

All CO isotopologues observed with CARMA are combined with the single dish data from the NRO45m telescope. The final beamsize, beam position angle (PA), velocity resolution (ΔV) and the rms per velocity channel in main-beam temperature units (σ_K) of the combined maps are presented in Table 3.2.

3.1.4 *The combined CO datasets*

In this subsection, I present and describe the structure seen in the combined CARMA-NRO datasets. In order to be able to convey the kinematic information along with the integrated intensity of the structures seen, I use 3 color (RGB) images of the region (Figures 3.4, 3.5, 3.6 for ^{12}CO, ^{13}CO and C^{18}O) that are adopted from Kong et al. (2018). Each color represents the integrated intensity of a certain velocity range; red from 9.8 – 12.1 km s^{-1} , green from 7.3 – 9.6 km s^{-1} and blue from 4.8 – 7.1 km s^{-1} . Some of the most relevant star forming regions are marked on each map. The extent of ^{12}CO and ^{13}CO is slightly larger because of the amount of diffuse gas contained in the southern region. The maps span an extensive area from -5 to -7° in declination; and include OMC-1, OMC-2, OMC-3 and OMC-4 in the north, L1641-N and NGC1999 clusters in addition to a variety of HH objects in the south. The imprint of the expanding Veil Bubble on the molecular gas is visible in ^{12}CO. This region is known as the KH-ripples (KH; Kelvin-Helmholz instability) and was discovered by Berné et al. (2010). The instability that produced the KH-ripples is caused by the two interacting phases of the gas; the high-velocity plasma fluid that is produced by the high-mass stars, and the low velocity, dense molecular gas. The northern portion of the gas, close to the star forming region OMC-3, is the under influence of yet another bubble; the NGC1977 driven by a B0 star. Both bubbles are observed in ionized Carbon, C$^+$ emission shown in Figure 3.7. Additionally, the dense C^{18}O gas highlights the filamentary structure of the cloud.

In addition to the bubbles, arcs and filaments, these maps bear a surfeit of kinematic information. The cloud has a striking large-scale velocity gradient where north of the ISF is redshifted with velocities of 11 km s^{-1}, whereas below OMC-1 the gas is a mixture of green and blue velocities, and blue dominating in the most southern tip of the observed area with velocities of $\sim$ 5km s^{-1}. The most active and dense region in the entire map, the OMC-1, shows complex kinematics in ^{12}CO and ^{13}CO due to the overlapping information from the gas that is exposed to stellar feedback and possible infall (Hacar et al. 2018) and/or explosive outflow motions (Bally et al. 2017). The southern part of the ISF and the L1641 cloud show structures that have a mixture of blue and green velocities. Using NRO45m ^{12}CO observations (Nakamura et al. 2012) suggested cloud-cloud collisions as an explanation for the existence of a mixture of structures with different velocities around the L1641-N region.

Additionally, the channel maps of the CO isotopologues are presented in Figures A.1, A.2, A.3. These figures demonstrate the plethora of information encompassed in the combined maps.

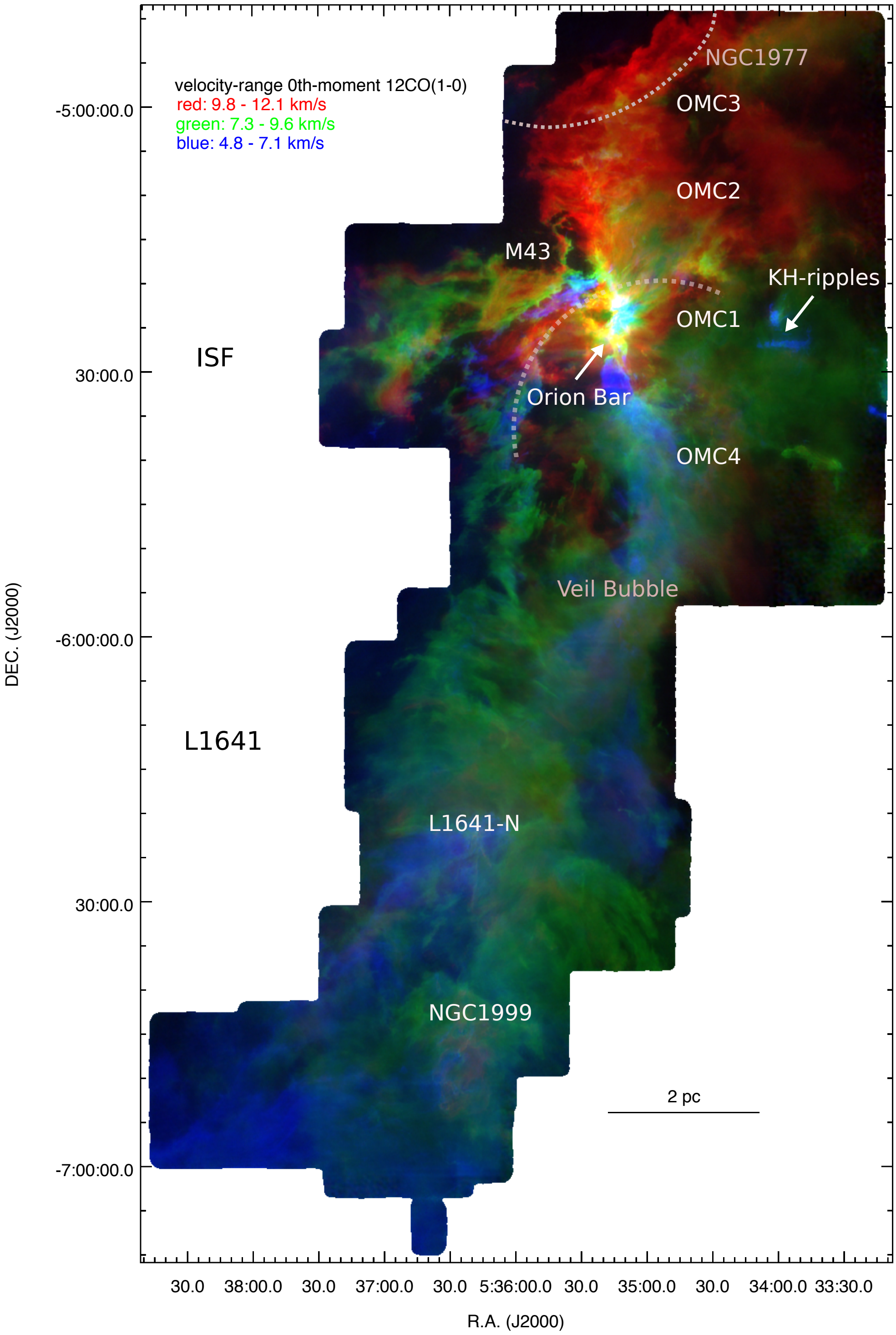

Figure 3.4: ^{12}CO RGB map, adopted from Kong et al. (2018).

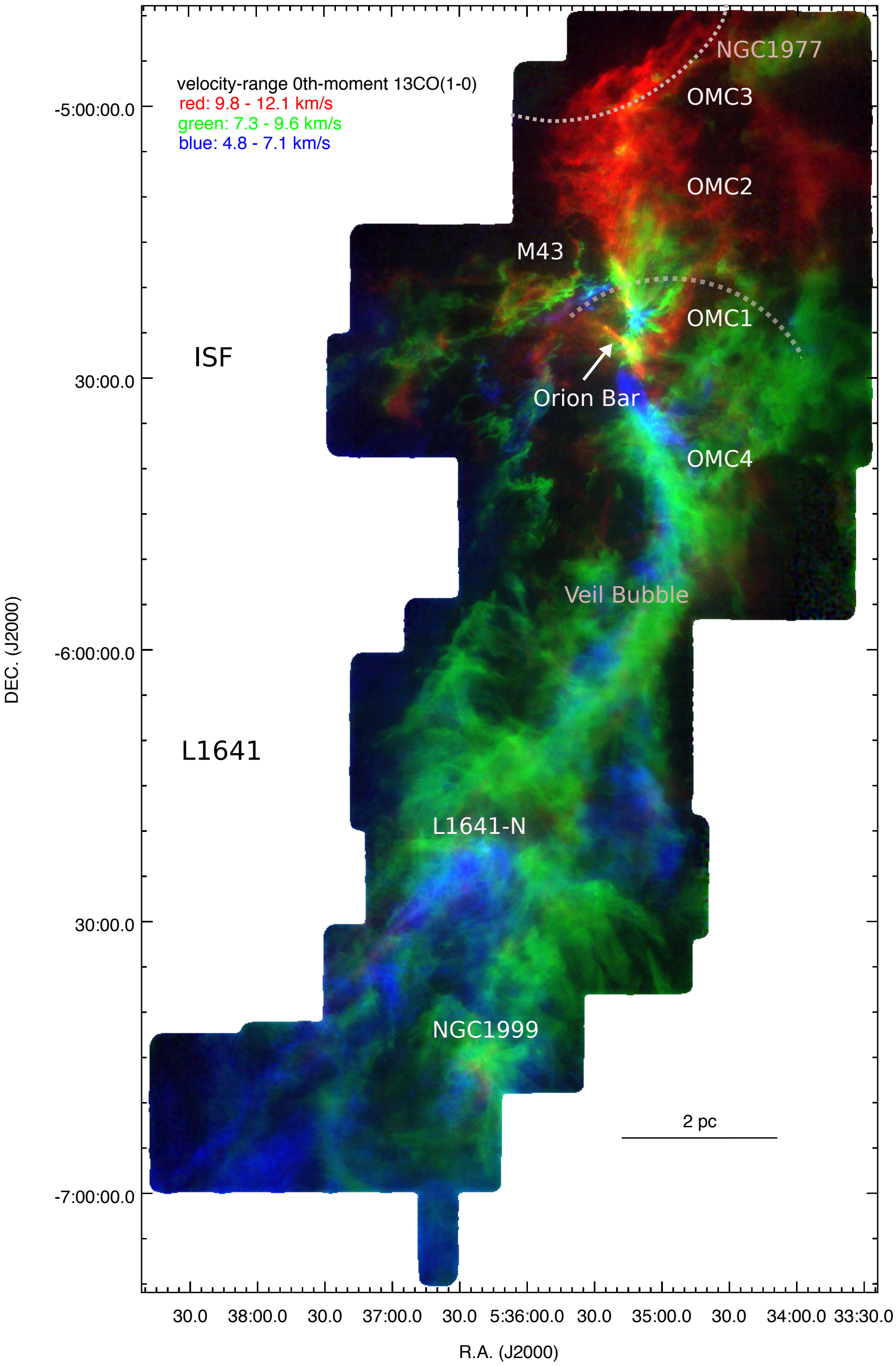

Figure 3.5: ^{13}CO RGB map, adopted from Kong et al. (2018).

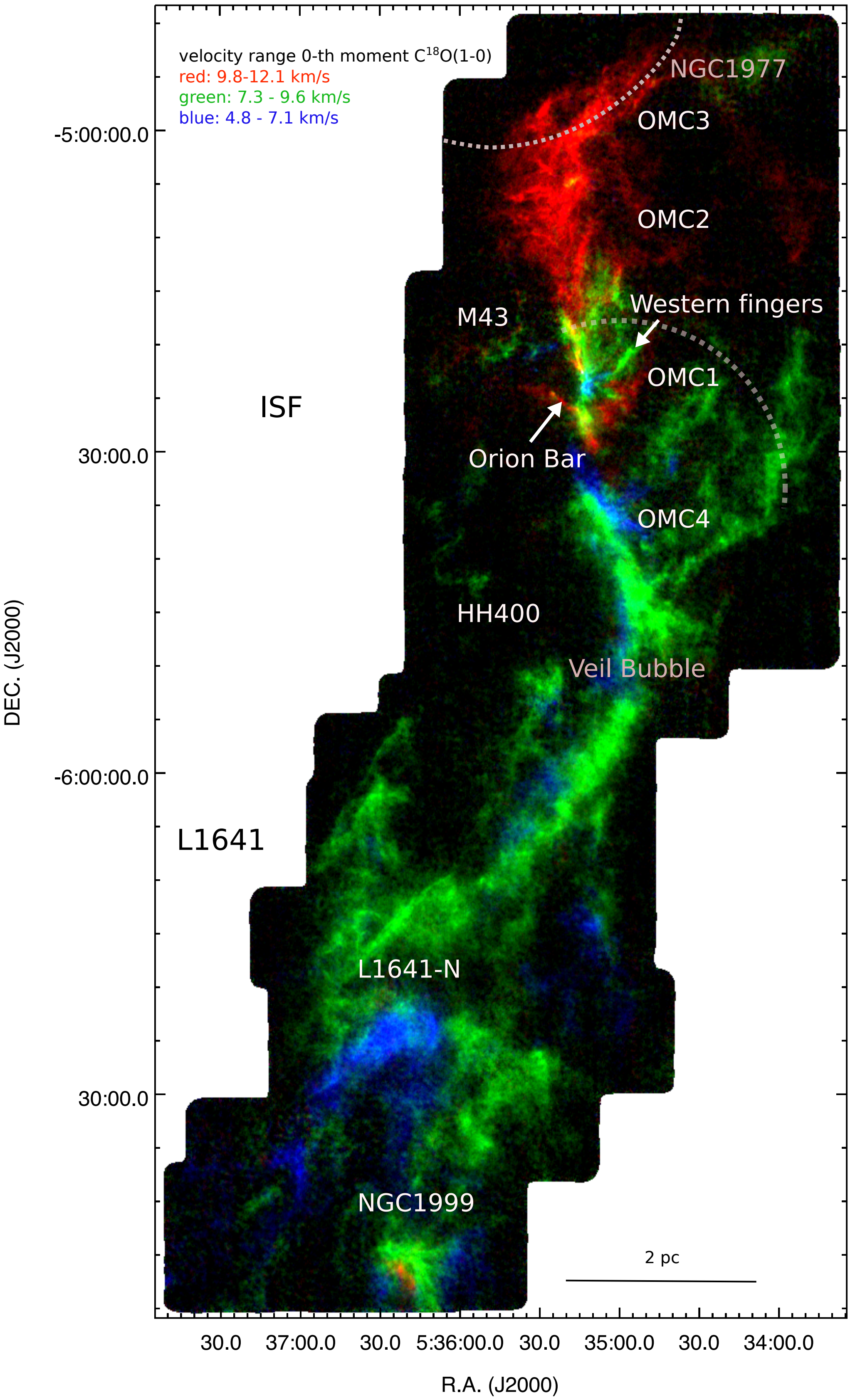

Figure 3.6: $C^{18}O$ RGB map, adopted from Kong et al. (2018).

3.2 C$^+$ SQUARE DEGREE PROJECT (C$^+$ SQUAD)

In addition to the CARMA-NRO Orion Survey, the work presented here also makes use of the [C II] emission data obtained within the framework of the C$^+$ SQUAD Project (PI: Alexander Tielens). The C$^+$ SQUAD team observed large scale [C II] emission using the SOFIA telescope.

3.2.1 *SOFIA Observations*

SOFIA is a 2.7 m single-dish telescope, mounted on a Boeing 747SP NASA aircraft (Becklin & Gehrz 2009). It is a joint project by NASA, and Deutsches Zentrum für Luft- und Raumfahrt (DLR). The SOFIA observations are executed above 99% of the water vapour in the atmosphere, at 12–14 km of altitude. SOFIA has 6 receivers (EXES, FIFI-LS, FORCAST, FPI+, GREAT, HAWC+) with a total wavelength coverage from 0.3–1600μm. The [C II] observations made use of the upGREAT receiver for the [C II] observations. upGREAT is a 14-pixel heterodyne receiver, an updated version of the single pixel German Receiver for Astronomy at Terahertz Frequencies (GREAT) receiver (Heyminck et al. 2012). upGREAT operates between 1.2 and 4.7 THz and is developed in Bonn and Cologne (PI: Rolf Güsten, MPIfR). The team has spent 42 hours of observing time to obtain a high sensitivity [C II] map of Orion A, that spans a degree (7 pc) in declination and right ascension.

The data reduction was done using Grenoble Image and Line Data Analysis Software (GILDAS)[2] developed by IRAM-Grenoble. The final data product has a 0.3 km s^{-1} velocity and 16.7 arcsec angular resolution (0.03 pc in spatial scales), and an rms of $\sim$ 1.5 K per velocity channel. This is the first large scale, velocity resolved, the [C II] map of Orion A that has ever been observed. The resulting channel maps are shown in Figure A.4; from -1.9 km s^{-1} to 14.3 km s^{-1} with 0.9 km s^{-1} increments.

3.2.2 *The [C II] dataset*

To exploit the amount of structure and kinematic information seen in the [C II] map, in Figure 3.7 I present an RGB image of the peak intensity of the emission. The reason why the peak intensities are used instead of integrated intensities (in contrast to the CO maps presented above) is the higher noise level present in the [C II] map, and when integrated, noisy features become more apparent. The red colors correspond to the peak intensities between 9.4 and 14.3 km s^{-1}, greens to 5 and 9.4 km s^{-1} and blue colors to -1 and 5 km s^{-1}.

The most fascinating structure seen in the [C II] map is the Orion Veil Bubble. The Veil Bubble is powered by energetic stellar winds from the O-stars of the Trapezium

2 http://www.iram.fr/IRAMFR/GILDAS

cluster at the heart of OMC-1. The features of the expanding bubble is carved into the diffuse ionized gas. The NGC1977 bubble in the north, in addition to the M43 and M42 H II regions can be seen in great detail.

The [C II] map, as the maps of the CO isotopologues, contains remarkable kinematic features. Similarly, the large-scale, north-south velocity gradient is also imprinted on the diffuse gas traced by the [C II] emission. The Veil shows a highly asymmetric behavior, with the eastern side of the peak emission having higher velocities (green) than to western side (blue). This is simply because the observer sees two sides of the expanding bubble, the one that is going away from us and the one that is approaching. The detailed analysis of the kinematics of this spectacular bubble, I refer to Pabst et al. submitted to Nature. Immediate south of the Orion Bar shows clear redshifted emission that is probably due to the expansion of the H II region. The exceedingly complex kinematics of the OMC-1 region seen in [C II] emission is coincident with the information that can be extracted from the ^{12}CO map shown in Figure 3.4. The western fingers have a mixture of green and blue velocities in addition to the Orion bar that appears to be more orange. At green velocities, the extension of the Orion Bar towards the south-west can be seen. This extended bar is not visible in the CO maps, but was previously observed in H I emission (van der Werf et al. 2013).

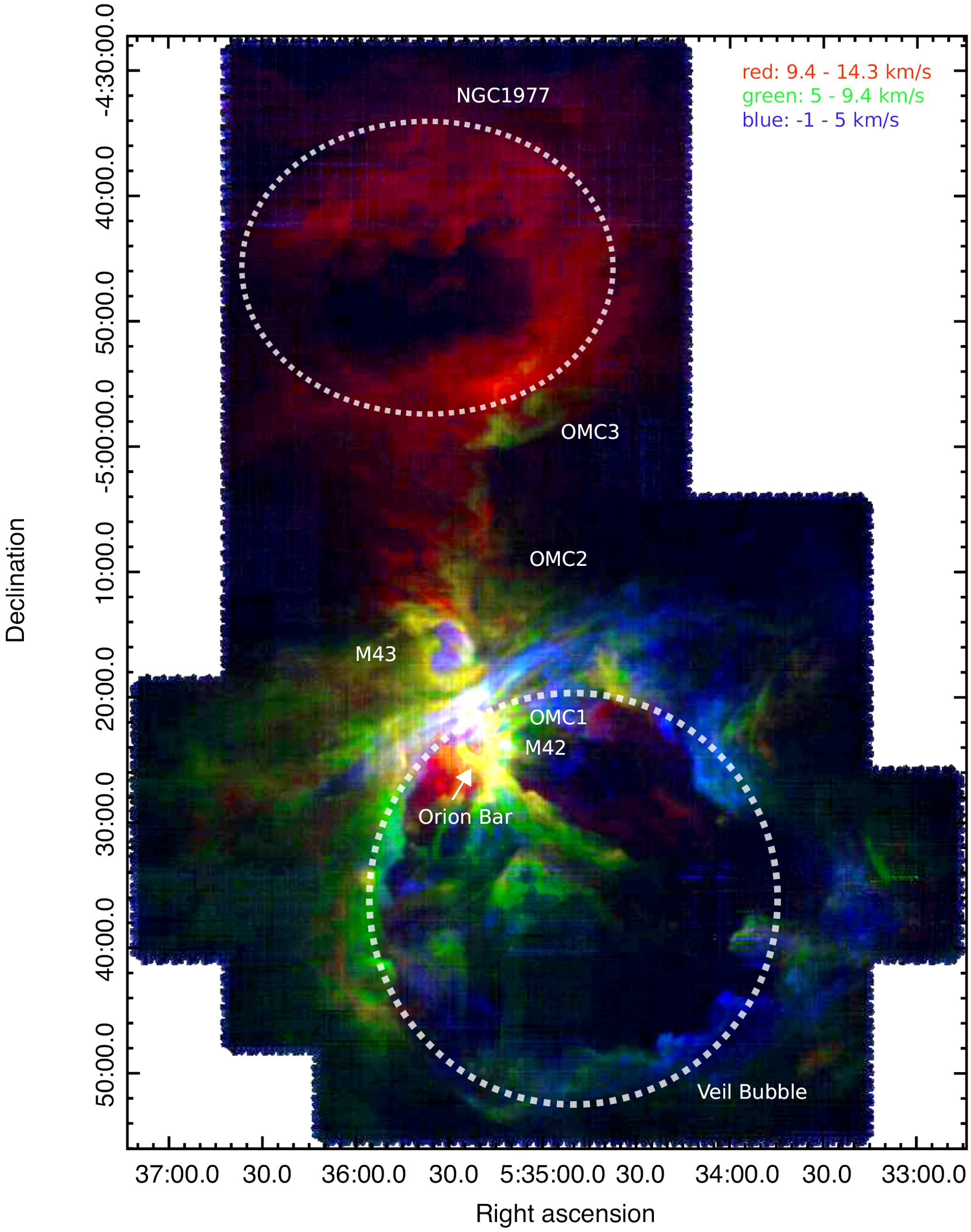

Figure 3.7: [C II] emission RGB peak intensity map.

4 DISPERSE: DISCRETE PERSISTENT STRUCTURES EXTRACTOR

4.1 FILAMENT IDENTIFICATION WITH `disperse`

In many previous studies (e.g. Arzoumanian et al. 2011; Schneider et al. 2012; Palmeirim et al. 2013; Panopoulou et al. 2014), the filaments were identified either on column density or integrated intensity maps that are only 2D (position-position). We would like to identify our filaments in the spectral line cubes in 3D (position-position-velocity). Amongst the commonly used structure identification algorithms such as getfilaments (Men'shchikov 2013) or FilFinder (Koch & Rosolowsky 2015), DisPerSE, Sousbie 2011) is the only one that can handle 3D datasets. Therefore, to ensure reproducibility we use `DisPerSE`; an automatic way to identify filaments.

4.1.1 *Methodology*

`DisPerSE` is designed to identify topological features such as peaks, filaments or voids in a given dataset. These features are identified using the "Discrete Morse Theory" (Forman 2002), and the noise in the data is dealt with an application of the "Persistence Theory" (Edelsbrunner et al. 2000).

In the simplest form; many astrophysical objects can be realized as distinct topological features. The Morse Theory (Milnor 1963), provides a definition for these structures. For example ascending or descending manifolds can be representative of filamentary structures; both in molecular clouds or in the cosmic web simulations, their stagnation points – the critical points, representing star clusters or dark matter halos. The Morse Theory, however, mathematically is only applicable to smooth, well defined and twice differentiable Morse functions. The astropyhsical observations (or simulations) are, on the other hand, discrete. Therefore, `DisPerSE` relies on the *Discrete* Morse Theory that is introduced for the first time by Forman (2002). Instead of assuming a continuous Morse function, the Discrete Morse Theory assigns discrete values to each cell.

In order to understand all the nomenclature mentioned in the above paragraph I give the definitions of these topological terms related to our filament identification:

- **Critical Points:** If the gradient of a function is equal to zero at point P; $\Delta_x f(\mathbf{p}) = 0$, then point P, with the coordinate $\mathbf{p}$ is a critical point of that function.
- **Morse Function:** A Morse function is a smooth generic function and its critical points are by definition non degenerate. Hence, for any critical point P; $\mathcal{H}_f(\mathbf{p}) \neq 0$ where $\mathcal{H}_f(\mathbf{p})$ is the *Hessian* matrix and $\mathcal{H}_f(\mathbf{p}) = d^2 f / dp_i dp_j(\mathbf{p})$.

- **Arcs:** An arc is a curve whose starting point and destination is a critical point. Arcs trace the gradient of the field.
- **Filaments:** A filament is composed of 2 arcs that start from the same saddle point and connect two maxima to one another.
- **Morse-Smale Complex (MSC):** a topological tessellation that contains information on how critical points and arcs are connected. Figure 4.1 illustrates a 2D density field (left) and its MSC (right).

For further definitions and detailed mathematical background of the Morse Theory, I refer the reader to Sousbie (2011).

Using the Morse Theory, `DisPerSE` calculates the MSC of a given dataset. However by definition, each critical point will be connected to another one with no restriction, leading to identification of a copious number of filaments. In addition, the existence of noise in astrophysical datasets leads to identification of critical points that are essentially not related to the underlying physical structure. Therefore, `DisPerSE` uses an additional concept, *persistence*, in order to evaluate which of these structures in the MSC are more prominent, and hence, more likely to be a real feature of the dataset. Persistence is defined as the difference of the values between two critical points that are connected with an arc (critical point pair). Hence, persistence defines the contrast between the critical points in a pair; the maxima and the saddle points. A high persistence level means that the maximum has higher contrast with respect to its surroundings. Eliminating those pairs with low persistence, in turn, leaves us with the most prominent structures that stand out from the rest. In addition to the persistence threshold, one can set up a detection threshold to eliminate peaks created by noise. This threshold is usually set to be a product of the noise level.

4.1.2 *User defined parameters*

`DisPerSE` is available for download and has an extensive tutorial for understanding its functions and user defined parameters[1]. Here, I will focus on the key parameters that play a vital role in determining the shape and number of filaments identified.

`DisPerSE` 's main function is called `mse` which calculates a MSC of a given dataset, and it can be directly run on a FITS[2] (Flexible Image Transport System). The persistence parameter is given to `Mse` as an argument. This can be set through two different ways. With the option `-interactive`, `DisPerSE` plots a persistence diagram where all the critical point pairs are plotted, and user can decide by eye where to set the persistence threshold. An example persistence diagram from the `DisPerSE` tutorial (see link on the

1 http://www2.iap.fr/users/sousbie/web/html/indexd41d.html

2 Most observational datasets come in or can be converted to the FITS format, however, `DisPerSE` can be applied to datasets in a regular grid or an unstructured network.

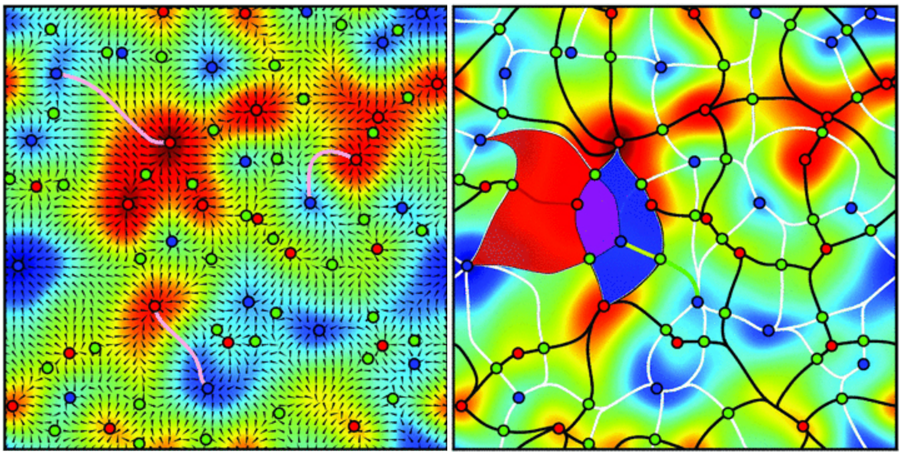

Figure 4.1: Left: A density field with gradient. The color scale indicates the gradient of the density field, with small black arrows marking the direction the gradient. The red, green and blue circles represent maxima, saddle points and minima, respectively. The pink lines indicate arcs that connect minima and maxima. Right: MSC of the density field shown in the left panel. The black lines that represent filaments (maxima - saddle point connections) and white lines represent anti-filaments (minima - saddle point connections). The blue, red and purple regions represent a descending manifold, and ascending manifold and their intersecting region, respectively. Filaments are the ridges of these manifolds. The yellow and green curves are arc connecting two minima and originating from the same saddle point. Credit: Sousbie (2011).

figure) is shown in Figure 4.2. The diagram shows a 2D histogram of the critical point pair distribution based on a column density map. The y-axis is the persistence (the difference between densities of the critical points in a pair) and the x-axis is the lowest density value of a pair. The pink dash-dot line marks the persistence threshold set by the user by eye. It can be seen that this threshold is set at a level above which the points stand out from the bulk of the distribution. These points above the threshold represent high persistence pairs; or in other way structures that are more prominent compared to the rest. In order to set the threshold the user can use Ctrl+left click, adjust it up and down by holding the Ctrl key and dragging the line around. When the threshold is at the desired position it can be applied to the MSC, that is already calculated prior to this point, by clicking Done on the diagram window. Another way to set persistence is without using the diagram. This can be done using the `-cut` option of `mse`. Unlike `-interactive`, `-cut` option is followed by a number, that is the absolute value of the desired threshold. The user can already decide this without seeing the persistence diagram, simple by setting the threshold as a factor of the noise rms in the data. Therefore a simple first step to running `DisPerSE` from the command line is as following:

```
> mse fitsFile.fits -interactive -upSkl -periodicity 0
```
or
```
> mse fitsFile.fits -cut 6.2e+20 -upSkl -periodicity 0
```

where the `-upSkl` option is set to identify filaments that connect maxima to saddle points. Anti-filaments, or void filaments, can be identified by using the option `-downSkl`. By default `DisPerSE` assumes periodic boundaries for the dataset. This is disabled by setting `-periodicity` to 0.

Once one of the above commands is run, `DisPerSE` produces a .MSC file where all the MSC information is stored. This file can be reused with the option `-loadMSC` followed by the name of the MSC file. This allows `DisPerSE` to skip the calculation of the MSC, and use the already existing one. The second file that `DisPerSE` produces through `mse` is an .NDSkl file. This is the so-called *skeleton file* where the information of filaments after the application of the persistence threshold is stored.

The next step is naturally to extract the information on filaments to a format with which we can work. Therein, the second command that needs to be run is `skelconv`. The `skelconv` command allows us to make further adjustments on the skeleton (e.g. smooth, assemble, etc) and write it as a FITS, ASCII or vtp file. Before we produce our final skeleton, we have to eliminate the filaments that are produced by noise. There can be cases where the noise in the data produces critical point pairs with high contrast, hence, high persistence. With `skelconv` we can set up another user defined cut level; the detection threshold. The detection threshold can either be visually inspected on the persistence diagram or can be set as a product of the noise level that is a known parameter for most observational datasets, or can be easily calculated.

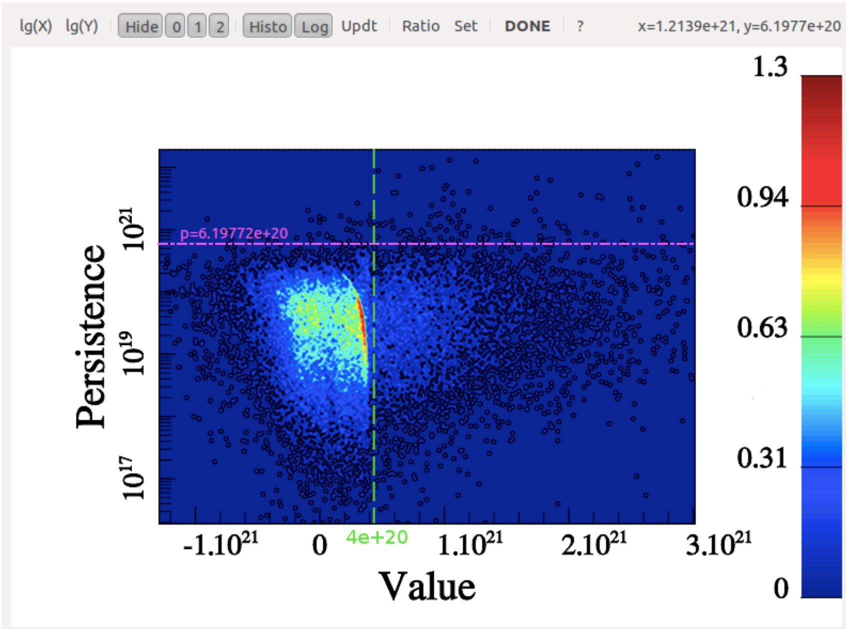

Figure 4.2: Example persistence diagram. The plotted distribution is the distribution of critical points. On the x-axis, the lower density of the two critical points in a pair is plotted. On the y-axis, the difference between the densities of the critical points is plotted. The pink line marks the persistence threshold, and the green dashed line marks the detection threshold. Image taken from `http://www2.iap.fr/users/sousbie/web/html/index55a0.html?category/Quick-start`

An example detection threshold is set on Figure 4.2 with a green dashed line. According to this diagram, now the only critical points that will be in the final skeleton are the ones that are above both the detection and the persistence threshold. These points are located on the upper right corner of the diagram. Unlike the persistence threshold, the detection threshold is set using the `skelconv` command. The second command, therefore, we run on the dataset is as follows:

```
> skelconv skeletonfile.NDSkl -breakdown -smooth 6
      -trimBelow 4e+20 -assemble 70 -toFITS
```

where the detection threshold is set by the `-trimBelow` option that is followed by the value of the threshold. The `-breakdown` option sets dummy critical points so that the arcs do not overlap with one another. As `DisPerSE` works on a pixel basis, depending on the resolution of the data the identified filaments can look wiggly. This can be smoothed out by using the `-smooth` option followed by a number that represents the number of pixels over which the filament should be smoothed. In the example above, this number is set to 6. `DisPerSE` also allows for connecting smaller filaments together to form larger structures. This can be done using the `-assemble` option. If two filaments form an angle smaller than the value set with `-assemble` they are merged to a single filament. In the example, this limit is 70 degrees. With the option `-toFITS` the resulting skeleton is written into a FITS file. However, instead of `-toFITS`, `-to vtp` or `-to ASCII` can be used depending on the desired output format. For further commands and options I refer the reader to the `DisPerSE` manual.

4.1.3 *Tests on synthetic data*

Using the above commands, I investigate how `DisPerSE` behaves in the presence of noise. As the observational data cannot be obtained without noise, the only way to conduct this experiment is to have a synthetic dataset with no instrumental or atmospheric noise. In the following, first, I study a simple case of isolated filaments, and then I look at filaments in a more sophisticated environment in simulated observations of a molecular cloud.

4.1.3.1 *Tests on simple filamentary networks*

I start with a very simple example where I put elongated structures as filaments in a fits file and add random Gaussian noise. These filaments are built to have Gaussian radial intensity profiles and different widths. Figures 4.3 and 4.4 show six different versions of this filamentary network including different levels of noise. In figures 4.3 and 4.4 left and right panels show the filaments and their respective radial intensity profiles. The intensity profiles are extracted from the locations marked by the black solid line close to the top left corner on each sub-panel. In Figure 4.3, from top to bottom, the sub-panels show the original network without any noise and with noise levels of 3% and 10% of the maximum intensity of the network (which is in arbitrary units). In Figure 4.4 the sub-panels show the same network with 20%, 30% and 50% noise. The goal of this exercise is to test `DisPerSE`'s behavior in detecting filaments when the noise level increases.

I run `DisPerSE` on these 6 cases of data with varying noise levels. The corresponding persistence diagrams are shown in Figure 4.5. The noise level increases from left to right and top to bottom and the pink dashed lines show the persistence threshold set for each case. In the example without noise (top left sub-panel), one can see the points with high persistence distinctly. This, however, gets less and less obvious with the increasing level of noise as the difference between the number of critical points found by `DisPerSE` increases. Furthermore, it becomes harder to distinguish between the *real* critical point pairs and the ones created by noise that have high persistence. From the case without the noise, we know that the *real* persistence threshold should be set to 0.142. However, the latter cases have critical point pairs created by noise close to the real persistence threshold. These pairs created by noise and those come from the real structures in the data are indistinguishable to `DisPerSE`. Therefore, to avoid including structures originate from the noise in the imperfect (noisy) datasets, the persistence threshold has to be increased with the increasing level of noise. It is still possible that the noise in a dataset could lead to critical point pairs with high persistence. Therefore, as explained in Section 4.1.2, a detection threshold needs to be set. For the 3 cases I examine here, there is no detection threshold for the noiseless case, and for the cases with noise, the detection threshold is always set to 5 times the noise level.

`DisPerSE` outputs the calculated skeleton files either in a fits format or vtp format that is easy to look at using a visualization software such as ParaView or DS9. However, when plotting the identified filaments on the data for publication purposes, these formats do not come in handy. For this purpose I have written a *filament extraction algorithm* that is python based, and can be applied to the fits file that contains the filaments. Each filament in the fits file has the value of their individual filament IDs. For example, all the pixels that belong to Filament 1, are given the value 1. Therefore, it is straight-forward to extract filaments by their IDs. The algorithm[3], therefore, picks all the filament coordinates with their corresponding IDs and writes them out in separate text files, which are easy to read and plot.

Figure 4.6 shows the identified filaments for the 6 different cases. Each individual filament identified through `DisPerSE` is shown as a coloured segment on the data. Even in the case with no noise, the filaments are broken into smaller segments at the connection points of filaments. This happens because where filaments cross each other, the intensity increases, and `DisPerSE` takes these high intensity points as maxima. With the increasing level of noise, the identified filaments become more wiggly and less of

3 All the algorithms that I developed for this work are publicly available at https://github.com/astrosuri/filchap for the community use.

straight lines. Up to the noise level of 20% the filamentary structure is similar to the case without noise. At a noise level of 20%, as the identified critical points from the real structures and the noisy ones blend in together, the persistence threshold that is set up using the persistence diagram eliminates a real filament as well. The filament on the bottom left corner on the images is no longer identifiable at a noise level of 20%. For the case of 30 and 50% noise level, the formerly identified coherent and elongated filaments vanish. The high levels of noise in the data causes the identification of disconnected and fragmented short segments along the filaments.

4.1.3.2 *Tests on complex maps*

As we have seen in Section 4.1.3.1, `DisPerSE`'s performance in detecting filaments decreases with the decreasing signal to noise ratio. However, this simple test is composed of filaments that are isolated and perfectly elongated. In this section, I investigate `DisPerSE`'s performance on the synthetic emission maps of molecular clouds, which provide a more realistic environment to investigate how the identification of the filamentary structure is affected by noise.

For the purpose of this exercise I use a column density map of a molecular cloud produced in the SILCC (SImulating the LifeCycle of molecular Clouds)-Zoom simulations (Seifried et al. 2017). These simulations are based on the original SILCC simulations that investigate the evolution of the multiphase ISM in a stratified galactic disk environment (Walch et al. 2015; Girichidis et al. 2016). The zoom-in simulations focus on the self consistent formation of molecular clouds within this environment with a high spatial resolution of 0.1 pc. Figure 4.7 shows the simulated column density map.

The molecular cloud has a very high dynamic range such that the column density of the filaments is already at level of 10% of the maximum column density, sometimes even lower. Therefore, when adding noise, I do not consider the maximum level emission in the entirety of the map like the previous section, instead, I consider the "maximum" emission level, as the level of filament column density which is $\sim$0.01 g cm^{-2}. This is because the maximum column density is quite high, and setting up a noise level of 10% of this value will add too much noise on the diffuser parts of the cloud, making filament identification impossible. Hence, when I add a conservative amount of noise based on the level of emission from the diffuser filaments, the behavior of `DisPerSE` can still be tracked without losing the emission to the noise. In the following, I examine the cases where a 3%, 10% and 20% noise level is introduced to the data. The identified filaments for each case is shown in Figure 4.8. From left to right and top to bottom, the panels show filaments identified in the case of no-noise, 3%, 10% and 20% noise.

The problem of filament identification with `DisPerSE` occurs when a low persistence threshold is used in a low signal to noise data. Figure 4.9 shows and example of the filaments identified in the case with 20% noise (as in Figure 4.8 bottom right panel) but with different detection and persistence thresholds. In the left panel, the detection threshold is set to 2.5 times the noise level; that is half the value used in the case

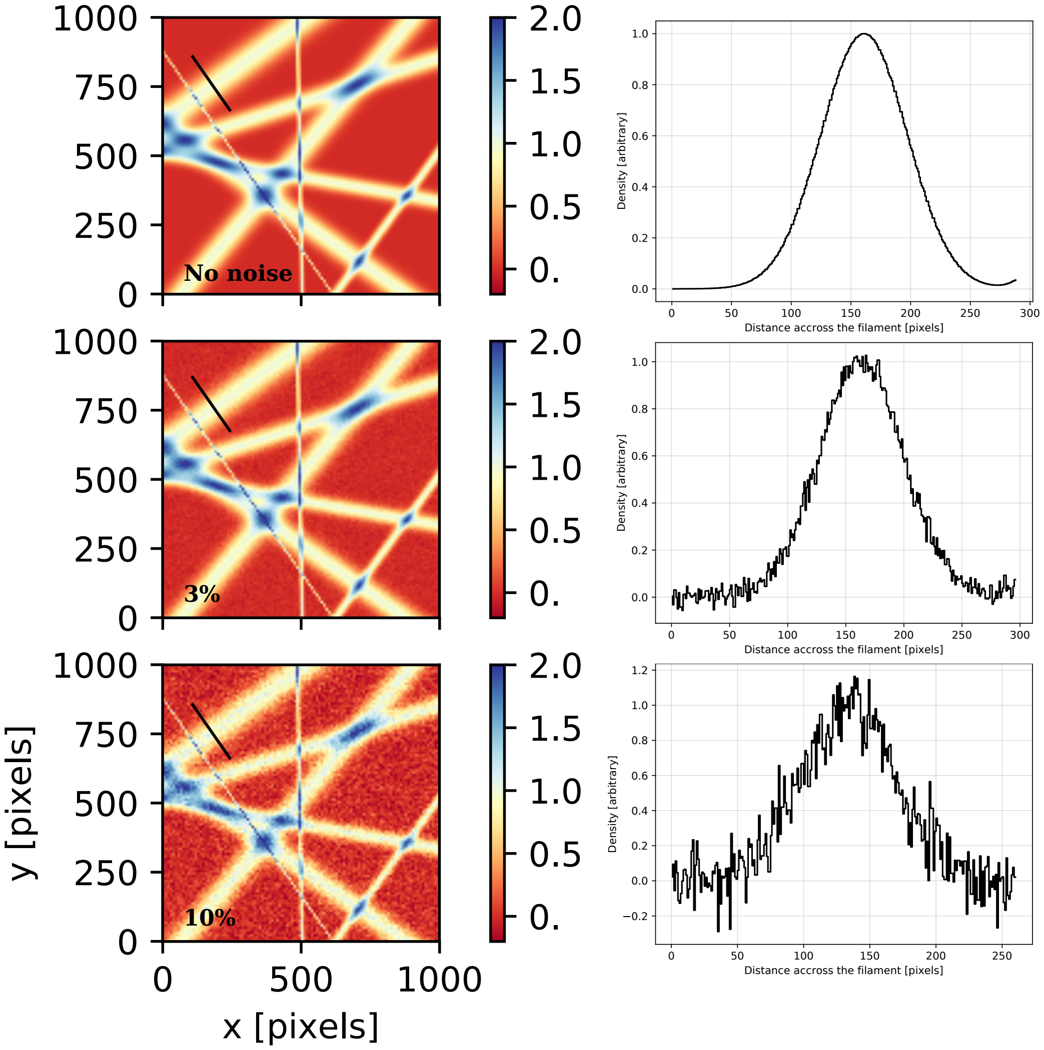

Figure 4.3: Top, middle and bottom panels show synthetic filamentary networks (left) and intensity profiles (right) extracted from a single filament in the network. The top panel is an example of a filamentary network created without noise. The middle and bottom panels show the same network with noise levels that correspond to 3% and 10% of the maximum intensity along the filaments, respectively. The black horizontal lines perpendicular to a filament's spine located in the top left corner indicate the position of perpendicular slices from which the intensity profiles are extracted.

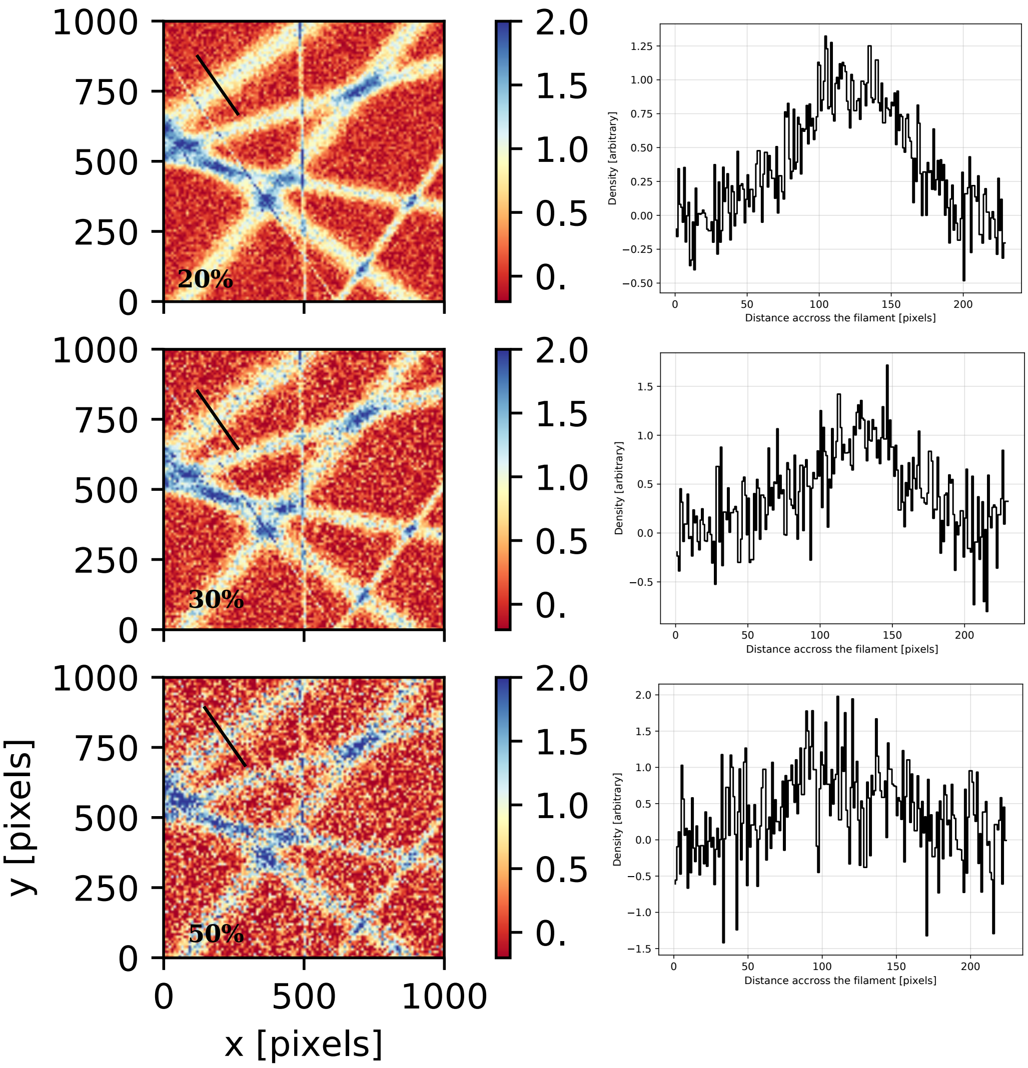

Figure 4.4: Same as Figure 4.3, but for the noise levels of 20, 30 and 50% from top to bottom, respectively.

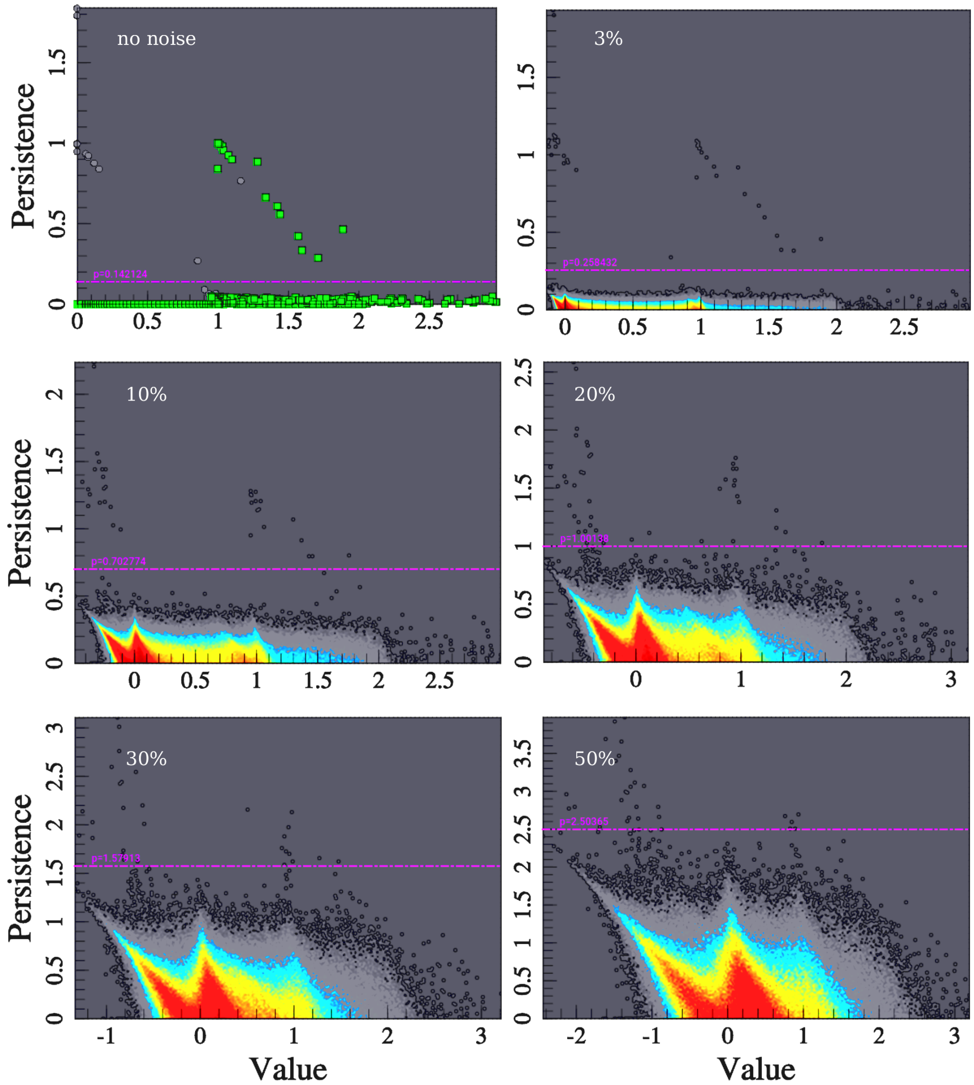

Figure 4.5: Top, middle and bottom panels show the persistence diagrams for a network without noise, and with noise levels increasing from 3% to 50% of the filament's maximum intensity, from left to right and top to bottom, respectively. The pink dashed line indicates the persistence level set to extract filaments.

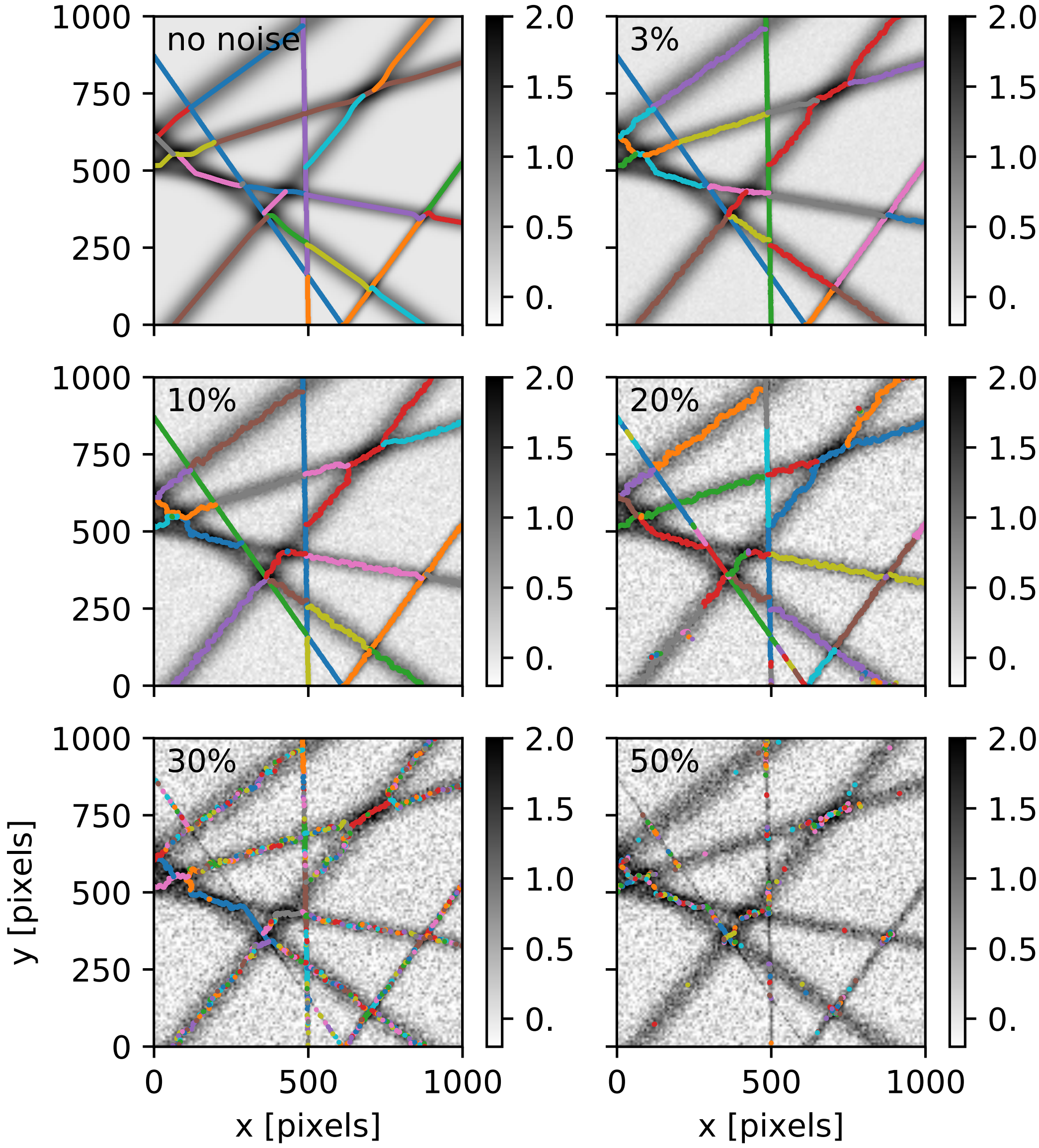

Figure 4.6: Top, middle and bottom panels show the identified filaments for the cases presented in Figure 4.3 and 4.4. Top left sub-panel shows the filaments identified in the case without noise, and the level of increases from left to right and top to bottom. The individual filaments are plotted with different colors for presentation purposes.

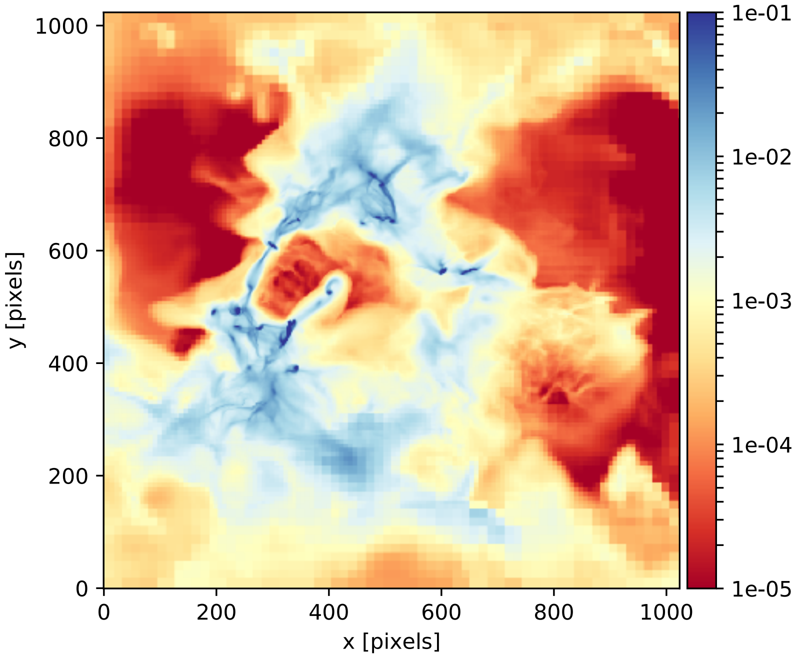

Figure 4.7: Column density map of a molecular cloud produced within the framework of SILLC Zoom simulations (Seifried et al. 2017). The map is in units of g cm^{-3}.

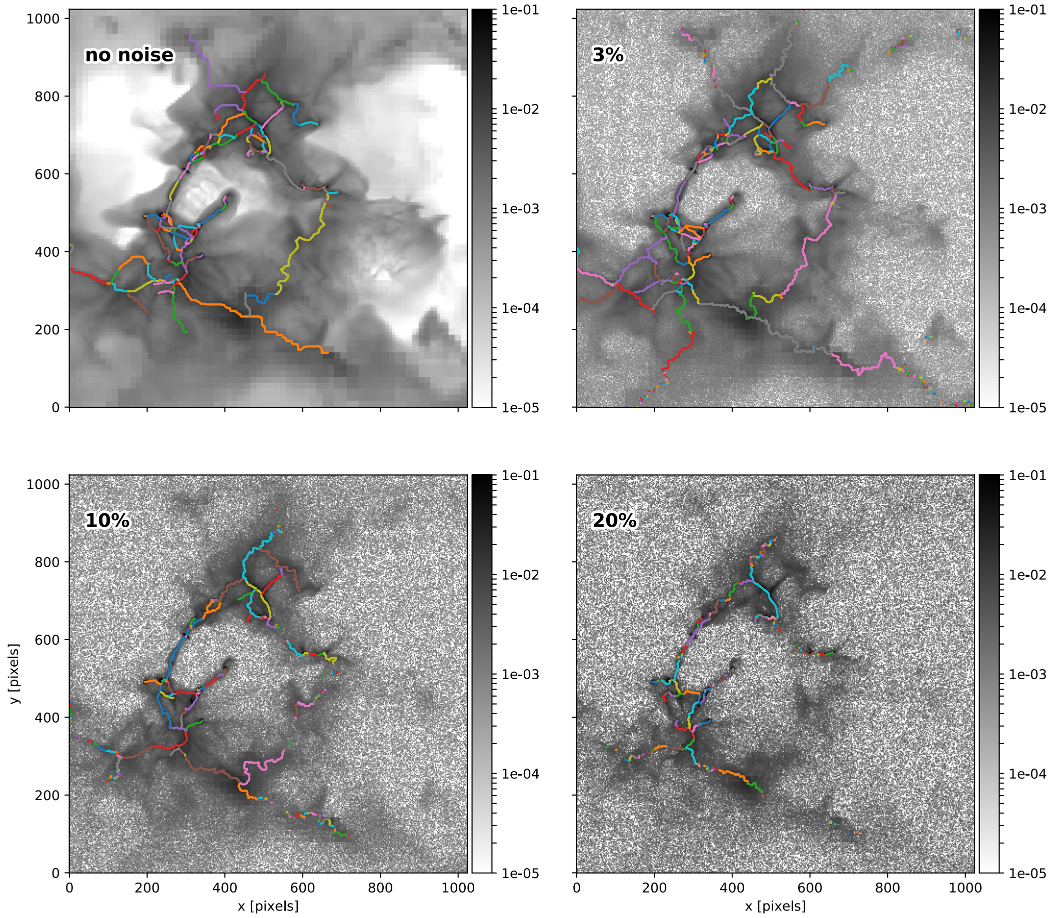

Figure 4.8: Filaments identified on a column density map from the SILCC-Zoom simulations. The top panel shows filaments identified for cases without any noise and a level of 3% noise. The bottom panel shows the cases of 10% and 20% of noise.

presented in Figure 4.8 bottom right panel. The filaments appear more coherent and much less fragmented, however longer filaments are identified then in the case without noise. This is because a lower level of signal is accepted when connecting the critical points. The right panel shows the case with a detection threshold 5 times the noise level, but persistence threshold set to half the value deducted from the persistence diagram. This is when the most fragmented filaments are detected. What is more interesting is that because of the high level of connected structures, `DisPerSE` creates fake *filamentary networks*. To illustrate the problem better, I would like to zoom in to the region that is indicated with a black box in Figure **??** right panel and compare this to some of the structures that are identified and published in an observed dataset.

The top panel of Figure 4.10 shows a zoom in to the region that is marked with a black box in the right panel of Figure 4.9. `DisPerSE` created a *hub* that is the connection point on many small filaments, created due to the high level of noise and a low level of persistence criterion. The middle and bottom panels of Figure 4.10 show two structures identified using `DisPerSE` on a part of the ATLASGAL[4] dataset (figures taken from Li et al. 2016). These structures are labeled as a complex network (middle) and an unclassified structure (bottom) and they look similar to the fake filamentary network that is shown in the top panel. Therefore, the experiments conducted in this section and the previous one, suggest that if a higher persistence level was used in filament identification in the ATLASGAL data, these complex networks would perhaps have not been identified.

Unfortunately, the observed datasets do not always have a high signal to noise that is uniform, especially in large scale surveys. In these cases, multiple combinations of the persistence and detection thresholds can be used. However, even with that compromise, the struggle boils down to (1) identifying filaments in regions with low levels of emission where one needs to lower the thresholds, which in turn causes identification of fake networks and too many filaments in the high signal to noise regions, (2) identifying filaments in high levels of emission where usually higher persistence level is enough, which prevents locating filaments in the low emission regions. Therefore, the selected thresholds are usually adjusted for `DisPerSE` to identify structures that are apparent to the most reliable, yet by no means perfect, source of filament identifier; the human eye. Although the optimal value for the thresholds is 5 times the noise level to prevent connecting critical points created by noise together, they can be adjusted to be higher for the higher signal to noise datasets, and can be slightly lower for the lower signal to noise datasets. The experiments run in these two sections suggest the persistence threshold set to less than 3 times the noise level can create fake filamentary networks. Therefore, these networks in the noisy datasets can always be used for a sanity check for the level of persistence.

4 APEX Telescope Large Area Survey of the Galaxy (ATLASGAL) is a Galactic survey that covered 420 square degrees towards the inner Galactic plane at 870 μm dust continuum emission using the Atacama Pathfinder Experiment (APEX) telescope with an angular resolution of 19.2 arcsec (Schuller et al. 2009).

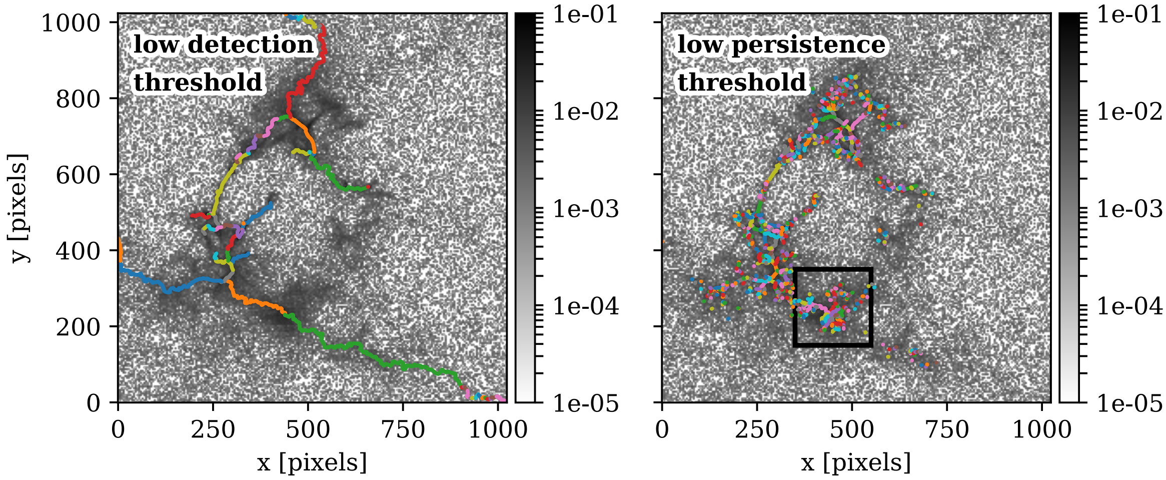

Figure 4.9: Filaments identified in the case of 20% noise. The left panel shows the case when the detection threshold is set to 2.5 times the noise level that is half of the value which was used profucing the filaments in Figure 4.8 bottom right panel. The right panel shows detection threshold 5 times the noise level, but persistence threshold set to half the value deducted from the persistence diagram. The black box is used to indicate the region that is zoomed in, in Figure 4.10 top panel.

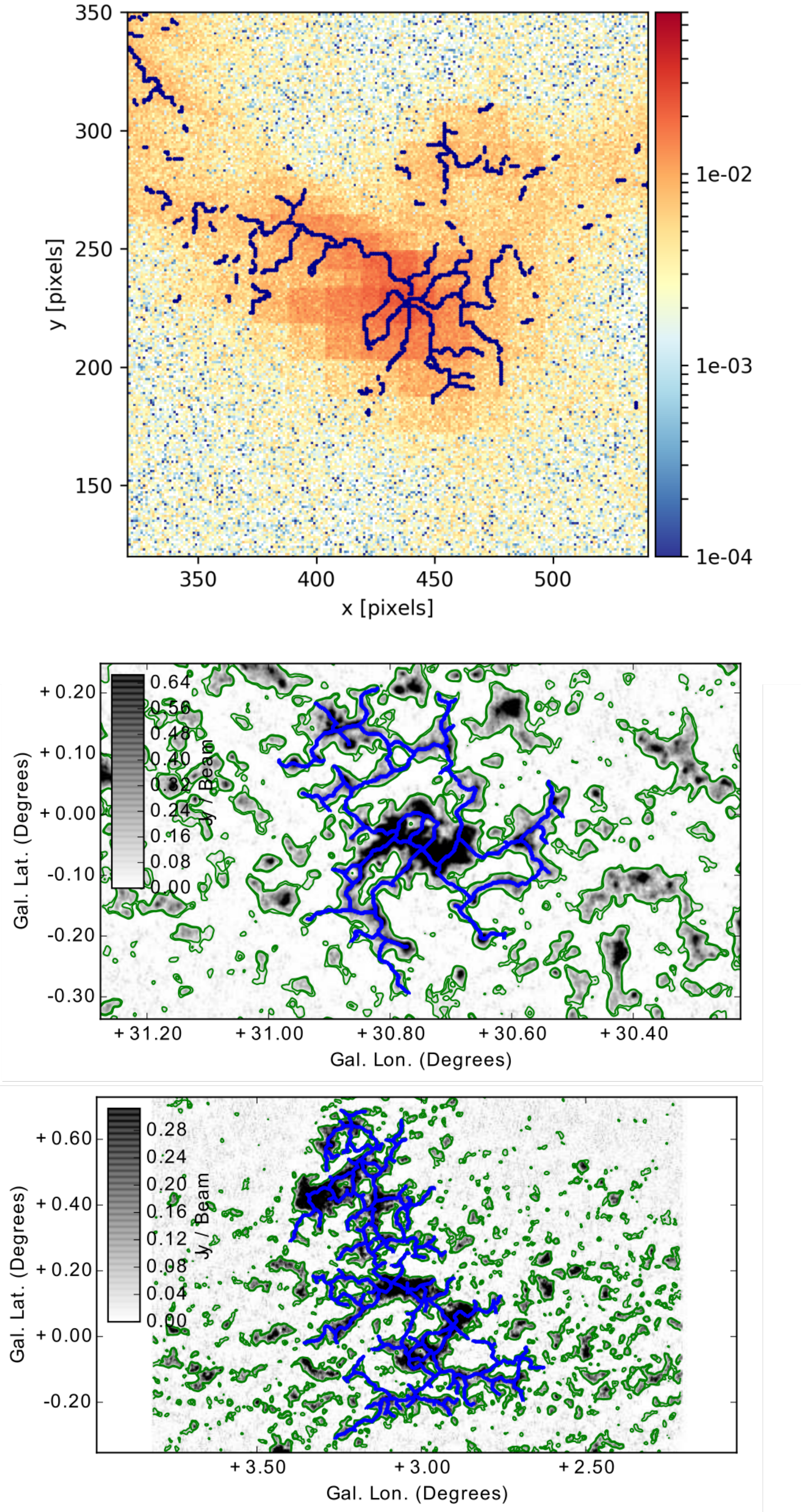

Figure 4.10: Top panel shows the fake filamentary network indicated with a black box in the right panel of Figure 4.9. The middle and bottom panels show two identified structures in the ATLASGAL dataset presented in Li et al. (2016). The structure shown in the middle panel was classified as a complex network, whereas the structure in the bottom panel was labeled unclassified.

5 FILCHAP: FILAMENT CHARACTERIZATION PACKAGE

In this chapter, I give a detailed explanation of a python package that I developed for the analysis of the data presented in Chapter 3.

The growing interest of the scientific community in the properties of filamentary structure triggered the need to write an automated algorithm that can be applied to any dataset, yielding statistics of the identified filaments. For this purpose, I have written `FilChaP`: Filament Characterization Package, that is a publicly available python based algorithm. `FilChaP` can be downloaded at: `https://github.com/astrosuri/filchap`.

My interest in producing such an algorithm has started with my master's thesis work (Suri 2014). I had produced several separate codes which I used to calculate filament properties on a preliminary ^{13}CO data cube from the CARMA-NRO Orion Survey. However, as I gained experience in coding, these preliminary codes have evolved into a more accurate, efficient and user friendly package. I have adopted a complete different way of calculating filament widths, while I kept the bit for the length calculation and removed the data specific, hardcoded variables. I have also written a *nearest neighbour* algorithm, to sort the `DisPerSE` skeleton points.

`FilChaP` uses filament coordinates (in this work, extracted using `DisPerSE`) as a base to calculate filament properties. It can be used in 3D mode for the position-position-velocity data cubes or in 2D mode for column density or integrated intensity maps. It calculates filament length, width, curvature, skewness and kurtosis. Then, these statistical properties can be easily examined, and compared to other observed datasets, and/or simulations.

5.1 USER DEFINED PARAMETERS

Before it starts to calculate properties, `FilChaP` needs to know a few specifics of the data. To make it easier for the user, I have created a parameter file; userDefined.param, which can be modified easily using any text editor. These parameters are in two groups, (1) those that can be tuned by exploring the parameter space, (2) those that are the properties of the data set and should be absolute values. The parameters that fall into the first category are as follows:

- `npix`: the number of pixels that will be used for perpendicular cuts. The resulting length of the perpendicular cut is equal to twice the `npix` value. If nothing is known about the width of the filaments prior to running `FilChaP`, one can give a rough estimation of about a few times 0.1 pc. Then, the intensity profiles should be checked to confirm all the emission form the filament is within the 2 $\times$ npix range.

- `avg_len`: number of skeleton points to average over. The consecutive intensity profiles along a single filament can be averaged to improve the signal to noise ratio. The avg_len parameter tells `FilChaP` how many intensity profiles should be averaged.

- `niter`: number of iterations for the baseline subtraction process of the intensity profiles (for more detail see Section 5.2.2).

- `lam`: weight for baseline subtraction (for more detail see Section 5.2.2).

- `smooth`: number of pixels to smooth the intensity profile with. This is needed to calculate the positions of the intensity maxima and minima which are needed to derive the positions of fitting boundaries.

The parameters that fall into the second category are as follows:

- `fits_file`: path to the fits file that will be used to derive intensities or column densities.

- `distance`: distance to the source in units of pc. Needed to calculate lengths within the cloud.

- `pixel_size`: size of 1 pixel in units of arcsec. Also needed to calculate lengths within the cloud.

- `dv`: velocity resolution of the data in km s^{-1}, if it is in PPV. This is needed when averaging the intensity profiles.

- `noise_level`: the noise level of the average intensity profile to calculate reduced chi-sq value. I note that, although the noise level is specific to an individual data set, it varies with the changing number of averaged profiles. Therefore, the user has to adjust this parameter whenever the `avg_len` is changed.

5.2 CALCULATION OF FILAMENT WIDTHS

Filament widths is a highly debated topic, and the width calculation process forms one of the core functions of `FilChaP`. Based on the shortcomings of the methods (fixed fitting range, averaged intensity profiles over an entire filament) that were criticized in previous works (e.g. Panopoulou et al. 2017), `FilChaP` has an improved and more flexible method to calculate filament widths. Some of these improvements is determining the boundaries of an intensity profile to fit, introducing a variable averaging length for averaging intensity profiles along a filament and assessing the goodness of the fits, which I present in Sections 5.2.3, 5.2.5 and 7.1.3.

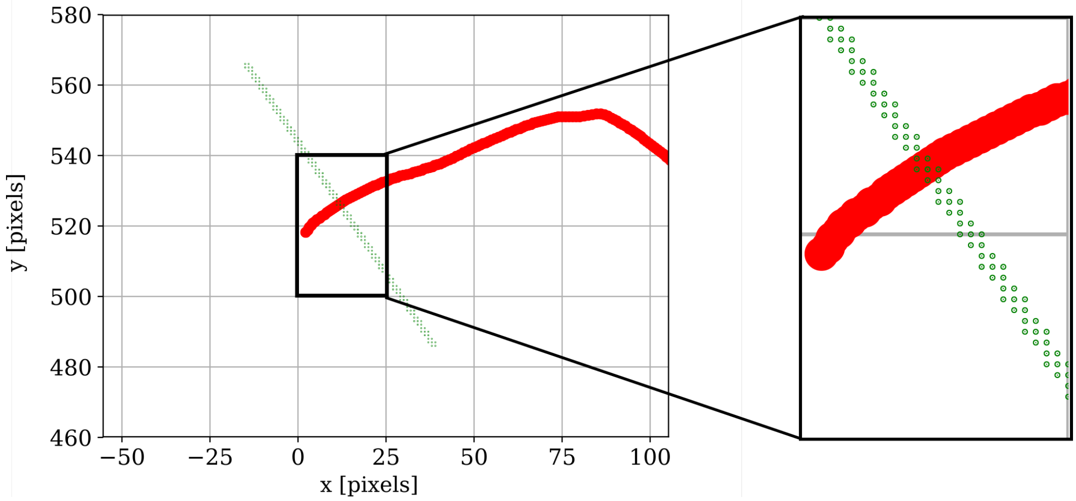

Figure 5.1: An example of how the perpendicular profiles are extracted. The red dots represent the disperse skeleton (as the resolution here is really high, the individual dots are blended), the green dots are the calculated perpendicular pixels at a given point along the skeleton.

5.2.1 *Building the intensity profiles*

For each identified filament, `FilChaP` extracts radial intensity profiles perpendicular to the filament spines. Firstly, it calculates coordinates of normals at each point along filament spines. The normals are perpendicular to the spine of the filaments, however they do not always cross the midpoint of individual pixels. The solution to this problem is to calculate the distances of each pixel close to the normal, and assign the closest ones as *perpendicular pixels*. `FilChaP` assigns pixels to this category if they are at a distance of less than 2 pixels. This method is adopted from Duarte-Cabral & Dobbs (2016). The perpendicular pixels that lie on or adjacent to the normals are then used to produce the radial intensity profiles. An example filament with a perpendicular cut is shown in Figure 5.1. The length of the perpendicular slice is set by the `npix` parameter.

Because points along the identified filament are always defined by a velocity coordinate too (x, y, v), we know the velocity range that the emission from a filament spans. One can see the exact structure of the filament in PPV space. `FilChaP` uses this 3D structure during the extraction of radial intensity profiles. In the studies of dust continuum emission the profiles are calculated over the entire velocity range. But because each point along our filaments has a velocity coordinate, `FilChaP` averages intensities at the velocity channel given by `DisPerSE` and the two adjacent velocity channels. Therefore the intensities from each perpendicular slice are integrated over a 3*`dv` range around the velocity channel at which the corresponding point on the filament is identified.

This method allows to eliminate the confusion in PP and PPV space if there is emission other than what belongs to the identified filament.

5.2.2 *Baseline subtraction*

Depending on the extended emission surrounding the filaments, their intensity profiles calculated using the method explained in Section 5.2.1 can have baselines that vary throughout the map; which affects their amplitudes and shapes. Hence, a baseline subtraction routine is required to permit an automatic fitting routine for the profiles. `FilChaP` uses the Asymmetric Least Squares Smoothing (AsLS) method that was introduced by Eilers (2005) for baseline subtraction in spectroscopic data. The idea for the majority of the baseline subtraction algorithms is simply having a smooth profile that follows the global gradient and represents the original profile without the emission or absorption features. Then this smooth profile, i.e. the baseline, is subtracted from the main profile.

The least square method, in principle, is a good approach for baseline subtraction. Imagine a noisy series of data y, and its smooth counterpart z. The deviation of z from y is given by the sum of squared differences between the two series; $S = \sum_i (y_i - z_i)^2$, and the smoothness of z can be expressed with a simple roughness parameter; $D = \sum_i \Delta(z_i)$. Therefore the least square function takes the following form;

$$Q = \omega S + \lambda D, \tag{5.1}$$

where ω and λ are the weights that provide the smallest value of Q. Then, the minimalization problem can be expressed in terms of matrices;

$$(W + \lambda D'D)z = Wy, \tag{5.2}$$

where W is the diagonal of ω (Eilers 2005). For the general least square smoothing, the weight is the same for both the negative and positive deviations of z. The AsLS method, on the other hand, ensures that the positive deviations are weighted less than the negative ones. This makes sense, because the signal in y that we are interested in is always positive. The asymmetric weight parameter; ω_i is then equal to p for $y_i > z_i$, and equal to $1 - p$ for $y_i < z_i$. Finally, a solution to Equation 5.2 can be found iteratively starting with a smooth z (calculated with symmetric weights), calculating the asymmetric weights; and then, using the new weights to calculate z. Figure 5.2 gives an explanation of how baseline subtraction process works. An example intensity profile with a baseline gradient is shown on the left panel. Before one can calculate the width of this profile, the gradient has to be eliminated. The red lines are the baselines calculated for different iterations. The weights converge rather fast after a number of iterations and the baseline icalculation is concluded. The baseline subtracted intensity profile is shown on the right panel.

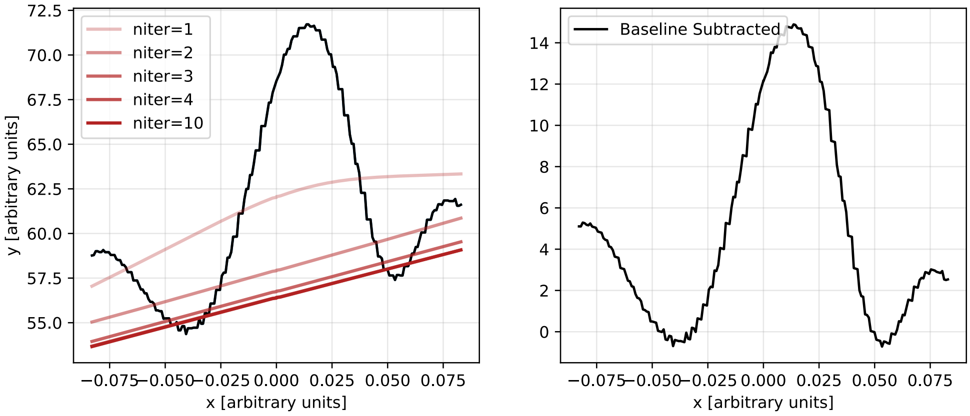

Figure 5.2: Demostration of the baseline subtraction process. *Left:*Profile with a baseline gradient overlaid with the calculated baselines at different iterations. *Right:* The same profile as in the left panel after the baseline subtraction.

Eilers (2005) also gives a `Matlab` algorithm for the AsLS baseline calculation and this can be find as a python code at `https://stackoverflow.com/questions/29156532/python-baseline-correction-library/29185844`. This simple algorithm is as follows:

```
def baseline_als(y, lambda, p, niter=10):
        L = len(y)
        D = sparse.csc_matrix(np.diff(np.eye(L), 2))
        w = np.ones(L)
        for i in xrange(niter):
                W = sparse.spdiags(w, 0, L, L)
                Z = W + lambda * D.dot(D.transpose())
                z = spsolve(Z, w*y)
                w = p * (y > z) + (1-p) * (y < z)
        return z
```

The algorithm takes the data y and 3 variables; `lambda`, `p` and `niter` which represent the smoothness of the series z, the weight for asymmetry and the number of iterations, respectively. The authors have explored the parameter space for `lambda` and `p`, and suggest that when the original data have peaks (or is in emmision and not absorption); 0.001≤`p`≤0.1 and 10^2 ≤`lambda`≤ 10^9 give good estimation on the weights. This algorithm is implemented in `FilChaP` and the variables can be adjusted in the userDefined.param.

5.2.3 *Determining boundaries*

One of the biggest problem in fitting an intensity profile such as the one shown in Figure 5.2, is to set the boundaries on a fit. I would like to express clearer that, the width calculated from the intensity profile always depends on the boundaries because the filaments are not isolated structures. There is always emission surrounding them, from other filaments, clumps, etc. Therefore, it is not surprising, when cutting a perpendicular slice through the filament spine, one also picks up emission from nearby structures. If this emission was non-existent and filaments were perfectly isolated, the boundaries of the fit would not affect the calculated width of the profile. In reality however, the larger the boundaries, the more emission from the surrounding structures will be included in the fit, resulting in a larger filament width. Therefore, one must acquire a method to set the boundaries around the emission from the filament itself.

In Figure 5.2, it can easily be estimated by eye that the emission from the filament is within the x - range; -0.04 – 0.05. Our brain picks this up because we are able to see the emission from the surrounding structures that peaks around -0.075 and 0.075. It is easier to detect boundaries by eye, than it is to tell the computer to detect them. Because human brain can do an immediate comparison between the strengths of the relative peaks to decide whether the neighbouring structures are significant, or not. The computer needs a criterion to identify a structure. In observational astronomy, a structure that can be sampled by 3 beams (or, 3 beam-sizes) is often accepted as a resolved structure. Therefore, I make use of this observational criterion to tell `FilChaP`, whenever it *sees* a minimum, that is the minimum of the neighbouring n points, it puts a boundary there. Here n represents the number of pixels (points) in 3 beams. In order to prevent picking up minima created by noise, `FilChaP` looks for boundaries on the profile that is smoothed with a Gaussian kernel of the size of a beam. In Figure 5.3 an example intensity profile is shown. The average intensity profile is shown with a solid black line where the boundaries are marked with two grey dashed lines. For the width calculation the profile is fitted with a Gaussian (blue), Plummer (p=2; yellow) and a Plummer (p=4; red) function which I explain in the upcoming section (Section 5.2.4).

5.2.4 *Fitting functions*

`FilChaP` uses 4 different methods to calculate the width of the intensity profiles; a Gaussian fit, two Plummer-like fits with power-law indices of 2 and 4, and the FWHM of the second moment of distribution. The column density profile (here similar to our average intenstiy profile) of a homogeneous and cylindrical filament is described by a Plummer-like function with an inner-flat part, R_{flat} and a power-law index, p,

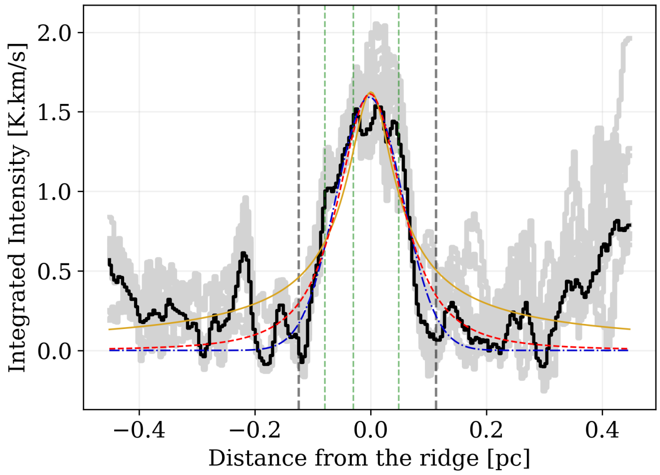

Figure 5.3: Example intensity profile extracted along a filament detected in $C^{18}O$ data. The solid black line is the average profile over 12 intensity profiles along a selected filament. Solid grey lines are these 12 profiles. The grey dashed lines mark the borders of the fits, which are shown in blue, yellow and red that correspond to Gaussian, Plummer (p=2) and Plummer (p=4) fits.

that describes the decline at large radii (Arzoumanian et al. 2011). This function is as follows:

$$\Sigma_p(r) = A_p \frac{\rho_c R_{flat}}{\left[1 + \left(\frac{r}{R_{flat}}\right)^2\right]^{\left(\frac{p-1}{2}\right)}}, \tag{5.3}$$

where ρ_c is the central density, and A_p is a finite constant that is related to the filament's inclination compared to the plane of the sky. As observers, we do not have the knowledge on the real third dimension of the filaments along the line-of-sight. Therefore, the inclination angle is often assumed to be zero. To prevent the degeneracy between the parameters ρ_c and R_{flat}, instead of fitting the power-law index I fix it to common literature values. I use p=4; as this value is often used to construct the density profile of a isothermal and homogeneous cylinder (Ostriker 1964), and p=2; as this is the fitted power-law index of various observed filaments (Arzoumanian et al. 2011).

Our fourth method benefits from the calculation of moments of distribution. The n^{th} moment of a distribution I is given by:

$$m_n = \frac{1}{N} \frac{\sum_i^N I_i \left(x_i - \bar{x}\right)^n}{\sigma^n}, \tag{5.4}$$

where $\bar{x}$ is the intensity weighted mean position of the profile, I_i is the intensity at position x_i, and σ is the intensity weighted standard deviation of the profile. The second moment is the variance of the distribution; and hence the FWHM of the intensity profile is $\sqrt{m_2} \times 2\sqrt{2ln2}$.

5.2.5 *The averaging length problem*

As emphasized in previous sections; the filaments are not isolated structures, and for sure, along their long axis the properties vary. One of these varying properties is their width. Previous studies (e.g. Arzoumanian et al. 2011) have explored the *mean* filament profiles; the intensity (or column density) profiles that are averaged over the entire length of a filament. Although this method increases the signal to noise ratio of the averaged profile, it also wipes out all the information on how filament width changes along the filament.

Figure 5.4 demonstrates how severe the effect of averaging can be. The four different sub-panels of the figure show intensity profiles averaged over different length scales along the filament. From left to right the top panel shows the profiles are averaged over 0.015, 0.045 pc which corresponds to length scales of 1 and 3 beam-sizes. The bottom sub-panels show the intensity profiles averaged over 0.075 pc (or 5 beam-sizes) and the entire filament. It can be seen that for all the cases except for the profile averaged along the entire filament, the intensity profile shows two peaks; one corresponding to our filament, the other corresponding to a nearby structure at -0.2 pc. The boundaries found by `FilChaP` separates these two structures, allowing a fit that only takes into account the filament of interest. These fits for the first three cases correspond to a FWHM of about 0.16 pc. When, however, all the intensity profiles along the filament are averaged into a single *mean* profile; the information on the nearby structure is completely lost, and the calculated width is 0.27 pc; almost twice the width of the single filament.

`FilChaP` has an implemented user defined parameter; `avg_len` that is used to decide the number of intensity profiles that should be used to have an averaged profile. For the analysis presented in Chapter 7, I use an averaging length of 3 beam-sizes (0.045 pc). This allows me to improve the signal to noise level without losing any information on the variation of the width along the filaments.

5.2.6 *Finding shoulders*

A function of `FilChaP` that I introduced for a quantitative measure of the complexity of the intensity profiles is the detection of *shoulders*. Shoulders of a profile indicate that the profile is not composed of a single function, but multiple. Figure 5.5 is a representation of how shoulders of a function are seen and can be detected (Clarke et al. 2018). The blue curve represents a function, $f(x)$, that is composed of two Gaussians with a peak at $x = 0$ and a shoulder at $x = 2$. The orange, green and red curves represent the

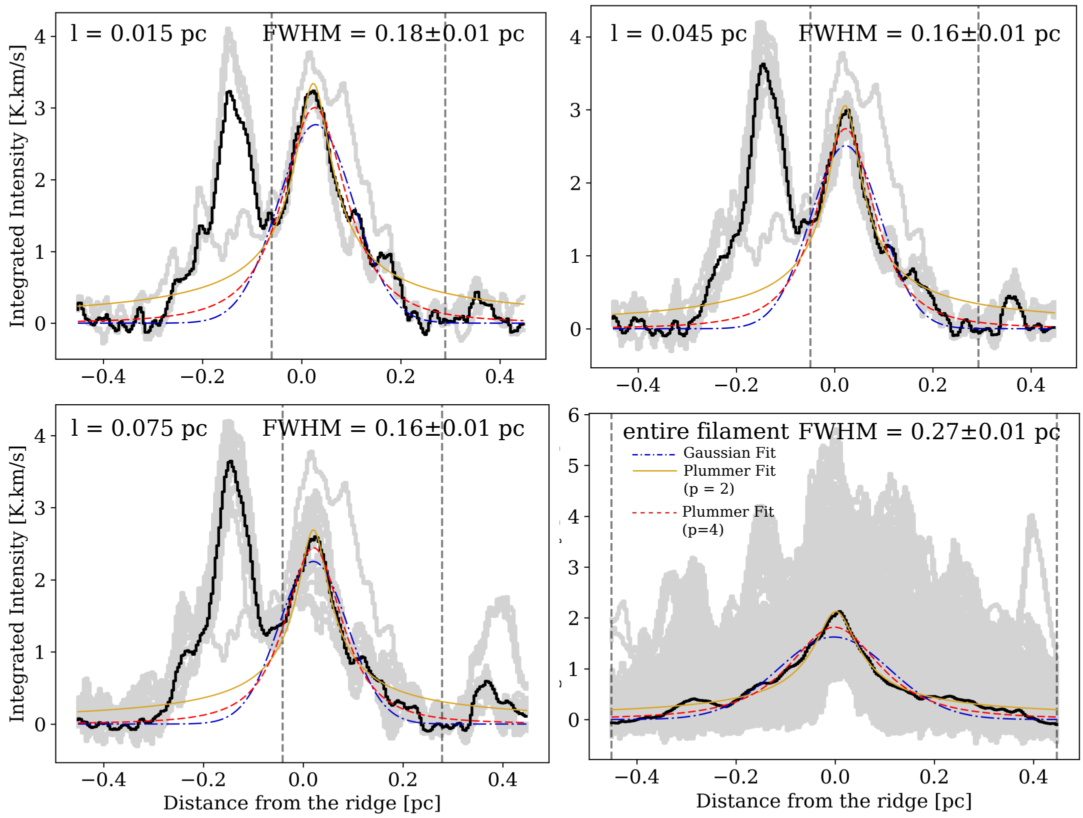

Figure 5.4: Plots showing the affect of averaging intensity profiles along different length scales. Individual intensity profiles are shown in grey, while averaged intensity profiles are shown in black. From the top left to bottom right the profiles are averaged over 0.015, 0.045, 0.075 pc and the entire filament with corresponding Gaussian FWHM of 0.18, 0.16, 0.16 and 0.27 pc.

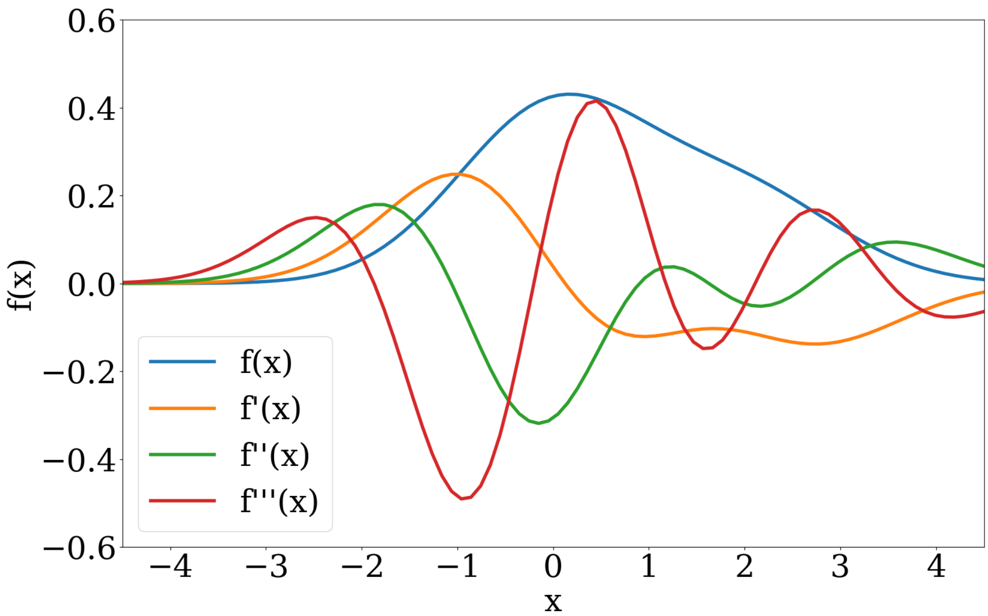

Figure 5.5: Derivatives of a function $f(x)$ that is shown with the blue curve. The orange, green and red curves show the first, second, and third derivatives, respectively. Figure credit: S. Clarke, Clarke et al. (2018).

first, second and third derivatives of this function, respectively. The position of the shoulder can be traced by the position of the local minimum of the second derivative. This method to identify shoulders in spectra was implemented in the Behind The Spectra (BTS) algorithm presented in Clarke et al. (2018), and is also implemented in `FilChaP` to trace the shoulders of an intensity profile.

5.3 TESTS ON THE WIDTH CALCULATION METHOD

As any trustworthy algorithm used in science, `FilChaP` is tested on synthetic data to ensure its credibility. For the test, I used two cases: Case 1; a network of filaments of same width and Case 2; a network of filaments that have different widths. The goal here is for `FilChaP` to produce 2 different distributions for 2 cases. One that is narrowly peaked around the common filament width of Case 1; and one that represents the distribution of initial filament widths that are used to construct the filamentary network of Case 2. Figure 5.6 shows the two different synthetic filamentary networks Case 1 and Case 2 (upper panel left and right) and the corresponding filaments identified with `DisPerSE` in each case. I have added random Gaussian noise to both maps; and the amount of noise is selected based on the peak intensity-to-noise ratio in the CARMA-NRO $C^{18}O$ integrated intensity map.

For Case 1, each of the synthetic filaments are created with a 25 pixel width which corresponds to a 0.1 pc filament width using the $C^{18}O$ pixel size. For Case 2, while creating the filaments I allowed the width to vary between 5 and 85 pixels. This provides and insight of `FilChaP`'s performance of calculating widths of narrow and wide filaments. The expectation for `FilChaP` is, for Case 1 to find a distribution that is peaked at around 25 pixels. For Case 2, on the other hand, I expect a distribution that represents all the different scales between 5 pixels and 85 pixels.

Figure 5.7 shows the `FilChaP` results for Case 1 (top) and Case 2 (bottom). The width distribution for Case 1 peaks, with a mean of 26.7±8.6 pixels where the error represents the 95% confidence level. For Case 2, both the true distribution of the widths that were used as input and the distribution that came out of `FilChaP` are shown. A better way to quantify the relation between the input and output width distributions that for the second case, one can calculate a correlation coefficient. The Spearman's-rho coefficient is a non-parametric way to assess relation between the two distributions. The value of Spearman's-rho can vary between -1 and +1, where -1 would indicate a perfect decreasing monotonic correlation, +1 would indicate an increasing monotonic correlation and 0 indicates no correlation between the two datasets. The Spearman's-rho between the input and output distributions of Case 2 is 0.78. This indicates a that the two datasets are strongly correlated. For Case 1, the width of the distribution comes from the errors of individual fits, and from the instances where filaments may cross one another in the map that may cause larger widths. For Case 2, however, in addition to these effects, the origin of the spread is actually the underlying different filament widths in the dataset. To conclude, the the tests for Case 1 and Case 2 has yielded width distributions that proves `FilChaP` that reliably can capture the properties of filaments that have different width distributions.

5.4 CALCULATION OF SKEWNESS AND KURTOSIS

The skewness and kurtosis give us information about the different shapes of the intensity profiles which can be related to the properties of the filaments in various environments. If a filament is affected by stellar feedback in a violent environment, I expect the intensity profile to be shaped in a way that the part of it that faces the direction of the feedback should be sharper. Kurtosis of a profile is a measure of its peakiness. It can point at those locations, for example, of high CO density, where the CO isotopologues may be optically thick. It can also indicate freeze out for $C^{18}O$ that causes the profiles to be flatter than peaky. Figure 5.8 is an example of skewness and kurtosis of two intensity profiles. These profiles are extracted from the ^{13}CO map and correspond to intensity slices from the Orion Bar, the most well-known PDR, and OMC-4, a dense star forming region, in green and grey, respectively. The green arrow

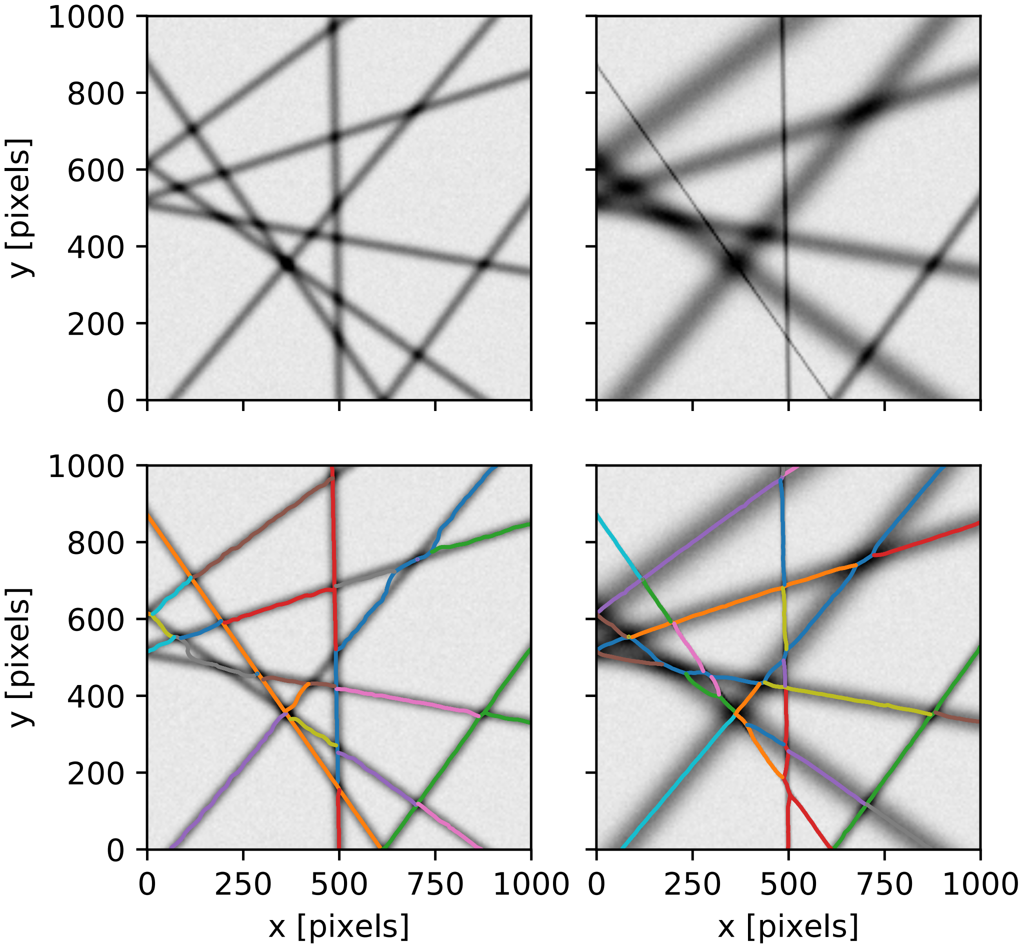

Figure 5.6: *Top*: Synthetic filamentary networks generated with prefixed filament widths. The left panel shows Case 1 where all the filaments have a same width of 25 pixels. The right panel shows Case 2 , where each filament has a different width (see Fig. 5.7). *Bottom*: Filaments identified by `DisPerSE` for both cases.

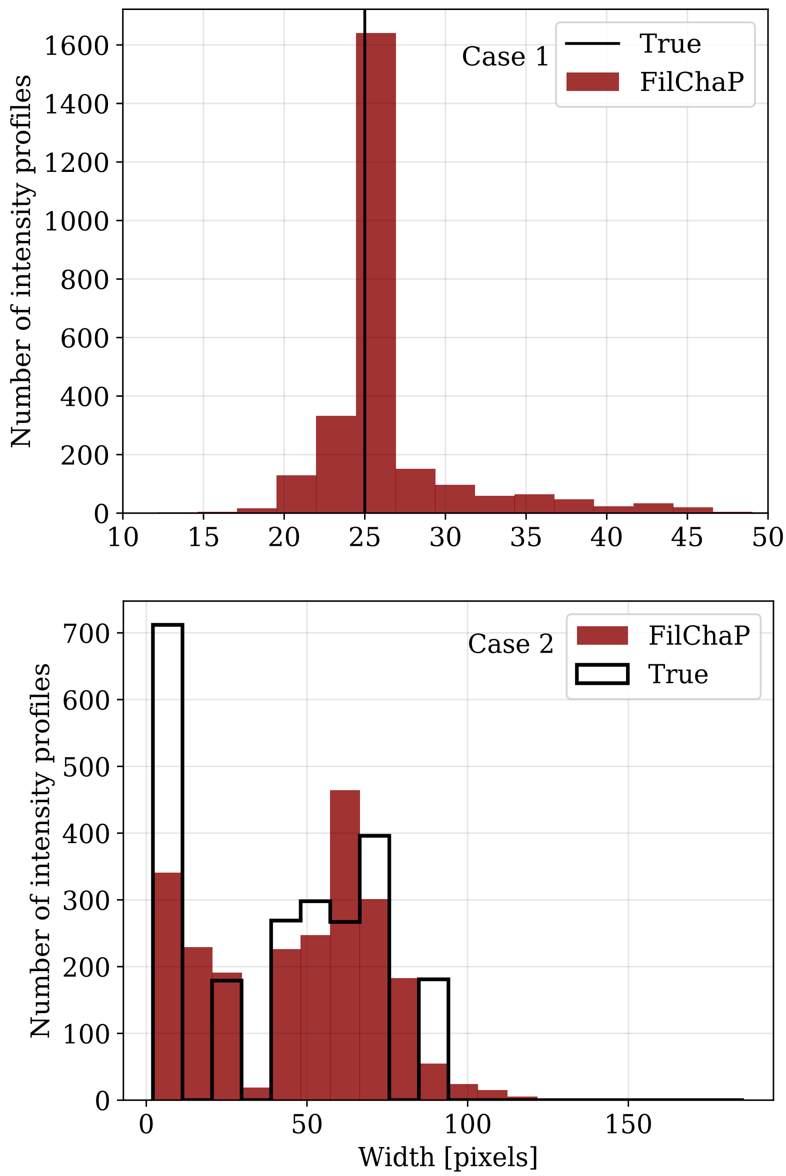

Figure 5.7: Distribution of filament widths for the test two cases presented in Figure 5.6. The top panel shows the resulting for Case 1 and bottom panel shows the distribution for Case 2.

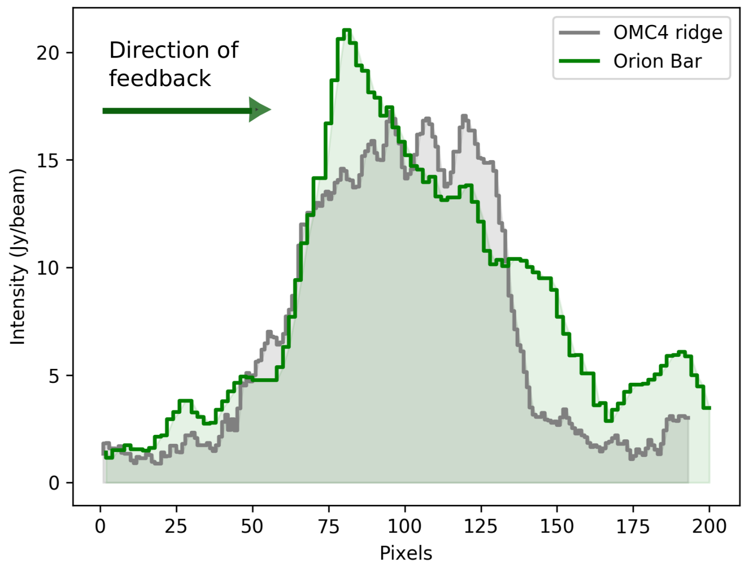

Figure 5.8: A demonstration of skewness and kurtosis based on different intensity profiles. The green profile that represents the Orion Bar is positively skewed, while the grey intensity profile for the OMC-4 region position has a flat top due to its density and is nor skewed in a preferred direction.

indicates the direction of the stellar feedback produced by the Trapezium cluster on to the PDR. As expected, the intensity profile shows that the PDR profile towards the feedback forms a sudden edge, unlike the side away from the feedback that gradually extends. The dense OMC-4, unaffected by the feedback, is not skewed. Figure 5.8 also highlights the differences between the peakiness of top of the intensity profiles, which can be related then to kurtosis. Chapter 8 compares filament properties in different tracers and touches upon the PDR nature of the filaments in feedback regions and compares properties of intensity profiles using skewness and kurtosis analysis.

5.5 CALCULATION OF LENGTH AND KINKINESS

For the filament length calculation, `FilChaP` obtains the *projected* distances between the each skeleton point along an identified filament. This is a projected distance, because observations of filaments we do not know the real 3rd dimension of the filaments. The kinkiness of a filament skeletons is obtained by dividing the distance between end points of the filament to its length. The kinkiness, then, is defined as $k = r/R$ where r is the distance between the end points and R is the length of the filament. $k = 1$ indicates a filament with no curvature.

These length and kinkiness of filaments, may vary with varying filament identification parameters. Hence, these distributions should be examined with caution. The filament identification can perhaps be improved by using different filament identification algorithms, detailed comparison of filamentary structures identified, and using different tracers to assess the length of filaments.

Part III

ANALYSIS AND RESULTS

The following chapters in this part are the core of this thesis work through which I intend to present results on the filamentary structure of the Orion A molecular cloud. In Chapter 6, I explain how the filaments are identified in the CARMA-NRO data. In Chapters 7 and 8, I present the results on the physical properties of filaments observed in different tracers. The results and discussion of Chapter 7, excluding the stability analysis, are the base of my publication Suri et al. (2019) that can be found in Appendix B. Figures 2, 5, 6, 7, 8, 9, 10, 11, B.1, B.2, B.3 and Table 1 from Suri et al. (2019) are reproduced in this part of the thesis with permission ©ESO. I note, however, because the publication of the article superseded the submission of the thesis, some figures and values in Table 1 slightly deviate in the refereed and published version of Suri et al. (2019) from the ones presented in this part of the thesis.

6 FILAMENT IDENTIFICATION IN THE CARMA-NRO DATA

This chapter is aimed at explaining the filament identification process on the CARMA-NRO Orion Survey data. As the ^{13}CO(1-0) data cube was combined earlier than the C^{18}O(1-0) cube, I first tried identifying filaments in the ^{13}CO data. Filaments in both datasets are identified using `DisPerSE` (see Chapter 4).

6.1 FILAMENT IDENTIFICATION ON THE ^{13}CO(1-0) DATA

In order to be able to identify the filamentary structure on the ^{13}CO data, I used a preliminary version of the dataset. The data combination has improved since then. However, as in the end I used the filaments identified in the C^{18}O datacube, I did not repeat filament identification on the latest ^{13}CO datacube published in Kong et al. (2018). Nevertheless, the results presented here remain to be well-founded as the improvements in the latest cube are on the size of the map and the determination of the flux scaling factor.

The CARMA-NRO datacubes can be classified as *large* datacubes in observational astronomy with sizes of $\sim$2000$\times$4000$\times$150 pixels and 4 GB of file size each. This means that `DisPerSE` has to work with 10^8 pixels. If the data was noise free, then the identified number of critical points would have been significantly less and perhaps handling of such a big dataset would have been computationally easier. However, `DisPerSE` is not made for such datacubes with noise. In Chapter 4, I have shown that as the noise increases, the number of identified critical points increase as well. The problematic part of the code is once the MSC is computed and a persistence threshold is set, all the critical points below the threshold have to be cancelled. This cancellation process within `DisPerSE` is not paralellized, therefore, it has to be done using a single computing core. In this case, the core eventually runs out of memory and `DisPerSE` quits without calculating the filaments with a `Segmentation Fault` error. Therefore, filament identification in such large datacubes, such as the CARMA-NRO data, using `DisPerSE` becomes trickier than one expects.

For the filament identification in the ^{13}CO datacube, I removed the *edge* velocity channels with no (or very little) emission to reduce the number of pixels along the third axis. In this process, I made sure that I include the emission from the majority of the structure, and no new structure appears in the channels that are cut. Then, I smoothed the resolution of the third axis from 0.11 km s^{-1} to 0.55 km s^{-1} . This has two positive effects; first the number of channels reduces by a factor of 5, second the signal-to-noise increases in each channel. In the end, after removing the edge channels

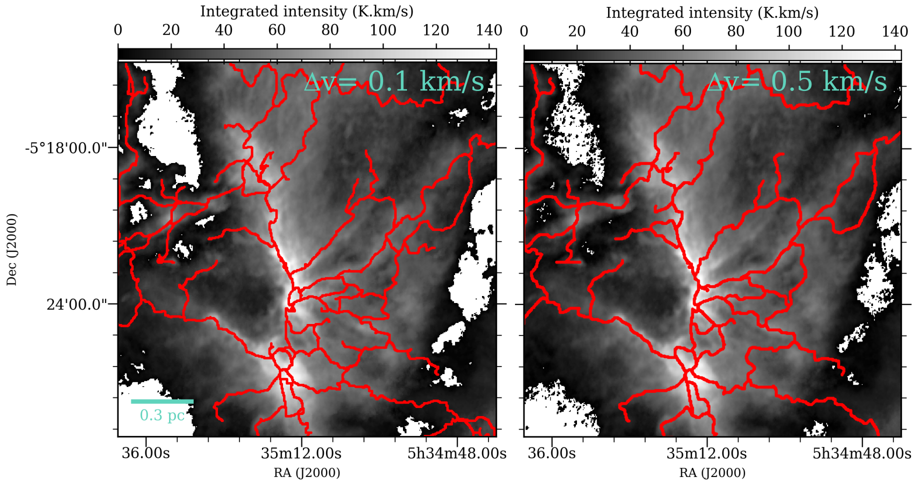

Figure 6.1: Filaments identified in the ^{13}CO datacube with 0.11 km s^{-1} (left) and 0.55 km s^{-1} velocity resolution in the OMC-1 region.

where no emission occurs and smoothing the resolution by a factor of 5, the number of pixels along the third axis reduces from 150 to 19. In order to filament identification, I selected a subset of the data around the OMC-1 region, and ran `DisPerSE` on both the cube with the original velocity resolution and the smoothed one. The resulting filaments are shown in Figure 6.1. The overall structure of the filamentary network is vastly similar, however, there are subtle differences. These differences arise from the fact that the 0.55 km s^{-1} data has better signal to noise, and the filaments are more coherent in intensity. The filaments identified in the 0.11 km s^{-1} cube but not in the smoothed one correspond to emission that is smoothed out and lost its significance compared to the rest of the structure in the map. After a persistence threshold hold of 5 K, detection threshold has a very little effect on the identified filaments simply because the more persistent critical point pairs have already higher intensities. Thus, the need for a detection threshold subsides when a higher persistence threshold is selected. Detection threshold becomes completely obsolete in our skeletons with 8 K persistence, and higher.

Compared to the C^{18}O(1-0) emission, the ^{13}CO is quite strong and has a much higher dynamic range. Therefore, it sets an excellent ground for further tests on `DisPerSE` parameters. Figure 6.2 shows the impact of varying persistence and detection thresholds. From left to right, the persistence threshold increases, and from top to bottom the detection threshold increases. The noise level of the data is 0.3 K per velocity channel. Therefore, the lowest persistence threshold used in this demonstration is already 8 times the noise level. Because of the high dynamic range of emission, the `DisPerSE` run with a very *low* persistence threshold (2 K; no detection threshold) leads to the identification of about 2000 filaments. These filaments are everywhere, and clearly

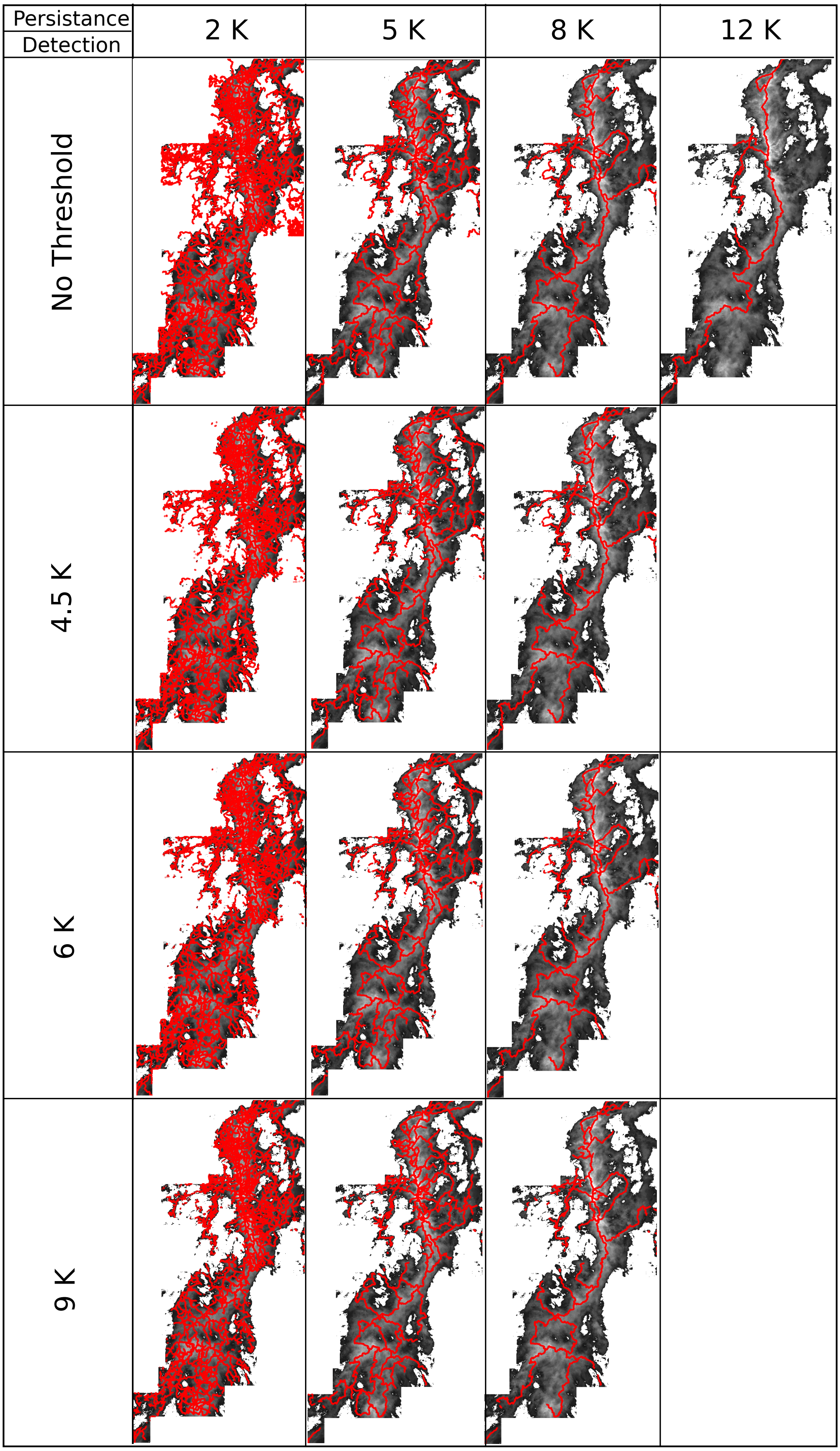

Figure 6.2: Filaments identified in the ^{13}CO datacube with different `DisPerSE` parameters.

some of them are created by the noise at the edges of the map. The critical points raising from noise peaks at the edges of the map can be discarded by using a high detection threshold, and this is demonstrated with the first column of the figure. However, even with the increase of the detection threshold, the 2 K persistence threshold does not seem to be high enough to pick out the most persistent structures. Only when I increase the persistence threshold to 5 K and higher, the "backbone" of the cloud starts to stand out from the rest of the structures.

6.2 FILAMENT IDENTIFICATION ON THE $C^{18}O(1\text{-}0)$ DATA

The filaments used in the analysis throughout this thesis are based on the filaments identified in the $C^{18}O$ data presented in this section. Compared to ^{13}CO, the $C^{18}O$ emission is much less extended, and is weaker on average by a factor of at least 5. Hence, the noise level of the data is the limiting factor in structure identification. In the case of ^{13}CO, we saw that even a persistence threshold of 8 times the signal-to-noise level was too low for identifying the most persistent structures. This is not the case for $C^{18}O$ due to lower levels of emission. In Chapter 4, I showed that the usage of persistence threshold less than 3 times the noise level leads to identification of artificial filamentary networks in noisy datasets. Therefore, for the $C^{18}O$ data, I choose to take both the detection and persistence threshold 4 times the noise level. Higher level of both thresholds leave the weak extended filaments unidentified.

The final version of the $C^{18}O$ data published in Kong et al. (2018) has a velocity resolution of 0.22 km s^{-1}. While the smoothing method described in the previous section in order to reduce the number of pixels along the velocity axis allows for `DisPerSE` to run on the entire map, it prevents extracting the exact velocity information along the filament, i.e. at which velocity channel the corresponding point was identified. Therefore, with $C^{18}O$, I follow a different strategy. Since I do not want to forfeit the velocity resolution, which will provide immense help when studying filament kinematics, I cut the map into two halves, north and south, of 1 degree in declination each. Once the filaments are identified in each half separately, I run `DisPerSE` on a third datacube that covers the overlap region between the two halves. This permits me to extract the filaments that connect the two portions of the map, and remove the artificial filaments created by the edge effects. The filaments identified in both portions individually are shown in Figure 6.3, with the northern region on the left and southern region on the right panel. At the very bottom of the northern region and the top of the southern region, some filaments are created due to the fact that emission was simply cut in these regions. Figure 6.4 shows the filaments identified in the intersection between the northern and southern region. Based on these filaments, I, by hand, identify the filaments that were created by the edge effects. I also add the connections between the two regions that was cut when the map was cut in half. The resulting set of filaments is overlaid on the full peak intensity map of $C^{18}O$ in Figure 6.5.

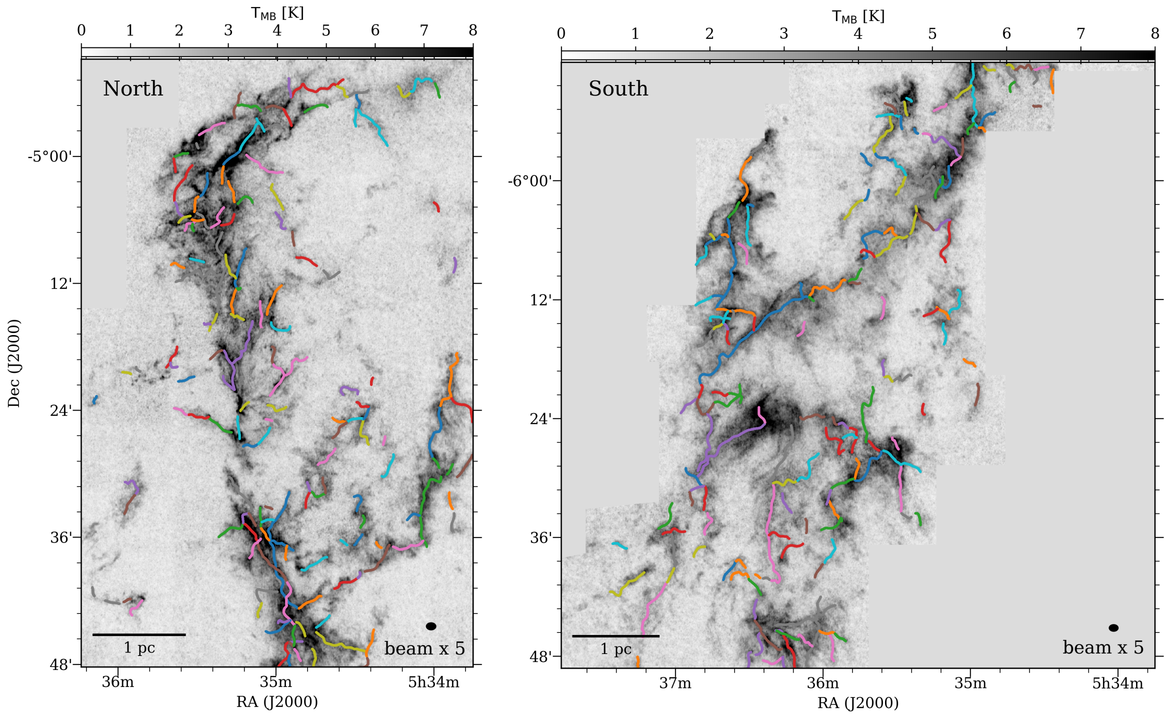

Figure 6.3: Filaments identified in the northern region (left) and the southern region (right) of the Orion A molecular cloud. Greyscale shows the C^{18}O peak intensity emission, while the colored segments indicate the filaments identified by `DisPerSE`.

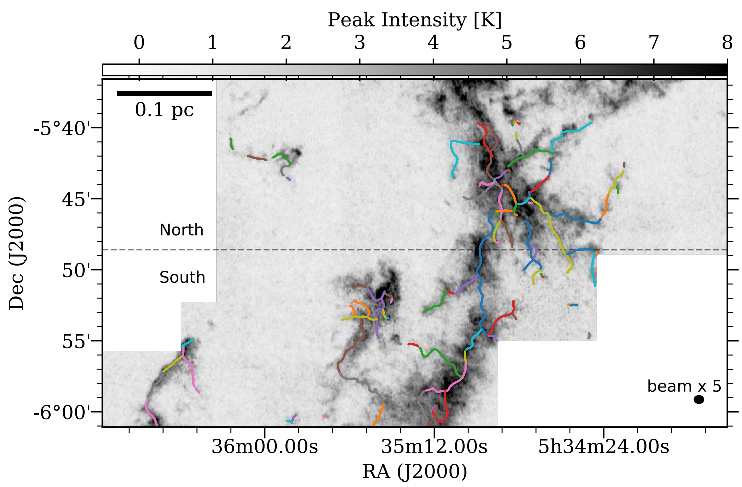

Figure 6.4: Filaments identified in the intersection of the northern the southern region of the Orion A molecular cloud.

The division of the map into two halves is not completely arbitrary. The northern portion of the ISF (here; the northern region) forms high mass stars, and is the densest part of Orion A. Below OMC-4 (here; the southern region) the emission is extended and no current activity of high mass star formation is seen. With `DisPerSE`, I identified 347 filaments in the northern region and 278 filaments in the southern region, 625 in total. These filaments have slightly different properties as I will explain in the following chapters. The different properties arise form the fact that the physical conditions in these two regions are not identical.

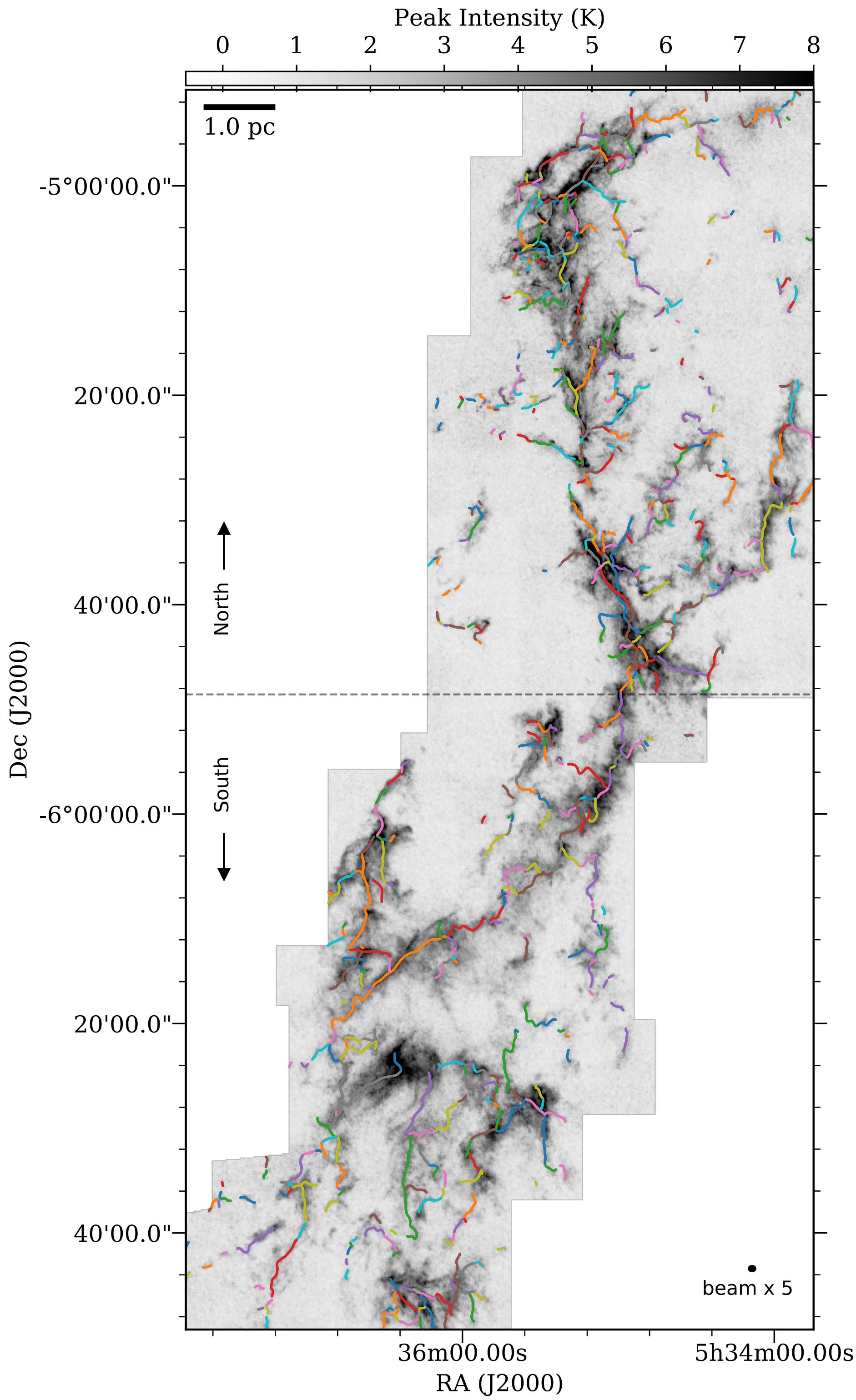

Figure 6.5: Filaments identified in the Orion A molecular cloud. Greyscale shows the $C^{18}O$ peak intensity emission, while the colored segments indicate the filaments identified by `DisPerSE`.

7

FILAMENTARY STRUCTURE IN $C^{18}O(1\text{-}0)$ EMISSION

This chapter focuses on investigating filament properties only on the densest gas tracer from the CARMA-NRO Orion Survey; $C^{18}O(1\text{-}0)$. The reason why is that the filaments are dense structures, and the line emission that traces more diffuse parts of molecular clouds may suffer from various physical processes (e.g. radiative feedback and opacity effects).

As it has been repeatedly mentioned throughout this work, it is of important to understand the properties of these filaments, to unravel the way to star formation in Orion A. For this purpose, in the following I explain the width of the $C^{18}O$ filaments (Section 7.1), and investigate their state of stability against fragmentation (Section 7.2). In Section 7.3, I included a discussion of the implications of the results of this chapter.

7.1 FILAMENT WIDTHS

The filament widths are calculated using `FilChaP` based on the filaments identified with `DisPerSE`. For each filament, `FilChaP` extracts radial intensity profiles perpendicular to the filament spines. This process is explained in detail in Chapter 5. Figure 7.1 is an example of the calculation of the intensity profiles along filaments. The top panel shows the perpendicular slices along the filament as red lines. Intensity profiles from a number of consecutive slices are then averaged to produce the averaged intensity profile. In this case; the number of intensity profiles to be averaged is equal to the number of pixels within three beam-sizes. I addressed the effects of the intensity profile averaging process in Section 5.2.5. The bottom panel of Figure 7.1 shows the average intensity profile in black solid line, and the individual intensity profiles in grey. The vertical grey dashed lines show the positions of the minima that `FilChaP` identified (see Section 5.2.3). These minima are set as boundaries for the fits. The fitted profiles are shown in blue, yellow and red, representing Gaussian and Plummer-like fits with p=2 and 4, respectively. The green dashed lines mark the positions of the identified *shoulders* of the profile (see Section 7.3.1).

7.1.1 *Distribution of filament widths*

With `FilChaP`, I calculated the widths of all the identified filaments. The resulting distributions are shown in Figure 7.2. The colored histograms represent the results for the northern region, the reults for southern region are shown in grey. The panels correspond to the distribution of widths (FWHM) calculated using Gaussian (top

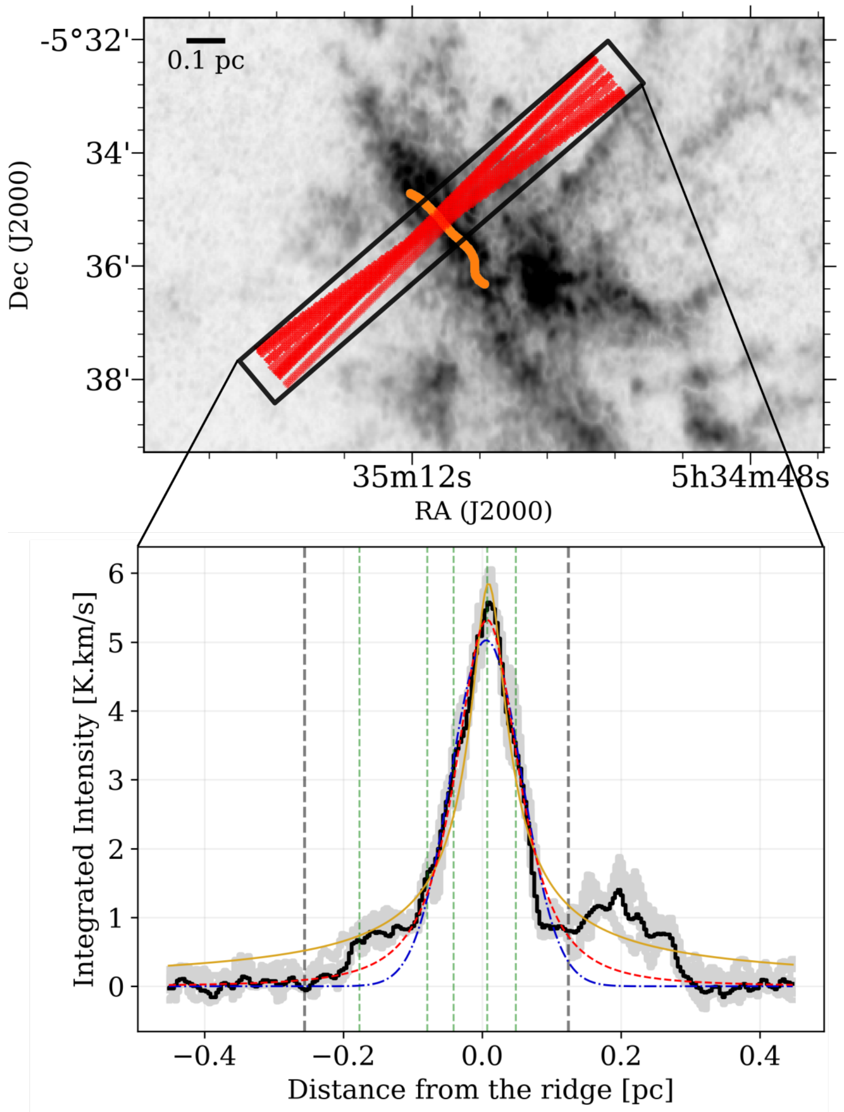

Figure 7.1: Example case of how `FilChaP` works with the given filament and data. *Top*: The greyscale shows $C^{18}O$ peak intensity emission from a selected sub region towards OMC-4. An identified filament spine is overlaid on the map in orange. Red lines represent a set of 12 perpendicular slices at an arbitrary position along the filament. The intensity profiles from the shown slices are averaged together to construct the final profile for the width calculation. *Bottom*: The black line represents the average intensity profile, and the grey lines are the individual profiles that come form each slice. Blue, yellow and red fits indicate Gaussian and Plummer-like fits with p=2 and 4, respectively. Boundaries for the fits are shown as grey vertical dashed lines. The shoulders are shown as green vertical dashed lines explained in Section 7.3.1.

left) and Plummer p=2 fits (top right), Plummer p=4 fit (bottom left) and the FWHM calculated from the second moment (bottom right). Black and red dashed lines indicate the "universal" filament width of 0.1 pc calculated using *Herschel* dust continuum maps, and the 0.03 pc width calculated from N_2H^+ emission map (Arzoumanian et al. 2011; Hacar et al. 2018). The dot-dashed line marks the spatial resolution (0.015 pc) of our $C^{18}O$ data. Figure 7.2 shows the different methods to calculate width result in quite similar distributions, except the Plummer p=2 fits having narrower widths overall. This is also expected because the Plummer (p=2) function is less sensitive to the wings of the profiles. The calculated median values of the distributions are $0.14^{+0.03}_{-0.02}$ pc and $0.16^{+0.04}_{-0.03}$ pc for the Gaussian fits, $0.11^{+0.03}_{-0.02}$ pc and $0.13^{+0.04}_{-0.03}$ pc for the Plummer p=2 fits, $0.13^{+0.03}_{-0.03}$ pc and $0.14^{+0.03}_{-0.03}$ pc for the Plummer p=4 fits, and finally, $0.13^{+0.03}_{-0.03}$ pc and $0.14^{+0.04}_{-0.03}$ pc for the FWHM based on the second moment for the northern and southern regions, respectively. The median widths found in this study are in agreement with the *Herschel* studies (e.g. Arzoumanian et al. 2011; André 2017). They are undoubtedly larger than the widths derived in high resolution ALMA studies (e.g. Hacar et al. 2018; Henshaw et al. 2017). A higher density tracer, N_2H^+, has been used in these ALMA studies and, therefore, narrower filaments found in N_2H^+ emission is not a surprise.

7.1.2 *Width variation along a single filament*

The distributions found in the previous section favour the idea of a "characteristic" filament width because they peak close to 0.1 pc with a spread of a factor of ~2. Different studies show varying spread around the peak filament width: for Arzoumanian et al. (2011); Palmeirim et al. (2013); Koch & Rosolowsky (2015) this value is 2, but a study by Juvela et al. (2012) shows that there is an order of magnitude spread around the mean width of 0.1 pc. In this study, I find that the cause of the spread of this distribution can be attributed to the fact that the filaments are not isolated homogeneous cylinders. The spread is less if the entire filament is represented by an averaged width because the variations along the filament spines are not taken into account.

Figure 7.3 gives an example of how the width changes along *a single filament*. This figure consist of two parts: on the left panel shown is a plot of filament width against the slice number along the filament. The slice number here represents the cross sections for radial intensity profiles along the length of the filament, as the slices are numbered from the beginning to the end of the filament spine. The blue, yellow, red and black lines represent widths calculated from Gaussian fits, Plummer fits with p=2 and 4, and the FWHM derived from the second moment of the distribution. The points *a*, *b*, *c* and *d* indicate the locations of the 4 intensity profiles shown in the right panel. These intensity profiles are selected because they hold information on how the width varies throughout the filament. The Plummer p=2 fit always gives narrower widths along the filament. This is valid for all the filaments as also can be seen from Figure 7.2. One can see from the intensity profiles, at point *a*, the intensity profile is the most narrow

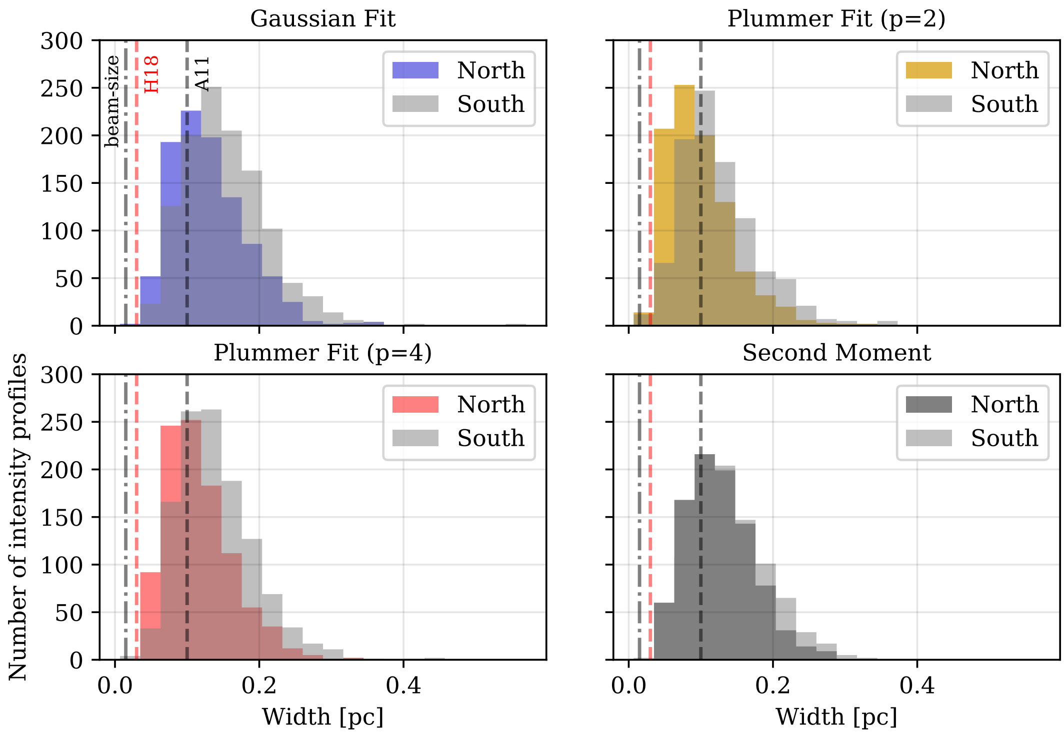

Figure 7.2: Distribution of filament widths in the northern (colored) and southern (grey) regions of Orion A (see Figure 6.5) calculated using Gaussian fits (top left), the second moment of the distribution (bottom right), and Plummer-like fits with power law indices p=2 (top right) and p=4 (bottom left). The dashed lines represent the filament widths from Hacar et al. (2018) in red, and the "characteristic" filament width (Arzoumanian et al. 2011) in black. The dot-dashed line indicates the beam-size of our observations.

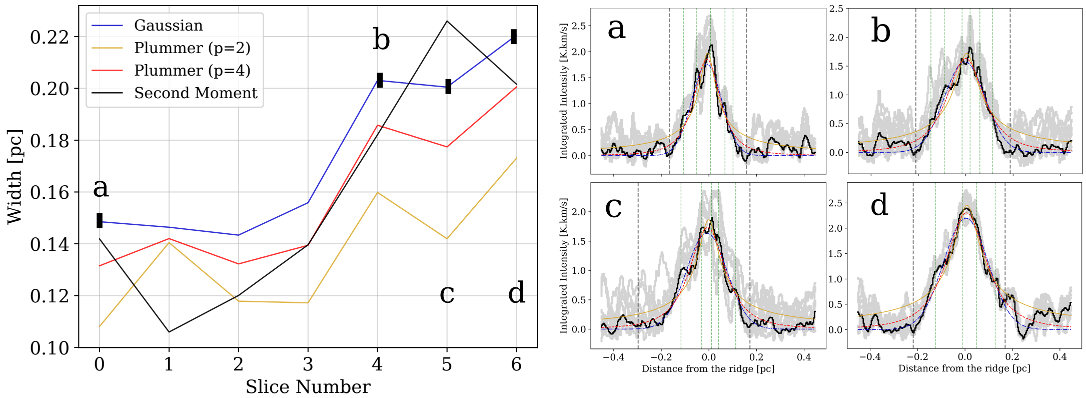

Figure 7.3: *Left*: Variation of filament width along the length of a selected filament. The slice number indicates the cross-sections along the filament. *Right*: Intensity profiles at points a, b, c and d marked in the left panel. These are representative points for the width variation. Grey dashed lines mark the fitting boundaries and the green dashed lines mark the positions of the identified shoulders (see Sect. 7.3.1).

one (0.15 pc, Gaussian FWHM) and it is sharp. The profile has some substructure, locations of which are marked by vertical green dashed lines. From point a to d the substructures wider, hence contributing sufficiently to the filament width. At point b and c, the shoulders on both sides of the peak get wider, which in turn increases the width to about 0.2 pc. The shoulders are identified within `FilChaP` (see Section 7.3.1) as local minima of the second derivative of the intensity profiles. The filament width is highly dependent on the inhomogeneities within the filament which can then be traced by these shoulders.

7.1.3 *Goodness of the fits*

Of course one can argue that the results from the fitted widths should have a measure of "goodness". In order to assess how good the fits are, I calculate the reduced chi-squared (χ^2_R) for each fit. By their reduced chi-squared values I can set a threshold of which fits should contribute to the results of this study such as the distributions shown in Figure 7.2. The reduced chi-squared is calculated as chi-squared per degree of freedom. Each fitting function used has 3 degrees of freedom; the amplitude, mean, and standard deviation for the Gaussian and amplitude, mean and the R_{flat} for the Plummer fits. The left panel of Figure 7.4 shows the resulting reduced chi-squared distributions. The median reduced chi-squared values of the fits are 1.1, 2.9, and 1.2 for the Gaussian, Plummer p=2 and Plummer p=4 fits, respectively. For a good fit, the reduced chi-squared value is 1. Because the noise level in our data is very low for the averaged

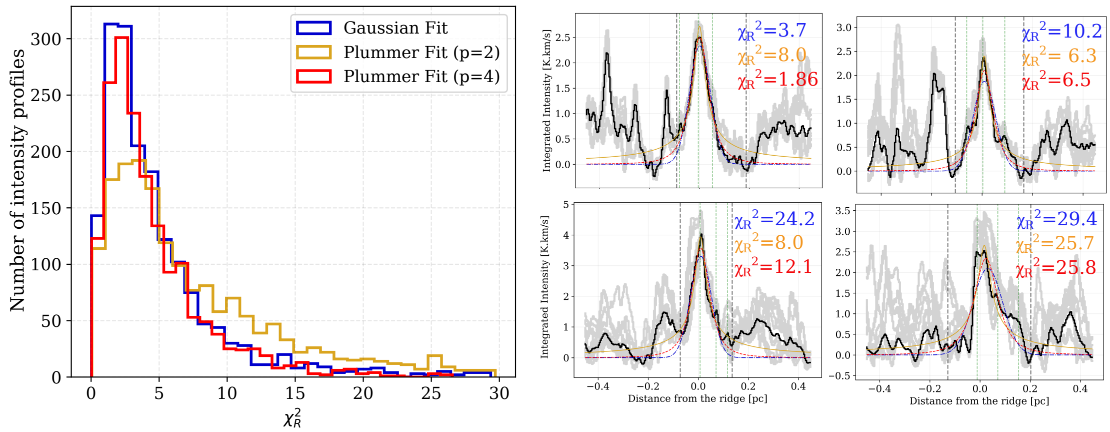

Figure 7.4: *Left*: Distribution of χ^2_R values for different fitting methods. *Right*: Examples of intensity profiles and resulting reduced chi-squared values.

intensity profiles (0.078 K) the reduced chi-squared values tend to be higher as the fits are expected to be "perfect" for a good fit with such low levels of noise. Therefore, there are higher reduced chi-squared values for intensity profiles with substructures which not perfect Gaussians. In fact, a closer inspection of the reduced chi-squared values revealed that up to 25, the fits still represent the intensity profiles. Figure 7.4 also shows four example profiles with varying reduced chi-squared values (right panel). The corresponding reduced chi-squared values for each fit for each profiles indicated on the top right corner in each subplot. The figure, blue, yellow, and red colors represent the Gaussian, Plummer with p=2 and Plummer with p=4 fits. Although the reduced chi-squared values are higher than 1, first three intensity profiles show that the fits are still valid and can be used when deriving results. However, the profiles with somewhat severely blending nearby structures or extended shoulders can cause bad fits with high reduced chi-squared ($\chi^2_R > 25$, bottom right subplot). A reduced chi-squared of 25 is where I draw the line of which fits are acceptable and which are not. This value also corresponds to the tail of the distribution (left panel). 97% of the reduced chi-squared values for the Gaussian fits are between 0 and 25, and this value is 93% for the Plummer p=2 and 98 % for p=4 fits. The fits with reduced chi-squared higher than 25 are not included in the analysis of this data. The width distributions shown in Figure 7.2 are plotted taken into account this criterion. I emphasize that, this threshold is applied to the results from each individual method; i.e. a profile can be fitted with a Plummer function with a good reduced chi-squared but not with a Gaussian function and when this is the case, only the good fit is accepted. Because the widths calculated from the second moment method has no reduced chi-squared values the results form this method are accepted only when the all the other three methods yield good fits.

7.1.4 *Dependence on the fitting range*

In this section, I would like to address an issue of the selected fitting range to calculate the width of an intensity profile that is raised by several authors including Smith et al. (2014b) and Panopoulou et al. (2017). It is always a problem to decide the boundaries of a profile when the length of the perpendicular slice is arbitrarily large. I tackle this problem by finding nearby significant structures that are resolved by at least 3 beam-sizes (see Section 5.2.3). This method assigns a unique fitting range (the range between the two boundaries) to each individual (average) profile. However, there still is a correlation between the fitting range and the calculated width. This is not an unexpected correlation. Even if the boundaries did not exist, the correlation would persist. This is simply because the baselines of the profiles are not perfectly smooth. This means, the further away from each other the boundaries are put, the more emission would enter in between them. Because once again, the filament profiles are not isolated, there is emission blending in from nearby structures and emission surrounding each and every filament. Therefore, the larger the fitting range, the more emission from the filaments' surroundings would the function to fit. The range would not effect the calculated width if the baseline of the intensity profiles were to be perfectly had no structures – that is as long as the fit includes the entirety of the emission. In contrary to an ideal baseline of an isolated filament profile, the observed intensity profiles have emission from the filaments surroundings. Therefore, there always exists a correlation between the fitting range and the filament width.

Various filament studies have set a fixed fitting range for all the intensity profiles (e.g. Arzoumanian et al. 2011; André et al. 2016; Federrath et al. 2016). This later affected the credibility of their results. With `FilChaP`, one is independent from this bias of the fitting range as much as possible as there is no specific fitting range fixed for each profile. But the fitting range is dependent on the environment of the filament, and it changes along the filament. In Figure 7.5 I plot the correlation between the fitting ranges for each individual profile against the derived widths calculated from the four different width calculation methods. Excluding the second moment widths which have no reduced chi-squared values, each point in these subplots are colored by the reduced chi-squared of that fit. The red diagonal lines show the 1-1 relation between the fitting range and the width. I observe the strongest correlation between the two parameters in the second moment (bottom right panel) width results. This result comes about because the second moment is not a fit and it is calculated based on the emission within the boundaries. While the 3 fitting methods can yield widths larger than the fitting range, the second moment method cannot. An example of why the width can be larger than the fitting range is shown in Figure 7.6. This is an example of a profile with multiple peaks. One of the peaks are separated by the boundary because it is a significant structure. When the boundary separates two closeby structures, the intensity profiles similar to that shown

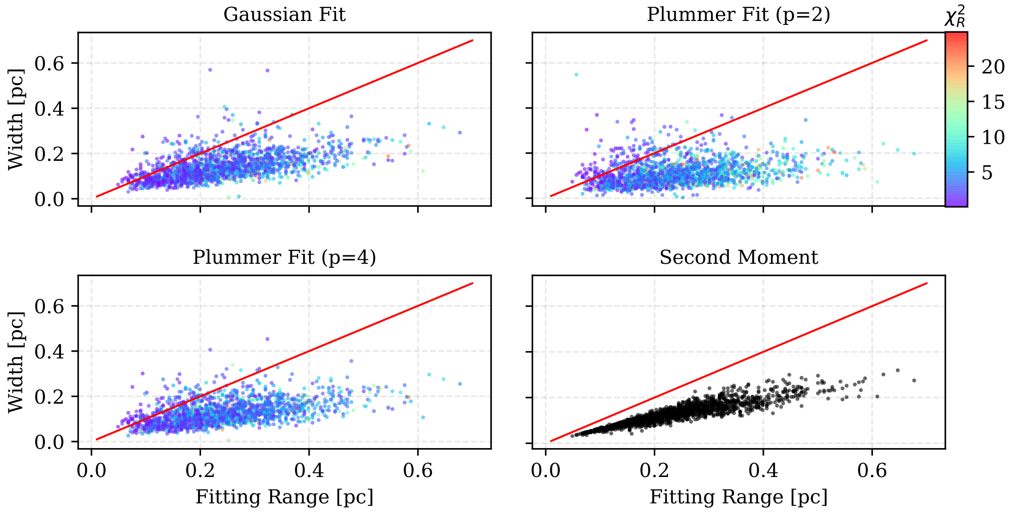

Figure 7.5: Four subpanels showing the correlation between the fitting range and the calculated width. The red lines correspond to the 1-1 relation between the two axes. For the first three subpanels the color-scale corresponds to the reduced chi-squared value of the fits.

in Figure 7.6 have to be fitted based on an incomplete and one-sided distribution. This is how the points above the 1-1 relation line in Figure 7.5 can be produced.

To conclude this section, I would like to point out that out of the 4 different methods I use here the Plummer (p=2) fit is the most independent from the fitting range. The calculated widths have a very shallow sub-linear relation to used the fitting range. It can be seen in the various intensity profiles shown in Figures 7.1, 7.4 and 7.6, the Plummer (p=2) does not give a good fit on the wings of the profile, it only fits the inner portion. I find this method to be most reliable when the profile has multiple peaks. But in general the Plummer p=2 fits lack the information on the wings of the profile. These fits also show the most clear correlation between the reduced chi-squared and the fitting range. The larger the fitting range, the higher the reduced chi-squared for the Plummer p=2 fits. This correlation points to the same root. The larger fitting range introduces more emission to be fitted on the wings of the profiles. As the function fails (or ignores) to fit the wings, the discrepancy between to profile and the fit increases and reduced chi-squared gets larger.

7.2 FILAMENT STABILITY

Previous studies have shown that star forming cores form preferentially along dense filaments (e.g Schneider et al. 2012). This can be explain with the fact that the self-gravitating filaments go through radial collapse fragment into clumps and cores.

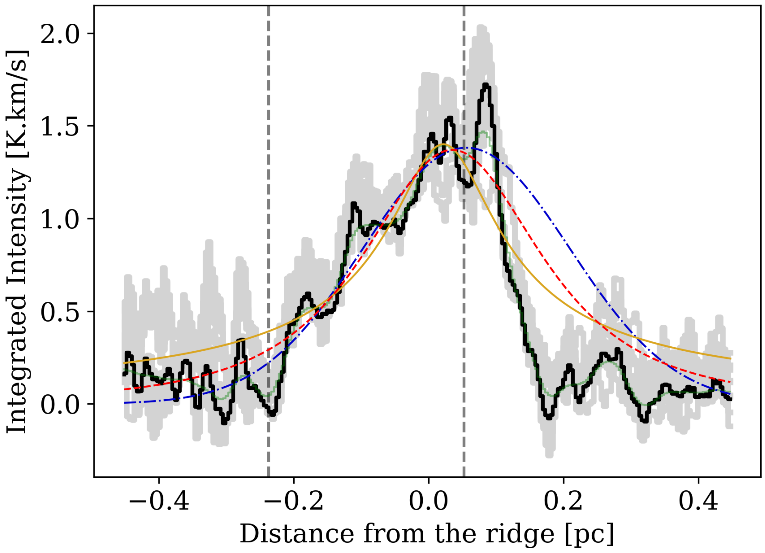

Figure 7.6: Example of an intensity profile when the calculated width is larger than the fitting range.

Filaments become gravitationally unstable when their mass per unit length exceeds a critical line mass; $M_{line,crit} = 2c_s/G$ where G is the gravitational constant and c_s is the sound speed (Ostriker 1964). The sound speed is equal to 0.2 km s^{-1} at a temperature of 10 K. Therefore, at 10 K, $M_{line,crit}$ = 16 $M_\odot$/pc. When a filament's line mass exceeds this critical value, $M_{line,fil} > M_{line,crit}$, the filament becomes unstable for gravitational collapse and fragmentation. If, on the other hand, a filament's line mass is smaller than the critical value, then the filament is unbound and it expands until the external pressure confines it (Inutsuka & Miyama 1992). Therefore, one of the most important parameters on filament studies is the *stability* parameter that is defined as the ratio of filament's line mass to the critical line mass.

The filament line mass can be estimated as $M_{line,fil} = N_c(H_2)W$ where $N_c(H_2)$ is the central column density of the filament spine and W is the calculated filament width (Arzoumanian 2017). The panels shown in Figure 7.7 present the three important factors that play a vital role in star formation. The left panel of Figure 7.7 shows the filaments overlaid on the C^{18}O peak intensity map where each point along the filament is colored by the column density at that point. The column densities at each skeleton point are taken from the large scale *Herschel* column density map of Orion A (Stutz & Kainulainen 2015). For this purpose I regridded the *Herschel* column density map to match the C^{18}O map. However, the column density value obtained from this map is a lower limit, because the angular resolution of the *Herschel* map (18 arcsec $\sim$ 0.03 pc) is lower than the $C^{18}O$ map. The middle and right panels of Figure 7.7 show the line masses along the filaments and the stability parameter. The filaments identified in the outskirts of the cloud have low column densities, line masses and are stable against gravitational collapse with low stability parameters (< 1). The dense ridge of the cloud, however, is unstable against fragmentation, with line masses that reach above 100 $M_\odot$/pc.

In order to visualize a better connection of the filament stability to the formation of new stars; I plot the filament stability (same as Figure 7.7 right panel), overlaid with the (non)star forming cores identified in the region. There are two large scale protostar catalogues of Orion A; published based on different surveys: (1) a Young Stellar Object (YSO) catalogue based on infrared Spitzer data (Megeath et al. 2012) and (2) a submillimeter catalogue based on 850 μm emission map form JCMT Gould Belt Survey (Lane et al. 2016). I particularly use a down-sized version of the JCMT core catalogue that is published with the Green Bank Ammonia Survey (Kirk et al. 2017). This catalogue has put several additional constraints on defining the cores from the Lane et al. (2016) catalogue. These constraints require cores to have peak fluxes and total fluxes of 3 times the signal-to-noise ratio. These protostars are identified in the dense NH_3 emission throughout the ridge of the ISF. Although the coverage in right ascension of the NH_3 map is much less than that of our CO map; the most unstable filaments are located at the ridge, therefore the comparison is fair. Figures 7.8, 7.9 and 7.10 show zoom-ins to the most active star forming regions of the cloud: OMC-2/3 and 1, OMC-4 and 5, and OMC-6, respectively. The orange boxes represent the location of starless cores, while the blue starts show the locations of the YSOs. The majority of the protostars lay on the identified filaments, and the most unstable filaments with the highest observed column densities harbour YSOs.

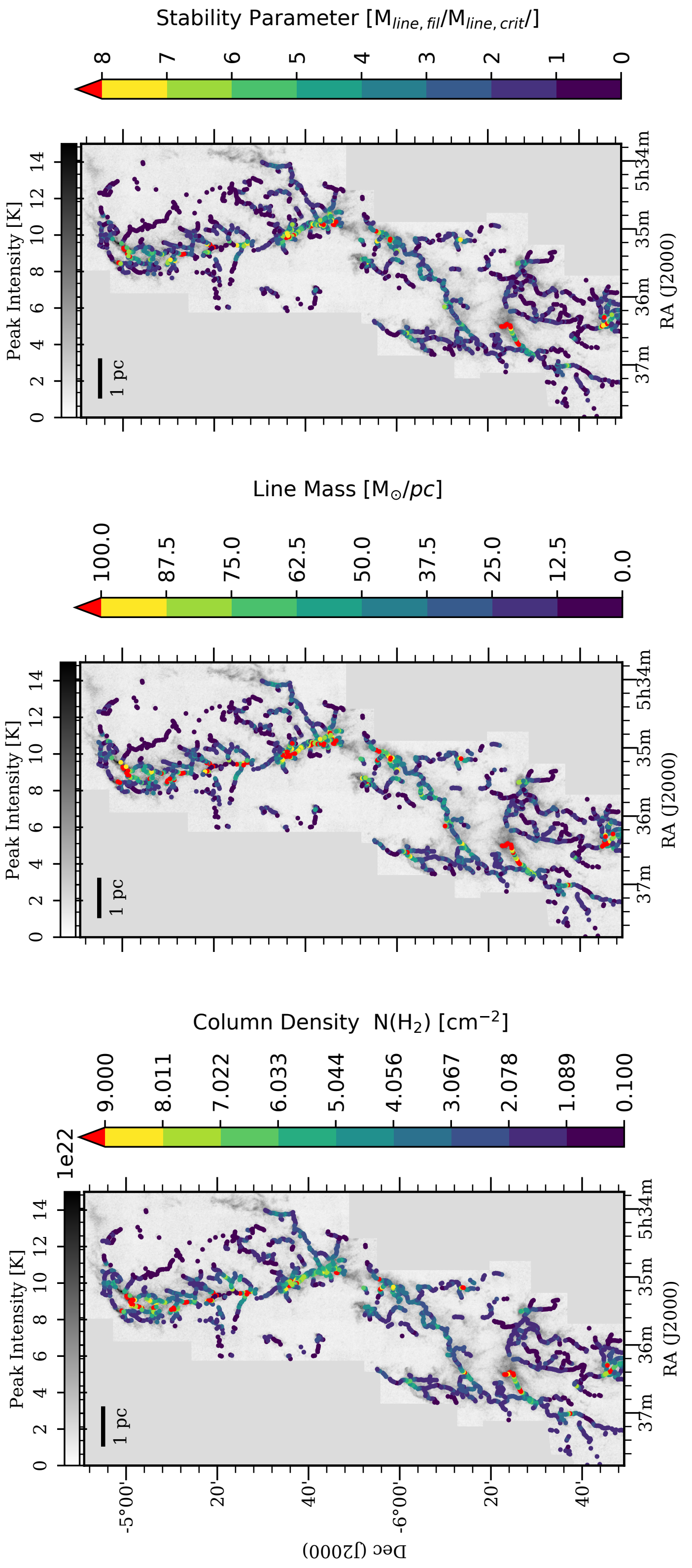

Figure 7.7: *Left*: N(H_2) column density along the identified filaments. The column density values are taken from the *Herschel* column density map published in Stutz & Kainulainen (2015). *Middle*: Line masses along the identified filaments. *Right*: Stability parameter along the identified filaments.

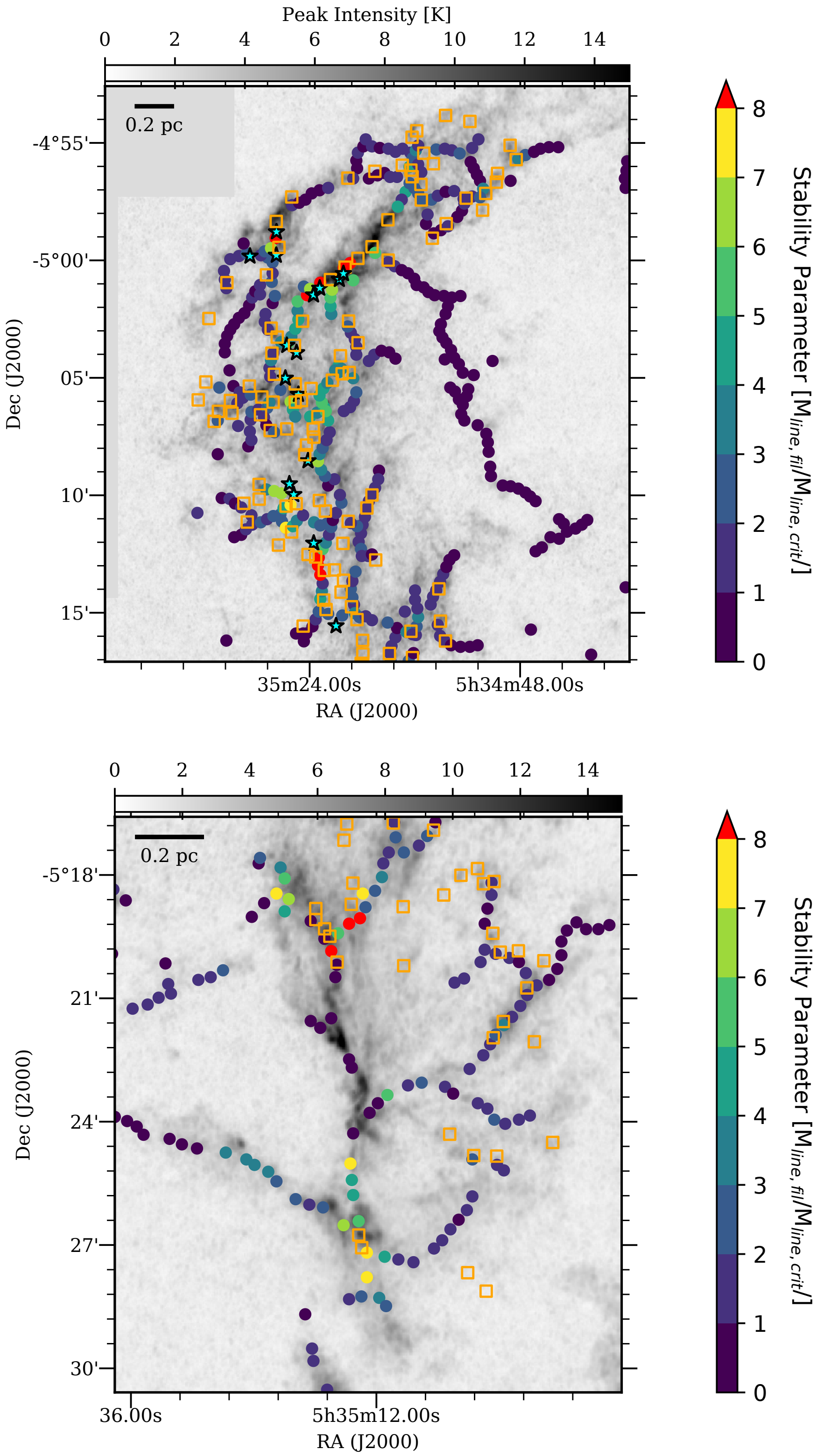

Figure 7.8: *Top*: Zoom in to the OMC-2/3 region in the north of Orion A where filaments are colored by the stability parameter. The orange boxes show the locations of starless cores and the blue stars show the locations of YSOs. *Bottom*: Same as the top panel but for the OMC-1 region.

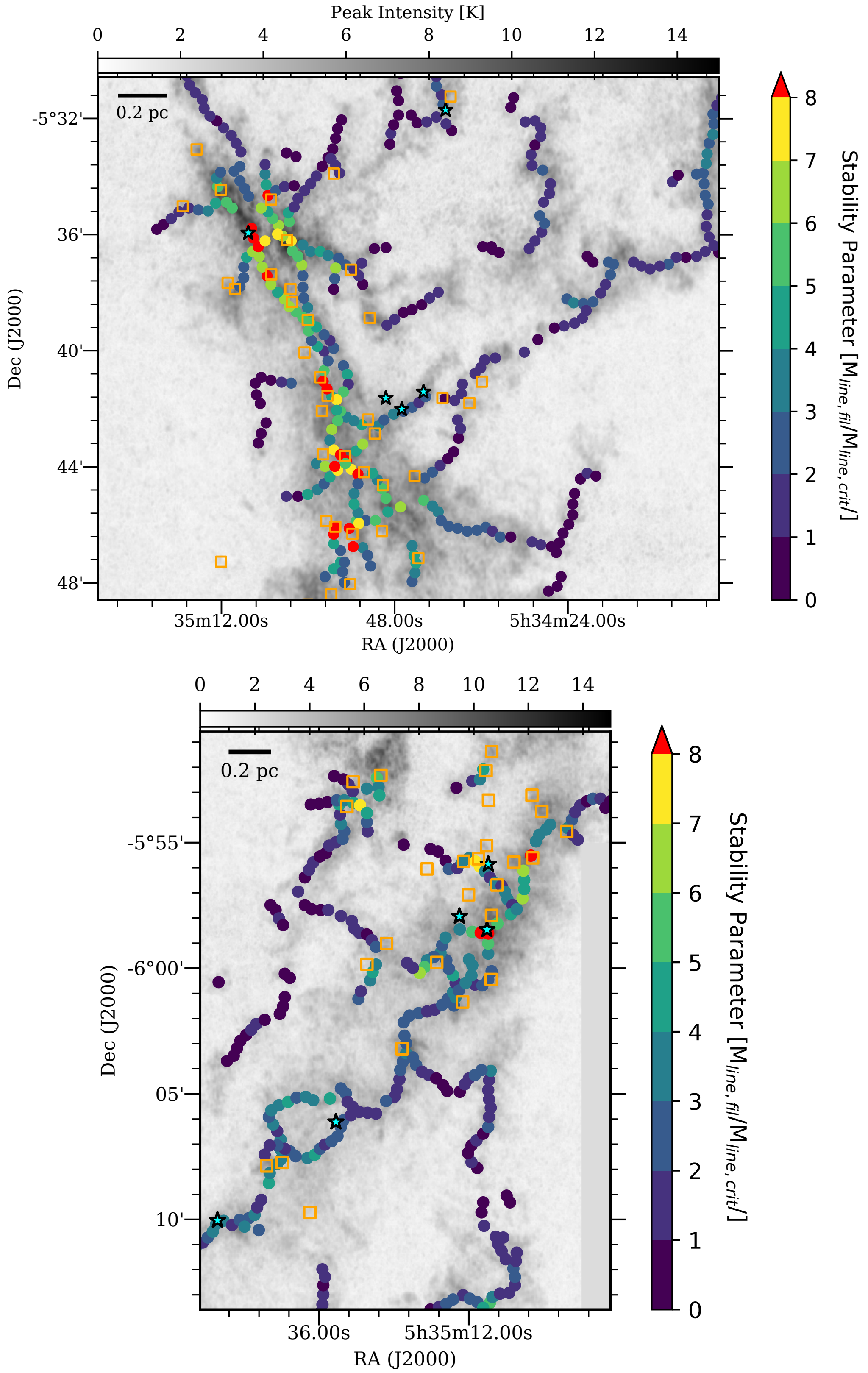

Figure 7.9: Same as Figure 7.8 but for the OMC-4 (top panel) and OMC-5 regions.

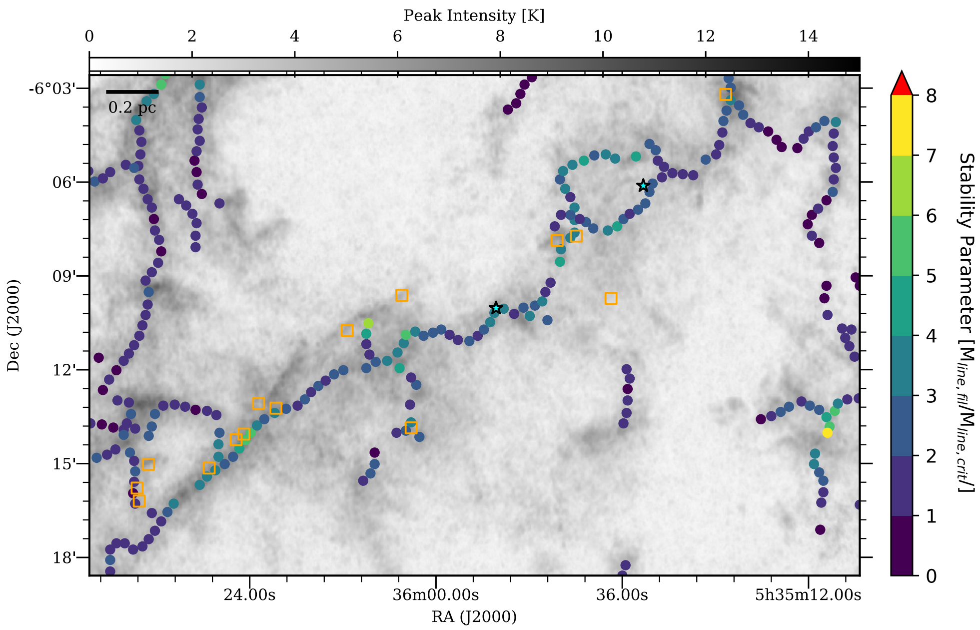

Figure 7.10: Same as Figure 7.8 but for the OMC-6 region.

7.3 DISCUSSION

This chapter holds a plethora of information on the properties of the identified filaments. Therefore, I would like to continue with a discussion section that aims at putting all this information into the context of star formation. For this purpose, I investigate how and why the filament width changes across the cloud, how the filament width scales with column density, what role does the turbulence play in keeping the filament width nearly constant and finally, how all of these results are affected by the selection of parameters in producing the filament catalogue.

7.3.1 *Variation of the filament width across the cloud*

Previously referring to Figure 7.3, I argued that the spread of the width distribution comes from the variation along individual filaments. I also argued that the variation is caused by the shoulders of the intensity profiles, and blending structures especially around the star forming hubs. Let us take a closer look into this argument. Figure 7.11 shows the variation of width and number of shoulders across the cloud. In the left panel, each point along the filament is colored by their width (Gaussian FWHM), and on the right panel the color scale represents the number of shoulders. Positions of the hubs where filaments merge are marked with arrows. This figure tells us two things,

(1) even though there seems to be a common width of filaments within a factor of a few, it is not constant across the cloud. It changes even along individual filaments, and (2) both the width and number of shoulders show a clear increase towards the hubs. This is inevitable because of structures blending in together. One other important aspect of this figure is that one can visually confirm that the increase in width, is clearly connected to the increase in the number of shoulders. This conclusion was already drawn in Figure 7.3, however here, one can see that the example filament discussed in Section 7.1.2 is not an isolated case. The narrowest filaments are the ones with the least number of shoulders and the locations of the widest points along the filaments seem to be a perfect match with the locations where 5 or more shoulders are detected. One can notice that some of the detected filaments are not shown here, this is because of the applied reduced chi-squared criterion.

To quantitatively demonstrate the linear relation between the number of shoulders and filament width, it is better to plot the two quantities against one another. In Figure 7.12 the grey circles show the width against number of shoulders for each profile. The red and blue circles represent the median width at each shoulder bin, for the northern and southern region, respectively. The errorbars are the interquartile range of widths at each bin. The solid and dashed black lines are the linear fits to the correlation, for the northern and southern regions. This figure demonstrates how complex the intensity profiles are. In the northern region the profiles with no shoulders account only for 30% of all the profiles, where in the southern region this value drops to 23%. The fact that the majority of the filaments are highly substructured implies that filaments cannot be treated as isolated perfect cylinders. Furthermore, from the intercepts of the linear fits, one can infer the width of a profile if it had no shoulders. The intercepts of the fits yield 0.06±0.01 pc and 0.08±0.01 pc filament widths for the northern and southern regions, respectively.

This picture confirms the idea of filament widths being relatively constant with a dispersion of a factor of a few. Theoretical work suggest that fragmenting supercritical filaments with $M_{line,fil} > M_{line,crit}$ may defy gravitational contraction due to existing substructure (Clarke et al. 2017). This substructure is argued to lessen the global effects of gravity and, in turn, resulting in constant filament widths. Because the filaments that are observed in $C^{18}O$ show substructure, they would break down into narrower structures if a higher density tracer is observed at a higher angular resolution. The recent work by (Hacar et al. 2018) confirms this scenario, as they observed filaments with 0.03 pc widths in N_2H^+ emission using high resolution ALMA observations.

7.3.2 *The lack of anti-correlation between the width and column density*

If the filaments have high column densities and are unstable against gravitational collapse along their short axes, then it is naively expected that they should also contract along their short axes. Therefore, I look for an anti-correlation between the column

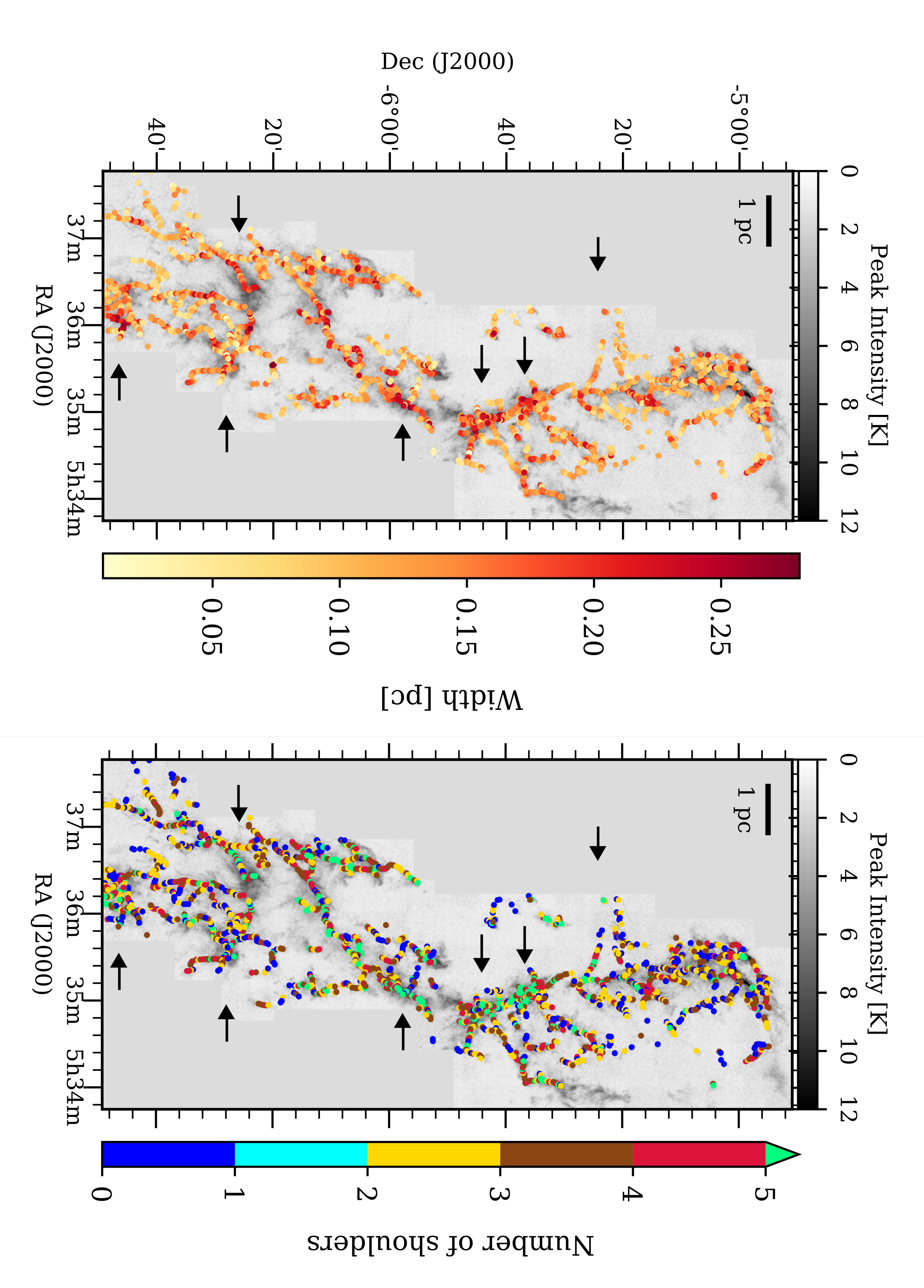

Figure 7.11: Filaments overlaid on the $C^{18}O$ map, colored by their width (left) and the detected number of shoulders (right). The arrows indicate the locations of star forming hubs.

density of the filament ridges and their widths. Figure 7.13 shows the central column density of filaments at each point along the filament spine, plotted against the width calculated at each of these points. As in Section 7.2 the column densities are take from the *Herschel* column density map published in Stutz & Kainulainen (2015). The blue, yellow, red and black colored points represent FWHM obtained from Gaussian fits, Plummer p=2 and p=4 fits and the second moment, respectively. The horizontal dashed line is the resolution of the observations (0.015 pc), and the solid diagonal line is the thermal Jeans length at 10 K; $\lambda_J = c_s^2/G\mu_H\Sigma_0$ where Σ_0 is the central column density (Arzoumanian et al. 2011). The usage of the Jeans length here refers to a state of hydrostatic equilibrium. The points on the left hand side of the Jeans length line are in equilibrium and on the right hand side they are not. However, whether Jeans instability is applicable to non-spherical and inhomogeneous filaments is a matter of debate. For the purpose of this work, the only instability parameter that I would like to endorse is the one calculated from the $M_{line,fil}$ to $M_{line,crit}$ ratio in Section 7.2. I, nevertheless, included the Jeans length in this figure in order for a comparison to previous work (see e.g. Arzoumanian et al. 2011; Heitsch 2013; Arzoumanian 2017).

Figure 7.13 does not show an anti-correlation between the column density and the width. Based on previous studies, we know that low-mass star forming regions such as Aquila, IC5146 and Polaris have shown such a lack of anti-correlation (Arzoumanian et al. 2011). Additionally, this work shows that even in a violently high-mass star forming region Orion A the lack of anti-correlation persists. Therefore, I propose that the variation of the filament widths is regulated mostly by the amount of substructure they contain (shoulders) and their environment (whether they are more isolated or in the vicinity to star forming hubs).

Arzoumanian et al. (2011) argued that supercritical filaments can retain a constant width through constant accretion from their surroundings. Then, a number of theoretical studies made an effort to understand why the filament width should be constant within a factor of a few while their central column densities vary by more than an order of magnitude. Heitsch (2013) tested this claim by studying infall onto isothermal filaments that are subject to external pressure. This study unravelled conditions at which the filament widths can indeed become independent from the underlying column densities. They found the best fitting model to the observations presented in Arzoumanian et al. (2011) is the case of magnetized filaments that are exposed to varying external pressure exerted by the accreted material. The results presented in Figure 7.13 also fit in with this scenario, however, the decrease in filament width towards higher column densities up to 10^{23} cm^{-2} as predicted by the model is not observed in our data.

7.3.3 *The uncorrelation between the velocity dispersion and column density*

One question that comes to mind about the uncorrelation between the width and column density is simply: "Are the filaments supported by turbulent pressure driven

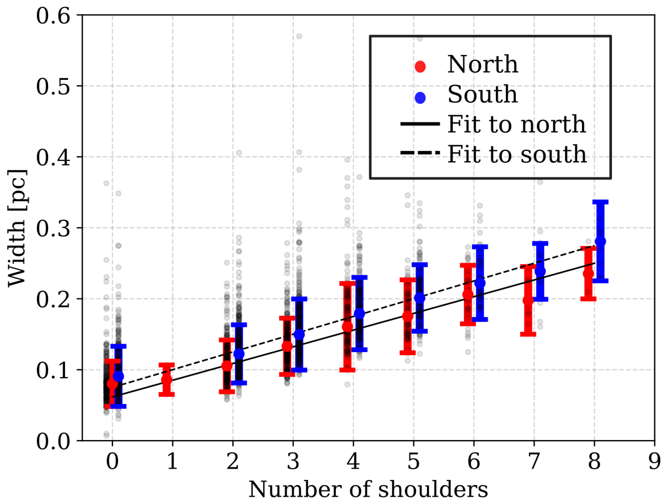

Figure 7.12: The correlation between the filament width and number of shoulders. The gray circles represent the width, where the red and blue circles are the median values at each number of shoulder bin. The error bars show the interquartile range.

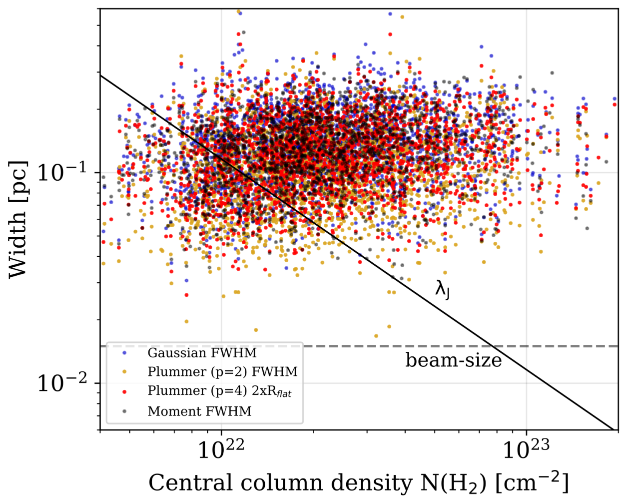

Figure 7.13: Variation of filament widths against column density. The widhts are colored based on the used methods, the FWHM of Gaussian fits are shown in blue and moment analysis in black, 2×R_{flat} for Plummer p=2 in yellow and p=4 in red. The dashed line marks the resolution of the observations. The solid line is the thermal Jeans length at a temperature of 10 K.

by the accretion flows?". If yes, what are the characteristics of these accretion flows, how fast and efficient they need to be to exert such turbulence. Here the efficiency is the efficiency needed to convert the kinetic energy of the accretion flow to internal turbulence.

For this purpose I look at the total velocity dispersion of the filaments. When we observe molecular line emission, the velocity dispersion we calculate as the second moment is,

$$\sigma_{obs} = \frac{\Delta v_{obs}}{\sqrt{8ln2}} \tag{7.1}$$

and this dispersion includes thermal and non-thermal components:

$$\sigma_{tot} = \sqrt{\sigma_{th}^2 + \sigma_{nt}^2}, \tag{7.2}$$

where σ_{th} is the contribution from the thermal emission of the observed molecule and σ_{nt} turbulent component. The thermal component can be directly calculated as

$$\sigma_{th} = \sqrt{\frac{kT}{\mu_{mol} m_H}}, \tag{7.3}$$

where k is the Boltzmann constant, T is the excitation temperature, μ_{mol} is the molecular weight of the observed molecule and m_H is the mass of the Hydrogen atom. By plugging in Equation 7.3 into Equation 7.2 one can estimate the non-thermal contribution to the observed velocity dispersion. For the $C^{18}O$ molecule the contribution from the thermal line emission can be calculated using a temperature of 10 K and its molecular weight is 30. These values yield; σ_{th} = 0.04 km s^{-1} . This is a lower limit as the gas temperature in Orion A is higher than 10 K at times, but an increase in temperature by a factor of 2 would increase the thermal velocity dispersion only by a factor of $\sqrt{2}$.

In order to estimate the velocity dispersion of the filaments I use two different methods. In the previous sections, I have shown that the observed filaments are not single entities, but they are composed of substructure. I would like to see the contribution of this substructure to the total observed velocity dispersion. As the $C^{18}O$ spectra is not complex (with multiple peaks along the line of sight) except for multiple structures seen in OMC-4, for simplicity I used the first and second moment maps (velocity centroid and dispersion) for this analysis. Figure 7.14 shows a sketch of how this can be calculated. Each perpendicular slice calculated to obtain the filament widths can also be used to extract information on how the velocity centroids and dispersion differs from one perpendicular pixel to another. Therefore, for each perpendicular slice I calculate the standard deviation of velocity centroids. The size of the perpendicular slice here is equal to the calculated fitting range from the `FilChaP` run for filament widths, thus, should include all the substructure. If the emission from all the all pixels within the fitting range along a perpendicular slice peaked at exactly the same velocity, the dispersion of the velocity centroids along that perpendicular slice would be zero. I define then the total velocity dispersion as follows:

$$\sigma_{extended} = std(m_1) + median(m_2), \tag{7.4}$$

where m_1 is an array of velocity centroids at every pixel along a perpendicular slice, and m_2 is an the corresponding velocity dispersions of each pixel. If the velocity dispersion along the slice does not vary, then, the total velocity dispersion is equal to the median velocity dispersion. If, however, the centroids vary, this dispersion is added to the median velocity dispersion to account for the contribution from the extended filament. Furthermore, a second way to calculate the total velocity dispersion previously used in literature is to only look at the velocity dispersion along the filament spine (σ_{spine}) without including the contribution of the extended surroundings of the filament (e.g. Arzoumanian 2017). Figure 7.15 shows the column density along the filament spine plotted against the total dispersion calculated using the two methods: $\sigma_{extended}$ and σ_{spine} in the upper and lower panels, respectively. Each point is colored by the line mass of the filament at that point. The distribution of σ_{spine} is scattered around a mean of 0.4 km s^{-1} and is independent of the underlying column density. The velocity dispersion calculated as $\sigma_{extended}$ is much higher with a mean value of 2.1 km s^{-1} . The comparison between σ_{spine} and $\sigma_{extended}$ demonstrate the importance of the contribution of the substructure within the filament. The velocity dispersion along the filament spine can only be used as a lower limit to estimate the turbulence within the filament. However, the estimation of the velocity dispersion from the extended filament might also be affected by the global velocity gradient of the cloud, at this point there is not an easy solution to detangle filaments from their immediate environment. Therefore, I accept the mean values of σ_{spine} and $\sigma_{extended}$ as lower and upper limits to the total velocity dispersion of filaments. Moreover, the thermal velocity dispersion (0.04 km s^{-1}) has very little contribution to the calculated total velocity dispersions σ_{spine} and $\sigma_{extended}$.

Now we can calculate the level of turbulence that is driven by accretion:

$$\sigma(t) = \left(2\epsilon R_f v^2(R_f)\frac{\dot{m}(t)}{m(t)}\right)^{1/3}, \tag{7.5}$$

where R_f is the filament's bounding radius, $v(R_f)$ is the accretion velocity, ϵ is the driving efficiency that is the efficiency at which the kinetic energy is converted to turbulence, $\dot{m}(t)$ is the accretion rate and $m(t)$ is filament's density at time t (Clarke et al. 2017; Heitsch 2013; Klessen & Hennebelle 2010). By numerically solving this equation we can calculated the accreted mass and velocity dispersion as a function of time (S. Clarke private communication). For solving the equation, I consider various

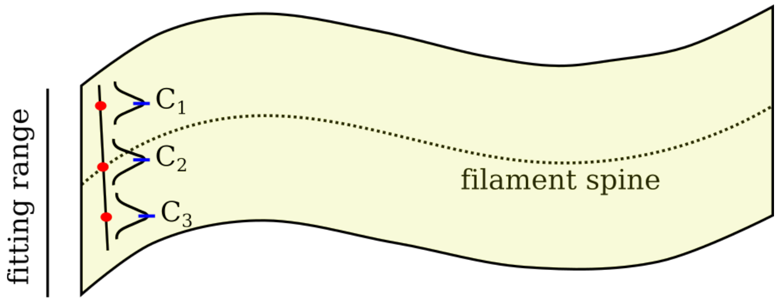

Figure 7.14: Sketch of a filament with a perpendicular slice. 3 pixels along the perpendicular slice are represented with red dots, and the spectra at each of these pixels are also shown. The centroids of the spectra are marked as $C1$, $C2$ and $C3$. The calculation of $\sigma_{extended}$ (see text) considers the dispersion of the velocity centroids along each perpendicular slice.

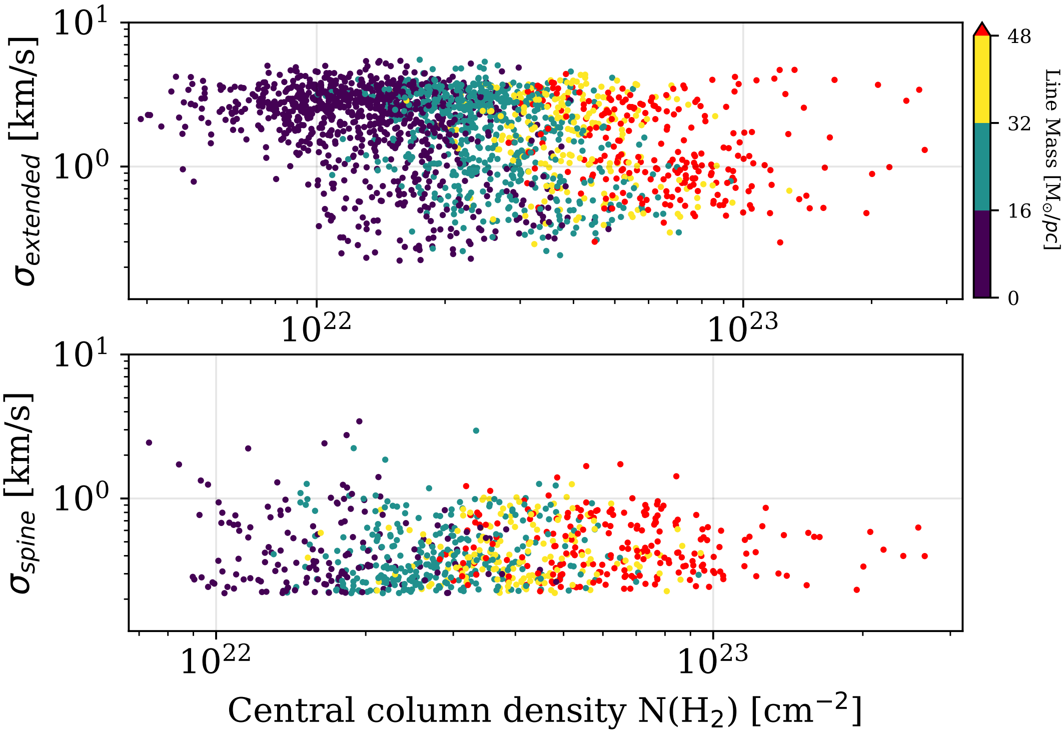

Figure 7.15: Total velocity dispersions calculated using two different methods, $\sigma_{extended}$ (top panel) and σ_{spine} (bottom panel), are plotted against the central column density. The scatter points are colored by the line mass of each at each point along a given filament.

combinations of parameters $v(R_f)$, ϵ and $m(t)$ with a bounding filament radius of 0.1 pc. Figure 7.16 shows the total velocity dispersion that can be achieved for each model as a function of time. The black solid, dashed and dotted lines are the solutions for increasing densities of 20, 50 and 75 cm^{-3} with an initial accretion velocity of 0 km s^{-1} and an efficiency of 10%. As the density of the accreting flow increases, the turbulence driven increases as well, reaching a velocity dispersion of about 0.5 km s^{-1} for a density of 75 cm^{-3}. The red solid, dashed and dotted lines indicate models for initial accretion velocities of 3, 5 and 10 km s^{-1} with a constant density of 20 cm^{-3} and an efficiency of 10%. The accretion velocities of 3 to 5 km s^{-1} result in a velocity dispersion around 1 km s^{-1} which is in between the upper ($\sigma_{extended}$) and lower (σ_{spine}) bounds for the observed velocity dispersions. The blue solid, dashed and dotted lines represent the solutions when the accretion velocity is kept constant at 3 km s^{-1} and the driving efficiency is varied between 5, 15 and 30%. With an accretion velocity of 3 km s^{-1}, the observed turbulence level is reached when the efficiencies are higher than 5%.

If we take the observed velocity dispersion between the upper and lower bounds to be approximately 1 km s^{-1}, the best fitting models are with accretion velocities of 3 to 5 km s^{-1}, represented by red (solid and dashed) and blue (dashed and dotted) lines (Figure 7.16). This means that in order to produce such turbulence that would produce the observed velocity dispersion of 1 km s^{-1}, we would need accretion velocities of 3 to 5 km s^{-1}.

From the model we can also infer the acquired line mass during accretion. Figure 7.17 shows how the line mass of the filament changes over time as the filament continues to gain mass through the accretion flow. Here, the solutions represented with blue lines and the red solid line overlap because the driving efficiency does not affect the line mass. The majority of our filaments have line masses between a few $M_\odot$/pc and 50 $M_\odot$/pc. Following the 3 km s^{-1} solution (best fit model) in Figure 7.17, filaments can accrete about 50 $M_\odot$/pc around 1 Myr. Therefore, I conclude, if our filaments have accreted most of their masses from their surroundings, the majority of them must be younger than 1 Myr (given the accretion velocity of 3 to 5 km s^{-1}). On the other hand, he most massive filaments with line masses of 100 $M_\odot$/pc and above are a few Myr old.

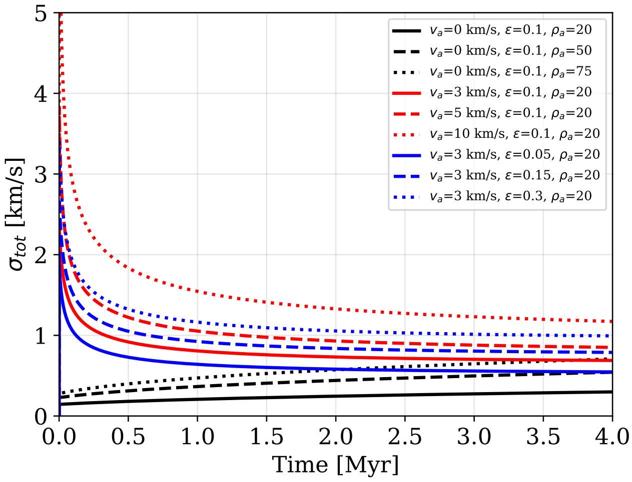

Figure 7.16: The level of velocity dispersion that can be driven by accretion flows onto filaments plotted as a function of time. The solutions are calculated numerically from Equation 7.5 for varying characteristics of the accreting flow. The black, red and blue lines indicate the solutions when density of the accreting gas, velocity of the accreting gas and the driving efficiency are varied, respectively.

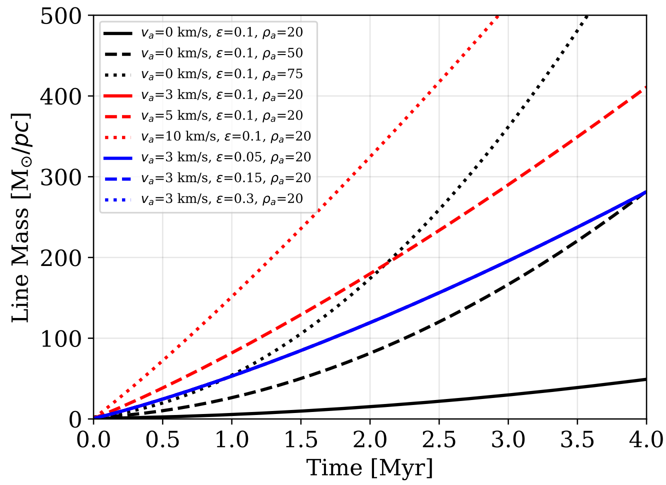

Figure 7.17: Line mass that can be achieved by varying accretion models presented in Figure 7.16. The solutions represented with blue lines and the red solid line overlap because the turbulence driving efficiency does not affect the line mass.

7.3.4 *The effect of filament selection on the calculated filament width*

In this section, I investigate how the selection criteria, the aspect ratio and the reduced chi-squared threshold affect the results. Previously, I presented the filament widths based on all the identified filaments with lengths larger than 3 beam-sizes, and with reduced chi-squared values lower than 25. I now vary this criteria and re-plot Figures 7.2, 7.12 and 7.13. I consider 3 different cases; (1) all the filaments whose intensity profiles are fitted with a reduced chi-squared less than or equal to 5, (2) filaments with aspect ratios larger than 2 whose intensity profiles are fitted with a reduced chi-squared less than or equal to 25, (3) filaments with aspect ratios larger than 2 whose intensity profiles are fitted with a reduced chi-squared less than or equal to 5. The goal of using these 3 different thresholds to produce the same figures as in previous sections is to show that the initial selection criteria has not introduced a bias in the results presented in this chapter.

Figure 7.18 shows the width distributions for the different calculations methods, the same as Figure 7.2, but for the 3 different selection criteria. The top, middle and bottom panels correspond to the criteria: where all the filaments used but the reduced chi-squared threshold is dropped to 5, where only those filaments with aspect ratios larger than two are used with the original reduced chi-squared threshold and where only the filaments with aspect ratios larger than 2 are used with a reduced chi-squared threshold of 5. Figures 7.19 and 7.20 are the same as Figures 7.12 and 7.13 but plotted for the 3 different criteria.

From Figure 7.18 it can be inferred that the widths calculated from the second moment of the distribution is the least affected from the changing criteria. This is because the second moment calculation does not have a chi-squared value, and a second moment is accepted if all the other fits (Gaussian and Plummer fits) of the corresponding intensity profile satisfies the criteria. The top and bottom panels reveal that in the northern region lower reduced chi-squared fits yield narrower filament widths, while in the southern region the filament widths are larger. Furthermore, the middle panel reveals that the aspect ratio has no influence on the results, as the distributions do not show a significant deviation from Figure 7.2. The median filament widths for these three cases and the original calculation of all filaments with reduced chi-squared values less than or equal to 25 are listed in Table 7.1.

Figure 7.19 shows that the slope and the intercept of the width versus number of shoulders relation slightly varies with different criteria. If one wants to infer the filament width with no detected substructure based on the intercept of these fits, the most narrow filament widths are detected when only those filaments with aspect ratios larger than 2 and with intensity profiles fitted with a reduced chi-squared less than or equal to 5 are used (bottom panel). Table 7.1 also includes the widths calculated from the intercepts of these linear fits.

The column density versus width relations for different selection criteria shown in Figure 7.20 shows a similar uncorrelation between the two quantities. This figure ensures that the independence of the filament width from the underlying column density found in this work is not affected by the filament selection.

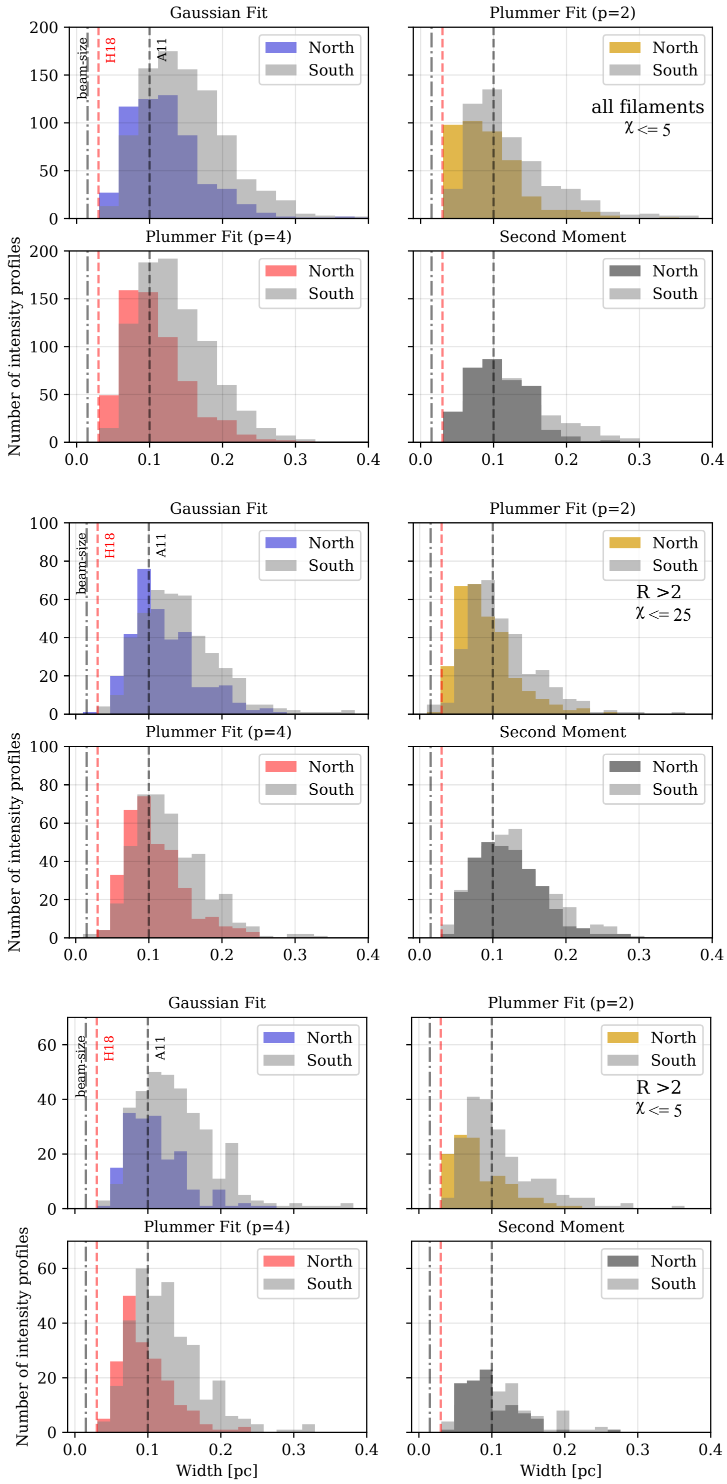

Figure 7.18: Same as Fig. 7.2

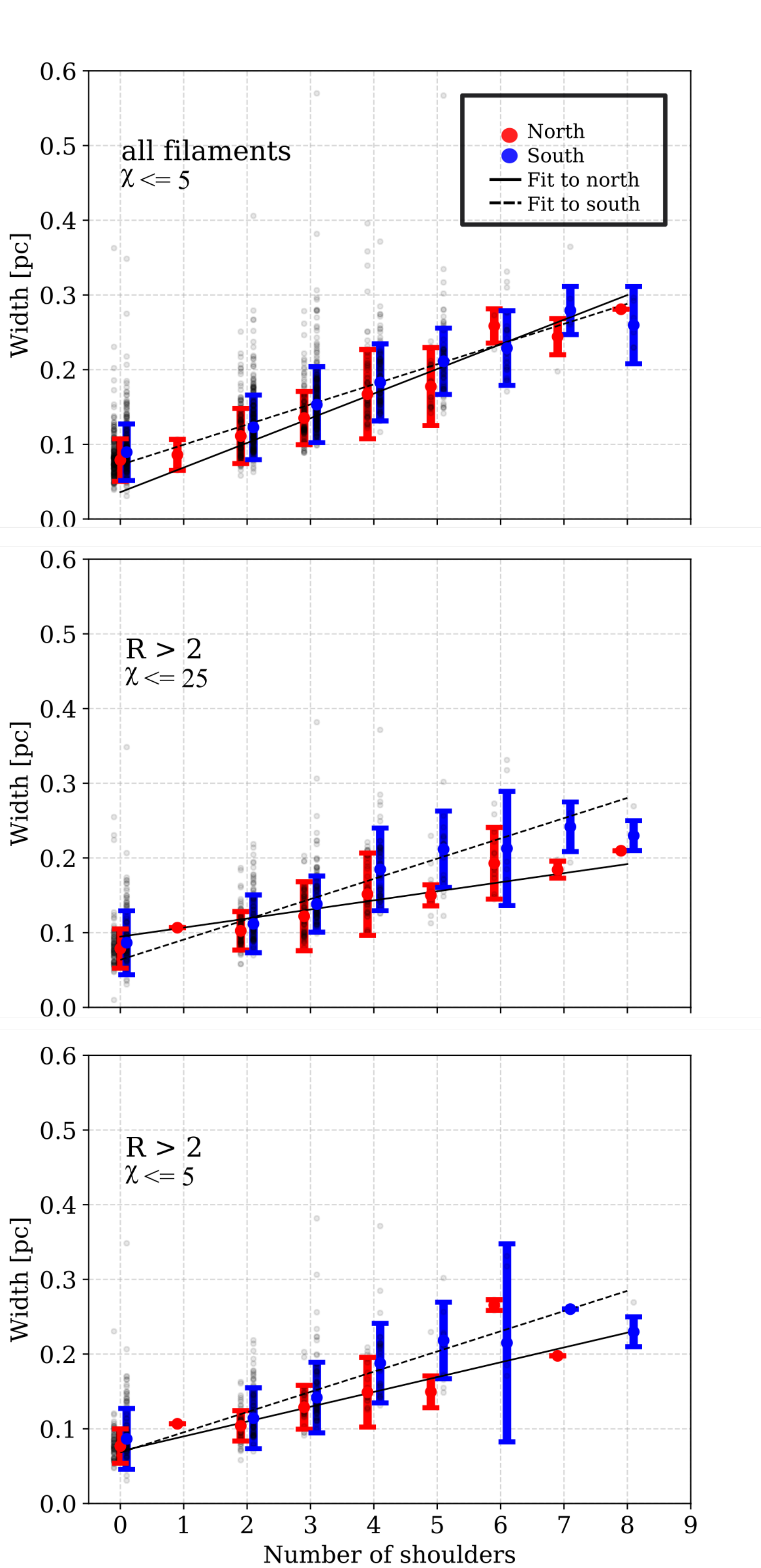

Figure 7.19: Same as Fig. 7.12 for the different criteria (aspect ratio and reduced chi-squared of the fits).

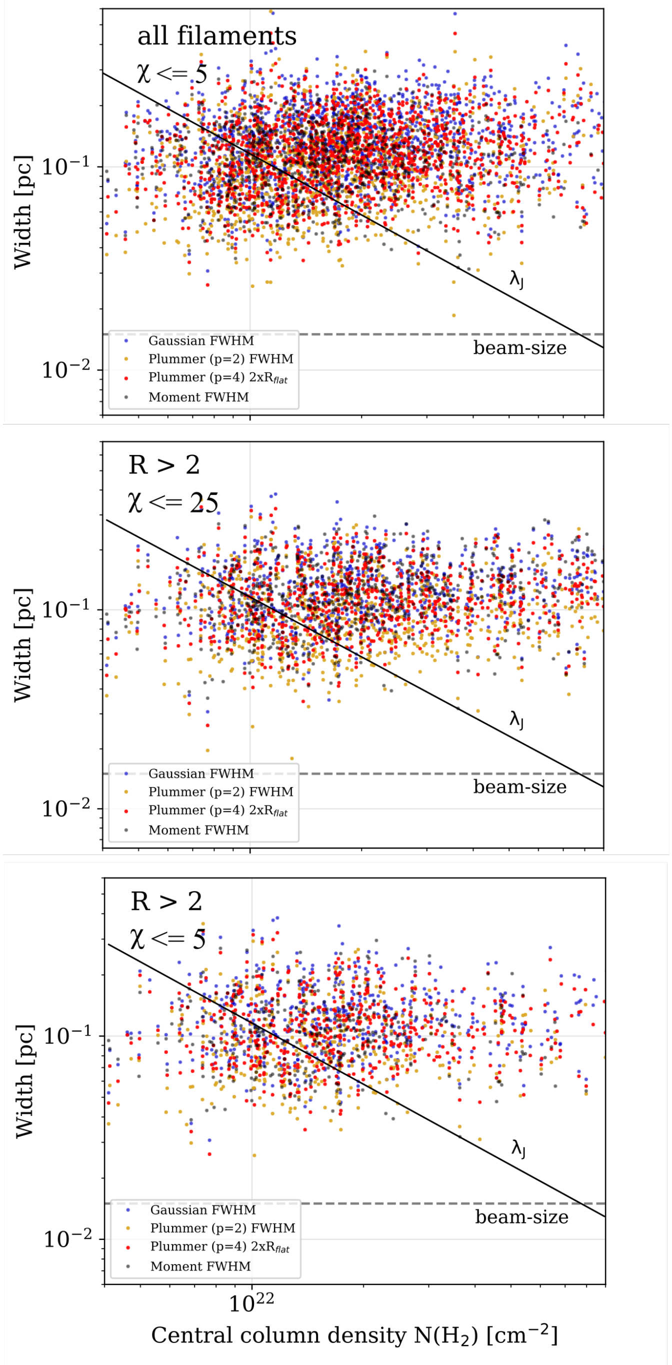

Figure 7.20: Same as Fig. 7.13 for the different criteria (aspect ratio and reduced chi-squared of the fits).

Table 7.1: Median filament widths according to different selecting criteria (see Fig. 7.18) and inferred filament width calculated from the fit intercepts (see Fig. 7.19).

Criteria	Gaussian north/south	Plummer (p=2) north/south	Plummer (p=4) north/south	Second Moment north/south	Intercept north/south
all, $\chi^2_R \leq 25$	$0.12^{+0.16}_{-0.09}$ pc	$0.09^{+0.12}_{-0.06}$ pc	$0.11^{+0.14}_{-0.08}$ pc	$0.12^{+0.15}_{-0.09}$ pc	0.06 ± 0.01 pc
	$0.15^{+0.19}_{-0.11}$ pc	$0.11^{+0.15}_{-0.09}$ pc	$0.13^{+0.17}_{-0.10}$ pc	$0.14^{+0.17}_{-0.1}$ pc	0.08 ± 0.01 pc
all, $\chi^2_R \leq 5$	$0.12^{+0.15}_{-0.08}$ pc	$0.09^{+0.12}_{-0.06}$ pc	$0.10^{+0.13}_{-0.08}$ pc	$0.10^{+0.14}_{-0.08}$ pc	0.04 ± 0.04 pc
	$0.14^{+0.18}_{-0.11}$ pc	$0.11^{+0.15}_{-0.07}$ pc	$0.13^{+0.17}_{-0.10}$ pc	$0.13^{+0.17}_{-0.09}$ pc	0.07 ± 0.04 pc
R > 2, $\chi^2_R \leq 25$	$0.11^{+0.15}_{-0.09}$ pc	$0.08^{+0.11}_{-0.06}$ pc	$0.10^{+0.13}_{-0.08}$ pc	$0.12^{+0.15}_{-0.08}$ pc	0.07 ± 0.06 pc
	$0.13^{+0.17}_{-0.10}$ pc	$0.10^{+0.13}_{-0.08}$ pc	$0.12^{+0.16}_{-0.09}$ pc	$0.12^{+0.15}_{-0.10}$ pc	0.07 ± 0.04 pc
R > 2, $\chi^2_R \leq 5$	$0.10^{+0.13}_{-0.08}$ pc	$0.07^{+0.10}_{-0.06}$ pc	$0.09^{+0.12}_{-0.07}$ pc	$0.09^{+0.12}_{-0.07}$ pc	0.09 ± 0.01 pc
	$0.13^{+0.17}_{-0.10}$ pc	$0.09^{+0.13}_{-0.07}$ pc	$0.12^{+0.15}_{-0.09}$ pc	$0.12^{+0.15}_{-0.09}$ pc	0.06 ± 0.04 pc

8 PHYSICAL PROPERTIES OF FILAMENTS IN DIFFERENT TRACERS

This chapter aims at presenting the physical conditions that are traced by the different CO isotopologues, [C II] and dust emission throughout the cloud.

8.1 MORPHOLOGY

8.1.1 *Spatial distribution of the observed tracers*

Emission from varying species trace a range of physical and chemical conditions throughout the cloud. Thus, the apparent morphology of the cloud, and therein filaments, depends on the observed tracer. The three observed CO isotopologues, ^{12}CO, ^{13}CO and C^{18}O, probe low (10^2 cm^{-3}), intermediate (10^3 cm^{-3}) and relatively high (10^4 cm^{-3}) density regions. As explained in Chapter 2, in ^{12}CO emission the structure is opaque and diffuse. ^{13}CO emission is optically thin in the outskirts of the cloud, tracing diffuse parts of the cloud in addition to the higher density structure that cannot be distinguished with the ^{12}CO observations. The C^{18}O emission reveals the high density filamentary skeleton of the cloud. In addition to these tracers, the [C II] map reveals the structure shaped by the stellar feedback in the region. The high resolution and dynamic range column density map reveals a plethora of dense and diffuse structures (Stutz & Kainulainen 2015). In the following, with a series of figures, I present how the filamentary skeleton that is traced by the C^{18}O emission relates to the other tracers.

Figures 8.1, 8.2, 8.3 and 8.4 show the ^{12}CO, ^{13}CO, dust and [C II] emission overlaid with C^{18}O peak intensity contours (left panels) and filaments identified in the C^{18}O data (right panels), respectively. The dotted red boxes in Figure 8.1 left panel mark the areas over which spectra discussed in Section 8.1.2 were extracted. It is interesting to see how the dense gas emission seen in the C^{18}O map fit in with its diffuse surroundings seen in ^{12}CO. This diffuse emission often traces protostellar feedback, and the filaments seen in C^{18}O form the backbone of the cloud. In this sense, the morphology of the dense gas is less affected by the feedback, yet the shell-like structures in the L1641 region are still visible, and they surround the C^{18}O filaments. The C^{18}O emission comes from a much more narrow portion of the cloud. Most of the dense structures see in the column density map perfectly overlap with the C^{18}O emission and the filaments. In northern part of the map, specifically towards the OMC-3 region, a small portion of the high column density dust does not have filamentary structure associated with it. The identified filaments and the peak C^{18}O intensity are shifted towards the east. This is likely due to the C^{18}O emission being frozen out onto dust grains at such high densities and therefore filaments identified in $C^{18}O$ follow the nearest high intensity peaks. The comparison with [C II] emission is particularly interesting because in such a violently star forming environment, one cannot expect filaments (and star formation) to evolve isolated from the strong UV radiation. With a closer look, one can see that the morphology of the $C^{18}O$ filaments within and at the edges of the Veil Bubble traced by C^+, resembles the morphology of the [C II] emission. I discuss this further in Section 8.2.3.

8.1.2 *Comparison of spectra*

The line profiles of the observed tracers hold a copious amount of detail when compared to one another. Comprehensive studies of comparing the spectra of Carbon-bearing species in different star forming regions show that the identified spectral components, velocity centroid gradients and velocity linewidths provide vital information on the origins and different phases of the gas (Beuther et al. 2014; Okada et al. 2015, 2018).

Figure 8.5 shows the spectra of each species averaged over five different regions of the map. These regions are marked in Figure 8.1 with red boxes and from north to south indicated as OMC-2/3, OMC-1, OMC-4, OMC-5 and L1641-N. To have the spectra in comparable T_{MB} scales the ^{12}CO intensities are divided by 3 and $C^{18}O$ intensities are multiplied by 5. As the [C II] map only covers the northern half of the map, there is no averaged spectra for the OMC-5 and L1641-N regions. The global red-to-blue velocity gradient in the cloud is imprinted on the averaged spectra of the selected regions from OMC-2/3 to L1641-N.

The spectra seem to be often composed of multiple components, and the linewidth of the [C II] emission changes drastically between the different regions. In order to have a more quantitative idea of the properties of these spectra, I fitted them individually using BTS[1] (Clarke et al. 2018). Figure 8.6 shows each averaged spectrum from the 5 different regions. From top to bottom, the plotted data represents averaged ^{12}CO, ^{13}CO, $C^{18}O$ and [C II] spectra. The fit results; amplitudes (T_{MB}), velocity centroids (v_c) and velocity linewidths (Δv) are given in Table 8.1.

As suspected from Figure 8.5, BTS detects multiple components in the majority of the spectra. These individual components are plotted onto each corresponding spectrum in Figure 8.6. For ^{12}CO the multiple components are harder to distinguish by eye except for the OMC-5 region. This is perhaps because of the more diffuse nature of the emission, however, it could also be that in some of these regions, BTS identifies optically thick spectra of the diffuse gas as multiple components. The individual components are easier to locate by eye in $C^{18}O$, e.g. towards the OMC-2/3 region, since the shoulders become more distinctive. The most prominent multi-component spectra is in the OMC-5 and L1641-N regions for the CO isotopologues. These components appear because of the

1 Behind The Spectra (BTS) is an automated multi-Gaussian fitting algorithm that is freely available at https://github.com/SeamusClarke/BTS

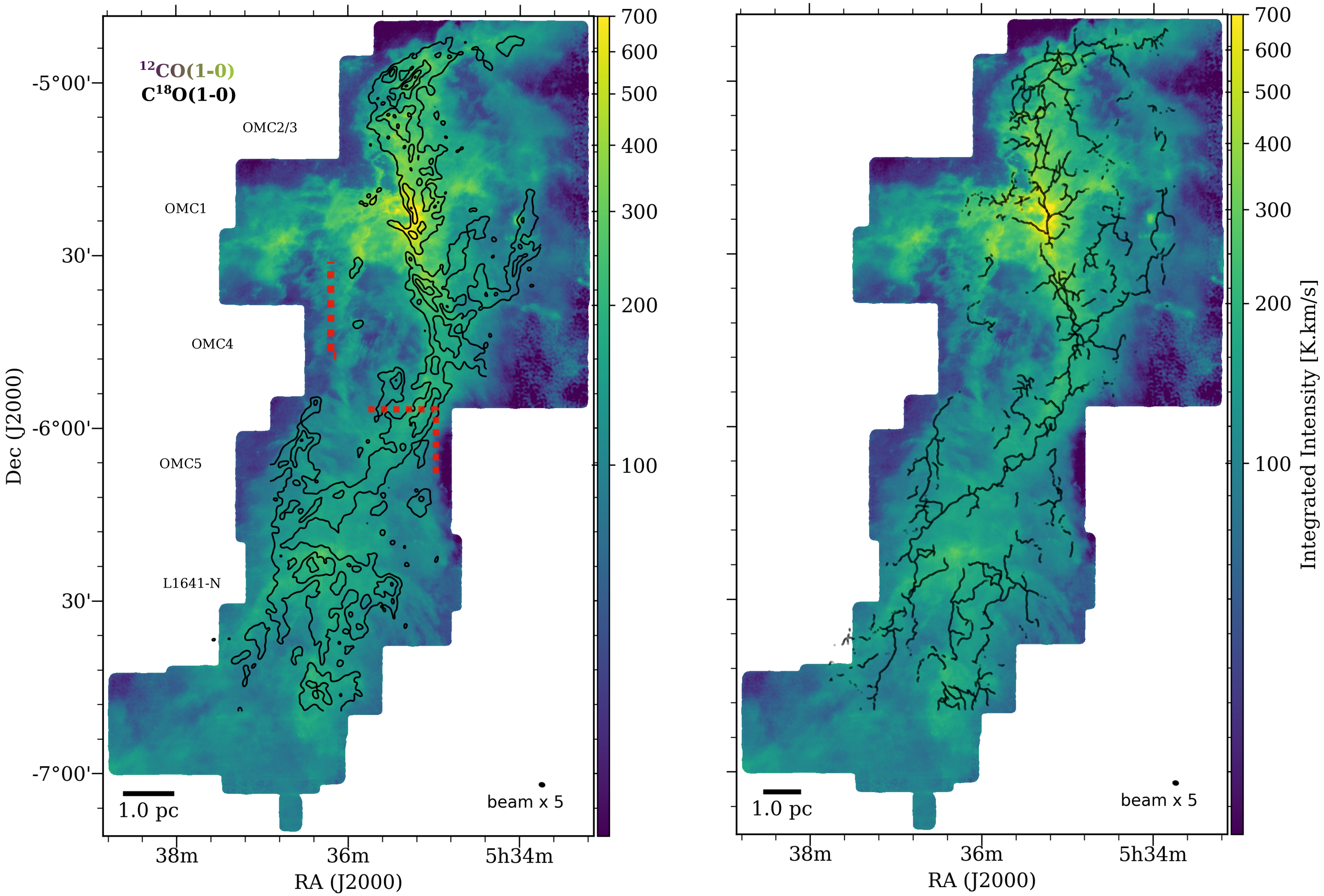

Figure 8.1: *Left:* ^{12}CO peak intensity emission overlaid with the C^{18}O peak intensity contours. The dotted red boxes mark the locations of the areas from which the average spectra were extracted. *Right:* ^{12}CO peak intensity emission overlaid with the filaments extracted from the C^{18}O data (see Section 6.2).

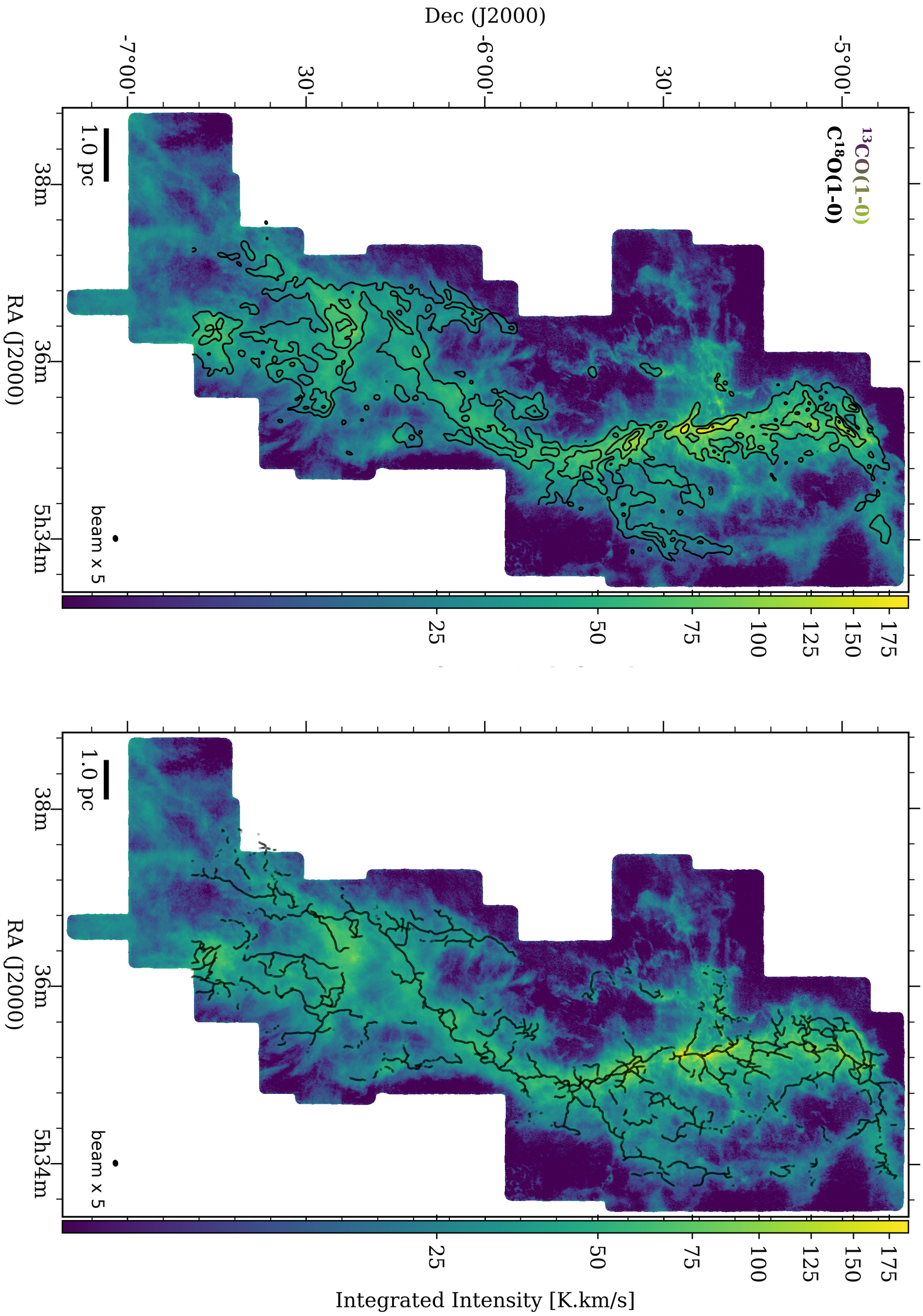

Figure 8.2: Same as Figure 8.1 but for the ^{13}CO peak intensity emission.

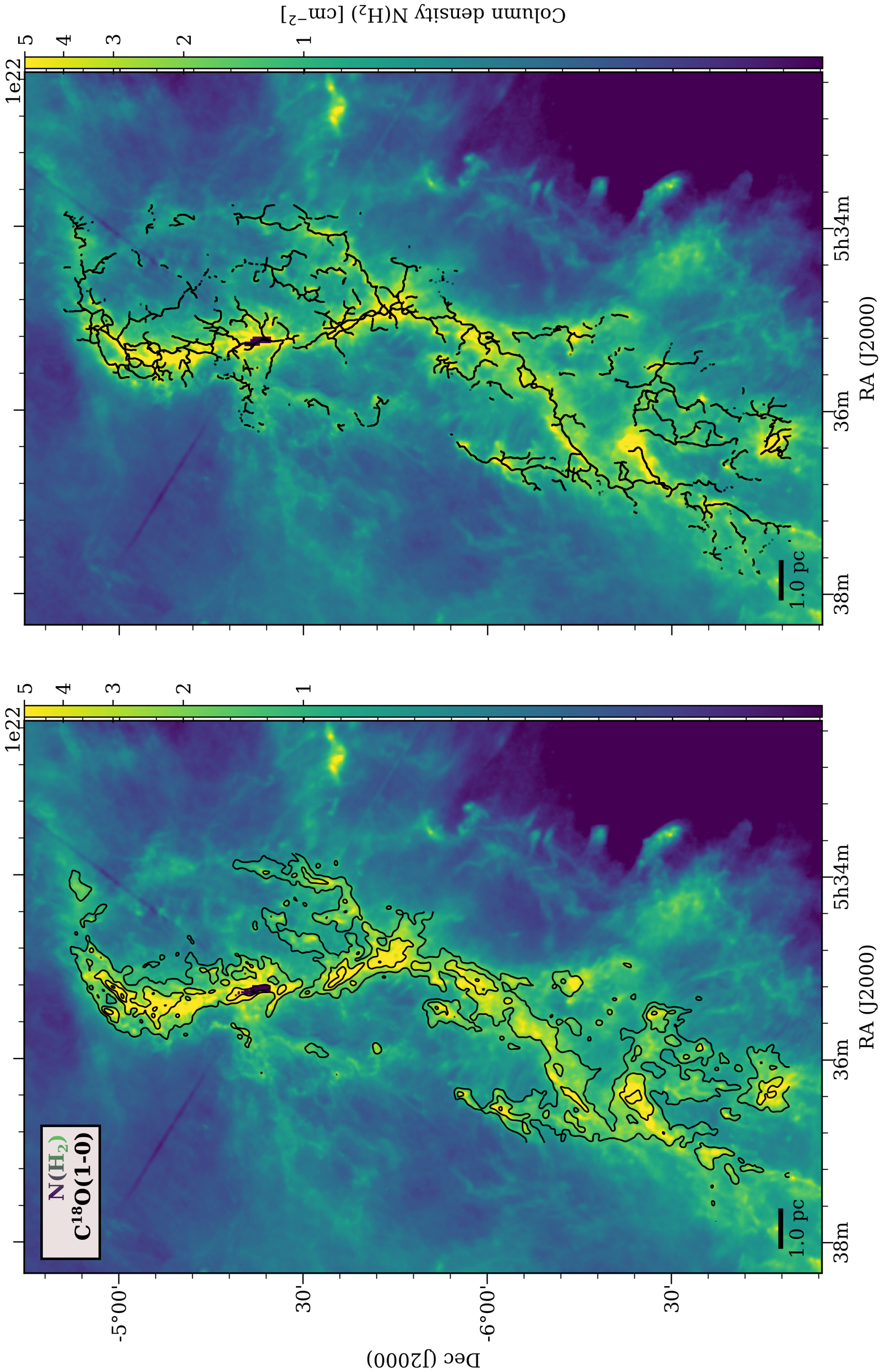

Figure 8.3: Same as Figure 8.1 but for the column density map.

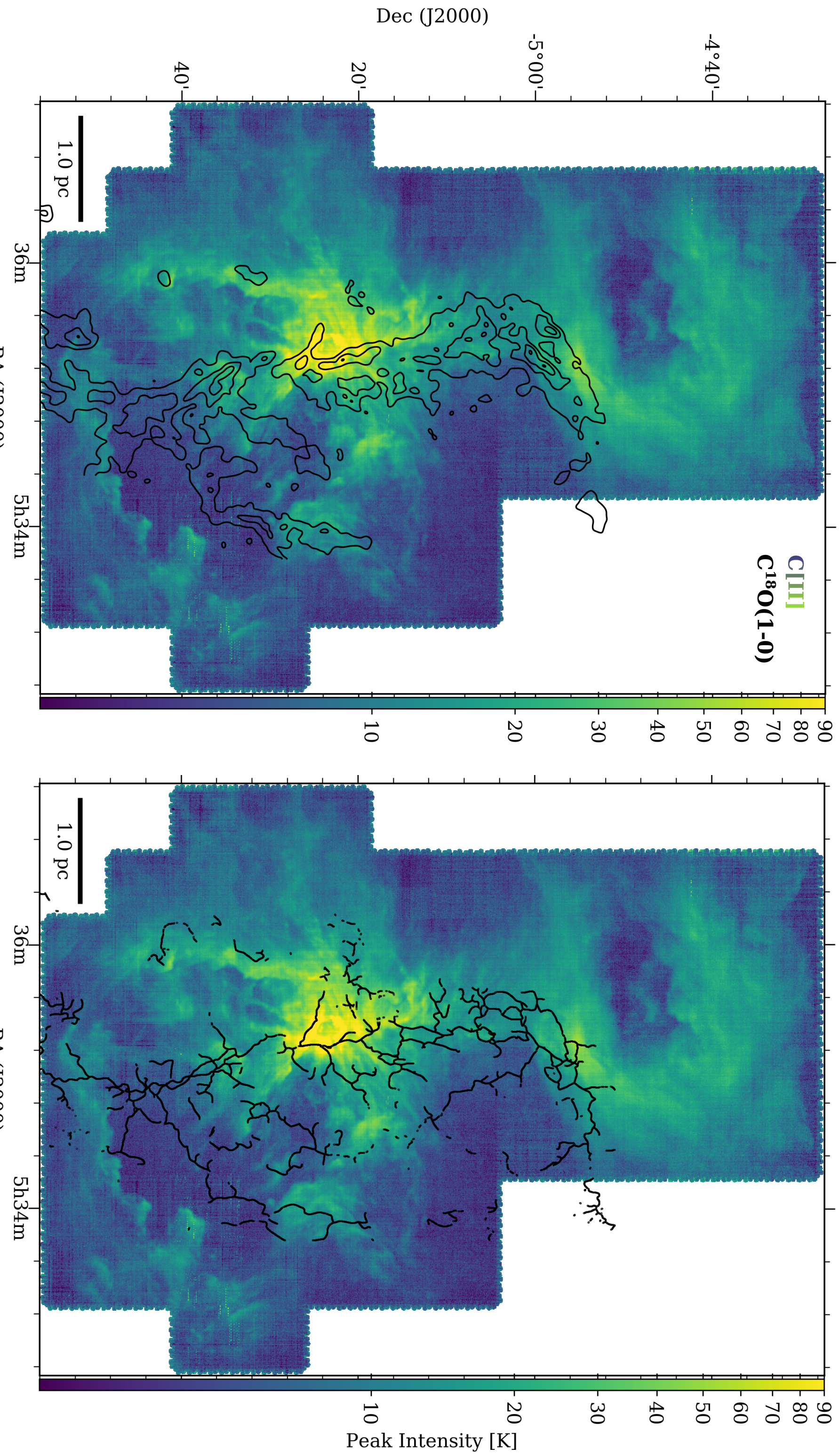

Figure 8.4: Same as Figure 8.1 but for the [C II] peak intensity emission.

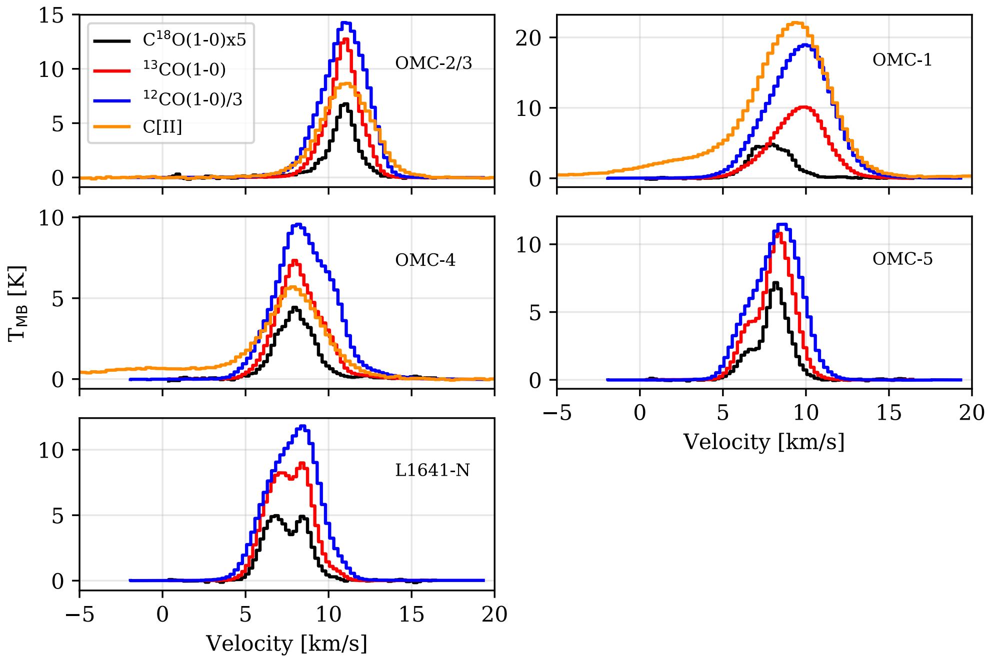

Figure 8.5: Comparison of different spectra averaged over 5 different regions marked with red boxes in Figure 8.1. The black, red, blue and orange spectra represent $C^{18}O$, ^{13}CO, ^{12}CO and [C II] emission. $C^{18}O$ emission is multiplied by 5, while ^{12}CO emission divided by 3 in order to reach comparable intensity scales in all tracers. There are no [C II] emission spectra shown for the OMC-5 and L1641-N regions because these regions are outside of the [C II] map's coverage.

two distinct kinematic features in the southern region of the cloud. These features can be easily seen in the 3-color integrated intensity maps of CO isotopologues presented in Figures 3.4, 3.5 and 3.6 where the south-west region of the cloud has green velocities while the south-east region of the cloud has blue velocities.

Between the CO isotopologues, larger ^{12}CO linewidths is expected because of Larson's linewidth-size relationship in molecular clouds (Larson 1981). While the [C II] linewidth in the OMC-2/3 region towards the north of the cloud is only marginally larger than that of the CO isotopologues, in the OMC-1 and 4 regions this difference grows larger. This is also because of the contribution of the Veil Bubble that has velocity linewidths of 4.3 and 6.9 km s^{-1} in OMC-1 and 4, respectively (see Table 8.1).

The [C II] spectra, also show an interesting multi-component behavior in the OMC-1 and OMC-4 regions. The broader component at low velocities in the spectra towards both of these regions comes from the expanding Veil Bubble that appears at negative velocities while no other emission from the region exists. The fainter component at high

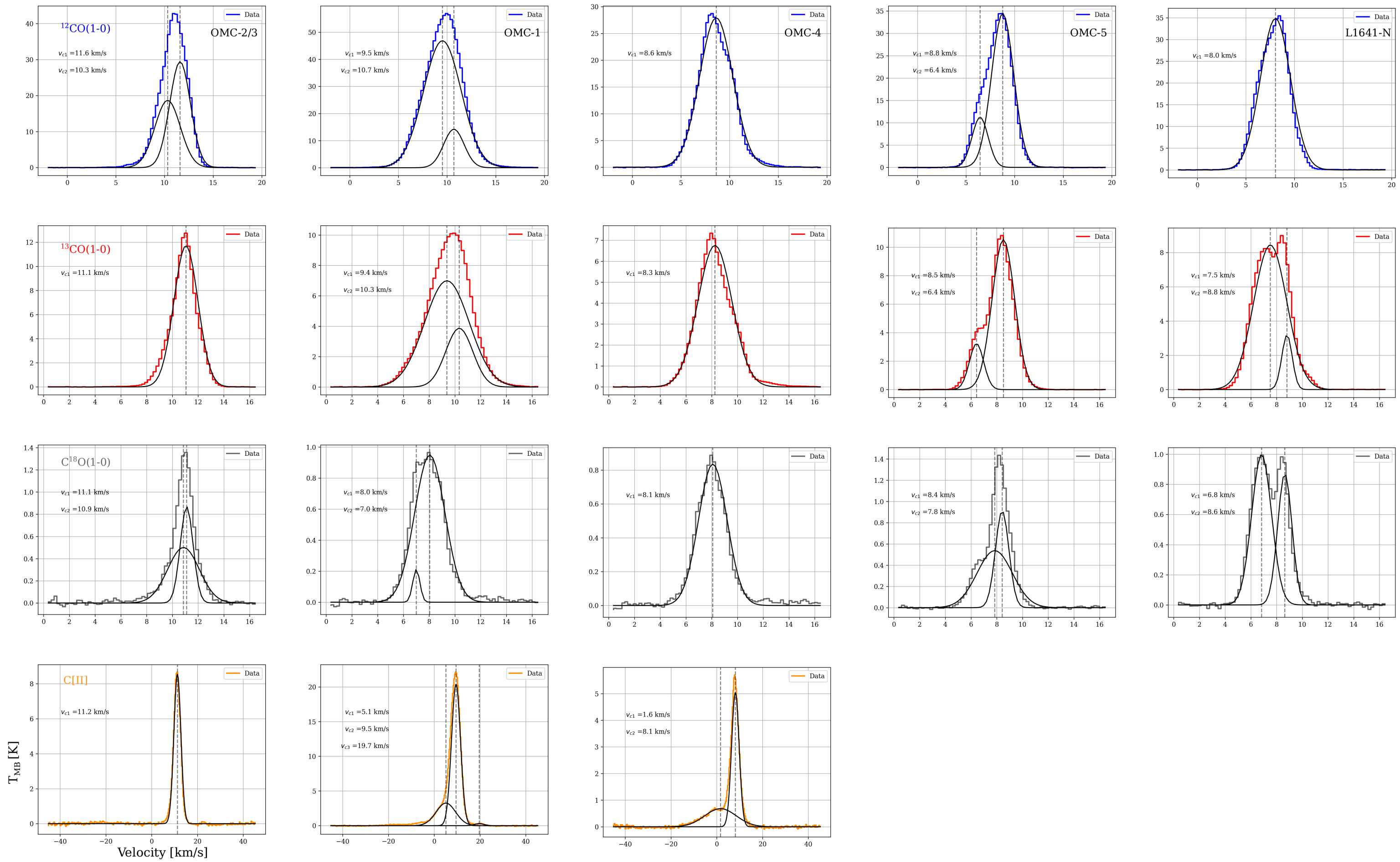

Figure 8.6: Averaged spectra of all the observed tracers towards fitted with the BTS algorithm. Panels represent: from top to bottom, ^{12}CO, ^{13}CO,C^{18}O and [C II] spectra, towards OMC-2/3, OMC-1, OMC-4, OMC-5 and L1641-N regions from left to right, respectively.

velocities comes from the rarer isotopologue [^{13}C II] emission that was picked up in the bandwidth of the observations.

8.2 FILCHAP RESULTS

After comparing the general properties of the cloud seen in different tracers, I will now compare the filament properties that one can obtain using these tracers. In Chapter 7, I investigated the filament properties as seen in C^{18}O emission. Following the work on C^{18}O, in this chapter, I present a comprehensive comparison of `FilChaP` results for different tracers. For a fair comparison I use the same filaments identified in the C^{18}O map using DisPerSE (see Chapter 6). I ran `FilChaP` on the following five datasets: C^{18}O integrated intensity map[2], dust column density map, ^{13}CO data cube and [C II] datacube and the results from these datasets form the base of this section. While I use C^{18}O integrated intensity, dust emission and ^{13}CO results for comparison with the C^{18}O datacube results presented in Chapter 7, I use [C II] results to analyze how filaments may be affected by stellar feedback.

8.2.1 *Width*

Because different tracers probe a variety of conditions in the cloud, it is unlikely that filaments traced by each of these tracers show the same exact properties. One of the most important filament properties discussed throughout this work is the filament width. Therefore, I start the comparison by looking at filament widths as seen in different tracers. I perform the comparison using two different methods: (1) histograms in Section 8.2.1.1, (2) Kernel Density Estimations (KDEs) in Section 8.2.1.2. Both sections includes the comparison of C^{18}O datacube results presented in the previous chapter to the widths derived from the ^{13}CO datacube, C^{18}O integrated intensity emission map and dust column density map.

8.2.1.1 *Comparison using histograms*

Figure 8.7 shows the calculated width distributions for ^{13}CO datacube, C^{18}O integrated intensity map and the dust column density map in the top, middle and bottom panels, respectively. The median widths calculated for these distributions are listed in Table 8.2. In this table, the original C^{18}O widths calculated in Chapter 7 are also given on the top row. There are four results that can be read from the width distributions and the median widths, and they can be listed as follows. Firstly, there seems to be barely any difference between the 2D (integrated intensity) and 3D (datacube) results for C^{18}O. I note that the integrated intensity map of C^{18}O is integrated over a velocity range of 10 km s^{-1} . In the contrary, during the analysis of the datacube, `FilChaP` reads the velocity of each

2 Integrated emission between 4.7 and 14.3 km s^{-1} .

Table 8.1: Fit results for the averaged spectra of ^{12}CO, ^{13}CO, $C^{18}O$ and [C II] towards the 5 different regions in Orion A.

Line	Component		OMC-2/3	OMC-1	OMC-4	OMC-5	L1641-N
$^{12}CO(1–0)$	1	$T_{MB}[K]$	29.4	46.9	27.9	34.4	34.9
		v_c [km/s]	11.6	9.5	8.6	8.7	8.0
		Δv [km/s]	1.1	1.9	1.7	1.1	1.6
$^{12}CO(1–0)$	2	$T_{MB}[K]$	18.7	14.2	–	11.2	–
		v_c [km/s]	10.3	10.7	–	6.4	–
		Δv [km/s]	1.3	1.1	–	0.8	–
$^{13}CO(1–0)$	1	$T_{MB}[K]$	11.7	7.0	6.8	10.5	8.5
		v_c [km/s]	11.1	9.4	8.3	8.6	7.5
		Δv [km/s]	0.9	1.7	1.3	0.9	0.6
$^{13}CO(1–0)$	2	$T_{MB}[K]$	–	3.9	–	3.2	3.2
		v_c [km/s]	–	10.3	–	6.4	8.8
		Δv [km/s]	–	1.1	–	0.6	0.4
$C^{18}O(1–0)$	1	$T_{MB}[K]$	0.8	0.9	0.8	0.9	1.0
		v_c [km/s]	11.1	8.0	8.1	8.4	6.8
		Δv [km/s]	0.5	1.2	1.1	0.5	0.8
$C^{18}O(1–0)$	2	$T_{MB}[K]$	0.5	0.2	–	0.5	0.8
		v_c [km/s]	10.9	7.0	–	7.8	8.6
		Δv [km/s]	1.2	0.3	–	1.4	0.6
[C II]	1	$T_{MB}[K]$	8.5	3.3	0.68	–	–
		v_c [km/s]	11.2	5.1	1.6	–	–
		Δv [km/s]	1.5	4.3	6.9	–	–
[C II]	2	$T_{MB}[K]$	–	20.4	5.0	–	–
		v_c [km/s]	–	9.5	19.7	–	–
		Δv [km/s]	–	2.0	1.6	–	–
[C II]	3	$T_{MB}[K]$	–	0.3	–	–	–
		v_c [km/s]	–	19.7	–	–	–
		Δv [km/s]	–	2.1	–	–	–

Table 8.2: Median filament widths calculated using different tracers.

Tracer	Gaussian north/south	Plummer (p=2) north/south	Plummer (p=4) north/south	Second Moment north/south
$C^{18}O_{datacube}$	$0.12^{+0.16}_{-0.09}$ pc	$0.09^{+0.12}_{-0.06}$ pc	$0.11^{+0.14}_{-0.08}$ pc	$0.12^{+0.15}_{-0.09}$ pc
	$0.15^{+0.19}_{-0.11}$ pc	$0.11^{+0.15}_{-0.09}$ pc	$0.13^{+0.17}_{-0.10}$ pc	$0.14^{+0.17}_{-0.1}$ pc
$^{13}CO_{datacube}$	$0.17^{+0.24}_{-0.12}$ pc	$0.14^{+0.21}_{-0.10}$ pc	$0.16^{+0.22}_{-0.11}$ pc	$0.15^{+0.19}_{-0.11}$ pc
	$0.21^{+0.28}_{-0.16}$ pc	$0.19^{+0.26}_{-0.14}$ pc	$0.21^{+0.26}_{-0.15}$ pc	$0.17^{+0.22}_{-0.12}$ pc
$C^{18}O_{mom0}$	$0.12^{+0.16}_{-0.08}$ pc	$0.09^{+0.14}_{-0.07}$ pc	$0.11^{+0.15}_{-0.08}$ pc	$0.09^{+0.13}_{-0.06}$ pc
	$0.13^{+0.17}_{-0.09}$ pc	$0.11^{+0.15}_{-0.08}$ pc	$0.12^{+0.16}_{-0.09}$ pc	$0.09^{+0.14}_{-0.07}$ pc
$N(H_2)$	$0.14^{+0.20}_{-0.10}$ pc	$0.09^{+0.15}_{-0.07}$ pc	$0.12^{+0.17}_{-0.09}$ pc	$0.16^{+0.21}_{-0.11}$ pc
	$0.15^{+0.2}_{-0.12}$ pc	$0.11^{+0.15}_{-0.09}$ pc	$0.14^{+0.18}_{-0.11}$ pc	$0.17^{+0.22}_{-0.12}$ pc

point along the filament and integrates the emission only from the adjacent velocity channels to produce the intensity profiles. This method is implemented in `FilChaP` to prevent structures along the line-of-sight at different velocities from contributing to the intensity profile of a particular filament. However, by only comparing the medians of these distributions, it is not possible to say the difference between the 2D and 3D analysis of the filaments. Secondly, comparing the results from two datacubes ^{13}CO and $C^{18}O$, for all the width calculation methods the ^{13}CO widths are larger. This is an expected results because the ^{13}CO emission traces a much more diffuse component of the gas than $C^{18}O$. The third result is that the widths derived from the dust column density map where a large dynamic range of scales are observed is similar to the widths derived from both $C^{18}O$ datacube and integrated intensity maps. Lastly, the widths in the southern region of the map for all the tracers are larger than the widths calculated towards the northern region. The largest widths of 0.2 pc, in fact, are observed in ^{13}CO emission towards the southern region. This result also meets the expectations, because we know that the northern part of the ISF is much denser and and the emission is more compact.

8.2.1.2 *Comparison using KDEs*

As unexpectedly the histogram analysis showed that there are no differences of widths calculated from 2D and 3D maps, I investigate the width distributions from each tracer in more detail. In particular, I want to understand the shape and spread of each of these distributions and quantify their resemblance in a more in depth way. Therefore, I employ a KDE comparison. As this is the first time throughout this work the KDEs are used, I would like to explain them and why I chose this method to continue further with the analysis. Probability density functions can be estimated using parametric

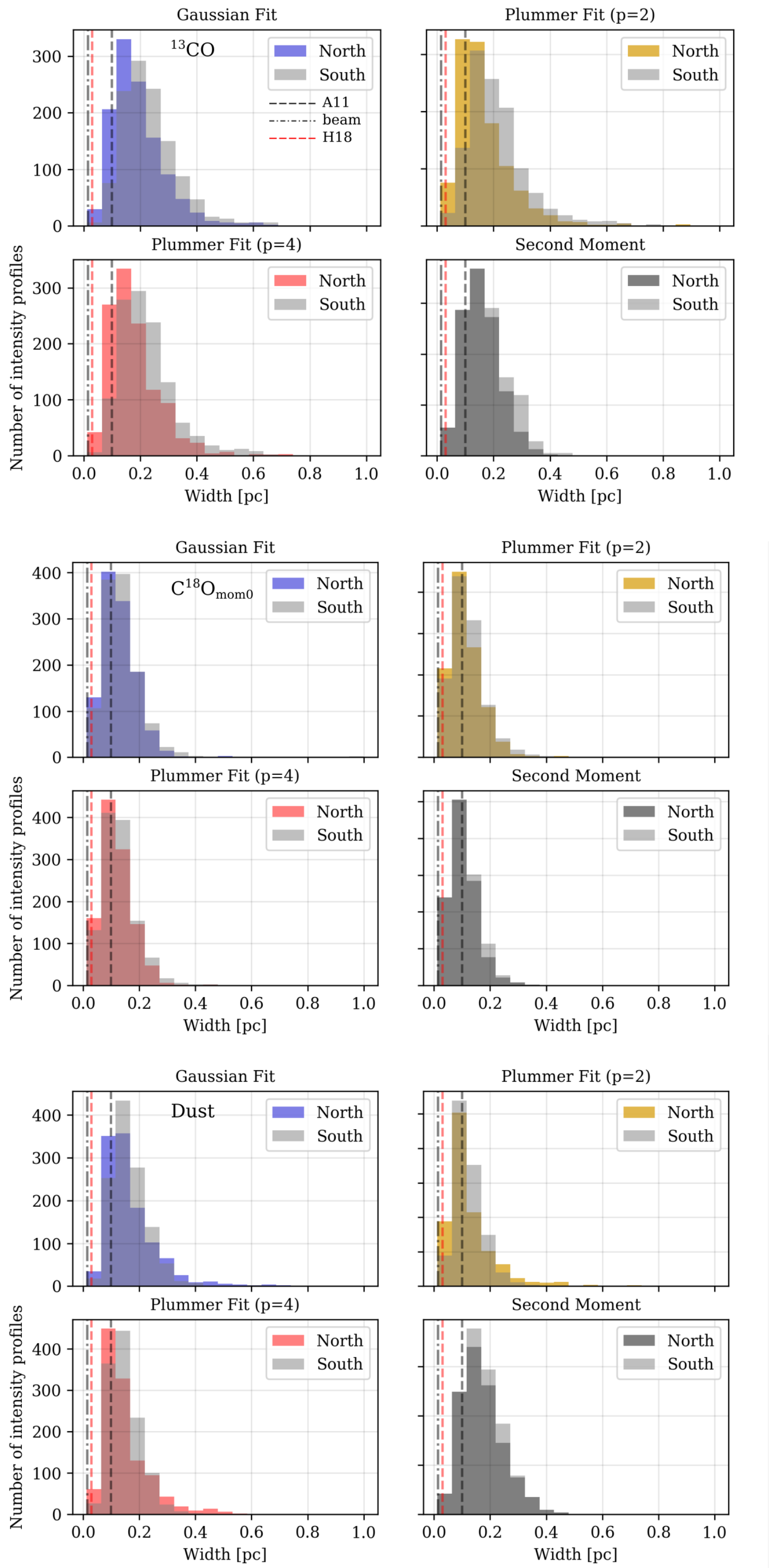

Figure 8.7: Comparison of filament widths seen in different tracers. Top, middle and bottom panels show distribution of filament widths calculated for ^{13}CO, C^{18}O integrated intensity and dust column density emission. The colored histograms represent the northern region Gaussian, Plummer p=2 and p=4 fits and widths calculated from the second moment in blue, yellow red and dark grey, respectively. The distributions for the southern region is always shown in light grey.

or non-parametric functions. Parametric functions assume that the parameters which define the function (e.g. variance and mean values of a Gaussian distribution) are defined over a strict and finite range. Non-parametric distributions, however, allow their parameters to be free of pre-imposed values. The KDE provides a non-parametric way of deducting a probability density function of a given dataset, and can be described as follows:

$$\hat{f}_N(x) = \frac{1}{Nh^D} \sum_{i=1}^{N} K\left(\frac{d(x, x_i)}{h}\right), \tag{8.1}$$

where $\{x_i\}$ are the measurements, N is the number points in the measurement set, K is the kernel function and h is the bandwidth (Ivezić et al. 2014). The kernel function is usually picked to be a Gaussian, but it can be any smooth function. The important parameter here is the bandwidth of the KDE; that is similar to the histogram bin width. To inspect the difference between a simple histogram and KDE, Ivezić et al. (2014) discusses different cases shown in Figure 8.8 (their Figure 6.1, p. 252). In all the sub panels of Figure 8.8 the true initial distribution of data is the same. The top panel shows two different histogram distributions of the same dataset, with same bin widths but with different bin replacement. The bin centers of the histogram in the top right panel is shifted by 0.25, compared to the top left panel. One can see that these two histogram distributions are completely different. In the middle panel, the left plot shows the histogram of the distribution when each bin center is set on the individual data points, and bins are allowed to overlap. This choice is a good representation of the underlying bimodal distribution of the dataset. The middle right panel, and the bottom panels show KDE distributions of the same dataset, with different kernel widths. Each data point in the KDE is represented with a Gaussian kernel. The case of the largest kernel width is shown on the bottom left panel where the bimodality of the distribution becomes questionable.

Unlike the histogram bin width and placement that is somewhat arbitrary and hard to estimate prior to data inspection, the KDE bandwidths can be estimated using a variety of methods. One of the most common methods is called the Silverman's rule of thumb and can be estimated as $1.06\sigma N^{-1/5}$ where σ is the standard deviation (Silverman 1986). Scott (1992) estimates the bandwidth as $h = 3.49\sigma N^{-1/3}$. Both of these estimations are derived assuming that the underlying distribution is Gaussian and the bandwidth is equal to the value that minimises the mean integrated squared error. For the complete derivation of the KDE bandwidth I refer to Ivezić et al. (2014) Chapter 6.

Now I apply the KDE method to compare the distributions of widths calculated using different tracers. To calculate and plot the KDEs I used the `python` package `seaborn`[3]. Figure 8.9 shows the density estimation of $C^{18}O$ widths against all ^{13}CO,

3 The `seaborn` package has a built-in wrapper for calculation KDEs using python's `scipy` package. More information on `seaborn` can be found at `https://seaborn.pydata.org/`.

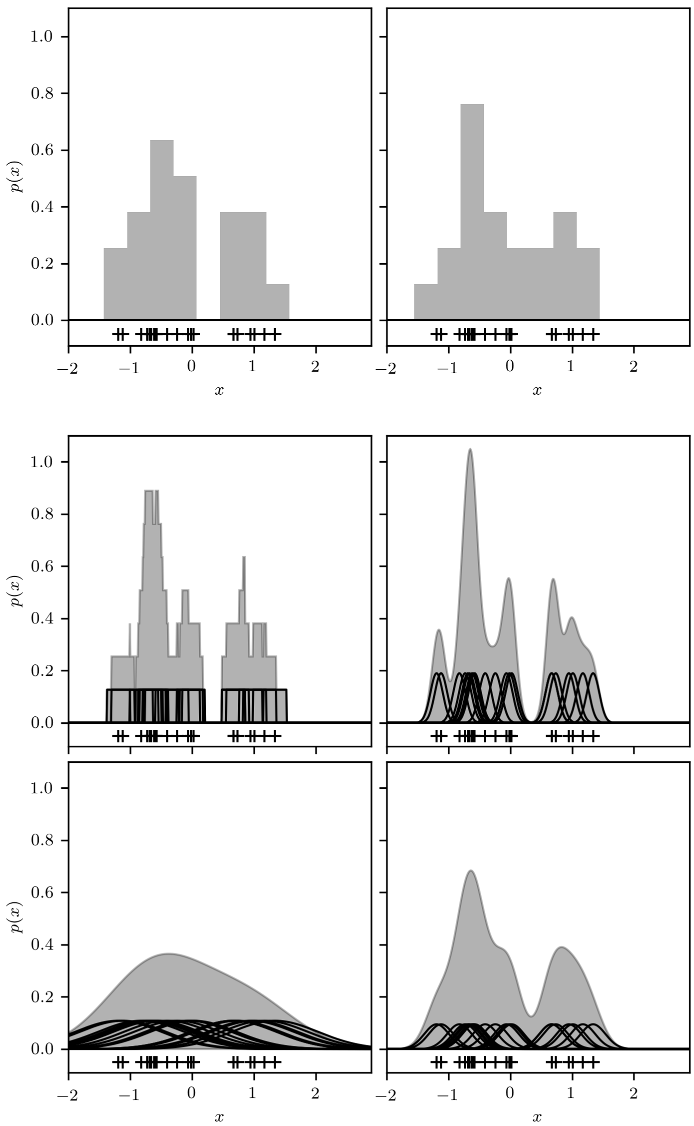

Figure 8.8: Comparison of histograms and KDEs using different bin and kernel widths. *Top:* Both panels show histograms of the same distributions with the same bin width but different bin centers. *Middle:* The left panel shows the histogram of the data when bins are allowed to overlap, and centered on each data point. The right panel shows the KDE of the distribution. *Bottom:* Both panels show KDEs of the distribution using larger kernel widths than that of middle right panel.

$C^{18}O$ integrated intensity and dust column density widths from top to bottom, and northern and southern regions in left and right panels. Each sub panel also shows the 1D KDEs for the corresponding distributions. The red dots show the actual data points. For the widths presented in this figure, I used the filament widths calculated from the Gaussian fits to the intensity profiles. For the comparison; the same plots for the 3 other width calculation methods are presented in Appendix A.2[4] In order to look for correlations between widths of $C^{18}O$ and the other tracers, I also calculate the Pearson correlation coefficient and the *p*-value. These values are also indicated in each sub panel. A Pearson coefficient of +1 indicates a positive and -1 indicates a negative linear correlation, whereas a coefficient of 0 indicates no linear correlation between the given quantities. From Figure 8.9 one can see that the highest correlation is calculated between the $C^{18}O$ and the ^{13}CO widths. This is interesting because, if one had only compared the median values of these distributions (see Table 8.2) ^{13}CO would have appeared as the most dissimilar. Therefore, I report that a visual comparison of histograms or median (or mean) values of the distributions are not adequate ways of comparing two such datasets. The real nature of the correspondence between the datasets can be revealed using KDEs and calculating correlation coefficients.

Figure 8.9 also reveals the lack of strong correlation between the $C^{18}O$ datacube widths and $C^{18}O$ integrated intensity and dust column density widths. Although the difference between the median values of these distributions are minute, as discussed in the previous section, the spread is large enough to lessen the quantitative value of correlation between the datasets. The spread is due to several effects; firstly the structures along the line of side with velocity differences larger than ± 0.22 km s^{-1} compared to the filament spine are not included in the intensity profiles calculate from the $C^{18}O$ datacube. On the other hand, *all* structures along the line of sight (regardless of their velocities) are included in the calculating of the intensity profiles from the $C^{18}O$ integrated intensity map. It is not possible to distinguish whether all of these structures along the line of sight are individual coherent filaments, as `DisPerSE` does not pick them up as filaments separately (except for the OMC-4 region where spatially overlapping filaments at different velocities can be seen). The integrated intensity map can also include extended emission (not necessarily coherent filaments along the line of sight) from all velocity channels from the surroundings of the filament contributing to different features in intensity profiles and, hence, resulting in dissimilar width distributions. The structure of the cloud along the line of sight cannot be determined using the dust column density map, either because the column density map is also a 2D representation of the entire cloud with no information on the velocities. Therefore, the widths calculated from the dust emission map also lack strong correlation with the $C^{18}O$ widths.

4 There is no difference between the comparison results obtained using the different width calculation methods, except that the second moment method shows less correlation in all the comparisons. This is likely to be a result of boundary selection within which the widths are calculated.

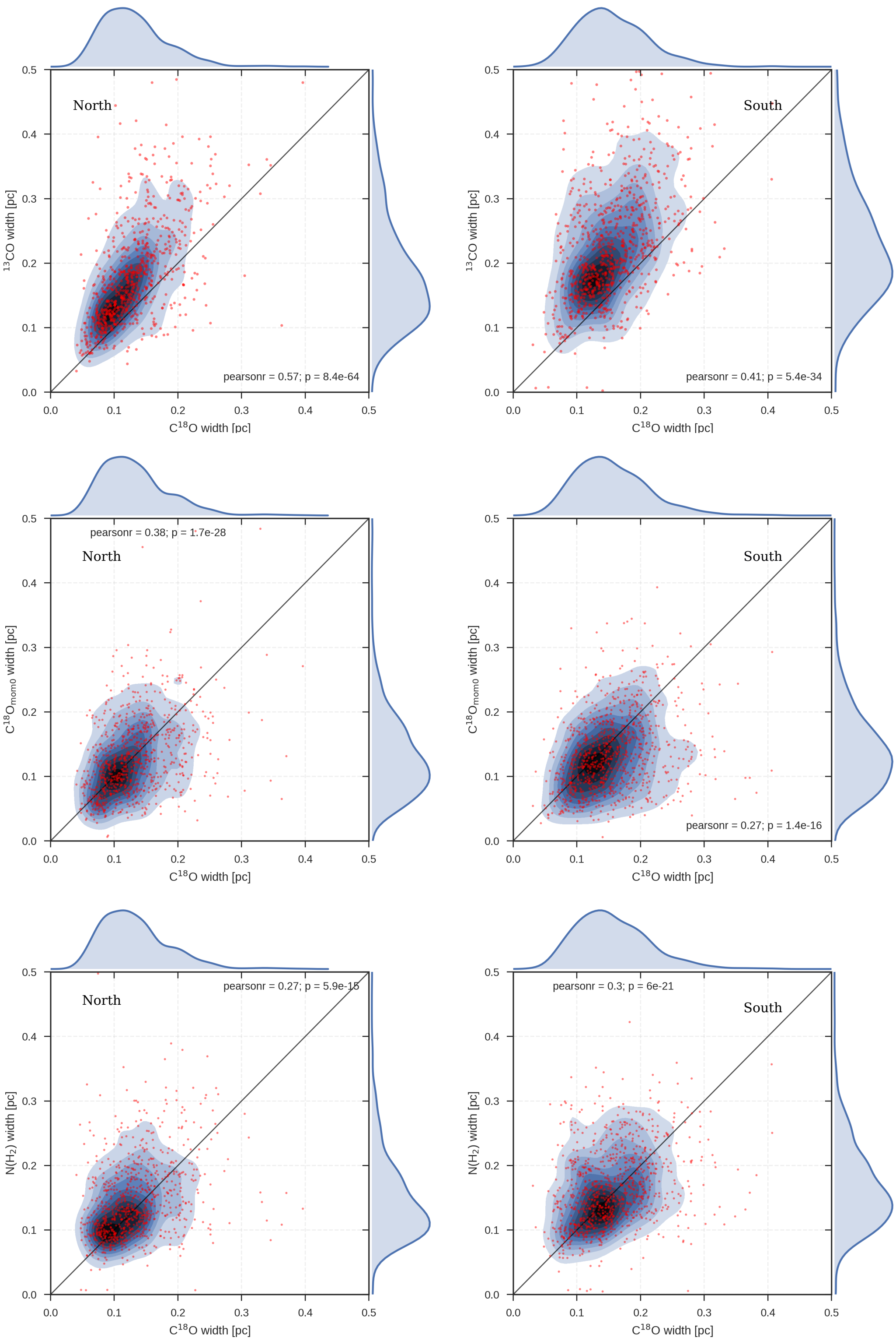

Figure 8.9: Comparison of filament widths calculated in different tracers using KDEs. From top to bottom shown are the comparisons between ^{13}CO and C^{18}O datacubes, C^{18}O integrated intensity and C^{18}O datacube, dust column density and C^{18}O datacube. Left and right panels show northern and southern regions of the map. The red points are the data points obtained by plotting the datasets against each other as scatter plots.

Another aspect shown in Figure 8.9 is the differences between the filament widths calculated towards the northern and southern regions of the map. This difference is the strongest in the case of ^{13}CO, with a relatively strong drop in the correlation coefficient from 0.57 to 0.41. As can be seen from the top panel of the figure, the cause of this drop is the increase in the ^{13}CO filament widths that is not compensated by a similar increase in the C^{18}O widths. The reason why the ^{13}CO widths increase in the south is that in the southern region the ^{13}CO emission gets much more diffuse and volume filling unlike the C^{18}O emission. There is very little difference between the correlation coefficients of the two other tracers towards northern and southern regions of the map. For the C^{18}O datacube and the C^{18}O integrated intensity map this is because the tracer is the same. Although the widths increase in the southern region, the increase is similar for both the datacube and the integrated intensity map. The dust column density map shows the same behavior as the C^{18}O integrated intensity map, except the correlation coefficient slightly increases in the southern region, however, not significant enough to draw conclusions.

Alongside with the differences of filament widths calculated using different datasets, this section emphasizes the importance of using "the right tools" for data inspection and evaluation. In this sense I find KDEs superior to histograms, because they are independent from the size of bin widths that histograms suffer from when evaluating the shape of probability distributions.

8.2.2 *Skewness and kurtosis*

Next, I compare the skewness and kurtosis of intensity profiles derived using different tracers. Skewness and kurtosis of each intensity profile are calculated in `FilChaP`.

8.2.2.1 *Kurtosis*

Kurtosis, the fourth moment of distribution, represents the peakiness of the tip and the heaviness of the tails of a profile. The word itself is derived from the Greek work *kurtos* which means "bulging". Figure 8.10 shows an example of three different tail shapes; exponential, heavy-tailed and light-tailed. In this section, we are only concerned with heavy-tailed, and light-tailed, distributions. The light-tailed distributions also usually have peaks broader than normal distributions, and are therefore called platykurtic (platy; "broad" in Greek). These distributions have negative kurtosis values. The heavy-tailed distributions on the other hand have thinner peaks but thicker tails compared to normal distributions, hence, they are named leptokurtic (lepto; "skinny" in Greek).

I am interested in finding out which one of these distributions resemble the intensity profiles that are derived from different tracers, whether the kurtosis differs from one tracer to the other and what physical process these numbers correspond to. For this purpose I plot KDEs of filament widths and the corresponding kurtosis values

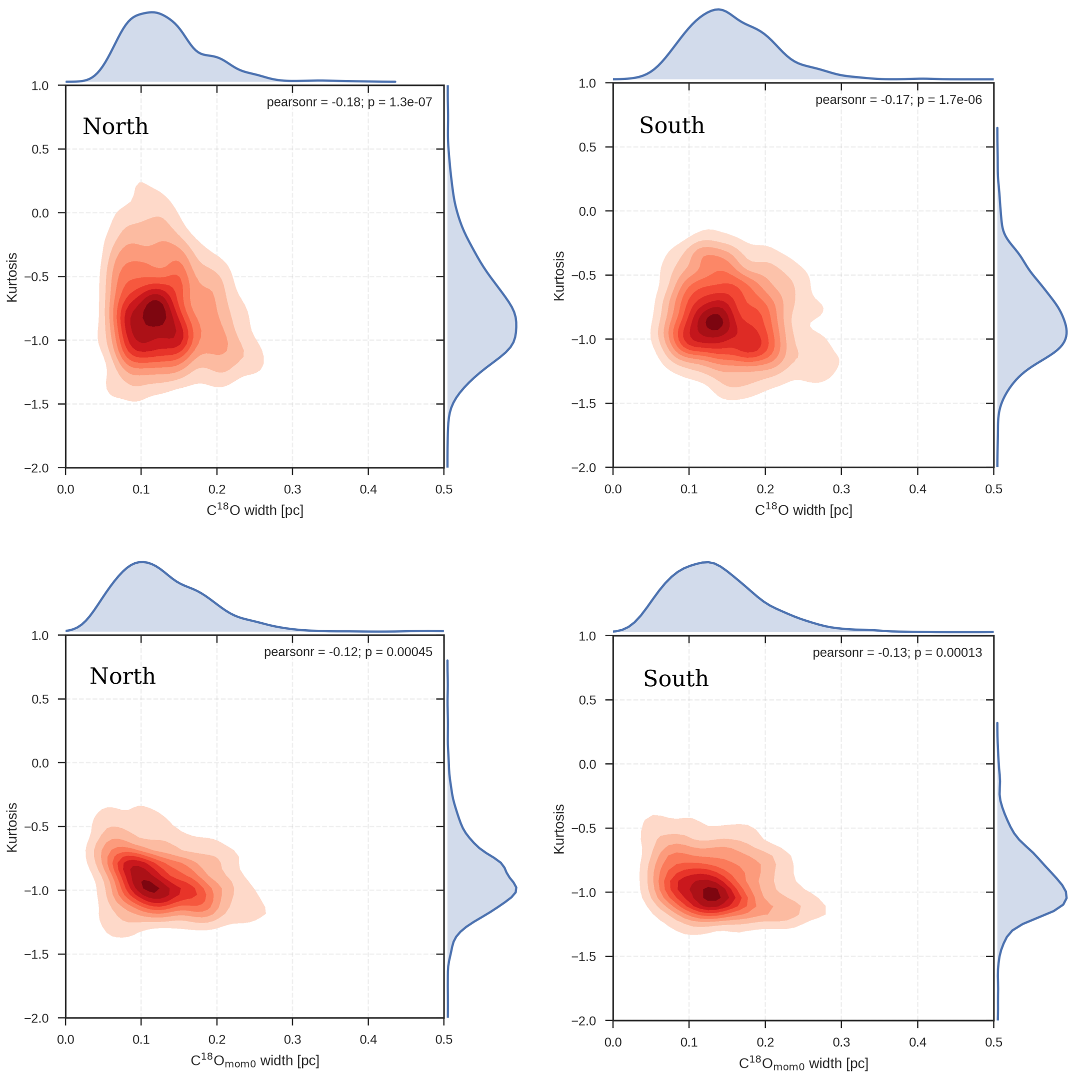

Figure 8.11: Correlation of filament widths and kurtosis shown using KDEs. Top panel shows the correlation between the kurtosis and $C^{18}O$ datacube widths in the northern (left) and southern (right) regions, respectively. The bottom panels shows the correlation between the kurtosis and $C^{18}O$ integrated intensity widths in the northern (left), and southern (right) regions, respectively.

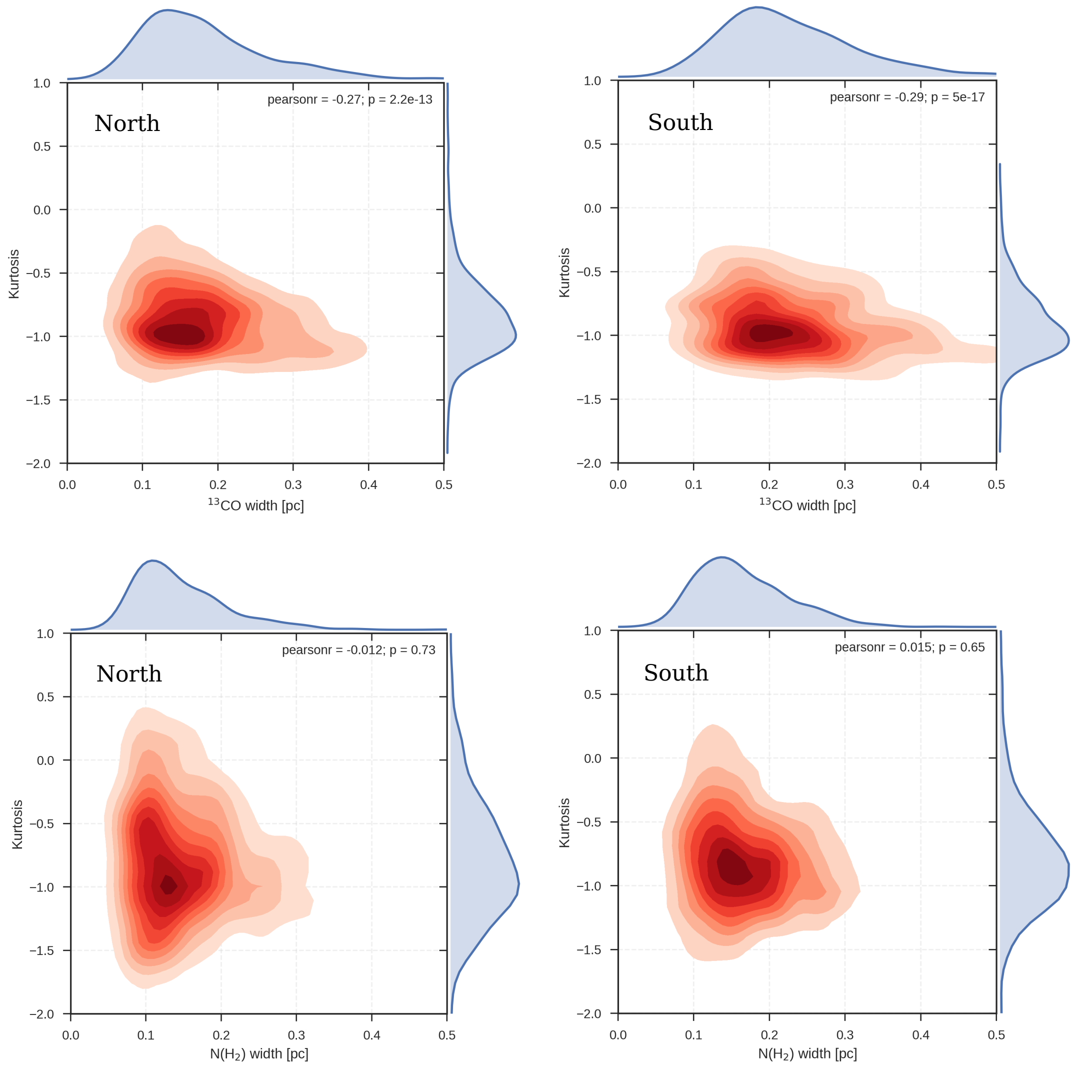

Figure 8.12: Correlation of filament widths and kurtosis shown using KDEs. Top panel shows the correlation between the kurtosis and ^{13}CO widths in the northern (left) and southern (right) regions, respectively. The bottom panels shows the correlation between the kurtosis and dust column density widths in the northern (left), and southern (right) regions, respectively.

of the intensity profiles derived from each tracer. Figure 8.11 shows these KDEs for C^{18}O datacube and C^{18}O integrated intensity maps in the top and bottom panels, respectively. The left and right panels show the KDEs for the northern and southern regions. Figure 8.12 shows the same correlation for the intensity profiles derived from the ^{13}CO and dust column density maps. The first result from these plots is that the majority of the profiles are platykurtic with kurtosis values peaking at around -1.0 for all the tracers. This means that for all the tracers, the intensity profiles have a similar shape. The kurtosis value being negative indicates that the profiles have a flatter top, and they may resemble Plummer functions more than Gaussians.

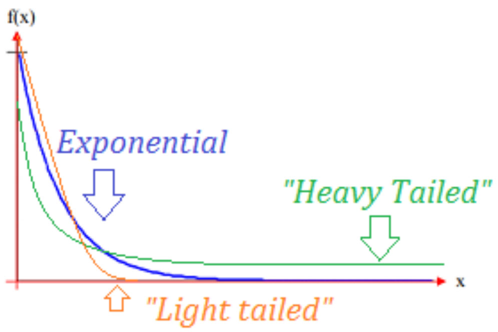

Figure 8.10: Tail shapes of a distribution. Credit: http://www.statisticshowto.com/heavy-tailed-distribution/

For the correlation between the width and kurtosis, the weakest correlation is found in the case of the dust column density widths with a correlation coefficient close to zero. However, there is a weak association of the width and kurtosis in the other tracers. In ^{13}CO, the Pearson coefficient is calculated to be -0.27 and -0.29, for the northern and southern regions respectively, indicating a weak negative linear correlation. The cause of this rather weak correlation is the broadening of the intensity profiles where the ^{13}CO has higher opacities. The opacity effects cause broadens the wings of a profile, while the peak flattens. The C^{18}O and C^{18}O integrated intensity widths show a weaker correlation with coefficients of the order of -0.15. The cause of this slight correlation could be the C^{18}O freeze-out. This would flattens the top of the C^{18}O intensity profiles and causes wider wings.

The general conclusion from the comparison of kurtosis values of the intensity profiles derived using different tracers is that when one looks at the correlation between kurtosis and width; (1) one finds that at narrower widths the kurtosis values are more scattered, (2) the majority of the filaments show negative kurtosis regardless of the observed tracer which may indicate they resemble Plummer-like functions more than Gaussian functions, (3) there exists a weak correlation between the width and kurtosis of ^{13}CO and C^{18}O filaments, which could be attributed to opacity effects, and freeze-out. However this correlation does not seem to be significant in either of the cases.

8.2.2.2 *Skewness*

Skewness is the third moment of distribution and it represents asymmetry. A profile can be skewed, or in other words distorted, towards left or right. How much a profile is skewed can be calculated based on the deviation from a normal distribution. The skewness of a normal distribution is zero. In this section, I compare the skewness of the filament intensity profiles of ^{13}CO, C^{18}O and dust column density emission. In a similar fashion to the analysis of the width distribution presented in Chapter 7, I look at how the skewness changes throughout the map. The purpose of this exercise is to understand whether there is an indication of stellar feedback imprinted on the intensity profiles that are skewed away from the source of radiation.

Figure 8.13 shows the filaments colored by skewness at each point calculated form the C^{18}O emission, ^{13}CO emission and dust column density maps from left to right, respectively. The skewness values shown are the absolute skewness values to make sure that there is no bias introduced caused by the direction of the perpendicular cut. As can be seen, there is a large difference between the skewness of the dust column density profiles and the skewness of the CO isotopologues. The skewness of the intensity profiles derived from the ^{13}CO and C^{18}O datacubes show no significant correlation with the location of the filaments. However, the profiles derived from the dust column density map show high skewness values at the immediate vicinity of feedback sources (e. g. vicinity of OMC-1 and NGC1977). Furthermore, the average skewness of the dust profiles are much higher compared to ^{13}CO and C^{18}O. I would like to investigate further whether this immense difference is a result of the feedback or the way the skewness is calculated.

In order to see why the profiles have such different skewness values I select intensity profiles from each tracer and look at the calculated skewness. Figure 8.14 shows the intensity profiles for all the tracers at a position where the skewness of the dust column density profile is three times higher than that of the C^{18}O profile. This figure illustrates the problems in calculating the higher moments of distribution. But before I come to that, I would like to highlight that the filament detected in C^{18}O and ^{13}CO emission is completely hidden in the radial profiles of the dust column density and the C^{18}O integrated emission maps amongst the emission from the surrounding structures at different velocities. Although the C^{18}O and ^{13}CO intensity profiles show the filament distinctly, the ^{13}CO profile has a more extended tail. This tail can also be seen in C^{18}O, however it appears to be more pronounced and hence, is separated with a boundary at around 0.12 pc. Because of this extended tail, the ^{13}CO emission appears twice as skewed (skewness is calculated to be -1.1 and 0.5 for ^{13}CO and C^{18}O, respectively). The dust column density profile has the highest skewness (1.4), but rather than stellar feedback, this skewness is only related to the fact that the emission from the filament is partially blended in with a nearby structure and only half of it can be resolved. In the case of the C^{18}O integrated intensity emission, the skewness is low (0.3), however, the intensity profile that belongs to the filament cannot be distinguished. Even though both the dust column density map and the integrated intensity map trace all the structures along the line of sight, the dust column density has a much higher dynamic range and is sensitive to the extended emission as well. Therefore, the skewness calculated from these tracers also differ by an order of a magnitude.

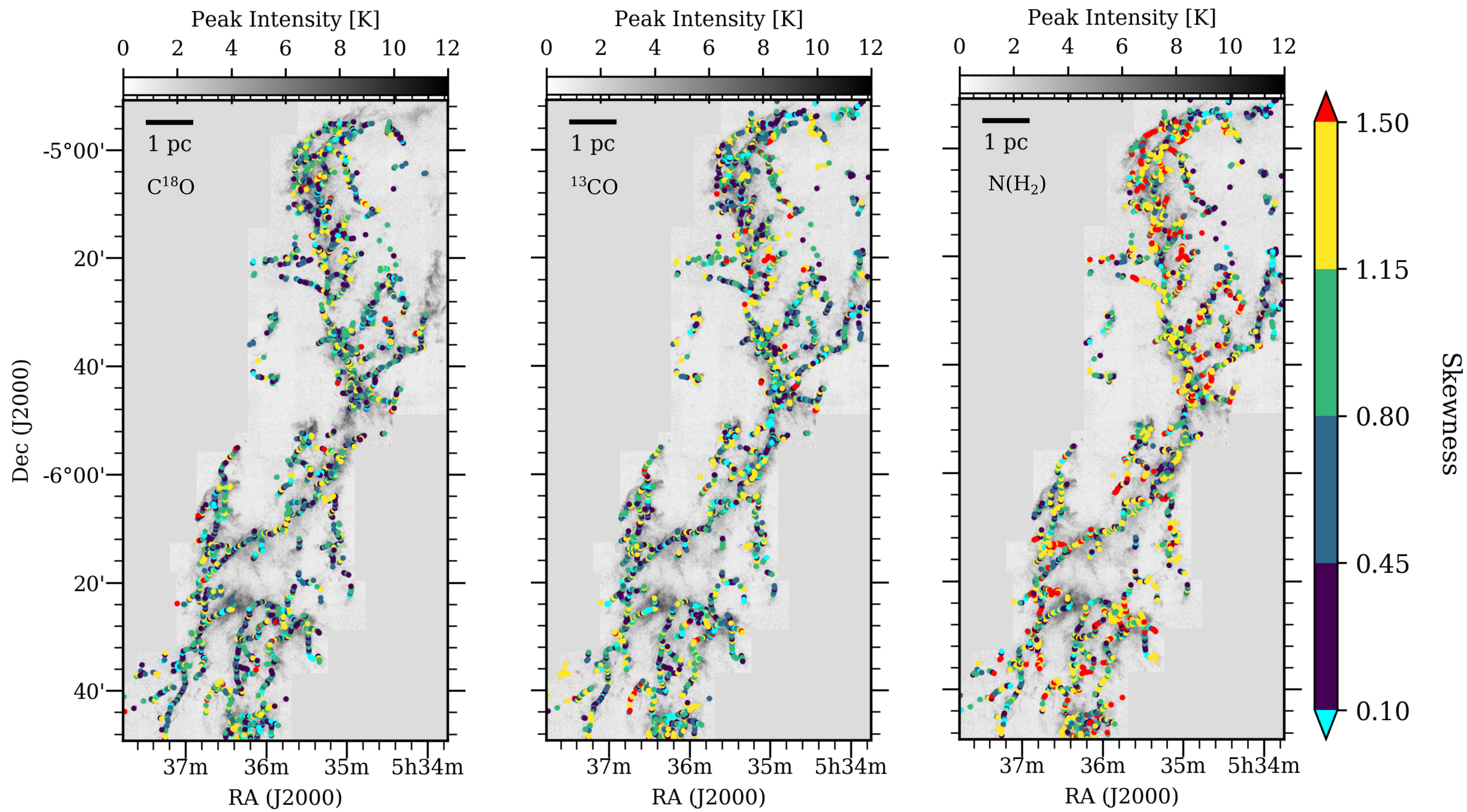

Figure 8.13: Skewness values of the intensity profiles derived from the $C^{18}O$ (left) and ^{13}CO datacubes (middle) and dust column density map (right) overlaid on the $C^{18}O$ peak intensity map.

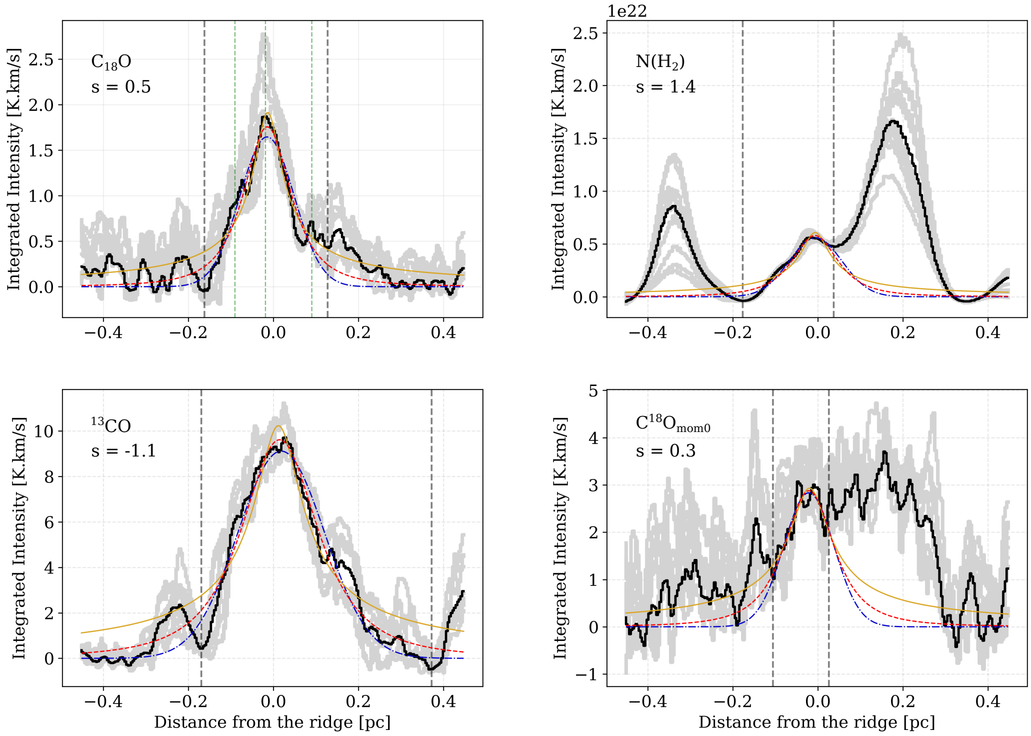

Figure 8.14: Comparison of intensity profiles calculated at the same position of the map, using different tracers. The solid black lines show the averaged profiles for which the filament properties are calculated. The grey lines show the profiles along the filament over which the averaged profile is calculated. *Top:* $C^{18}O$ and dust column density profiles shown in the left and right panels. *Bottom:* ^{13}CO and $C^{18}O_{mom0}$ intensity profiles in the left and right panels. The grey dashed lines indicate the fitting boundaries.

8.2.3 *PDRs or filaments?*

As explained in previous sections, C^+ is enhanced between the molecular gas and the atomic gas by the FUV radiation (5.16 eV $< h\nu <$ 13.6 eV). Because Orion A is bathed by strong UV radiation that is produced by the Trapezium cluster near OMC-1 and the 42 Ori near OMC-3, I predict that the filaments must be affected by this radiation too. In order to demonstrate that filaments may show a chemical layering resembling PDRs, I used `FilChaP` to produce intensity profiles of all species (^{13}CO, C^{18}O, [C II], N(H_2) and dust temperature ($T_{\rm dust}$)) perpendicular to the filament spines. The $T_{\rm dust}$ map used in this work is unpublished and was produced using *Herschel* observations (private comm. Dr. Amelia Stutz).

In order to demonstrate the spatial layering of the observed tracers towards the filaments, I have selected 4 example filaments. Figure 8.15 shows the location of these filaments in the northern Orion A in the middle panel, and the radial intensity, column density and dust temperature profiles of the filaments. In each panel showing the profiles the black, dark red and blue lines correspond to C^{18}O, ^{13}CO and [C II] emission, respectively, the orange line corresponds to the dust column density emission and the bright red line corresponds to the dust temperature along the perpendicular slice. The emission peaks of C^{18}O, ^{13}CO and the dust column density are close together in all cases. [C II] peak however is shifted in all cases, enhanced towards the direction where the filaments face UV radiation. The enhancement of [C II] emission is followed by an enhancement in the dust temperature.

The shift of the [C II] peak and the chemical layering is a common occurring throughout the map. In order to quantify the amount of this shift, I identified the emission peaks in each intensity profile and plotted the differences on the C^{18}O peak intensity map. Figure 8.16 shows the distances between the C^{18}O and [C II] peaks throughout the northern Orion A on the left panel, and the distances between ^{13}CO and [C II] peaks on the right panel. There exists a chemical layering of species for the majority of the filaments, and this shift in most cases is between 0.1 - 0.15 pc. The densest filaments in the inner ridge of the ISF show very little shift implying that perhaps the high column density filaments are much less affected by the UV radiation. However, further studies of in-depth PDR modeling is necessary to draw conclusions from this analysis.

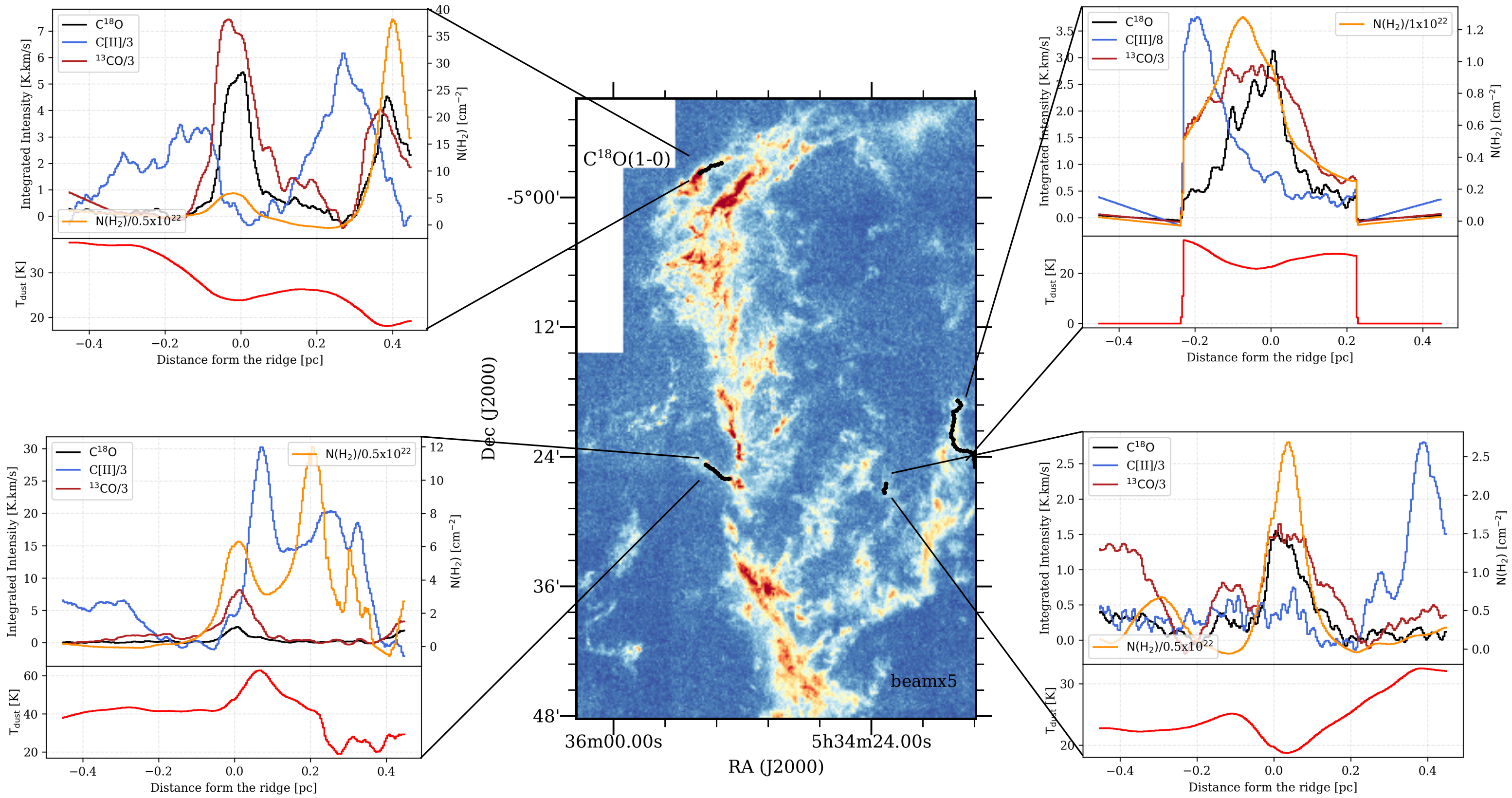

Figure 8.15: Locations of the 4 selected filaments in the northern Orion A and their intensity profiles. The black, dark red and blue lines correspond to the intensity profiles calculated from the C^{18}O, ^{13}CO and [C II] datacubes. The orange line corresponds to the intensity profile obtained using the dust column density map and the bright red line corresponds to the dust temperature along the perpendicular slice.

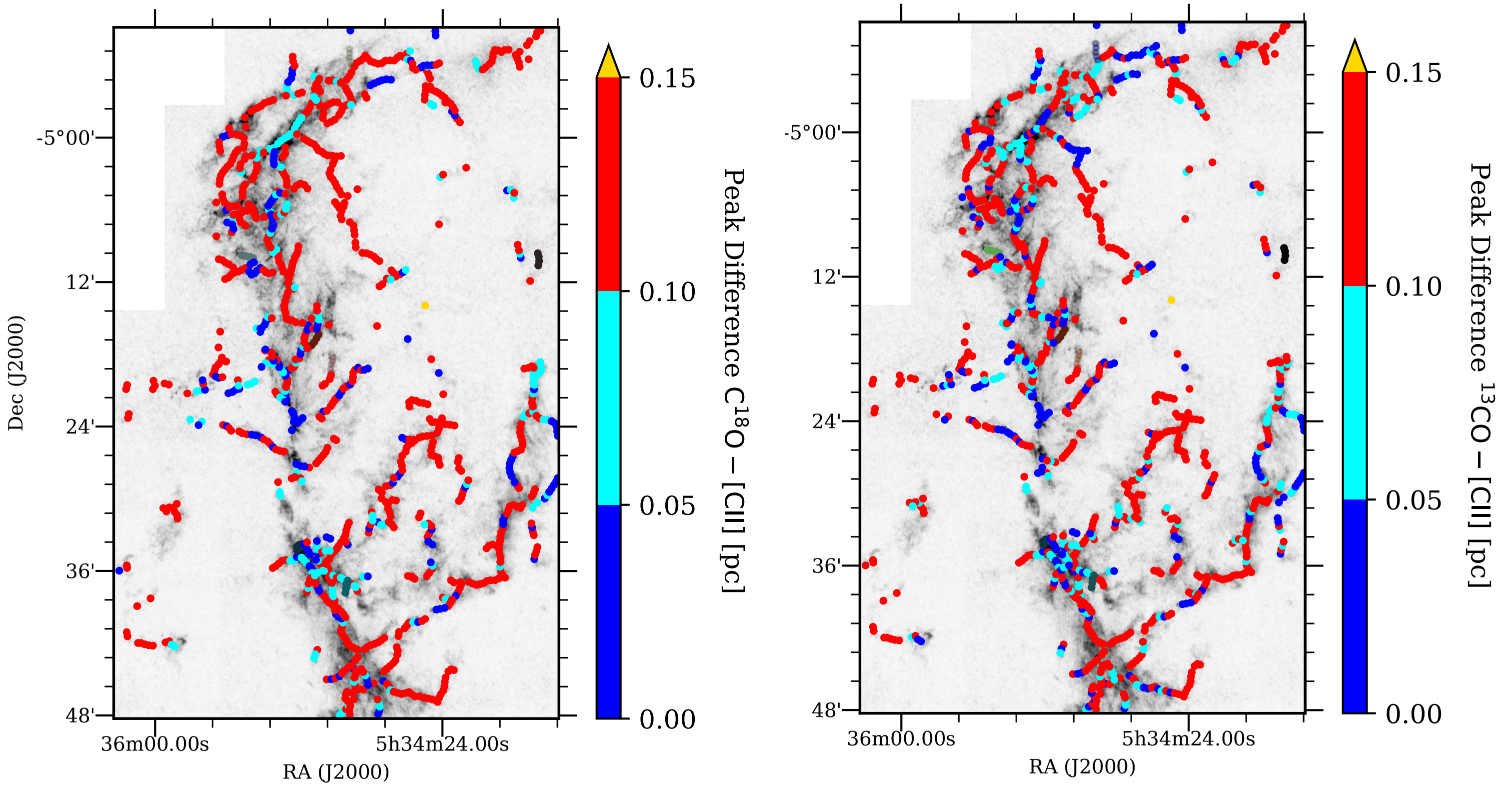

Figure 8.16: The spatial shift between the peak intensity of $C^{18}O$ and [C II] emission (left) and between the ^{13}CO and [C II] emission (right).

Part IV

EPILOGUE

The last part of this work is intended to summarize the results that have been discussed thus far, and present ideas for future work.

9 CONCLUSIONS

In order to understand star formation in the most nearby high-mass star forming molecular cloud, Orion A, the CARMA-NRO Orion Survey team has conducted observations both at CARMA and NRO. I contributed to the observations held at CARMA spending in total a month at the telescope between 2014 and end of 2015. My hands on experience that not only included executing observations, but working with the telescopes at the observing site and helped me to understand the principles of radio astronomy and radio interferometry much better. Furthermore, I contributed to the interferometric data reduction during the data acquisition at CARMA.

I investigated the performance of the structure identification algorithm `DisPerSE` using simulated filaments and simulated molecular clouds. I found that as the signal to noise level decreases, DisPerSE tends to identify *filamentary networks*. These filamentary networks are not identified in the simulations with no noise, but only seem to appear in noisy datasets when the persistence threshold is set to less than 3 times the noise level. Therefore, the identification of fake filamentary networks can easily be avoided.

I identified filaments in the CARMA-NRO ^{13}CO and C^{18}O(1-0) datasets. However, as C^{18}O traces denser and more filamentary gas, I used the filaments identified in the C^{18}O map throughout this work. In order to analyze the properties of the identified filaments, I developed `FilChaP`, a python-based filament characterization algorithm. `FilChaP` uses `DisPerSE` filaments on 2D or 3D datasets to calculate filament lengths, widths, curvatures, skewness and kurtosis.

By analyzing the C^{18}O dataset, I found the:

- the filaments have a median of 0.1 pc width, however, the width along the filaments varies throughout the cloud.
- the calculated widths in the north is slightly narrower than the widths in the southern portion of the cloud.
- the variation of the width (0.05 – 0.3 pc) correlates with the amount of substructure that the filaments have. For a filament width no substructure the filament width is 0.06$\pm$0.01 pc and 0.08$\pm$0.01 pc in the northern and southern regions, respectively.
- there is a lack of correlation between filament widths and column density that was also shown in previous studies such as Arzoumanian et al. (2011). The fact that filaments with high column densities still keep a constant width was attributed to accretion onto the filaments.

- Looking at the velocity dispersion of the substructure of the filaments, and not only the filament spine, I showed that the substructure contributes to the filament velocity dispersion, immensely. If the accretion onto the filaments is responsible for the observed velocity dispersions, I showed that to drive such a level of turbulence one needs accretion velocities of $3-5$ km s^{-1}.

The comparison of emission from different tracers has revealed that structures along the line of sight affect the filament properties excessively. However, in order for a comparison one must use reliable tools. In this sense, I found that comparison of 2D KDEs are sufficient. By comparing the filament calculated from the $C^{18}O$ datcube, to those calculated form the $C^{18}O$ integrated intensity map, ^{13}CO datacube and dust column density map I found:

- the highest correlation of widths are calculated between the $C^{18}O$ and ^{13}CO datacubes,
- there is a large scatter between the widths calculated from $C^{18}O$ datacube and $C^{18}O$ integrated intensity, as well as the dust column density maps,
- the filament widths calculated from $C^{18}O$ integrated intensity and dust column density correlate with each other
- the filament widths in the southern region of the map is always larger, reaching 0.2 pc in ^{13}CO emission.

I have also looked at the higher order moments, kurtosis and skewness, of the filament profiles, and compared them in different tracers. I found that:

- the narrower the widths the more scattered the kurtosis values,
- the kurtosis values for the majority of the profiles in *all* tracers is negative, indicating a better correspondence to Plummer-like profiles
- there is a weak correlation between the filament widths and kurtosis for ^{13}CO and $C^{18}O$ that could be attributed to opacity effects and freeze-out, respectively.
- for the skewness, depending on the boundaries of the intensity profiles within which the skewness values are calculated, one gets highly different results. I found skewness to be unreliable, and not quite representative of stellar feedback given the current methods. However, the methods can be improved in the future.

Lastly, I found that the majority of the filaments in the northern Orion A is affected by the strong UV radiation produced by the high-mass stars. Most of these filaments show chemical layering of dense and ionized gas that resemble clumpy PDRs. However, the highest column density filaments along the dense ridge of the ISF stay less affected, perhaps shielded from the ionizing radiation.

10 OUTLOOK

In this work, I have presented a comprehensive analysis of the filamentary structure of the Orion A molecular cloud. However, as any scientific study, there are aspects of this work that can be improved, and open questions that can be answered in the near future. For example, for filament identification, I used the `DisPerSE` algorithm. However, there are other methods that can be applied to compare the identified filaments, such as Friends in velocity (FIVE) developed by Hacar et al. (2013). FIVE decomposes a datacube by fitting Gaussians to each spectra and groups the spectra that form coherent structures in velocity space. FIVE is unfortunately not publicly available, however there are similar methods recently developed in-house by Dr. Seamus Clarke and can be applied to the CARMA-NRO dataset in the future. Usage of such an algorithm will also help studying filament kinematics on which I would like to write another paper. I would, however, like to note that the recent study by Clarke et al. (2018) shows that filaments that may seem coherent in velocity space, do not necessarily correspond to coherent entities in the 3D PPP space. Therefore, studying filament kinematics and deriving conclusions has to be done with caution.

The `FilChaP` algorithm can be improved in several ways. Firstly, I would like to implement a method to identify fitting boundaries in a more robust way: including also an intensity threshold. At the moment the boundaries are put around the peak of the emission from the filament wherever a minima with a significance of 3 beam-sizes is found. The intensity threshold will ensure that this minima is close to the noise level and therefore the wings of intensity profile of the filament always goes to the noise level. This will help prevent having filament widths larger than the size of the boundaries. The significant peaks within the boundaries will then be identified as substructure. I predict that this method will also improve the skewness analysis, as the boundaries would be less biased. Secondly, I would like to make FilChaP compatible with PPP datasets, therefore, it can also be applied to simulated data.

From the observational side, no amount of data is ever sufficient to study all the aspects of an object. Therefore, I would like to write an observing proposal for a large program to observe atomic carbon, C I, emission throughout Orion A. At the moment the APEX telescope has the ability to do this. With the C I data at hand, one can study the distribution of neutral atomic gas, and an in-depth analysis of PDRs would be possible.

To complete this work, I will write a paper on the filament properties seen in different tracers presented in Chapter 8. Such a study has never been published before and I think it proves that the properties structure we observe is highly dependent on the tracer that we choose to observe it with.

Part V

APPENDIX

A

ADDITIONAL PLOTS

A.1 CHANNEL MAPS

In this section, I present the channel maps of the observed tracers from the CARMA-NRO Orion Survey and the C^+ SQUAD Project. Figures A.1, A.2, A.3 show the channel maps of ^{12}CO, ^{13}CO and C^{18}O, respectively. The ^{12}CO channel maps are between 4.6 km s^{-1} and 13.6 km s^{-1} with an increment of 0.5 km s^{-1} . For the ^{13}CO, the maps between 5.4 km s^{-1} and 13.4 km s^{-1} are plotted with an increment of 0.5 km s^{-1} . For C^{18}O the maps between 5.9 km s^{-1} and 11.6 km s^{-1} are plotted with an increment of 0.4 km s^{-1} .

The channel maps for the [C II] emission is shown in Figure A.4 for the velocities ranging between -1.9 km s^{-1} and 14.3 km s^{-1} with 0.9 km s^{-1} increments.

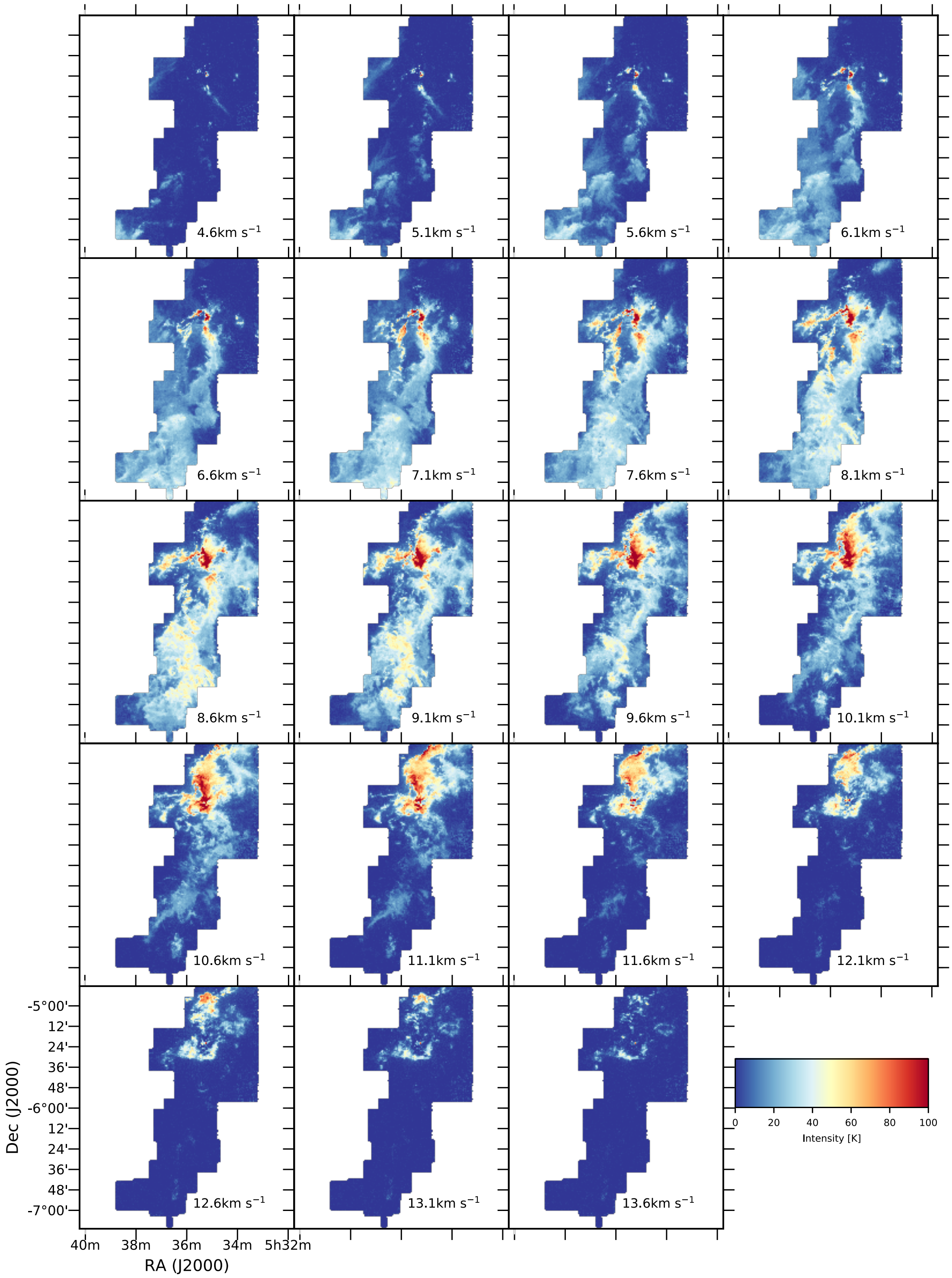

Figure A.1: ^{12}CO channel maps. The maps are shown for the velocities ranging from 4.6 km s^{-1} to 13.6 km s^{-1} with 0.5 km s^{-1} increments.

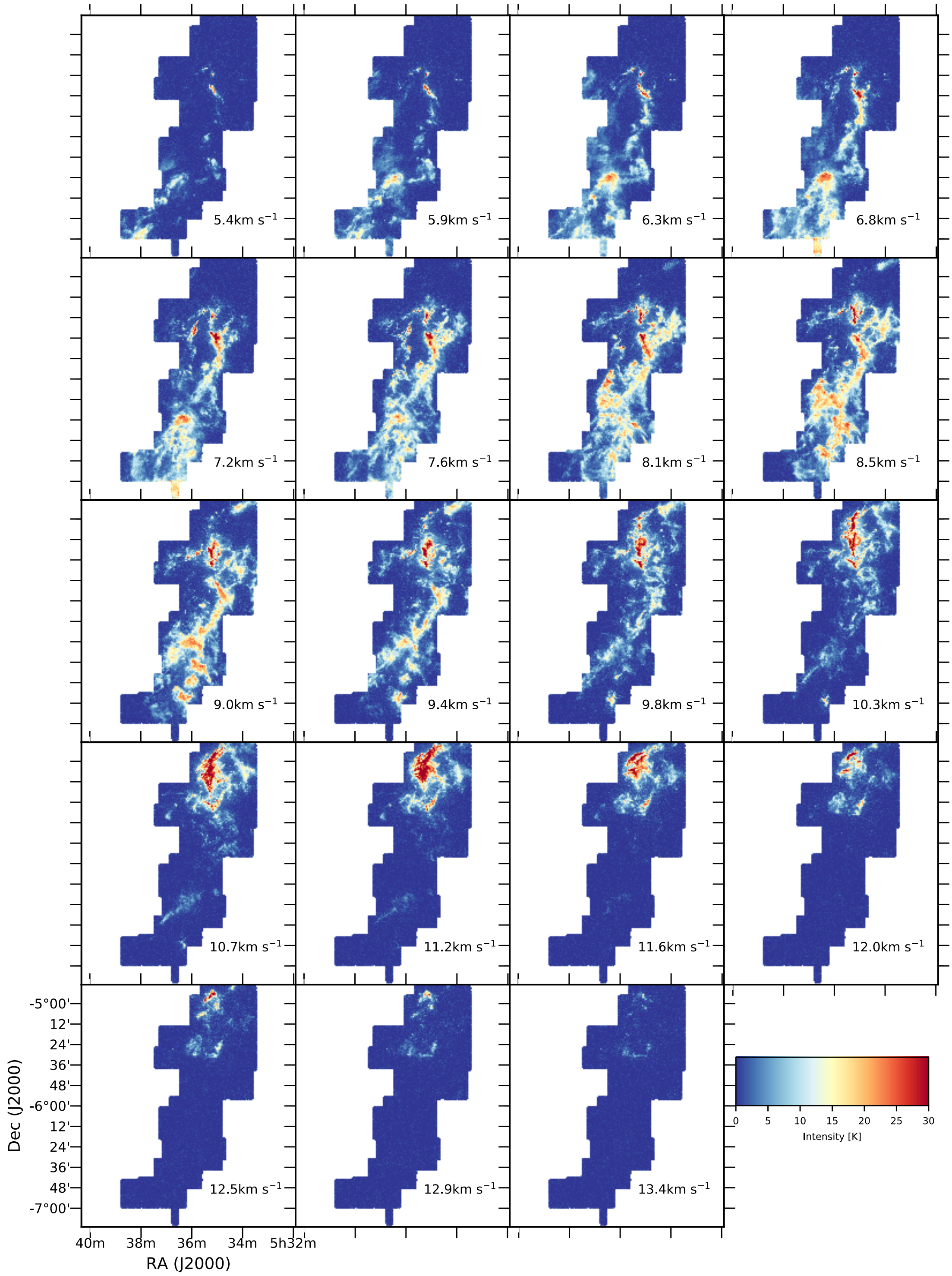

Figure A.2: ^{13}CO channel maps. The maps are shown for the velocities ranging from 4.6 km s^{-1} to 13.4 km s^{-1} with 0.9 km s^{-1} increments.

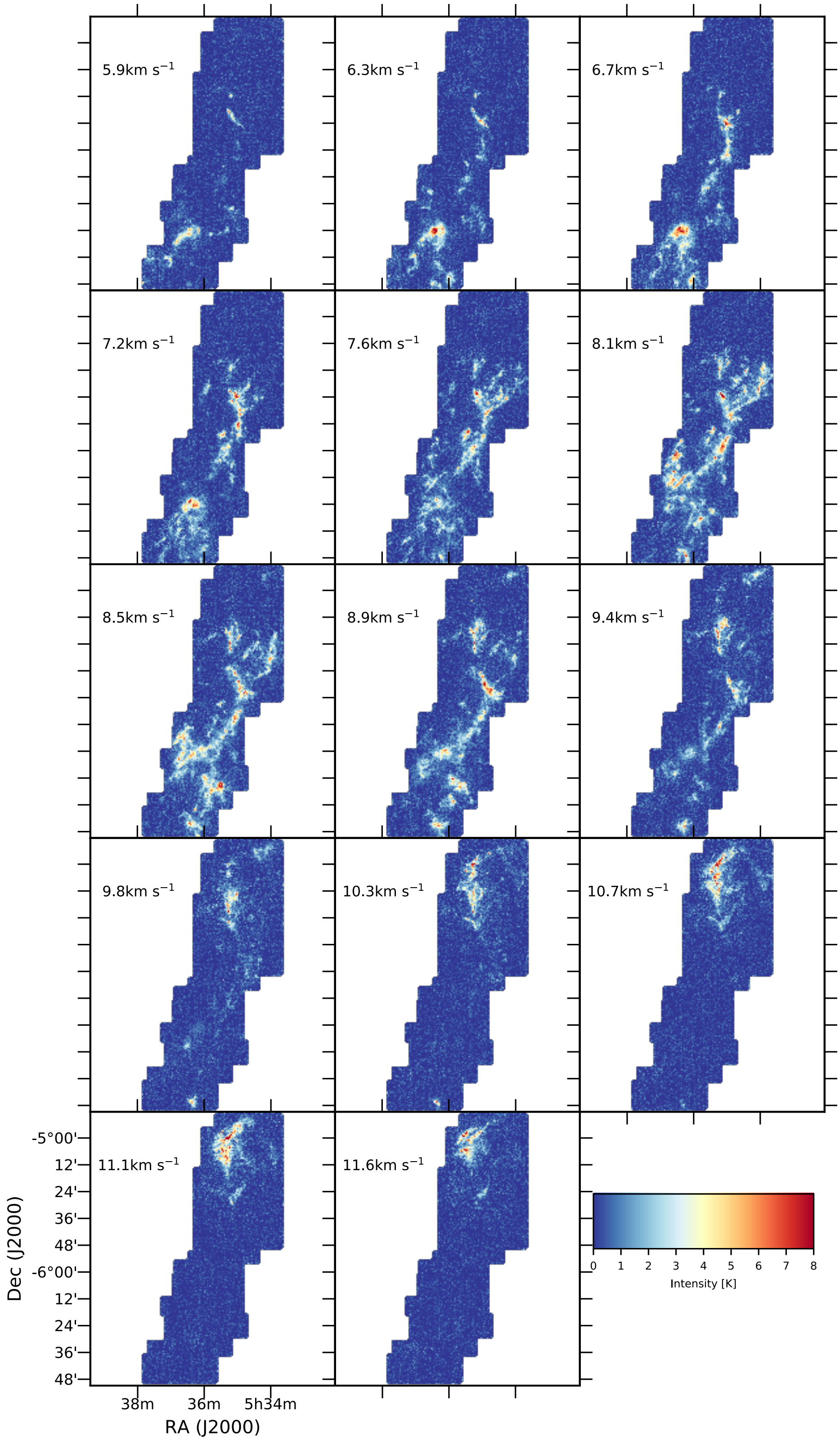

Figure A.3: $C^{18}O$ channel maps. The maps are shown for the velocities ranging from 5.9 km s^{-1} to 11.6 km s^{-1} with 0.4 km s^{-1} increments.

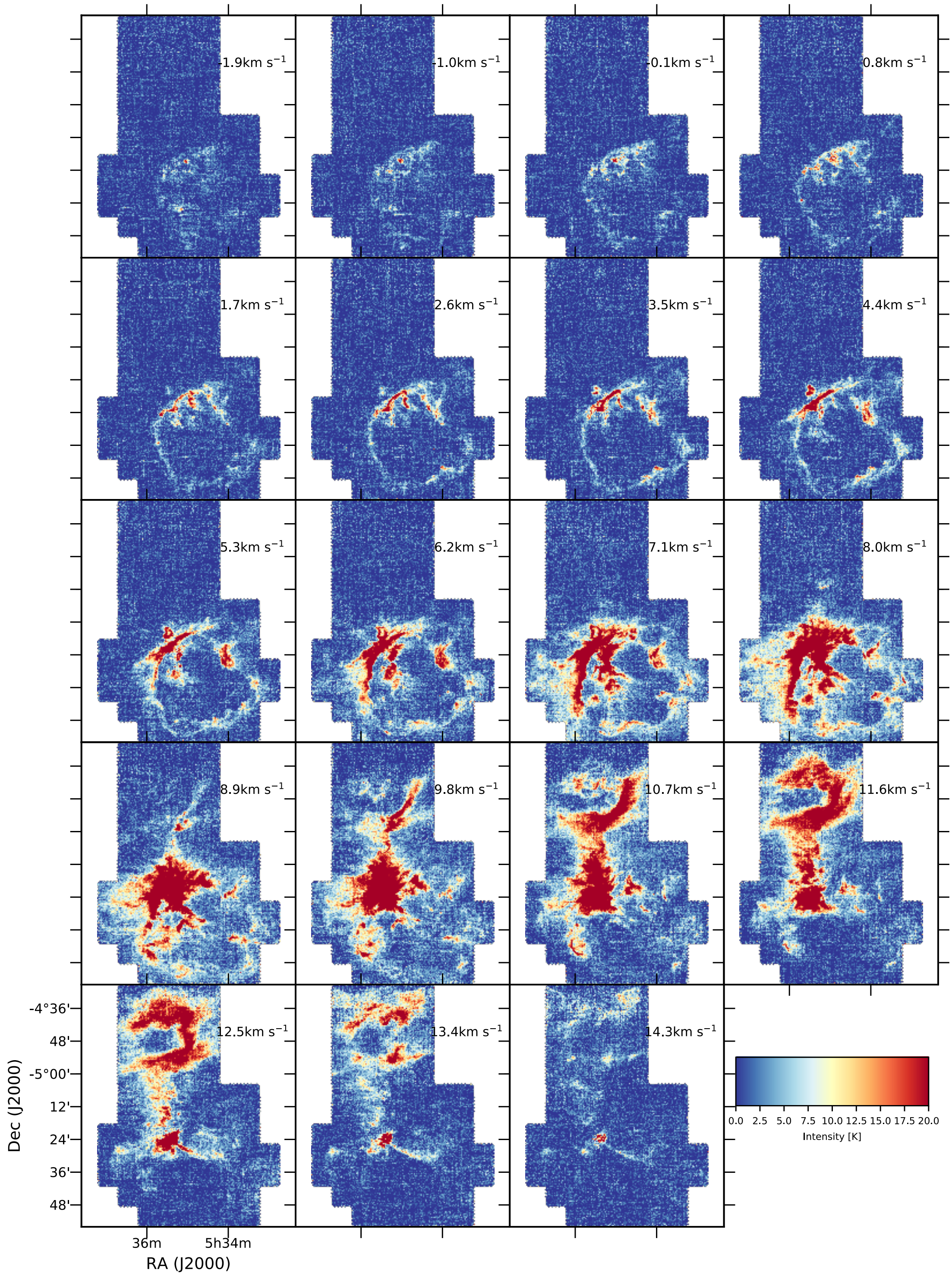

Figure A.4: C^+ channel maps from C^+ SQUAD Project. The map is shown for the velocities from -1.9 km s^{-1} to 14.3 km s^{-1} with 0.9 km s^{-1} increments.

A.2 KDE PLOTS

Additional plots for the KDE comparison between the filament widths calculated using Plummer p=2 and p=4 fits and the second moment of distribution is shown in Figures A.5, A.6, A.7, respectively. The results for the Gaussian fits are presented in Section 8.2.1.2. Essentially, there is no difference between the methods that would yield different correlations between the widths calculated using different tracers. The second moment method, however, yields a slightly lower correlation for all the tracers, which could be an effect of the boundary selection.

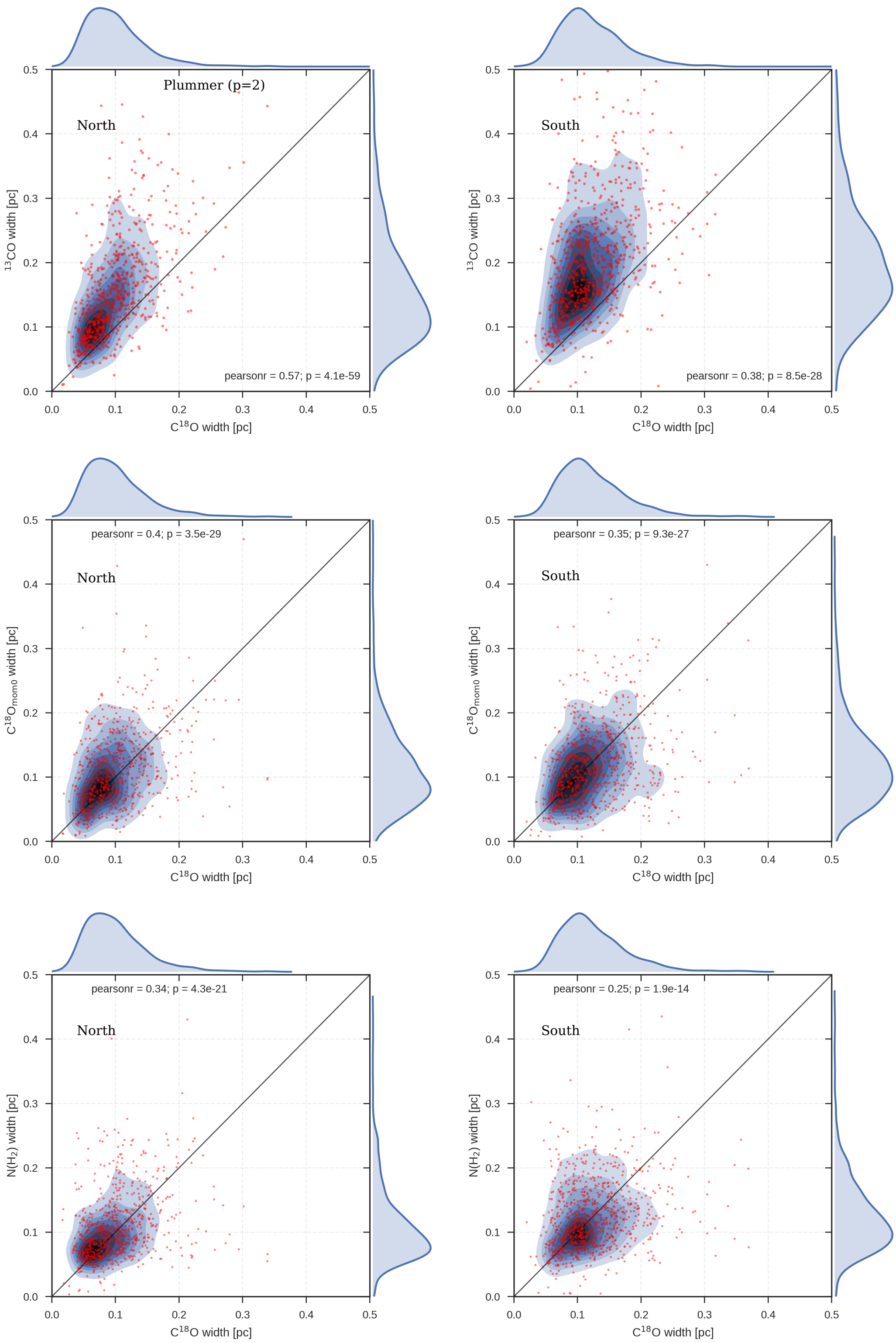

Figure A.5: Comparison of filament widths seen in different tracers calculated for the Plummer p=2 fits. From top to bottom shown are the comparisons between ^{13}CO and C^{18}O datacubes, C^{18}O integrated intensity and C^{18}O datacube, and dust column density and C^{18}O datacube. Left and right panels show the widths calculated for the northern and southern regions of the map.

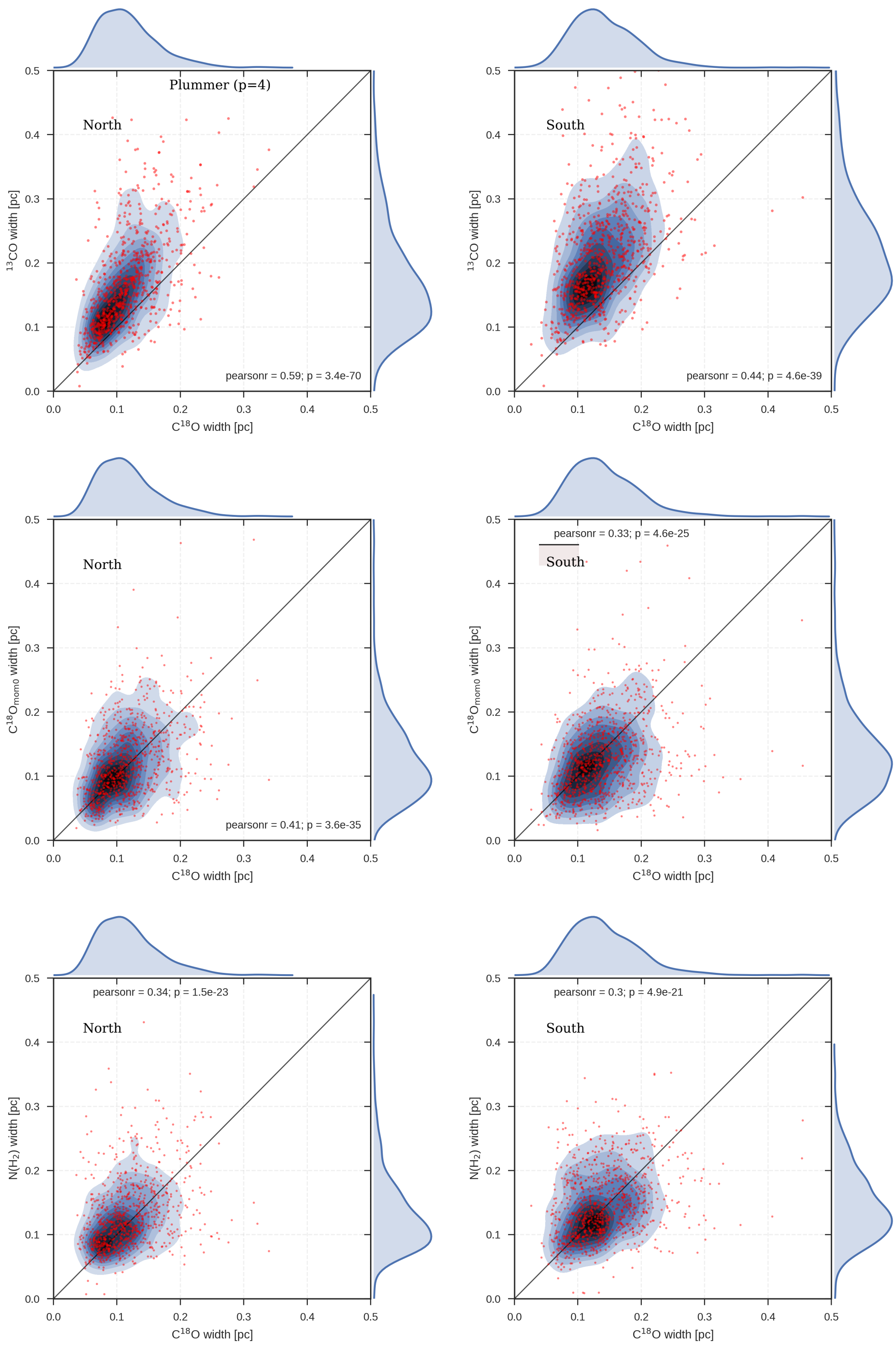

Figure A.6: Same as Figure A.5 but for the Plummer p=4 fits.

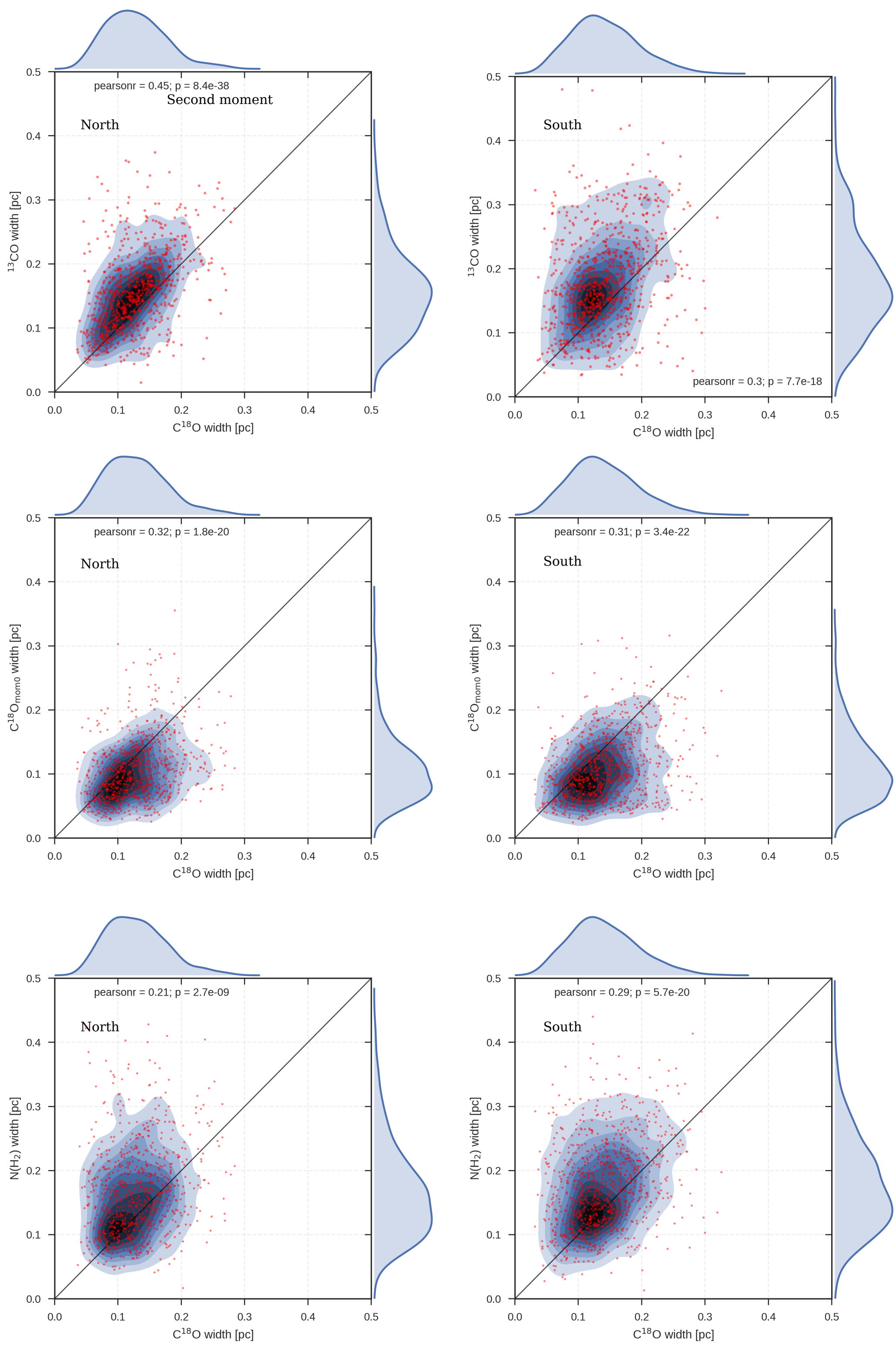

Figure A.7: Same as Figure A.5 but for the widths calculated from the second moment of distribution.

B PUBLICATION

The publication, Suri et al. (2019), presented in this chapter is reproduced with permission ©ESO.

A&A 623, A142 (2019)
https://doi.org/10.1051/0004-6361/201834049

Astronomy & Astrophysics

The CARMA-NRO Orion Survey

Filamentary structure as seen in $C^{18}O$ emission

Sümeyye Suri[1,⋆], Álvaro Sánchez-Monge[1], Peter Schilke[1], Seamus D. Clarke[1], Rowan J. Smith[2], Volker Ossenkopf-Okada[1], Ralf Klessen[3], Paolo Padoan[4,5], Paul Goldsmith[6], Héctor G. Arce[7], John Bally[8], John M. Carpenter[9], Adam Ginsburg[10], Doug Johnstone[11,12], Jens Kauffmann[13], Shuo Kong[7], Dariusz C. Lis[14,15], Steve Mairs[16], Thushara Pillai[17], Jaime E. Pineda[18], and Ana Duarte-Cabral[19]

(Affiliations can be found after the references)

Received 8 August 2018 / Accepted 2 January 2019

ABSTRACT

Context. We present an initial overview of the filamentary structure in the Orion A molecular cloud utilizing a high angular and velocity resolution $C^{18}O(1–0)$ emission map that was recently produced as part of the CARMA-NRO Orion Survey.

Aims. The main goal of this study is to build a credible method to study varying widths of filaments which has previously been linked to star formation in molecular clouds. Due to the diverse star forming activities taking place throughout its ~20 pc length, together with its proximity of 388 pc, the Orion A molecular cloud provides an excellent laboratory for such an experiment to be carried out with high resolution and high sensitivity.

Methods. Using the widely-known structure identification algorithm, DisPerSE, on a three-dimensional (PPV) $C^{18}O$ cube, we identify 625 relatively short (the longest being 1.74 pc) filaments over the entire cloud. We studied the distribution of filament widths using `FilChaP`, a `python` package that we have developed and made publicly available.

Results. We find that the filaments identified in a two square-degree PPV cube do not overlap spatially, except for the complex OMC-4 region that shows distinct velocity components along the line of sight. The filament widths vary between 0.02 and 0.3 pc depending on the amount of substructure that a filament possesses. The more substructure a filament has, the larger is its width. We also find that despite this variation, the filament width shows no anticorrelation with the central column density which is in agreement with previous *Herschel* observations.

Key words. ISM: clouds – stars: formation – ISM: structure – ISM: individual objects: Orion A – methods: statistical

1. Introduction

Over the past decade, it has become clear that stars preferentially form along and at the junctions of filaments inside cold, dense molecular clouds (e.g. Schneider et al. 2012). Filaments pervade molecular clouds whether these clouds form high-mass or low-mass stars, or lack star formation entirely (André et al. 2010, 2016). Earlier studies of dust continuum observed with the *Herschel* Space Observatory suggest a "universal width" of the observed filaments (Arzoumanian et al. 2011). The distribution of widths of 90 filaments having column densities of 10^{20}–10^{23} cm^{-2} peaks at 0.1 pc with very little dispersion (±0.03 pc, Arzoumanian et al. 2011). However, work by Smith et al. (2014) shows that the calculated filament width is dependent on the fitting range considered when analyzing the radial profiles. They find that the degeneracy between the central density of the filaments and their inner flat-radius raises uncertainties. We also refer to Panopoulou et al. (2017) for the shortcomings of fitting methods used in calculating filament widths. Moreover, higher angular resolution observations that allow study of high density filaments within molecular clouds suggest widths as narrow as 0.01 pc (Sánchez-Monge et al. 2014; Hacar et al. 2018), while observations of tracers such as ^{13}CO have revealed filaments with 0.4 pc widths (Panopoulou et al. 2014). For the study of filament properties, in particular their widths, molecular line observations allow studying intertwined filamentary networks which otherwise appear as single objects when observed in dust emission due to projection of three-dimensional information (position–position–velocity, PPV) on to two-dimensional column density space, therefore providing a more accurate determination of the filament properties. Understanding the role of filaments in the process of star formation requires high spatial and spectral resolution studies of, ideally, multiple molecular emission lines that trace different densities within the cloud, as well as continuum emission. This way, filament properties can be calculated for different tracers that probe a variety of physical and chemical conditions. Investigating physical and kinematic properties of filaments weighted by the environmental and chemical conditions allows us to gain an understanding of how filaments form, how this relates to the formation of molecular clouds, how mass flow and/or accretion onto filaments leads to the formation of new stars (see e.g. Ostriker 1964; Larson 1985; Inutsuka & Miyama 1992; Pon et al. 2012; Fischera & Martin 2012; Heitsch 2013; Smith et al. 2014, 2016; Clarke & Whitworth 2015; Seifried & Walch 2015; Clarke et al. 2016, 2017; Chira et al. 2018).

In this work, we have studied filament properties toward the closest site of ongoing high-mass star formation, the Orion A molecular cloud ($d \approx 388$ pc, Kounkel et al. 2017). Orion A is amongst the most studied regions in the Galaxy (e.g. Bally et al. 1987; Johnstone & Bally 1999; Shimajiri et al. 2009; Nakamura et al. 2012). The northern Orion A region, encompassing

⋆ *Current address*: Max Planck Institute for Astronomy, Königstuhl 17, 69117 Heidelberg, Germany.

OMC-1, OMC-2, OMC-3 and OMC-4, is commonly referred as the integral shaped filament (hereafter, ISF, Bally et al. 1987). The whole ISF is subject to ionizing UV radiation produced by the Trapezium stars ~1 pc in front of the molecular cloud (van der Werf et al. 2013). Moreover, the NGC1977 HII region, powered by a B0V type star, 42 Ori, could produce a radiation field as strong as 2000 times the standard value of the ISRF ($G_0 \simeq$ 2000) on the OMC-3 filaments, depending on the 3D orientation of the star relative to the northern ISF. Toward the south, the ISF extends to the L1641 region that is more diffuse compared to the northern portion, and less affected by the UV radiation due to the lack of high-mass stars.The structures seen in Orion A are therefore shaped not only by the gravitational potential of OMC-1, but also by the feedback from high-mass and low-mass (proto)stars.

So far, large-scale spectral line emission maps of the Orion A cloud have been obtained only with low angular resolution, while high angular resolution observations have been obtained only toward selected subregions of the cloud. For example, while Bally et al. (1987) observed a 1.5 square degree region of the ISF with a 0.1 pc resolution, Kainulainen et al. (2017) observes a 3 × 11 arcmin (0.33 × 1.24 pc) region toward OMC-2 with a ~1200 AU resolution. Similarly, Hacar et al. (2018) observes a narrow field around the OMC-1/OMC-2 regions with high angular resolution (1750 AU) using a map combining data from ALMA and the IRAM 30 m telescope. The current work, on the other hand, provides a first look into filament properties that are obtained with high angular resolution in an extensive map of the Orion A molecular cloud.

In Sect. 2, we summarize the large scale and high angular resolution observations from the CARMA-NRO Orion Survey. In Sect. 3 we introduce our methods to calculate physical properties of filaments. Based on these methods we present filament properties as observed in $C^{18}O$ emission, see Sect. 4. Finally, we summarize our results in Sect. 5.

2. Observations

In order to image an extended region toward Orion A with high angular resolution and high sensitivity, the CARMA-NRO Orion Survey (PI: J. Carpenter) was granted ~650 h of observing time at the Combined Array for Millimeter-Wave Astronomy (CARMA). The observations were carried out between 2013 and 2015 using 15 antennas (6 and 10 m dishes) of the array with D and E configurations resulting in an angular resolution of about 8 arcsec (0.015 pc at a distance of 388 pc). Outflow and diffuse gas tracers (^{12}CO and ^{13}CO), warm dense gas tracers (CS and $C^{18}O$), a cold dense gas tracer (CN) and a shock tracer (SO) along with the 3 mm continuum were observed simultaneously. The interferometric observations were combined with single dish observations in order to account for extended emission. The single dish observations were carried out at the 45 m telescope at the Nobeyama Radio Observatory (NRO45m). The NRO45m data were taken using two different receivers; BEARS between 2007 and 2009 for ^{12}CO, and between 2013 and 2014 for ^{13}CO and $C^{18}O$, and FOREST between 2014 and 2017. These observations are described in detail in Shimajiri et al. (2014) and Kong et al. (2018), respectively. For combination and joint deconvolution of the interferometer and single dish data in the *uv*-domain the method presented by Koda et al. (2011) was followed. The data combination results in 0.47 K rms noise level in 0.22 km s^{-1} channels. Details on the imaging are presented in the CARMA-NRO Orion Survey data paper Kong et al. (2018).

The combined (CARMA+NRO45m) data spans two degrees in declination including the ISF in the north and the L1641 cloud in the south. In Fig. 1, we show the $C^{18}O$ moment maps; integrated intensity, centroid velocity and velocity dispersion (from left to right). The data highlights the filamentary nature of the cloud (see Fig. 1, left panel), as well as hub-like structures where filaments merge. A plethora of kinematic information accompanying the filamentary structure can be seen in the velocity centroid map (Fig. 1, middle panel). In addition to the well known north-south velocity gradient from 13 to 5 km s^{-1}, we see gradients perpendicular to the spine of the ISF appearing in OMC-4 and -5 regions. The kinematics of the filamentary structure will be discussed in a following paper.

3. Filament properties

Filament identification is done by employing the structure identification algorithm *Discrete Persistent Structures Extractor*, DisPerSE (Sousbie 2011). DisPerSE uses the Morse theory to derive information on the topology of a given data set. It builds up a tessellation consisting of critical points – those points where the gradient of the intensity goes to zero, namely: minima, maxima and saddle points. It connects maxima and saddle points via arcs, which are then called filaments. DisPerSE has been a widely used tool to extract filamentary structures both in observational and synthetic datasets (e.g., Arzoumanian et al. 2011; Schneider et al. 2012; Palmeirim et al. 2013; Panopoulou et al. 2014; Smith et al. 2016; Chira et al. 2018). In order to identify filaments in the CARMA-NRO Orion Survey we used the $C^{18}O$ datacube. The $C^{18}O$ emission allows us to trace denser regions of the cloud. It is optically thin and less affected by stellar feedback compared to ^{12}CO and ^{13}CO, therefore it is a better choice to trace dense filaments. The ^{12}CO emission traces more diffuse and optically thick parts of the cloud (see Fig. 5 in Kong et al. 2018), and therefore we refrain from using it for the analysis of the filamentary structure. The ^{13}CO map shows filamentary structure in addition to the extended emission (see Fig. 6 in Kong et al. 2018), but it can be optically thick in the densest parts of the ISF.

We applied DisPerSE on the $C^{18}O$ datacube with a persistence and a noise threshold of 2 K (4σ). Persistence is a term that refers to the contrast between the values of the identified critical points. High persistence means that the identified maximum has higher contrast with respect to its surroundings. Eliminating those critical point pairs with low persistence, in turn, leaves us with the most prominent structures that stand out from the rest. For further discussion on persistence and the general mathematical background of the algorithm we refer to Sousbie (2011).

After running on a PPV cube, DisPerSE provides us with filament coordinates for each identified filament on the PPV space. This has an advantage over the column density filaments identified in *Herschel* maps (e.g. André et al. 2016), because we are able to disentangle the velocity structure of the filaments instead of looking at integrated emission over all the structure along the line of sight.

Figure 2 shows the identified filaments overlaid on the $C^{18}O$ peak intensity map. In total, 347 filaments are identified in the northern region (ISF) and 278 filaments in the southern region (northern part of the L1641 cloud). The properties of these filaments are unaffected by the recent distance measurements to the cloud that showed a distance gradient throughout Orion A (Grossschedl et al. 2018). The gradient starts being effective below galactic longitude 210° (or approximately −6°30′) close to the southern border of our map. The filaments show slightly different properties in the northern part of the cloud compared

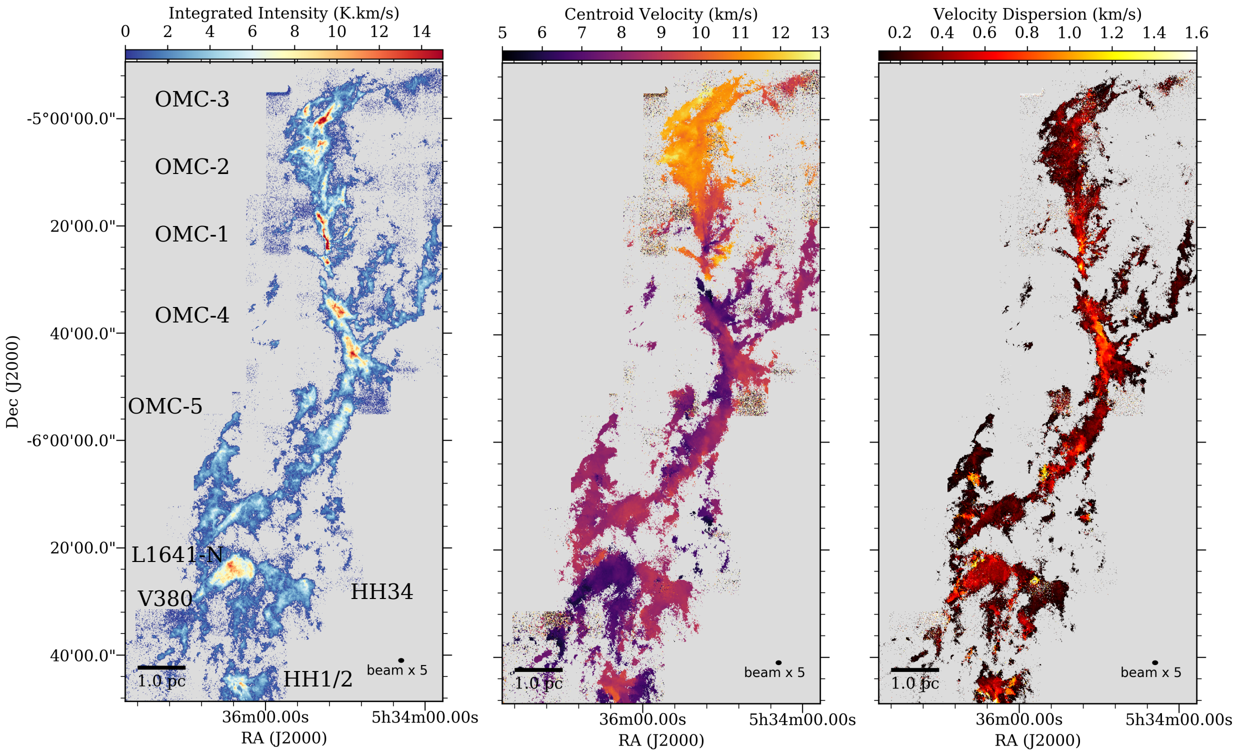

Fig. 1. Moment maps of $C^{18}O$ J = 1–0. *From left to right panels*: integrated intensity emission, the centroid velocity, and the velocity dispersion. Relevant star-forming regions are marked on the integrated intensity map. Beam-size shown in the bottom left corner is five times the real beam size (5 × 0.015 pc) of the observations for demonstration purposes.

to the more diffuse filaments identified in the southern part (see the following sections and Figs. 5 and 10). A large number of filaments identified by DisPerSE have short lengths (<0.15 pc), and seem to be continuations of one another, resulting in a longer but fragmented (as seen in $C^{18}O$) filament. We therefore did not exclude them from further analysis, in particular for the width determination. However, properties of only those filaments with an aspect ratio larger than 2:1 are shown in the Appendix B.

In order to study filament properties, we have developed a python package: the Filament Characterization Package `FilChaP`[1] that utilizes the coordinates of the identified filaments and derives their physical properties. In the following section, we present the analysis performed by `FilChaP`.

3.1. Calculation of the filament width

For each filament, we extracted radial intensity profiles perpendicular to the filament spines. This is done by first calculating coordinates of a perpendicular line at each sample point along each spine. These sample points are separated by 1.5 beam sizes (0.023 pc) in order to provide statistical independence. This separation value was found by visual inspection of the pixels employed to produce intensity profiles, making sure the same pixels are not used multiple times in consecutive slices. However, depending on a filament's curvature, the slices may occasionally cross one another at larger radial distances from the spines. The pixels that lie on or adjacent to the calculated perpendicular lines are used to produce the radial intensity profiles in a similar fashion to Duarte-Cabral & Dobbs (2016).

This process is shown in Fig. 3. On the top panel of the figure the peak intensity map toward the OMC-4 region that is overlaid with an identified filament spine is shown. Two perpendicular slices from which we extracted intensity profiles are also overlaid on the filament spine in red. An intensity profile was constructed using intensities of the pixels that are perpendicular to the filament spine at a sample spine point. These "perpendicular pixels" were found on or at the immediate vicinity of the calculated perpendicular line by looking for pixels that are at most one pixel away from the perpendicular line. The middle panel of Fig. 3 shows an expanded view of the region marked with a green box in the top panel, in order to provide a more detailed look into the perpendicular slices. The perpendicular pixels are shown with red crosses marking the center of each pixel. There are occurrences for which the calculated perpendicular lines do not cross exactly pixel centers. In that case, `FilChaP` takes the mean of the intensities from pixels that lie adjacent to the perpendicular lines. A complete radial intensity profile is achieved by plotting intensities from perpendicular pixels at each radial distance from the filament spine.

The bottom panel of Fig. 3 shows the averaged (over the shown two perpendicular slices) and baseline subtracted[2] intensity profile with a black solid line. In order to obtain the averaged profiles, we took the mean of the intensities at each radial distance from the spine. The negative distances from the spine point to the northeast direction, and positive distances to southwest of the filament. The shoulders of the averaged profile are also shown in the bottom panel of Fig. 3. A shoulder is identified where there is a local minimum in the second derivative of

[1] Publicly available at https://github.com/astrosuri/filchap

[2] See Appendix A for baseline subtraction.

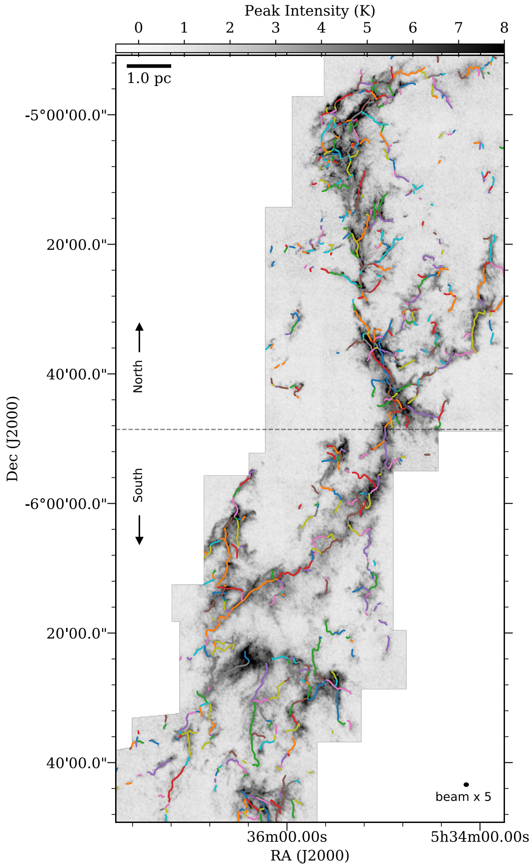

Fig. 2. Filaments identified in the Orion A molecular cloud. Grayscale shows the $C^{18}O$ peak intensity emission, while the colored segments indicate the filaments identified by `DisPerSE`.

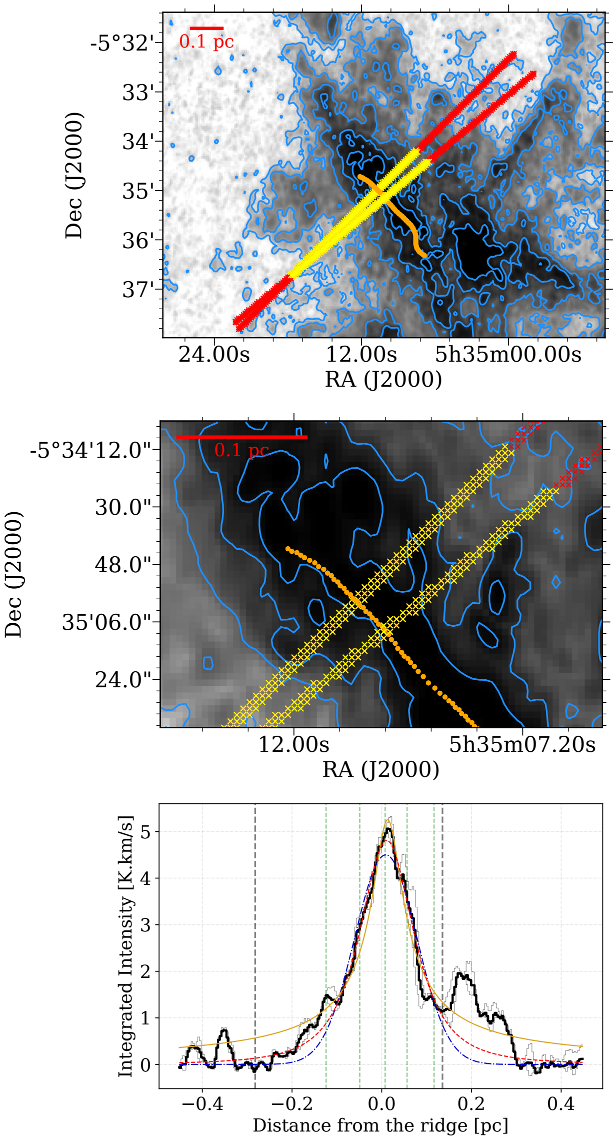

Fig. 3. *Top panel*: $C^{18}O$ peak intensity emission overlaid with a filament spine (in orange) and 2 perpendicular slices (in red and yellow). The yellow portion of the slices indicate the extent of emission fitted with `FilChaP`. The green box indicates the magnified region shown in the middle panel. Contours indicate emission levels of 2, 3, 5, 7, 9, 11 K. *Middle panel*: expanded view of the perpendicular slices. The perpendicular pixels used to extract the intensities at each radial bin are marked with crosses. *Bottom panel*: intensity profiles (gray lines) extracted from the slices overlaid on the map in the middle panel. Blue, yellow, and red curves fitted to the averaged intensity profile (black) indicate Gaussian and Plummer-like fits with $p = 2$ and 4, respectively. The vertical gray dashed lines show the positions of the identified minima considered during the fitting procedure (see Sect. 3.1). Vertical green dashed lines correspond to shoulders as explained in Sect. 4.1.

an intensity profile. Within `FilChaP` the shoulders are always identified on the smoothed intensity profiles. For this study, the smoothing length is the beam size. We also require the integrated intensity of a shoulder to be at least five times the noise level of the averaged profile which on the order of 1 K km s^{-1}. This threshold is set in order to discard less significant peaks.

As each point on the identified filament is defined by a velocity coordinate as well, we know the velocity range spanned by our filament. This information allows us to disentangle filamentary structure in PPV space. Therefore, we utilized this information when calculating the radial intensity profiles in the following way. The intensity profiles are not calculated on the integrated intensity map that is obtained from the entire velocity range of the cloud (as was done in the dust continuum studies). Instead, the intensities from each perpendicular slice are integrated over the two neighboring velocity channels around the velocity at which the filament is identified. For example, if a point along the filament is at a velocity of 5.5 km s^{-1} the intensity profile that is perpendicular to this point is calculated from the integrated intensity between 5.28 and 5.72 km s^{-1} with the velocity channel width being 0.22 km s^{-1}. This helps reduce the confusion in PPV space by discarding emission other than that which belongs to the identified filament and it makes sure that the emission included in the construction of the intensity profiles is not separated from the velocity at which the filament is identified by more than twice the sound speed (approximately 0.2 km s^{-1} at 10 K, close to our velocity resolution), providing coherence. The velocity coordinate along the filaments often change, therefore, the integrated intensities are computed individually for each PPV point along a filament.

3.1.1. Filament width determination methods

In order to calculate the widths, we employed four different methods, a Gaussian fit, two fits with Plummer-like functions with power law indices $p = 2$ and 4, and the second moment of distribution. Plummer-like functions have been used to describe the column density of a filament with a dense and flat inner portion and a power-law decline at larger radii (Arzoumanian et al. 2011):

$$\Sigma_p(r) = A_p \frac{\rho_c R_{\rm flat}}{\left[1 + \left(\frac{r}{R_{\rm flat}}\right)^2\right]^{\left(\frac{p-1}{2}\right)}} \quad (1)$$

where ρ_c is the central density, $R_{\rm flat}$ is the radius within which the density is uniform, p is the power law index, and A_p is a finite constant that is related to the filament's inclination compared to the plane of the sky (here we assume that this angle is zero). The nth moment of a distribution I is given by:

$$m_n = \frac{1}{N} \frac{\sum_i^N I_i\,(x_i - \bar{x})^n}{\sigma^n} \quad (2)$$

where $\bar{x}$ is the intensity weighted mean position of the profile, I_i is the intensity at position x_i, and σ is the intensity weighted standard deviation of the profile. The second moment is the variance of the distribution and therefore we calculate the width of the profile as $\sqrt{m_2} \times 2\sqrt{2\ln 2}$. For the fits, we use the curve_fit function contained within the scipy.optimize package with the default Levenberg-Marquardt algorithm.

We refrained from fitting the power law index of the Plummer-like function due to the degeneracy between p and $R_{\rm flat}$. Instead, we use the literature values of the index; $p = 4$ for the density of a homogeneous isothermal cylinder (Ostriker 1964) and $p = 2$, the value derived in *Herschel* studies when p is fitted as a free parameter (Arzoumanian et al. 2011), which is attributed to non-isothermality of these objects (e.g. Lada et al. 1999) or to magnetic fields (e.g. Fiege & Pudritz 2000).

The profiles are fitted only within the boundaries set by the minima around the peak. These boundaries are shown in the right hand side of Fig. 3 as gray vertical dashed lines. The minima are automatically calculated through `FilChaP` by first smoothing the profiles with a Gaussian having a width of the beam-size of the observations, and then looking at minima around the peak with a significance of approximately three beam-sizes. If multiple minima are detected on each side of the spine we take the ones that are located closer to the maxima as boundaries. The effect of the fitting range on the calculated widths is further discussed in Sect. 3.2.2.

3.1.2. Treating the bias caused by the averaging length

Previous studies (e.g. Arzoumanian et al. 2011) calculated filament widths using intensity profiles that are averaged over the entire length of a filament. Although averaging helps to obtain a smooth radial intensity profile, it has the disadvantage that any information that could be used to understand how and why the width changes along a single filament is lost. Therefore, we first study the effect of averaging intensity profiles by averaging over a length of 0.015 (a beam-size), 0.045, and 0.075 pc and finally over the entire filament. Figure 4 shows how averaging intensity profiles over different length scales affects the results. The length scale over which the profiles are averaged is indicated on the top left corner of each panel. The panels in which we average over shorter length scales (top left and right, bottom left) show marginal change in width. The bottom right panel, however, shows the scenario if we were to average over the length of the filament, the resulting width is twice as large as the previous values. Thus, not only do we overestimate the filament width by averaging, but we also lose information on the substructure of the filament. We then chose to average intensity profiles over a length of 0.045 pc (three beam-sizes) for further analysis. While this approach gives us a chance to smooth the profiles over 12 points (three beam-sizes) along the filament, it helps us avoid deriving overestimated parameters. Furthermore, we are able to follow the gradient of the width along the identified filaments.

3.2. Distribution of filament widths

Using the method described in Sect. 3.1, we calculate the widths of all the 625 filaments identified by DisPerSE in Orion A. The results are shown in Fig. 5 where the distribution for the northern region is shown by the colored and the southern region by the gray histograms. The four subplots show the distribution of widths (FWHM) calculated using Gaussian (left) and Plummer $p = 2$ fits (right) in the top panel, Plummer $p = 4$ fit (left) and the FWHM calculated from the second moment of distribution (right) in the bottom panel. Black and red dashed lines in each subplot plot indicates the "characteristic" widths found by Arzoumanian et al. (2011) in *Herschel* dust continuum, and Hacar et al. (2018) in N_2H^+ emission. The dot-dashed line indicates the spatial resolution of the data.

All four methods yield similar distributions, with the Plummer $p = 2$ fits resulting in slightly narrower widths[3]. The median values[4] of the distributions are $0.12^{+0.15}_{-0.09}$ and $0.14^{+0.18}_{-0.11}$ pc for the Gaussian fits, $0.09^{+0.13}_{-0.07}$ and $0.11^{+0.14}_{-0.08}$ pc for the Plummer $p = 2$ fits, $0.11^{+0.14}_{-0.08}$ and $0.13^{+0.16}_{-0.09}$ pc for the Plummer $p = 4$ fits, and finally, $0.12^{+0.15}_{-0.09}$ and $0.12^{+0.15}_{-0.09}$ pc for the FWHM derived from the second moment for the northern and southern regions, respectively. These results are very close to what has been reported by the *Herschel* studies (e.g. Arzoumanian et al. 2011; André 2017) and are larger than the width reported based on ALMA studies of filaments (e.g. Hacar et al. 2018; Henshaw et al. 2017), which is not unexpected considering that N_2H^+ is less extended and traces higher densities along filament spines.

The existence of a "characteristic" filament width is still highly debated (see Panopoulou et al. 2017; André 2017). In studies such as Arzoumanian et al. (2011), Palmeirim et al. (2013) and Koch & Rosolowsky (2015) the spread of the filament width distribution is less than a factor of two around the median width. On the other hand, a study by Juvela et al. (2012) shows that there is an order of magnitude deviation from the mean width (0.1–1.0 pc). Our distributions shown in Fig. 5 indicate a very significant, about an order of magnitude spread around the median value regardless of the method. The origin of this wide distribution may be due to the fact that the filaments are

[3] Using the deconvolution formula given in Könyves et al. (2015), the deconvolved filament width would be $\sqrt{0.1^2 - 0.015^2} = 0.098$ pc using an observed width of 0.1 pc and our beamsize of 0.015 pc. This shows that for our high-resolution data the beamsize does not play a crucial role for our calculated filament widths and there is no need for deconvolution.

[4] All the errors cited on the median widths throughout this work are the first and third quartiles. The uncertainties on the widths derived from the intercept of the linear relation between number of shoulders and the width (see Sect. 4.1) come from the error on the fitting.

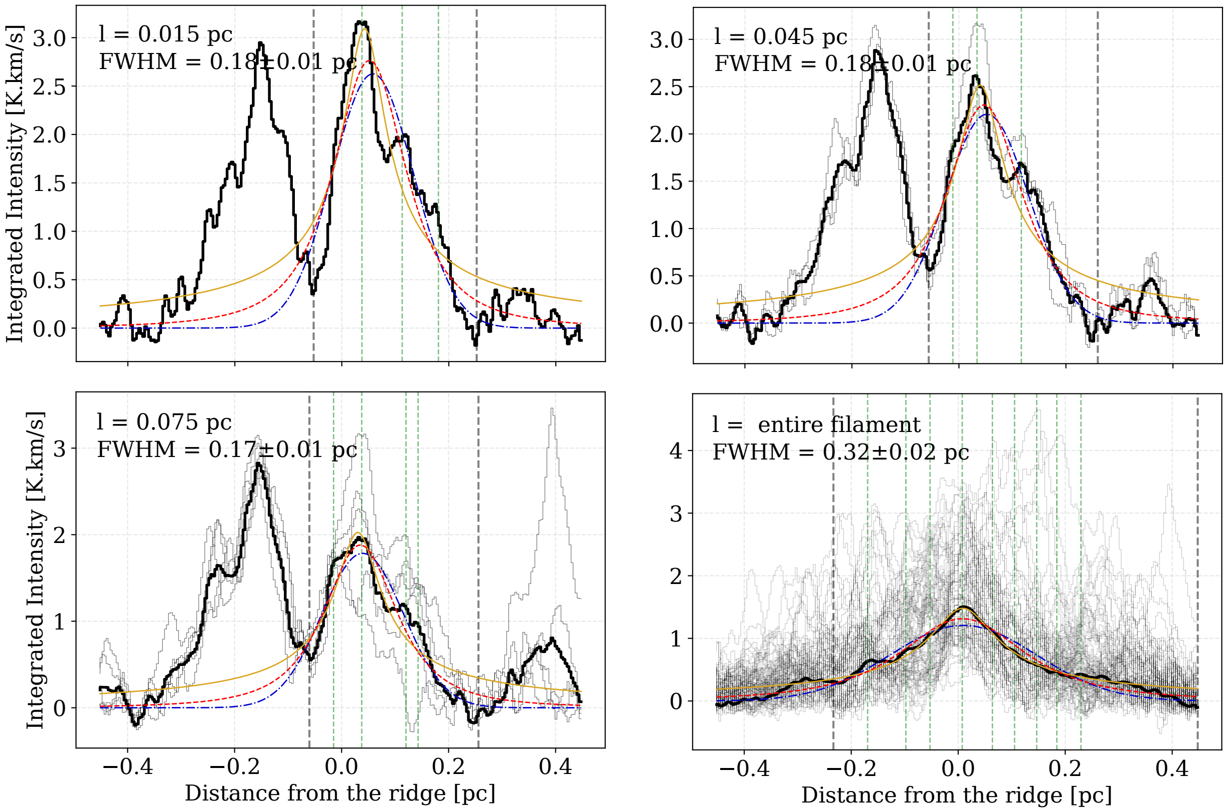

Fig. 4. Effect of averaging intensity profiles along different length scales. Individual intensity profiles are shown in gray, while averaged intensity profiles are shown in black. Blue, yellow, and red curves fitted to the averaged intensity profile (black) indicate Gaussian and Plummer-like fits with $p = 2$ and 4, respectively. The gray vertical dashed lines indicate the fitting boundaries and the green vertical dashed lines indicate the shoulders identified by `FilChaP`. *From top left to bottom right panels*: profiles are averaged over 0.015, 0.045, 0.075 pc and the entire filament with corresponding Gaussian FWHM of 0.18, 0.18, 0.17 and 0.32 pc.

not isolated homogeneous cylinders. They may have variations along their length that are not taken into account if the entire filament is represented by an averaged number. In Fig. 6 we show an example of how the width changes along a single filament. In the left panel, we plot the slice number along the filament (cross-sections for radial intensity profiles) against the calculated width at the corresponding slice. The Plummer $p = 2$ fit yields narrower widths along the filament, this agrees with the general picture that we have drawn from Fig. 5. The right panel shows four subplots corresponding to four intensity profiles along the filament that are marked by "a", "b", "c" and "d" in the left panel. These intensity profiles are selected to be representative of how the width changes. At point "a", the intensity profile is the narrowest and peaky with a width of 0.12 pc (Gaussian FWHM). As we progress from point "a" to "b" we see that the substructures (apparent at around 1 $\mathrm{K\,km\,s^{-1}}$, close to five times the noise level of the averaged profile) that appear at point "a" get wider, hence the width increases. At point "b" the intensity profile is broad and the width is the largest, reaching 0.2 pc. From point "c" to "d" the shoulders on both sides of the peak (shown in green dashed lines) get wider and acquire higher intensities, which in turn causes the increase in width. The unresolved inhomogeneities within the filament itself that can be traced by these shoulders in the profile cause the filament's width to vary.

3.2.1. Goodness of the fits

In order to assess the goodness of our radial intensity profile fits we calculate the reduced chi-squared values for each individual fit and for the three different methods that we employed. The reduced chi-squared is simply calculated as chi-squared per degree of freedom[5]. The resulting distributions of reduced chi-squared of all the fits are shown in the left panel of Fig. 7. The median reduced chi-squared values of our fits are 0.6 for the Gaussian and Plummer $p = 4$ fits, and 0.8 for the Plummer $p = 2$ fits. The reduced chi-squared value for a good fit is expected to be close to 1. However, by inspecting the intensity profiles and their corresponding reduced chi-squared values, we see that with the reduced chi-squared values up to 6, the fits still describe the underlying intensity profiles well. The right panel of Fig. 7 shows four different intensity profiles, overlaid with the calculated fits and the corresponding reduced chi-squared values for each fit. In both panels of the figure, blue, yellow, and red colors represent the Gaussian, Plummer with $p = 2$ and Plummer with $p = 4$ fits. Profiles with blending structures or extended shoulders such as the example shown in the bottom right subplot leads to poor fits with high reduced chi-squared ($\chi^2_R > 6$). For the Gaussian fits, 98% of the reduced chi-squared values lie between zero and six,

[5] We have three degrees of freedom per fit; the amplitude, mean, and standard deviation (or $R_{\rm flat}$ for the Plummer fits).

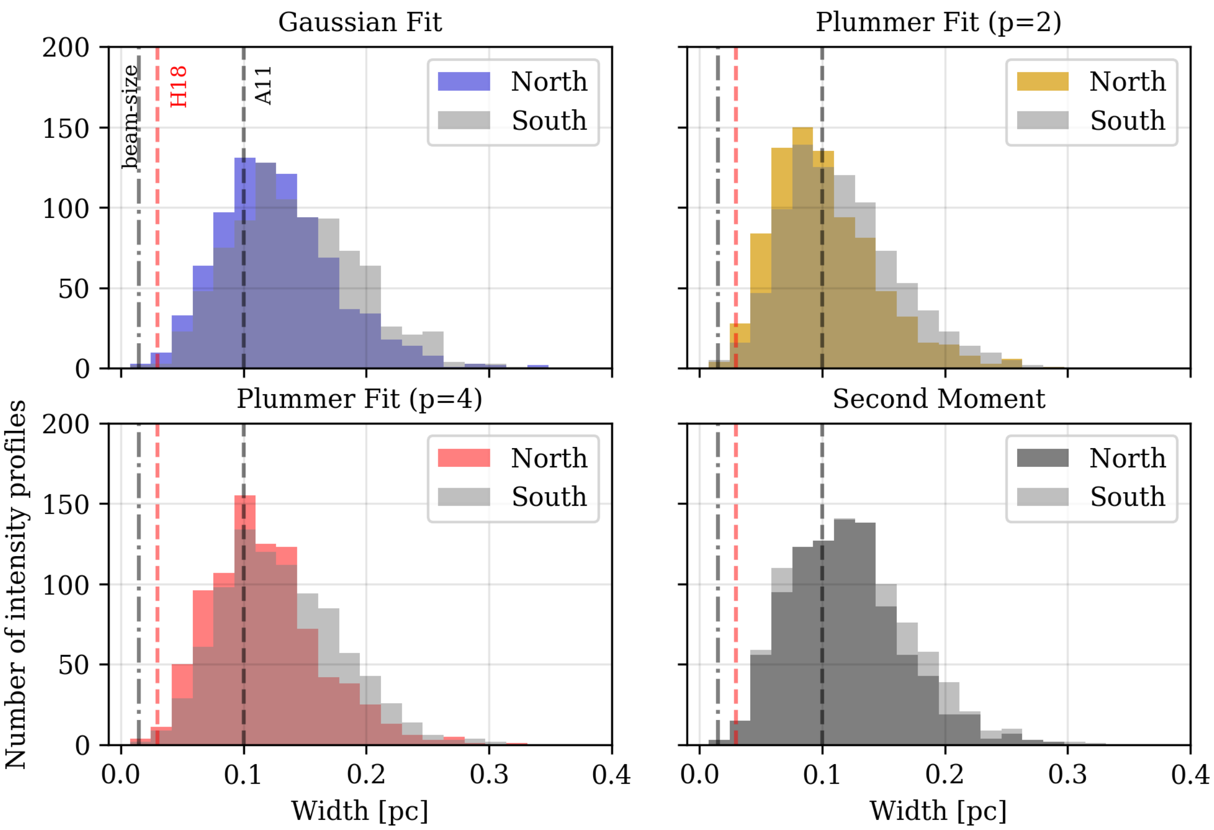

Fig. 5. Distribution of filament widths in the norther (colored) and southern (gray) regions of Orion A (see Fig. 2) calculated using Gaussian fits (*top left panel*), the second moment of distribution (*bottom right panel*), and Plummer-like fits with power law indices $p = 2$ (*top right panel*) and $p = 4$ (*bottom left panel*). The vertical dashed lines represent the filament widths from Hacar et al. (2018) in red, and the "characteristic" filament width (Arzoumanian et al. 2011) in black. The dot-dashed line indicates the beam-size of our observations.

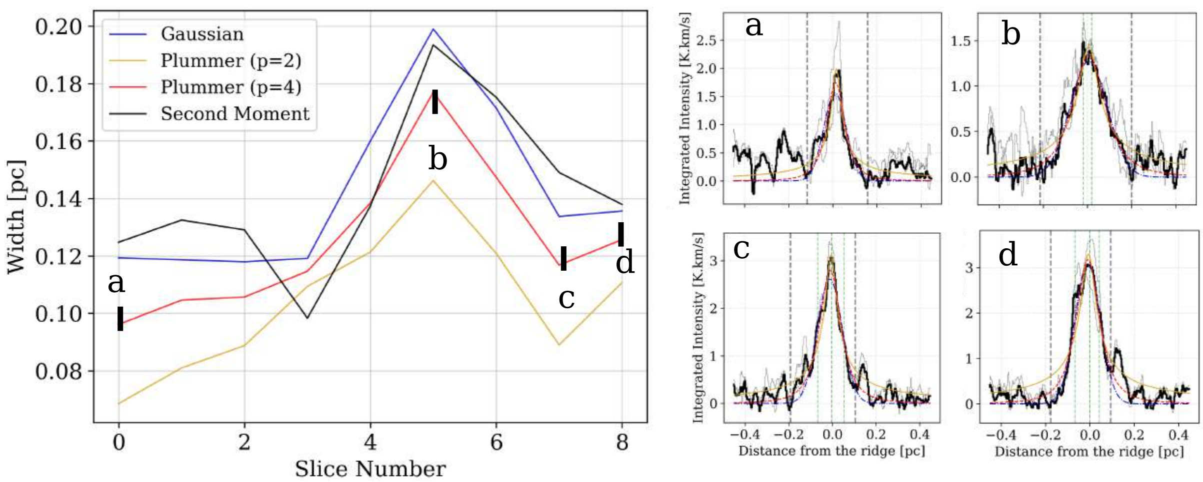

Fig. 6. *Left panel*: variation of filament width along the length of a single filament taken as an example. The slice numbers correspond to different positions along the filament. Each slice shown here represents the averaged value over two consecutive perpendicular cuts. These slices are always separated by 1.5 beamsizes (0.0225 pc) and the length of the filament is 0.4 pc. *Right panel*: selected intensity profiles at points "a", "b", "c", and "d" show in the left panel. These points are selected to best represent the variation of the width along the filament. Vertical gray dashed lines indicate the boundaries of the fits while the green dashed lines indicate the shoulders of the profiles.

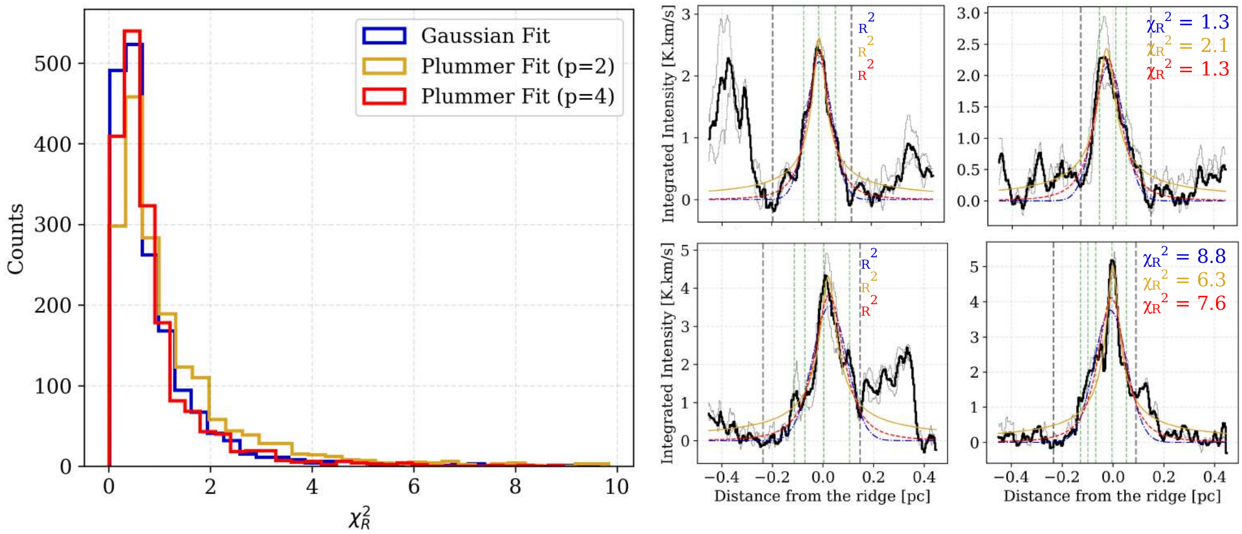

Fig. 7. *Left panel*: χ_R^2 values for each radial intensity profile fit for the different methods used in the width determination. *Right panels*: four examples of profiles with different reduced chi-squared values. *Bottom right panel*: example of a fit discarded due to its large reduced chi-squared.

while this value is 97% for the Plummer $p = 2$ and 99% for Plummer $p = 4$ fits. We confirm by eye that the tail of the reduced chi-squared distribution ($\chi_R^2 > 6$) corresponds to questionable fits. The reason for this is the complexity of the intensity profiles. As the width of these profiles are hard to estimate, they are discarded from further analysis. We note that the reduced chi-squared criterion applies for the Gaussian and Plummer fits individually; a profile can have a good reduced chi-squared for Plummer $p = 2$ fit but not for the Gaussian, and in this case only the Plummer $p = 2$ width is accounted for. As we do not have a reduced chi-squared value for the widths calculated from the second moment method, we take those second moment widths where the reduced chi-squared criterion is satisfied in all the other three methods.

3.2.2. Dependence on the fitting range

Arzoumanian et al. (2011) and later studies of filaments (e.g. André et al. 2016; Federrath et al. 2016) refrain from fitting the wings of the column density profiles, and the fitted inner range of the profiles is always the same for each and every column density slice. Smith et al. (2014) and Panopoulou et al. (2017) show that a correlation between the fitting range and the calculated width of these profiles exists. This correlation is not unexpected. Depending on the portion of the profiles that is fitted, the larger the fitted area, the wider the width of the profile will be. This behavior arises from the fact that the filament profiles are not isolated. Therefore, the larger the fitting range, the more emission the function will try to fit. In an ideal case, where the baseline was perfectly smooth, the fitting range should not affect the width of the distribution. In real observed data, however, the filament profile is accompanied by extended emission as well as emission from nearby filaments and hubs. Hence, a linear correlation between the fitting range and the resulting width is inevitable. To be as independent of this bias as much as possible, instead of forcing a fixed boundary for our fits, we calculate a unique fitting range for every individual profile. This is done automatically within `FilChaP` by looking for minima around the peak intensity of the filament. If the minima have a significance of three beam sizes (which corresponds to a well resolved nearby or blended structure) their locations mark the boundaries for the fitting range. In this approach, each profile has its own fitting range which depends on the filament's environment.

Figure 8 shows the correlation between the fitting ranges for each individual profile and the derived widths based on the four different methods. The scattered points are colored by the χ^2 of each fit, except for the second moment widths, as those are not fitted but calculated directly from the distribution. The red diagonal lines correspond to a 1:1 relation between the two axes. The strongest correlation between the fitting range and the width is for the case of the second moment (bottom right panel). This is purely because the second moment is calculated based on the boundaries of the distribution, so that the larger the distance between the boundaries the larger is the width. As is also seen from this panel, the second moment width of the distribution cannot be larger than the fitting range. For the Gaussian and Plummer fits, the widths can occasionally be larger than the fitting range, these are the points that lay above the 1:1 correlation line. These points are excluded from the analysis as they originate from profiles with multiple peaks that are not straightforward to analyze.

Of the four different methods used to calculate the filament widths, the Plummer ($p = 2$) fit seems to be the most independent of the fitting range as it shows the shallowest increase with the increasing fitting range. However, as can be seen in the various intensity profiles shown in Figs. 3 and 7, the Plummer ($p = 2$) only fits the very inner portion of the profile. This is acceptable when one has multiple peaks, but it excludes the information on the wings of the profile. This is the reason why the widths calculated from the Plummer ($p = 2$) are always narrower and less dependent on the fitting range than the ones estimated from the other methods. Furthermore, because it fits a substructured profile better, it has fewer points above the 1:1 relation between the fitting range and width. However, we refrain from drawing conclusions of filaments' state of isothermality based on the power-law indices of the Plummer fits, because the difference between the $p = 2$ and $p = 4$ seem to be sensitive to, at least in

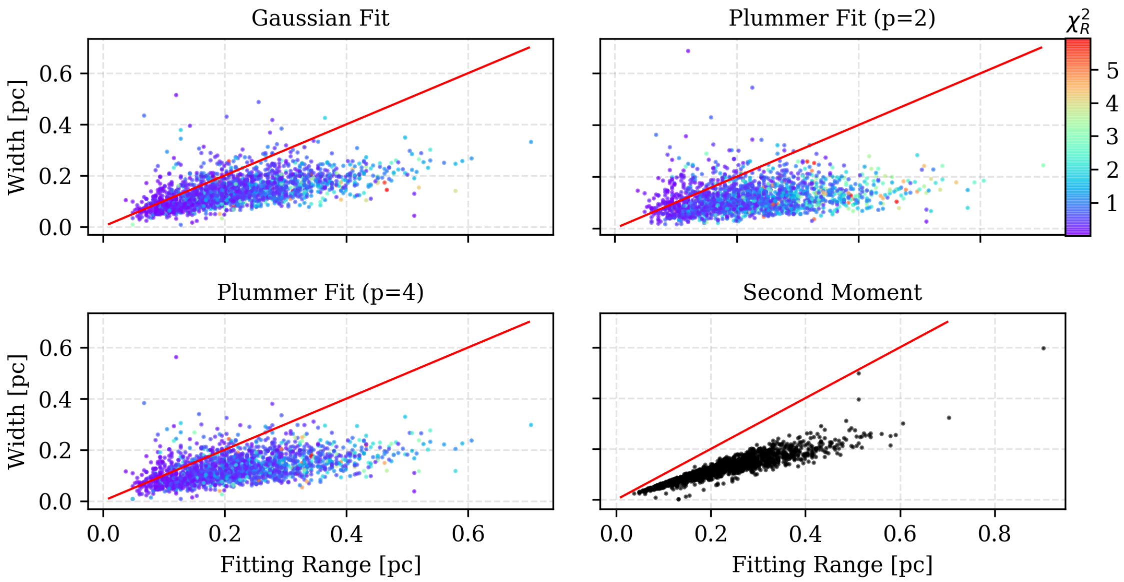

Fig. 8. Correlation between the calculated filament widths and the fitting range on the radial intensity profile over which the width is calculated. The red diagonal line shows the 1:1 correlation between the two parameters. The strongest correlation is observed when instead of the fits, the second moment of the distribution is used. The color bar indicates the reduced chi-squared values for the fits. There is also a slight correlation between the reduced chi-squared and the fitting range.

this work, the amount of background emission observed toward individual filaments.

4. Discussion

4.1. Variation of the filament width across the cloud

As shown in Fig. 6 we see that the filament width varies even along a single filament. This variation is often caused by blending structures. Close to hubs, where filaments meet, the intensity profiles get wider as many structures merge into one another. We followed the variation of width along each filament by plotting the width (Gaussian FWHM) on the $C^{18}O$ map[6]. This spatial variation is shown on the left hand side of Fig. 9 with the points along each filament colored by the width calculated at that point. The corresponding colorbar indicates the calculated width. In order to demonstrate the complexity of the radial intensity profiles we also calculate the number of shoulders identified in each profile. The shoulders appear as bumps within the boundaries within which we calculate the width of the filaments, further proving that these radial profiles are not simple single-component Gaussians. Examples of the intensity profiles with detected shoulders are shown in the right hand panels of Fig. 7. In this example, the boundaries are shown with the gray dashed lines that clearly separate the emission of the filament from a nearby structure that appears at around 0.2 pc (bottom right subplot). The green dashed lines indicate the locations of the detected shoulders that correspond to bumps within the filament profile that are not significant enough to be separate structures. Up to this point, we have qualitatively shown that filament profiles are substructured and complex which in turn leads to variation of filament widths. A possible correlation between the number of shoulders, the locations of filaments, and the filament widths would indeed allow us to study this phenomenon quantitatively. We plot the identified filaments on the $C^{18}O$ peak intensity map, this time with each point colored by the number of shoulders detected in the corresponding intensity profile. Figure 9 shows how this number changes along the filaments and across the cloud.

Figure 9 suggests a clear correlation between the filament width and the number of shoulders. To demonstrate this correlation better, in Fig. 10 we show the detected number of shoulders plotted against the corresponding widths of each individual profile. The data points are plotted as gray circles, and their median values are shown as red and blue filled circles for the northern and the southern regions of the map, respectively. The error bars on the median values indicate the interquartile range. The majority of the filament profiles have at least one shoulder detected. The existence of such highly complex intensity profiles implies that filaments are not perfectly isolated cylinders, but that they have substructures within them. Figure 10 clearly shows that there is a linear correlation between the number of shoulders and the width: the higher the number of shoulders, the wider is the calculated width. Clarke et al. (2017) suggest that filaments may retain wide widths even when supercritical, due to substructure. This substructure lessens the global effects of gravity and produces wider filaments. The linear correlation we find in Fig. 10 supports this view. This correlation suggests widths of 0.09 ± 0.02 and 0.12 ± 0.01 pc for filaments without shoulders, for the northern and southern region, respectively.

4.2. Lack of correlation between filament width and column density

To account for the variation of the filament width throughout the ISF, we also checked for a possible (anti-)correlation between the column density along the filaments and their width. Figure 11 shows the central column density at every point along the spine of the filaments plotted against the corresponding width at that

[6] The relative width between the slices of a filament is meaningful no matter which method is used (see Appendix A).

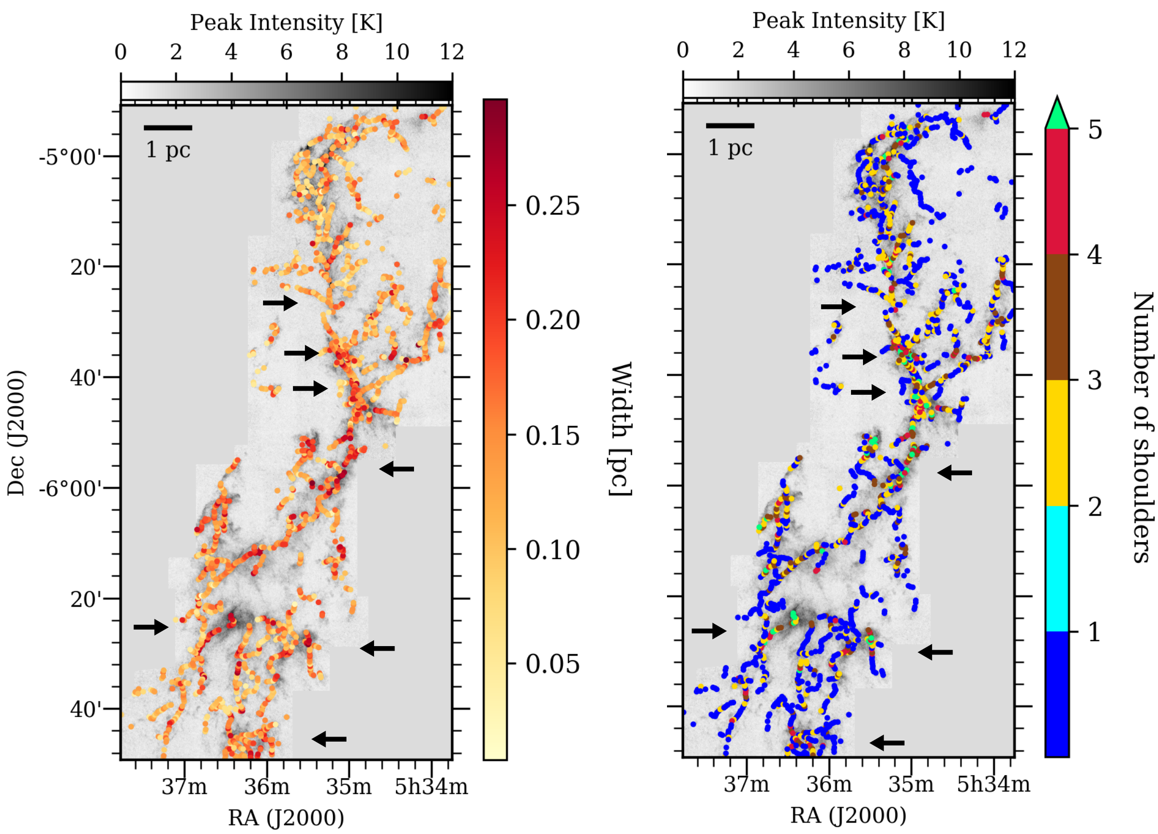

Fig. 9. Filament width (*left panel*) and number of shoulders (*right panel*) for the filaments identified in Orion A overlayed on the $C^{18}O$ peak intensity map. The color of each point along filaments represents the width (*left panel*) and the number of shoulders (*right panel*) at that point, corresponding to the colorbar shown in the right side of the panels. The arrows indicate the positions of hubs at which the filaments converge.

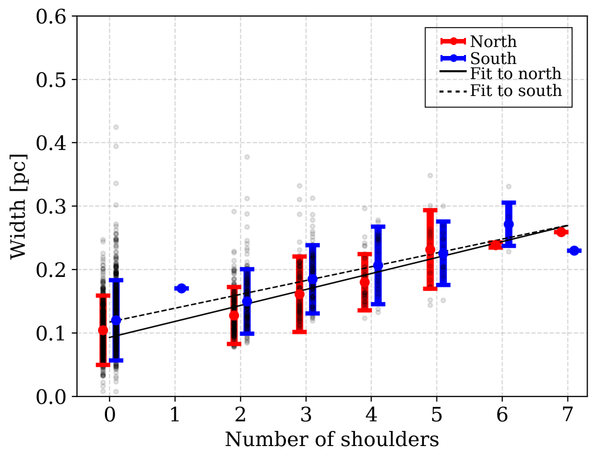

Fig. 10. Variation of the filament width with respect to detected number of shoulders in the corresponding intensity profile. The gray circles represent the data points, the red and blue filled circles are the median values. The shown error bars on the median values represent the interquartile range.

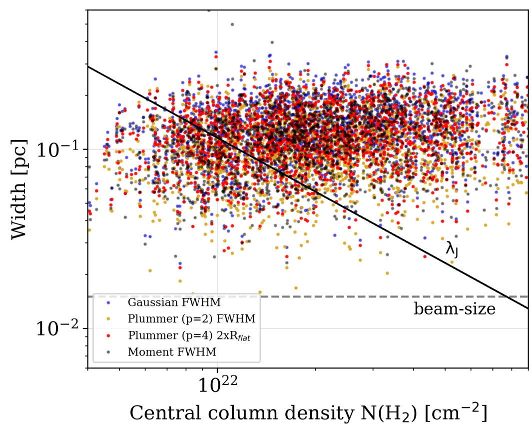

Fig. 11. Filament widths calculated using the four different methods plotted against the central column density at each point where the width is calculated. The colors represent FWHM of Gaussian fits (blue), moment analysis (black), Plummer $p = 2$ (yellow) and $p = 4$ (red). The dashed line represents the resolution of our observations and the solid diagonal line the thermal Jeans length at 10 K.

point calculated using different methods. The column density of each pixel along the identified filaments is taken from the *Herschel* dust column density map published in Stutz & Kainulainen (2015). Ideally, if the filaments are super-critical, and thus gravity-dominated (right hand side of the λ_J line where λ_J is the Jeans length at 10 K; $\lambda_J = c_s^2/G\mu_H\Sigma_0$ where Σ_0 is the central column density; Arzoumanian et al. 2011), they would contract to fragment and form cores, hence leading to an anticorrelation between the width and the central column density. However, this does not appear to be the case. This lack of anticorrelation has been found by Arzoumanian et al. (2011) in low-mass star forming regions; Aquila, IC5146 and Polaris. We confirm that even in a high-mass star forming region that is as active and complex as Orion A, the decoupling of filament widths from the central column densities of the filament spine persists. We propose the width variation along filaments is indeed mostly regulated by environmental effects, that is, their positions relative to the hubs and whether the filaments are rather isolated or are connected to or disconnected from surrounding structures.

Arzoumanian et al. (2011) speculate that the decorrelation of the width and central column density can be explained with turbulent filament formation through compression (e.g. Padoan et al. 2001) for the subcritical filaments, and the super-critical filaments may be able to maintain an approximately constant width if they are continuously accreting from their surroundings. Following Arzoumanian et al. (2011), Heitsch (2013) study gravitational infall onto isothermal filaments that are subject to external pressure to see for which conditions the filament width can be independent of the column density. Their model that best fits the lack of correlation seen in observations is for the magnetized filaments that are subject to varying external pressure due to ram pressure exerted by the infalling material. Our results in Fig. 11 can be directly compared to the results in Heitsch (2013), particularly their Fig. 4. Even though their best fitting model represents the majority of our data points, we see no decrease in filament width toward higher column densities up to 10^{23} cm^{-2} as the model predicts.

5. Conclusions

We present a study of the filament properties in the Orion A molecular cloud as seen in the emission of the dense gas tracer $C^{18}O$, produced by the CARMA-NRO Orion Survey (Kong et al. 2018). We identified 625 filaments in the 3D datacube (PPV) using the DisPerSE algorithm. In this first paper, which will be followed by a series of papers including the analysis of filament kinematics and filament properties in different tracers (^{13}CO, dust and C^+), we investigated the physical properties of filaments with an emphasis on the filament width.

Based on the shortcomings of the methods that led to the identification of a "universal" filament width, criticized in previous works by Smith et al. (2014) and Panopoulou et al. (2017) we developed an improved and automated method to study characteristics of filaments; `FilChaP`, a python based algorithm. In this method, while calculating the filament widths: (i) the radial intensity profiles are not averaged over the length of an entire filament, but over a number of consecutive slices that represent a region three beam-sizes in length, (ii) there is no fixed fitting range for these profiles that would force a prefixed width. Instead, each profile has its own fitting range. This range is set by the minima around the peak emission from the filament. The minima are required to have a significance of three beam-sizes, (iii) we used four different methods to derive filament widths; with a Gaussian fit, two Plummer-like fits with $p = 2$ and $p = 4$, and the FWHM derived from the second moment of the intensity distribution and (iv) we judge the goodness of each fit by looking at their reduced chi-squared values to prevent "poor" fits biasing the results. We find the following key points:

– The median filament widths are $0.14^{+0.03}_{-0.02}$ and $0.16^{+0.04}_{-0.03}$ pc for the Gaussian fits, $0.11^{+0.03}_{-0.02}$ and $0.13^{+0.04}_{-0.03}$ pc for the Plummer $p = 2$ fits, $0.13^{+0.03}_{-0.03}$ and $0.14^{+0.03}_{-0.03}$ pc for the Plummer $p = 4$ fits, and finally, $0.13^{+0.03}_{-0.03}$ and $0.14^{+0.04}_{-0.03}$ pc for the FWHM derived from the second moment for the northern and southern regions, respectively.
– The width, regardless of the method used, is not correlated with the central column density. Although there is more than an order of magnitude scatter in width, neither sub nor super-critical filament widths are coupled to the column density. The Heitsch (2013) model with magnetized and externally pressured filaments best reproduces the observed decorrelation. The model agrees with our observations except for high column densities (10^{23} cm^{-2}) where narrower widths are predicted. We found that even at these high column densities traced by our filaments the lack of correlation persists, however, we note that we have a statistically smaller sample at the higher column density end. Accreting filaments in a magnetized environment similar to Heitsch (2013) model are already observed in Taurus (e.g. Palmeirim et al. 2013) with striations of material perfectly aligned with the magnetic field surrounding the main filament. A similar analysis using, for example, BISTRO polarization data (Pattle et al. 2017) can be conducted with the CARMA-NRO Orion Survey data in a future study.
– Given the lack of correlation with the column density, we attribute the gradient of the widths all across the cloud to the fact that the filaments are not isolated, homogeneous structures. They are composed of substructure, surrounded by nearby filaments and they form hubs. Connected and disconnected filaments have fluctuating widths. We find that the majority of filaments closer to the star forming hubs have larger widths. We quantify the complexity of the intensity profiles by looking at the number of shoulders that each profile has. This examination reveals a linear relation between the filament widths and the number of shoulders. From this linear relation we obtain widths of 0.09 ± 0.02 and 0.12 ± 0.01 pc for a filament with no substructure in northern and southern Orion A, respectively. We suggest that the complexity of the intensity profiles contribute significantly to the spread of the filament width distribution.
– The majority of the identified filaments do not resemble the fibers reported in a study toward the Taurus molecular cloud which spatially overlap but are distinct coherent structures in velocity space along the line-of-sight (Hacar et al. 2013). The only fiber-like filaments we find are located in the OMC-4 region where we observe clear multiple velocity components along the line of sight that form coherent structures. The fact that the filaments identified in N_2H^+ toward the northern ISF by Hacar et al. (2018) and the majority of the filaments identified in this study do not show a spatial overlap implies that the general picture of the filamentary structure in Orion A may differ from what has been observed toward the low mass star forming region Taurus.

Acknowledgements. We thank the referee for their insightful comments that helped improve this manuscript and FilChaP. S.S., A.S.M., P.S. and V.O.O. acknowledge funding by the Deutsche Forschungsgemeinschaft (DFG) via the Sonderforschungsbereich SFB 956 Conditions and Impact of Star Formation (subprojects A4, A6, C1, and C3) and the Bonn-Cologne Graduate School. S.D.C. acknowledges support from the ERC starting grant No. 679852 RAD-FEEDBACK. R.J.S. gratefully acknowledges support from an STFC Ernest Rutherford fellowship. This research was carried out in part at the Jet Propulsion Laboratory which is operated for NASA by the California Institute of Technology. P.P. acknowledges support by the Spanish MINECO under project AYA2017-88754-P (AEI/FEDER,UE). H.G.A. and S.K. acknowledge support from the National Science Foundation through grant AST-1140063. H.G.A. and

S.K. acknowledge support from the National Science Foundation through grant AST-1140063. Software: astropy (Price-Whelan et al. 2018), matplotlib (Hunter 2007), scipy (Jones et al. 2001), pandas (McKinney 2010), APLpy (Robitaille & Bressert 2012).

References

André, P. 2017, C. R. Geosci., 349, 187
André, P., Men'shchikov, A., Bontemps, S., et al. 2010, A&A, 518, L102
André, P., Revéret, V., Könyves, V., et al. 2016, A&A, 592, A54
Arzoumanian, D., André, P., Didelon, P., et al. 2011, A&A, 529, L6
Bally, J., Langer, W. D., Stark, A. A., & Wilson, R. W. 1987, ApJ, 312, L45
Chira, R.-A., Kainulainen, J., Ibáñez-Mejía, J. C., Henning, T., & Mac Low, M.-M. 2018, A&A, 610, A62
Clarke, S. D., & Whitworth, A. P. 2015, MNRAS, 449, 1819
Clarke, S. D., Whitworth, A. P., & Hubber, D. A. 2016, MNRAS, 458, 319
Clarke, S. D., Whitworth, A. P., Duarte-Cabral, A., & Hubber, D. A. 2017, MNRAS, 468, 2489
Duarte-Cabral, A., & Dobbs, C. L. 2016, MNRAS, 458, 3667
Eilers, P. H. C. 2003, Anal. Chem., 75, 3631
Federrath, C., Rathborne, J. M., Longmore, S. N., et al. 2016, ApJ, 832, 143
Fiege, J. D., & Pudritz, R. E. 2000, MNRAS, 311, 85
Fischera, J., & Martin, P. G. 2012, A&A, 542, A77
Grossschedl, J. E., Alves, J., Meingast, S., et al. 2018, A&A, 619, A106
Hacar, A., Tafalla, M., Kauffmann, J., & Kovács, A. 2013, A&A, 554, A55
Hacar, A., Tafalla, M., Forbrich, J., et al. 2018, A&A, 610, A77
Heitsch, F. 2013, ApJ, 776, 62
Henshaw, J. D., Jiménez-Serra, I., Longmore, S. N., et al. 2017, MNRAS, 464, L31
Hunter, J. D. 2007, Comput. Sci. Eng., 9, 90
Inutsuka, S.-I., & Miyama, S. M. 1992, ApJ, 388, 392
Johnstone, D., & Bally, J. 1999, ApJ, 510, L49
Jones, E., Oliphant, T., Peterson, P., et al. 2001, SciPy: Open source scientific tools for Python
Juvela, M., Ristorcelli, I., Pagani, L., et al. 2012, A&A, 541, A12
Kainulainen, J., Stutz, A. M., Stanke, T., et al. 2017, A&A, 600, A141
Koch, E. W., & Rosolowsky, E. W. 2015, MNRAS, 452, 3435
Koda, J., Sawada, T., Wright, M. C. H., et al. 2011, ApJS, 193, 19
Kong, S., Arce, H. G., Feddersen, J. R., et al. 2018, ApJS, 236, 25
Könyves, V., André, P., Men'shchikov, A., et al. 2015, A&A, 584, A91
Kounkel, M., Hartmann, L., Loinard, L., et al. 2017, ApJ, 834, 142
Lada, C. J., Alves, J., & Lada, E. A. 1999, ApJ, 512, 250
Larson, R. B. 1985, MNRAS, 214, 379
McKinney, W. 2010, in Proceedings of the 9th Python in Science Conference, eds. S. van der Walt, & J. Millman, 51
Nakamura, F., Miura, T., Kitamura, Y., et al. 2012, ApJ, 746, 25
Ostriker, J. 1964, ApJ, 140, 1529
Padoan, P., Juvela, M., Goodman, A. A., & Nordlund, Å. 2001, ApJ, 553, 227
Palmeirim, P., André, P., Kirk, J., et al. 2013, A&A, 550, A38
Panopoulou, G. V., Tassis, K., Goldsmith, P. F., & Heyer, M. H. 2014, MNRAS, 444, 2507
Panopoulou, G. V., Psaradaki, I., Skalidis, R., Tassis, K., & Andrews, J. J. 2017, MNRAS, 466, 2529
Pattle, K., Ward-Thompson, D., Berry, D., et al. 2017, ApJ, 846, 122
Pon, A., Toalá, J. A., Johnstone, D., et al. 2012, ApJ, 756, 145
Price-Whelan, A. M., Sip'ocz, B. M., Günther, H. M., et al. 2018, AJ, 156, 123
Robitaille, T., & Bressert, E. 2012, Astrophysics Source Code Library [record ascl:1208.017]
Sánchez-Monge, Á., Beltrán, M. T., Cesaroni, R., et al. 2014, A&A, 569, A11
Sánchez-Monge, Á., Schilke, P., Ginsburg, A., Cesaroni, R., & Schmiedeke, A. 2018, A&A, 609, A101
Schneider, N., Csengeri, T., Hennemann, M., et al. 2012, A&A, 540, L11
Seifried, D., & Walch, S. 2015, MNRAS, 452, 2410
Shimajiri, Y., Takahashi, S., Takakuwa, S., Saito, M., & Kawabe, R. 2009, PASJ, 61, 1055
Shimajiri, Y., Kitamura, Y., Saito, M., et al. 2014, A&A, 564, A68
Smith, R. J., Glover, S. C. O., & Klessen, R. S. 2014, MNRAS, 445, 2900
Smith, R. J., Glover, S. C. O., Klessen, R. S., & Fuller, G. A. 2016, MNRAS, 455, 3640
Sousbie, T. 2011, MNRAS, 414, 350
Stutz, A. M., & Kainulainen, J. 2015, A&A, 577, L6
van der Werf, P. P., Goss, W. M., & O'Dell, C. R. 2013, ApJ, 762, 101

[1] I. Physikalisches Institut, Universität zu Köln, Zülpicher Str. 77, 50937 Köln, Germany
e-mail: suri@mpia.de
[2] Jodrell Bank Centre for Astrophysics, School of Physics and Astronomy, University of Manchester, Oxford Road, Manchester M13 9PL, UK
[3] Zentrum für Astronomie, Universität Heidelberg, Albert-Ueberle-Str. 2, 69120 Heidelberg, Germany
[4] Institut de Ciències del Cosmos, Universitat de Barcelona, IEEC-UB, Martí i Franquès 1, 08028 Barcelona, Spain
[5] ICREA, Pg. Lluís Companys 23, 08010 Barcelona, Spain
[6] Jet Propulsion Laboratory, California Institute of Technology, 4800 Oak Grove Drive, Pasadena, CA 91109, USA
[7] Department of Astronomy, Yale University, New Haven, CT 06511, USA
[8] Department of Astrophysical and Planetary Sciences, University of Colorado, Boulder, CO, USA
[9] Joint ALMA Observatory, Alonso de Córdova 3107, Vitacura, Santiago, Chile
[10] National Radio Astronomy Observatory, 1003 Lopezville Road, Socorro, NM 87801, USA
[11] NRC Herzberg Astronomy and Astrophysics, 5071 West Saanich Road, Victoria, BC V9E 2E7, Canada
[12] Department of Physics and Astronomy, University of Victoria, Victoria, BC V8P 5C2, Canada
[13] Haystack Observatory, Massachusetts Institute of Technology, 99 Millstone Road, Westford, MA 01886, USA
[14] Sorbonne Université, Observatoire de Paris, Université PSL, CNRS, LERMA, 75014 Paris, France
[15] Cahill Center for Astronomy and Astrophysics 301-17, California Institute of Technology, Pasadena, CA 91125, USA
[16] East Asian Observatory, 660 N. A'ohoku Place, Hilo, HI 96720, USA
[17] Max-Planck-Institut für Radioastronomie, Auf dem Hügel 69, 53121 Bonn, Germany
[18] Max-Planck-Institut für extraterrestrische Physik, Giessenbachstrasse 1, 85748 Garching, Germany
[19] School of Physics and Astronomy, Cardiff University, Cardiff CF24 3AA, UK

Appendix A: `FilChaP`: filament characterization package

`FilChaP` is a python-based software package that can be used to characterize physical properties of filaments. `FilChaP` derives radial intensity profiles perpendicular to filament spines from which it calculates filament width, skewness and kurtosis. In addition, `FilChaP` can also calculate filament length and curvature, as well. The algorithm is publicly available for download[7]. The download folder includes a python tutorial with an example filament skeleton and a 3D fits cube which the users can utilize to run FilChaP and derive filament properties. The version of `FilChaP` used to produce the results in this paper has a specific DOI[8] and is archived on Zenodo.

`FilChaP` requires filament coordinates as an input file to derive information on filaments. For this particular study, we have used the output filaments of DisPerSE. These output filaments are simple ASCII files indicating filament ID, x-coordinate (RA), y-coordinate (Dec), z-coordinate (velocity channel). These four parameters are given for each point along a filament. If the filaments are identified on a 2D map instead, then the z-coordinate that corresponds to the velocity channel does not exist in the output file and is not required by `FilChaP`, and the code can be used in 2D mode.

The filament width calculation method, as it is the main focus of this study, is explained thoroughly in Sect. 3.1. Below we explain the baseline removal method used, and present "synthetic" filament networks, which we constructed with known widths for the purpose of testing `FilChaP`.

A.1. Baseline subtraction

`FilChaP` uses asymmetric least squares smoothing (AsLS) method for baseline subtraction (Eilers 2003). A commonly used way of achieving a baseline is to smooth the profile until peaks or dips of interest are no longer prominent. The most common smoothing method is the least square method which minimizes the deviations of the smooth counterpart h, from the noisy data, f. The least square method weighs both negative and positive deviations of h from f the same. In the AsLS method however, deviations from the estimated baseline are weighted asymmetrically, with the positive deviations being weighted less. Because if $f - h$ is a good representation of f's baseline, the deviations should always be positive ($f > h$) due to the fact that f will always have signal (peaks) that take values higher than h.

Figure A.1 shows an example of the baseline subtraction process. On the left panel a representative intensity profile with a baseline gradient is shown. This gradient has to be removed before `FilChaP` can fit a function to calculate its FWHM. The different shades of solid red lines represent the AsLS baselines, h, calculated at different number of iterations. After only a few iterations the calculated weights quickly converge, hence a final baseline is obtained. The right panel of the plot shows the baseline subtracted profile. Eilers (2003) gives a `MATLAB` code for the iterative process of calculating the baselines, and this code is converted to `python`[9]. This python code is used by `FilChaP`. One possible drawback of the AsLS method is that once the baseline is removed a portion of the emission could go below zero. In the future we plan to use `STATCONT` to prevent this (Sánchez-Monge et al. 2018).

A.2. Tests on the width calculation method

Figure A.2 shows the generated filaments width equal widths (Case 1; top left), and unequal widths (Case 2; top right). The exercise here is to see whether in two different cases, (1) where all filaments have the same width and (2) where all filaments have a different width, `FilChaP` can recover the width distribution. Both cases have an amount of random Gaussian noise that is selected based on the peak intensity-to-noise ratio in our $C^{18}O$ integrated intensity map. In Case 1, all the filaments have a 25 pixel width. In the $C^{18}O$ map, 25 pixels correspond to a 0.1 pc filament width in spatial scales. For Case 2, we allowed filament width to vary between 5 and 85 pixels. This is to assess `FilChaP`'s performance in detecting extreme cases of narrow filaments and diffuse filaments. While for Case 1 we expect to find a distribution that is strongly peaked at around 25 pixels, for Case 2 we expect a wide distribution that has the contribution from all the different scales from 5 to 85 pixels. Figure A.3 shows the `FilChaP` width calculation result for Case 1 (top panel) and Case 2 (bottom panel). As anticipated, the width distribution for Case 1 has a narrow peak, with a mean of 26.5 ± 4.2 pixels (where the error corresponds to the 95% confidence level). For Case 2, we plot both the true input distribution of filament widths and the `FilChaP` output distribution. In order to quantify the association between the input and output width distributions for Case 2, we calculated Spearman's rank correlation coefficient. This coefficient gives a non-parametric measure of the relation between the two distributions which are connected with a monotonic function. The coefficient takes values between -1 and $+1$, where the coefficient takes a value of -1 in case of a perfect decreasing monotonic correlation, $+1$ in case of an increasing monotonic correlation and 0 in case of no correlation. The Spearman's rank coefficient between our the two distributions of Case 2 is 0.77; indicating a strong link between the two datasets. It is clear that the spread of the distribution for Case 1 comes from the errors of individual fits, and the fact that the filaments cross each other at various points throughout the map, which in turn introduces larger widths. For Case 2, in addition to large filament widths at crossing points and the fitting errors, the large spread comes from the underlying dissimilarities between the filament widths. In comparison, the two different cases produce significantly different width distributions that `FilChaP` successfully captures.

A.3. Additional functions

In addition to the filament width, `FilChaP` calculates filament skewness, kurtosis, length and curvature. The second moment of the intensity profiles is calculated to assess their FWHM, along with the second moment, the third and fourth moments; skewness and kurtosis are also calculated within the width calculation function of `FilChaP`. The length and curvature are calculated in separate functions, based on the filament spines extracted using DisPerSE.

A.3.1. Skewness and kurtosis

The skewness and kurtosis provide information about the shape of the intensity profiles. This shaped can be related to physical

[7] https://github.com/astrosuri/filchap
[8] https://doi.org/10.5281/zenodo.2222325
[9] https://stackoverflow.com/questions/29156532/python-baseline-correction-library/29185844

A&A 623, A142 (2019)

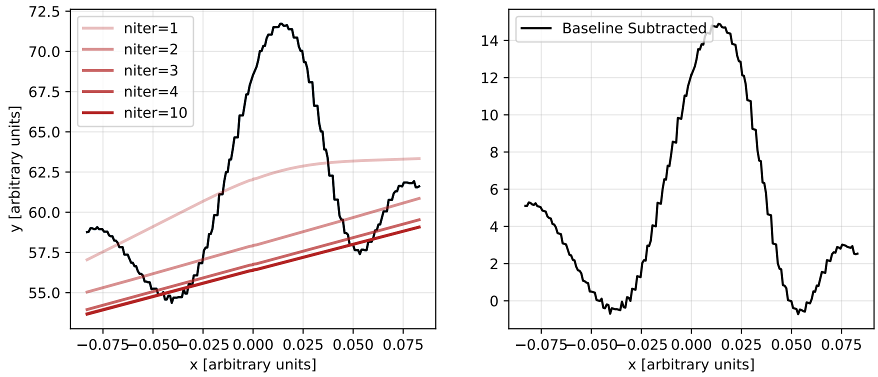

Fig. A.1. Example baseline subtraction process. *Left panel*: data with a baseline gradient is shown with the black solid curve. The curves with different shades of red represent the AsLS baselines calculated with different number of iterations. The solutions for the baseline converge rather quickly within ten iterations. *Right panel*: baseline subtracted profile.

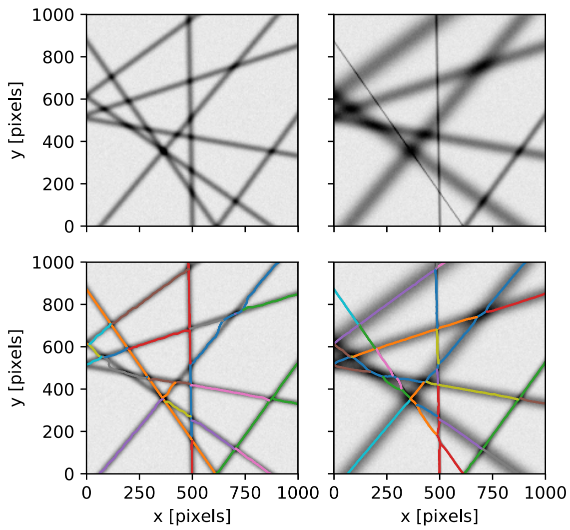

Fig. A.2. *Top panels*: synthetic filamentary network generated with prefixed filament widths on a 1000×1000 pixel grid. On the left, all the filaments have a same width of 25 pixels, while on the right, each filament has a different width that vary from 5 to 85 pixels (see Fig. A.3). *Bottom panels*: filaments identified by `DisPerSE`.

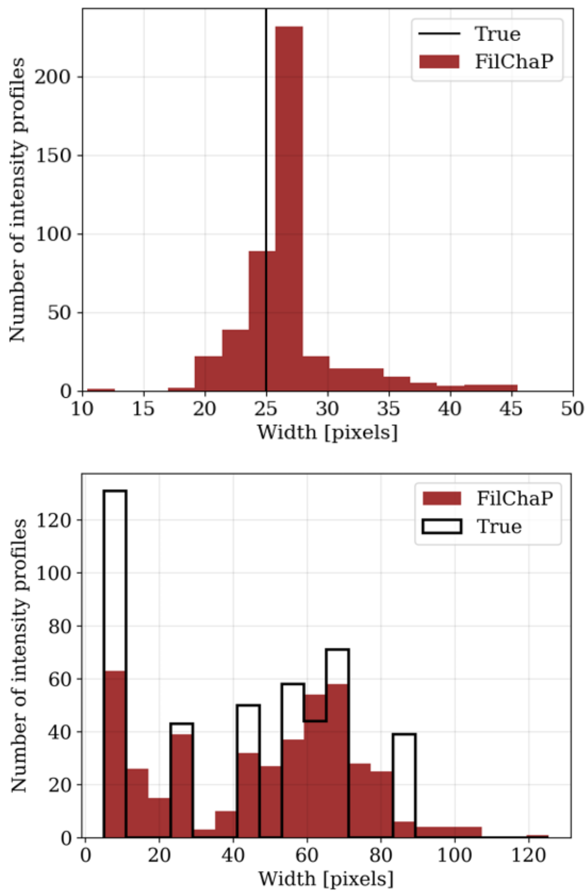

Fig. A.3. Distribution of filament widths for the test two cases presented in Fig. A.2. For Case 1 (*top panel*) the input widths of all the filaments are 25 pixels (solid black line) and the mean of the width distribution calculated with `FilChap` is 26.5 ± 4.2 pixels. For Case 2 (*bottom panel*), the true distribution of the input filament widths is given with the black histogram, and the width calculation that results using `FilChap` is given with the red histogram. The Spearman correlation coefficient between the two datasets is 0.77.

properties of the filaments and their environments. For example, if a filament is in a feedback region, we expect the intensity profile to be sharper on the side where the filament faces the direction of the feedback. Kurtosis, on the other hand, is a measure of peakiness. Therefore it can indicate locations of high-density, as the CO isotopologues may get optically thick, or in case of $C^{18}O$, freeze out that causes the profiles to flatten in the top. Figure A.4 demonstrates how we can detect the variations of skewness and kurtosis in Orion A. The two plotted intensity profiles are calculated from the ^{13}CO emission map and show slices across the Orion Bar, a well-known PDR and OMC-4, the dense star forming region, in green and gray, respectively. The direction of the feedback to the PDR from the Trapezium cluster is shown with a green arrow. The side of the PDR profile toward the feedback forms a sharp edge, whereas the side away from the feedback extends slowly. The OMC-4 ridge shows no such skewness as it is much less affected from the feedback. This plot also shows the difference between the peakiness of both profiles, which can then be quantified with the kurtosis parameter. The following paper on comparing filament properties in different tracers (Suri et al., in prep.) touches upon the PDR nature of the filaments in feedback regions and compares properties of intensity profiles using skewness and kurtosis analysis.

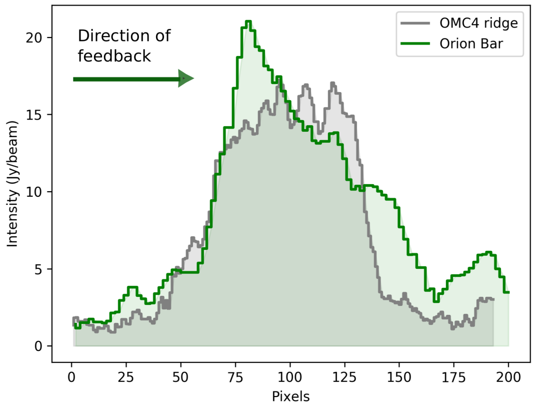

Fig. A.4. Comparison of two intensity profiles with different values of skewness and kurtosis. The intensity profile for the Orion Bar position is positive skewed with a tail to the right, while the intensity profile of the OMC4 ridge position is flat in the top resulting in a platykurtic or negative kurtosis distribution. `FilChaP` determines the skewness and kurtosis of the filament intensity profiles.

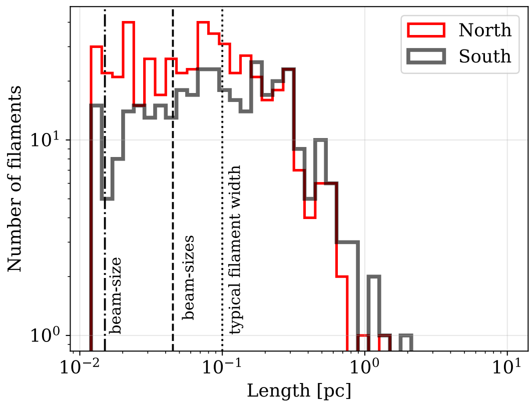

Fig. A.5. Distribution of filament lengths in the north (red) and south (black). The dot-dashed, dashed and the dotted lines respectively indicate a beam-size, three beam-sizes and the typical filament width found in this study.

A.3.2. Length and curvature

In order to obtain the filament length, `FilChaP` calculates the projected distances between the consecutive skeleton points along a filament. This is a projected distance, because in observational datasets we do not have a knowledge on the spatial third dimension of the filaments. In addition, the code offers calculating "kinkiness", or in other words; curvature, of filaments by comparing the calculated length of the filament to the distance between the start and end points. Therefore, we define curvature as $k = r/R$ where r is the distance between the end points and R is the calculated length of the filament. A k value of unity indicates a straight filament.

These two properties of filaments; length and curvature, are highly dependent on the parameters used to identify filaments with DisPerSE. Therefore, we note that the resulting statistics should be interpreted with caution. However, the credibility of these parameters can be improved in the future by testing different filament identification methods, comparing identified

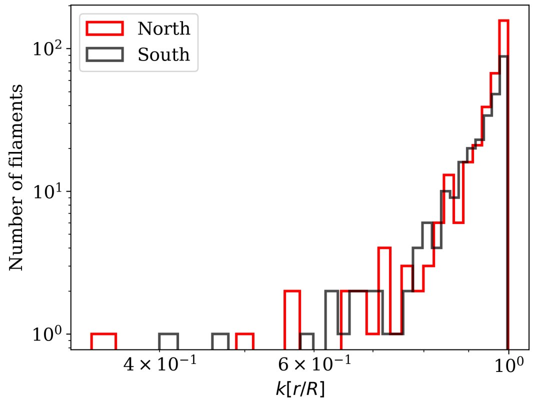

Fig. A.6. Distribution of filament kinkiness, k, where $k = r/R$ with r being the distance between the end points and R the calculated length of the filament. The majority of the filaments in Orion A are found to be unbent.

filamentary structures to one another, and using multiple tracers to assess the connection. Nevertheless, for the identified filaments in $C^{18}O$ using DisPerSE with the set of parameters explained in Sect. 3, we measured filament length between 0.03 and 1.8 pc. Figure A.5 shows the distribution of the resulting filament lengths for the northern (red) and southern Orion A (black). The dashed vertical line at 0.045 pc indicates three beam-sizes, and for the width calculations we discard the structures that are shorter than 0.045 pc.

The curvature values of filaments in Orion A north and south are shown in histograms in Fig. A.6. There are a few filaments that appear to be more bent, and have k values of between 0.3 and 0.9. The most bent filament in the north is located in OMC4 ridge. Majority of filaments, however, have very low curvature.

Appendix B: Additional material

In Sect. 3, we presented width distributions for all the identified filaments that are longer than three beam-sizes and are fitted with a reduced chi-squared less than six. Here, we reproduce Figs. 5, 10, and 11 considering different criteria on filament and profile selection. We look at the width distributions of (1) all filaments and intensity profiles fitted with a reduced chi-squared less than or equal to two, (2) filaments with aspect ratios larger than two and intensity profiles that are fitted with a reduced chi-squared less than or equal to six, (3) filaments with aspect ratios larger than two and intensity profiles fitted with a reduced chi-squared less than or equal to two. This different selection criteria are aimed to ensure that we do not introduce any bias in the determined widths when including all the filaments that are longer than three beam-sizes and have a reduced chi-squared less than six.

The width distributions for the cases mentioned above are shown in Fig. B.1 top, middle and bottom panels, respectively. For the majority of the cases, regardless of the criteria, the southern region of Orion A has filaments with larger widths as found in Fig. 5. The distribution of Plummer-like ($p = 2$) fits results in the most narrow median filament width ($0.08^{+0.12}_{-0.06}$ pc) when only those filaments with an aspect ratio larger than two and a reduced chi-squared value less than two is selected. The median filament widths for these

Table B.1. Median filament widths according to different selecting criteria (see Fig. B.1), and inferred filament width when no shoulders are identified in the intensity profile (intercept of the linear fits of Fig. B.2).

Criteria	Gaussian north/south	Plummer ($p = 2$) north/south	Plummer ($p = 4$) north/south	Second moment north/south	Intercept north/south
All, $\chi_R^2 \leq 6$	$0.12^{+0.15}_{-0.09}$ pc $0.14^{+0.18}_{-0.11}$ pc	$0.09^{+0.13}_{-0.07}$ pc $0.11^{+0.14}_{-0.08}$ pc	$0.11^{+0.14}_{-0.08}$ pc $0.13^{+0.16}_{-0.09}$ pc	$0.12^{+0.15}_{-0.09}$ pc $0.12^{+0.15}_{-0.09}$ pc	0.09 ± 0.02 pc 0.11 ± 0.01 pc
All, $\chi_R^2 \leq 2$	$0.12^{+0.15}_{-0.09}$ pc $0.14^{+0.18}_{-0.11}$ pc	$0.09^{+0.12}_{-0.07}$ pc $0.11^{+0.14}_{-0.08}$ pc	$0.11^{+0.14}_{-0.08}$ pc $0.12^{+0.16}_{-0.10}$ pc	$0.11^{+0.14}_{-0.08}$ pc $0.12^{+0.15}_{-0.08}$ pc	0.10 ± 0.01 pc 0.11 ± 0.01 pc
$R > 2$, $\chi_R^2 \leq 6$	$0.12^{+0.15}_{-0.09}$ pc $0.13^{+0.17}_{-0.09}$ pc	$0.09^{+0.12}_{-0.07}$ pc $0.10^{+0.14}_{-0.08}$ pc	$0.10^{+0.14}_{-0.08}$ pc $0.12^{+0.15}_{-0.09}$ pc	$0.12^{+0.15}_{-0.09}$ pc $0.11^{+0.15}_{-0.08}$ pc	0.09 ± 0.02 pc 0.11 ± 0.01 pc
$R > 2$, $\chi_R^2 \leq 2$	$0.11^{+0.15}_{-0.09}$ pc $0.12^{+0.17}_{-0.09}$ pc	$0.08^{+0.12}_{-0.06}$ pc $0.10^{+0.13}_{-0.07}$ pc	$0.10^{+0.14}_{-0.08}$ pc $0.12^{+0.15}_{-0.08}$ pc	$0.11^{+0.15}_{-0.08}$ pc $0.11^{+0.15}_{-0.08}$ pc	0.08 ± 0.03 pc 0.11 ± 0.01 pc

three cases in the northern and southern regions are listed in Table B.1. The median widths in all cases are in the range 0.08–0.14 pc, similar to the range found when considering all the filaments.

In Fig. B.2, we reproduce the correlation between the filament width and the number of shoulders for the varying selection criteria considered above (i.e., aspect ratio and reduced chi-squared). Similar linear fits are found in all cases. The inferred filament width when no shoulders are identified in the intensity profiles for each of the cases considered is listed in the last column of Table B.1.

Finally, in Fig. B.3 we investigate that the no correlation found between filament widths and H_2 column density is not biased by the selection of the filaments. The bottom panel in Fig. B.3 is the most strict selection of filaments (filaments with aspect ratio larger than two and reduced chi-squared less than five) suggest no correlation between width and column density as discussed when considering all the filaments.

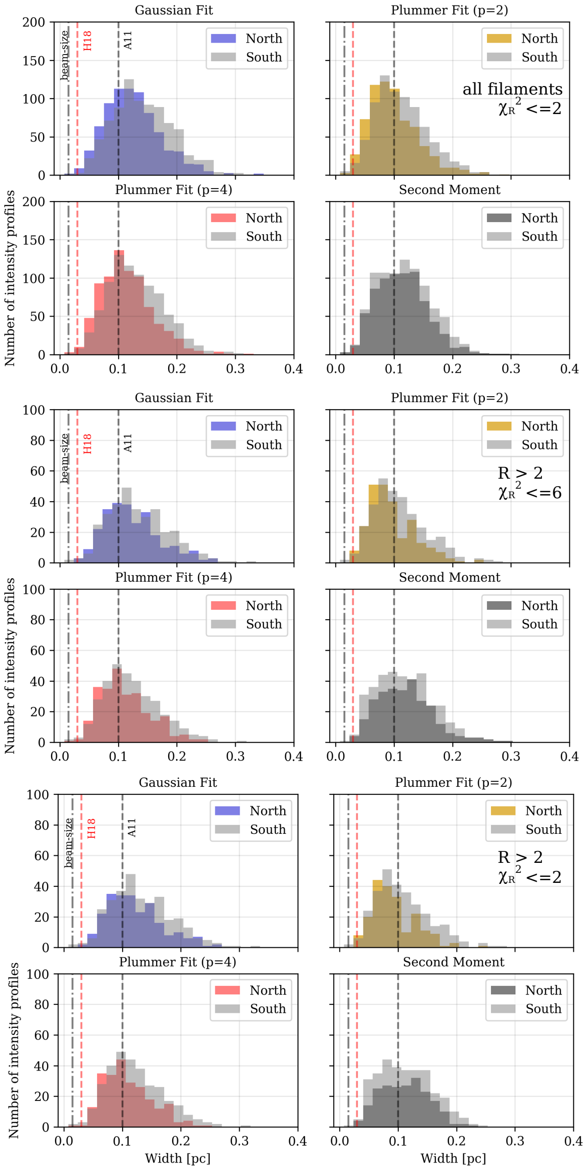

Fig. B.1. Width distributions for four different width calculation methods (Gaussian, Plummer-like with $p=2$ and $p=4$ and second moment, as shown in Fig. 5) when the filament aspect ratio and the reduced chi-squared criteria are varied. *Top four panels*: distributions of all filaments and intensity profiles fitted with a reduced chi-squared less than or equal to two. *Middle four panels*: width distributions for filaments with aspect ratios larger than two and fits with chi-squared less than or equal to six. *Bottom four panels*: width distributions for filaments with aspect ratios larger than two and reduced chi-squared values less than or equal to two.

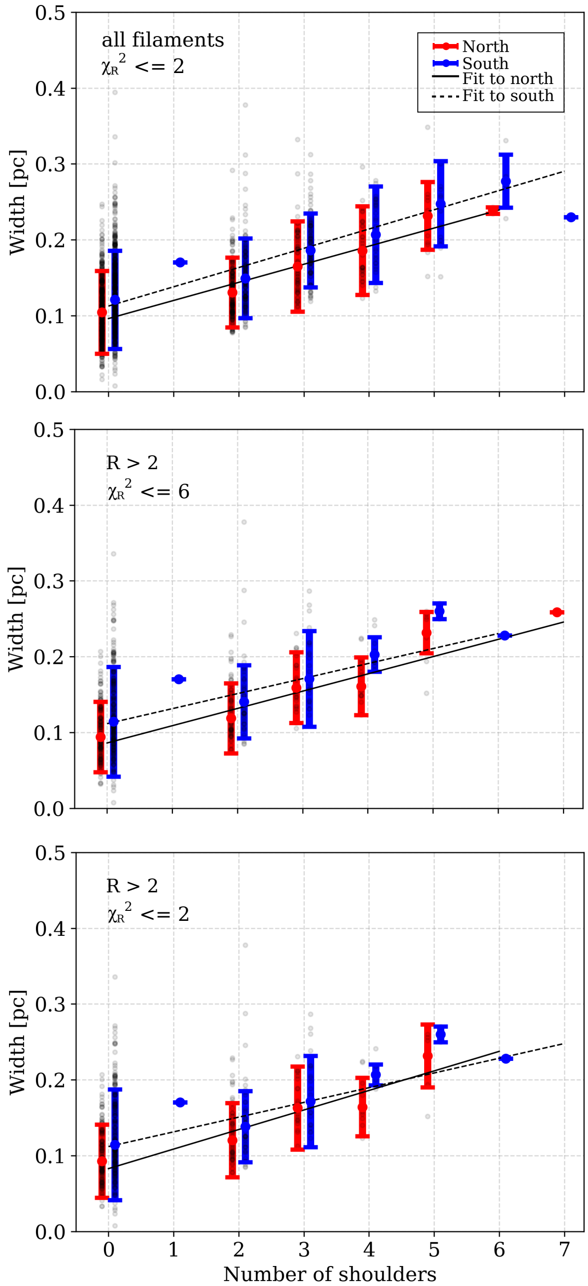

Fig. B.2. Same as Fig. 10 for the different criteria (aspect ratio and reduced chi-squared of the fit) studied in Appendix B.

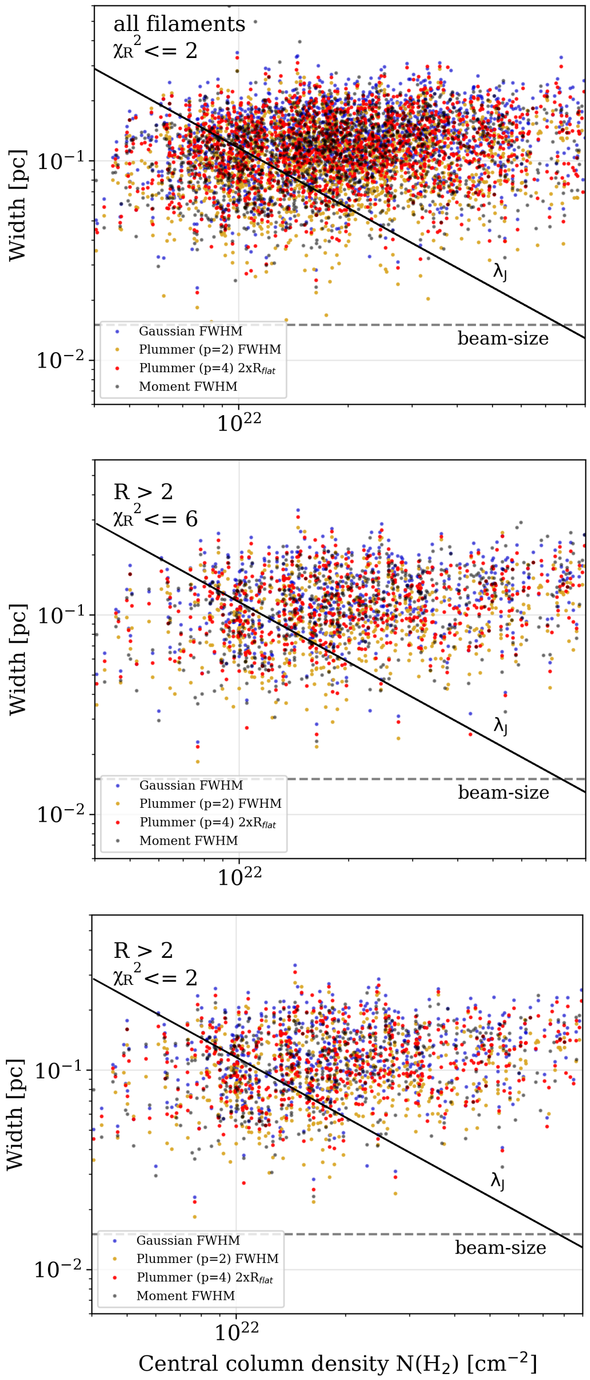

Fig. B.3. Same as Fig. 11 for the different criteria (aspect ratio and reduced chi-squared of the fit) studied in Appendix B.

BIBLIOGRAPHY

Ali, B. & Noriega-Crespo, A., A Mid-Infrared Survey of L1641N with ISOCAM. 2004, ApJ, 613, 374

André, P., Interstellar filaments and star formation. 2017, Comptes Rendus Geoscience, 349, 187

André, P., Men'shchikov, A., Bontemps, S., et al., From filamentary clouds to prestellar cores to the stellar IMF: Initial highlights from the Herschel Gould Belt Survey. 2010, A&A, 518, L102

André, P., Revéret, V., Könyves, V., et al., Characterizing filaments in regions of high-mass star formation: High-resolution submilimeter imaging of the massive star-forming complex NGC 6334 with ArTéMiS. 2016, A&A, 592, A54

Arzoumanian, D., Properties of interstellar filaments as derived from *Herschel*, *Planck*, and molecular line observations. 2017, ArXiv e-prints

Arzoumanian, D., André, P., Didelon, P., et al., Characterizing interstellar filaments with Herschel in IC 5146. 2011, A&A, 529, L6

Ballesteros-Paredes, J., Hartmann, L., & Vázquez-Semadeni, E., Turbulent Flow-driven Molecular Cloud Formation: A Solution to the Post-T Tauri Problem? 1999, ApJ, 527, 285

Ballesteros-Paredes, J., Hartmann, L. W., Vázquez-Semadeni, E., Heitsch, F., & Zamora-Avilés, M. A., Gravity or turbulence? Velocity dispersion-size relation. 2011, MNRAS, 411, 65

Bally, J., Ginsburg, A., Arce, H., et al., The ALMA View of the OMC1 Explosion in Orion. 2017, ApJ, 837, 60

Bally, J., Langer, W. D., Stark, A. A., & Wilson, R. W., Filamentary structure in the Orion molecular cloud. 1987, ApJ, 312, L45

Barnard, E. E., On a great nebulous region and the question of absorbing matter in space and the transparency of the nebulae. 1910, ApJ, 31

Becklin, E. E. & Gehrz, R. D. 2009, in Astronomical Society of the Pacific Conference Series, Vol. 417, Submillimeter Astrophysics and Technology: a Symposium Honoring Thomas G. Phillips, ed. D. C. Lis, J. E. Vaillancourt, P. F. Goldsmith, T. A. Bell, N. Z. Scoville, & J. Zmuidzinas, 101

Beckwith, S. V. W., Sargent, A. I., Chini, R. S., & Guesten, R., A survey for circumstellar disks around young stellar objects. 1990, AJ, 99, 924

Berné, O., Marcelino, N., & Cernicharo, J., Waves on the surface of the Orion molecular cloud. 2010, Nature, 466, 947

Beuther, H., Ragan, S. E., Ossenkopf, V., et al., Carbon in different phases ([CII], [CI], and CO) in infrared dark clouds: Cloud formation signatures and carbon gas fractions. 2014, A&A, 571, A53

Blitz, L. & Shu, F. H., The origin and lifetime of giant molecular cloud complexes. 1980, ApJ, 238, 148

Chabrier, G., The Galactic Disk Mass Function: Reconciliation of the Hubble Space Telescope and Nearby Determinations. 2003, ApJ, 586, L133

Clarke, S. D., Whitworth, A. P., Duarte-Cabral, A., & Hubber, D. A., Filamentary fragmentation in a turbulent medium. 2017, MNRAS, 468, 2489

Clarke, S. D., Whitworth, A. P., Spowage, R. L., et al., Synthetic $C^{18}O$ observations of fibrous filaments: the problems of mapping from PPV to PPP. 2018, MNRAS, 479, 1722

Cox, P. & Mezger, P. G., The Galactic infrared/submillimeter dust radiation. 1989, A&A Rev., 1, 49

Draine, B. T. 2011, Physics of the Interstellar and Intergalactic Medium

Draine, B. T. & Lee, H. M., Optical properties of interstellar graphite and silicate grains. 1984, ApJ, 285, 89

Duarte-Cabral, A. & Dobbs, C. L., What can simulated molecular clouds tell us about real molecular clouds? 2016, MNRAS, 458, 3667

Edelsbrunner, H., Letscher, D., & A., Z., Topological Persistence and Simplification. 2000, 41st Ann. Symp. Foundations of Computer Science, IEEE Comput. Soc. Press, Los Alamitos, CA, p. 454

Eilers, P. H. and Boelens, H. F., Automated algorithm for baseline subtraction in spectra. 2005, J. Raman Spectrosc.

Emerson, J., McPherson, A., & Sutherland, W., Visible and Infrared Survey Telescope for Astronomy: Progress Report. 2006, The Messenger, 126, 41

Federrath, C., Rathborne, J. M., Longmore, S. N., et al., The Link between Turbulence, Magnetic Fields, Filaments, and Star Formation in the Central Molecular Zone Cloud G0.253+0.016. 2016, ApJ, 832, 143

Field, G. B., Goldsmith, D. W., & Habing, H. J., Cosmic-Ray Heating of the Interstellar Gas. 1969, ApJ, 155, L149

Forman, R., Discrete Morse theory and the cohomology ring. 2002, Transactions of the American Mathematical Society, 354, 5063

Girichidis, P., Walch, S., Naab, T., et al., The SILCC (SImulating the LifeCycle of molecular Clouds) project - II. Dynamical evolution of the supernova-driven ISM and the launching of outflows. 2016, MNRAS, 456, 3432

Gómez, G. C. & Vázquez-Semadeni, E., Filaments in Simulations of Molecular Cloud Formation. 2014, ApJ, 791, 124

Hacar, A., Tafalla, M., Forbrich, J., et al., An ALMA study of the Orion Integral Filament: I. Evidence for narrow fibers in a massive cloud. 2018, ArXiv e-prints

Hacar, A., Tafalla, M., Kauffmann, J., & Kovács, A., Cores, filaments, and bundles: hierarchical core formation in the L1495/B213 Taurus region. 2013, A&A, 554, A55

Hailey-Dunsheath, S. 2009, PhD thesis, Cornell University

Heitsch, F., Gravitational Infall onto Molecular Filaments. II. Externally Pressurized Cylinders. 2013, ApJ, 776, 62

Hennebelle, P., On the origin of non-self-gravitating filaments in the ISM. 2013, A&A, 556, A153

Hennebelle, P. & Pérault, M., Dynamical condensation in a magnetized and thermally bistable flow. Application to interstellar cirrus. 2000, A&A, 359, 1124

Henshaw, J. D., Jiménez-Serra, I., Longmore, S. N., et al., Unveiling the early-stage anatomy of a protocluster hub with ALMA. 2017, MNRAS, 464, L31

Heyer, M., Krawczyk, C., Duval, J., & Jackson, J. M., Re-Examining Larson's Scaling Relationships in Galactic Molecular Clouds. 2009, ApJ, 699, 1092

Heyminck, S., Graf, U. U., Güsten, R., et al., GREAT: the SOFIA high-frequency heterodyne instrument. 2012, A&A, 542, L1

Hollenbach, D. J. & Tielens, A. G. G. M., Photodissociation regions in the interstellar medium of galaxies. 1999, Reviews of Modern Physics, 71, 173

Inutsuka, S.-I. & Miyama, S. M., Self-similar solutions and the stability of collapsing isothermal filaments. 1992, ApJ, 388, 392

Ivezić, Ž., Connelly, A. J., VanderPlas, J. T., & Gray, A. 2014, Statistics, Data Mining, and Machine Learningin Astronomy

Johnstone, D. & Bally, J., Large-Area Mapping at 850 μm. V. Analysis of the Clump Distribution in the Orion A South Molecular Cloud. 2006, ApJ, 653, 383

Juvela, M., Ristorcelli, I., Pagani, L., et al., Galactic cold cores. III. General cloud properties. 2012, A&A, 541, A12

Kirk, H., Friesen, R. K., Pineda, J. E., et al., The Green Bank Ammonia Survey: Dense Cores under Pressure in Orion A. 2017, ApJ, 846, 144

Klessen, R. S. & Glover, S. C. O., Physical Processes in the Interstellar Medium. 2016, Star Formation in Galaxy Evolution: Connecting Numerical Models to Reality, Saas-Fee Advanced Course, Volume 43. ISBN 978-3-662-47889-9. Springer-Verlag Berlin Heidelberg, 2016, p. 85, 43, 85

Klessen, R. S. & Hennebelle, P., Accretion-driven turbulence as universal process: galaxies, molecular clouds, and protostellar disks. 2010, A&A, 520, A17

Koch, E. W. & Rosolowsky, E. W., Filament identification through mathematical morphology. 2015, MNRAS, 452, 3435

Koda, J., Sawada, T., Wright, M. C. H., et al., CO(J = 1-0) Imaging of M51 with CARMA and the Nobeyama 45 m Telescope. 2011, ApJS, 193, 19

Kong, S., Arce, H. G., Feddersen, J. R., et al., The CARMA-NRO Orion Survey. 2018, ArXiv e-prints

Könyves, V., André, P., Men'shchikov, A., et al., The Aquila prestellar core population revealed by Herschel. 2010, A&A, 518, L106

Kounkel, M., Hartmann, L., Loinard, L., et al., The Goulds Belt Distances Survey (GOBELINS) II. Distances and Structure toward the Orion Molecular Clouds. 2017, ApJ, 834, 142

Kroupa, P. 2001, in Astronomical Society of the Pacific Conference Series, Vol. 228, Dynamics of Star Clusters and the Milky Way, ed. S. Deiters, B. Fuchs, A. Just, R. Spurzem, & R. Wielen, 187

Krumholz, M. R., Klein, R. I., & McKee, C. F., Molecular Line Emission from Massive Protostellar Disks: Predictions for ALMA and EVLA. 2007, ApJ, 665, 478

Kurtz, S. 2005, in IAU Symposium, Vol. 227, Massive Star Birth: A Crossroads of Astrophysics, ed. R. Cesaroni, M. Felli, E. Churchwell, & M. Walmsley, 111–119

Kurtz, S., Cesaroni, R., Churchwell, E., Hofner, P., & Walmsley, C. M., Hot Molecular Cores and the Earliest Phases of High-Mass Star Formation. 2000, Protostars and Planets IV, 299

Lada, C. J., Alves, J. F., & Lombardi, M., Near-Infrared Extinction and Molecular Cloud Structure. 2007, Protostars and Planets V, 3

Lane, J., Kirk, H., Johnstone, D., et al., The JCMT Gould Belt Survey: Dense Core Clusters in Orion A. 2016, ApJ, 833, 44

Larson, R. B., Turbulence and star formation in molecular clouds. 1981, MNRAS, 194, 809

Li, G.-X., Urquhart, J. S., Leurini, S., et al., ATLASGAL: A Galaxy-wide sample of dense filamentary structures. 2016, A&A, 591, A5

Lin, C. C., Mestel, L., & Shu, F. H., The Gravitational Collapse of a Uniform Spheroid. 1965, ApJ, 142, 1431

Mathis, J. S., Rumpl, W., & Nordsieck, K. H., The size distribution of interstellar grains. 1977, ApJ, 217, 425

Matzner, C. D. & McKee, C. F., Efficiencies of Low-Mass Star and Star Cluster Formation. 2000, ApJ, 545, 364

McKee, C. F. & Ostriker, E. C., Theory of Star Formation. 2007, ARA&A, 45, 565

McKee, C. F. & Ostriker, J. P., A theory of the interstellar medium - Three components regulated by supernova explosions in an inhomogeneous substrate. 1977, ApJ, 218, 148

Megeath, S. T., Gutermuth, R., Muzerolle, J., et al., The Spitzer Space Telescope Survey of the Orion A and B Molecular Clouds. I. A Census of Dusty Young Stellar Objects and a Study of Their Mid-infrared Variability. 2012, AJ, 144, 192

Meingast, S., Alves, J., Mardones, D., et al., VISION - Vienna survey in Orion. I. VISTA Orion A Survey. 2016, A&A, 587, A153

Men'shchikov, A., A multi-scale filament extraction method: getfilaments. 2013, A&A, 560, A63

Michelson, A. A. & Morley, E. W., On the Relative Motion of the Earth and of the Luminiferous Ether. 1887, Sidereal Messenger, vol. 6, pp.306-310, 6, 306

Milnor, J., Morse Theory, vol. 51 of. 1963, Annals of mathematics studies

Minamidani, T., Nishimura, A., Miyamoto, Y., et al. 2016, in Proc. SPIE, Vol. 9914, Millimeter, Submillimeter, and Far-Infrared Detectors and Instrumentation for Astronomy VIII, 99141Z

Molinari, S., Swinyard, B., Bally, J., et al., Clouds, filaments, and protostars: The Herschel Hi-GAL Milky Way. 2010, A&A, 518, L100

Nakamura, F., Miura, T., Kitamura, Y., et al., Evidence for Cloud-Cloud Collision and Parsec-scale Stellar Feedback within the L1641-N Region. 2012, ApJ, 746, 25

Okada, Y., Güsten, R., Requena-Torres, M. A., et al., Velocity profiles of [CII], [CI], CO, and [OI] and physical conditions in four star-forming regions in the Large Magellanic Cloud. 2018, ArXiv e-prints

Okada, Y., Requena-Torres, M. A., Güsten, R., et al., Velocity resolved [C ii], [C i], and CO observations of the N159 star-forming region in the Large Magellanic Cloud: a complex velocity structure and variation of the column densities. 2015, A&A, 580, A54

Oort, J. H., Outline of a theory on the origin and acceleration of interstellar clouds and O associations. 1954, Bull. Astron. Inst. Netherlands, 12, 177

Ostriker, J., On the Oscillations and the Stability of a Homogeneous Compressible Cylinder. 1964, ApJ, 140, 1529

Padoan, P., Juvela, M., Goodman, A. A., & Nordlund, Å., The Turbulent Shock Origin of Proto-Stellar Cores. 2001, ApJ, 553, 227

Palmeirim, P., André, P., Kirk, J., et al., Herschel view of the Taurus B211/3 filament and striations: evidence of filamentary growth? 2013, A&A, 550, A38

Panopoulou, G. V., Psaradaki, I., Skalidis, R., Tassis, K., & Andrews, J. J., A closer look at the 'characteristic' width of molecular cloud filaments. 2017, MNRAS, 466, 2529

Panopoulou, G. V., Tassis, K., Goldsmith, P. F., & Heyer, M. H., ^{13}CO filaments in the Taurus molecular cloud. 2014, MNRAS, 444, 2507

Polychroni, D., Schisano, E., Elia, D., et al., Two Mass Distributions in the L 1641 Molecular Clouds: The Herschel Connection of Dense Cores and Filaments in Orion A. 2013, ApJ, 777, L33

Pudritz, R. E. & Kevlahan, N. K.-R., Shock interactions, turbulence and the origin of the stellar mass spectrum. 2013, Philosophical Transactions of the Royal Society of London Series A, 371, 20120248

Reipurth, B., Devine, D., & Bally, J., Herbig-Haro Flows from the L1641-N Embedded Infrared Cluster. 1998, AJ, 116, 1396

Salpeter, E. E., The Luminosity Function and Stellar Evolution. 1955, ApJ, 121, 161

Sánchez-Monge, Á. 2011, PhD thesis, Universitat de Barcelona

Sault, R. J., Teuben, P. J., & Wright, M. C. H. 1995, in Astronomical Society of the Pacific Conference Series, Vol. 77, Astronomical Data Analysis Software and Systems IV, ed. R. A. Shaw, H. E. Payne, & J. J. E. Hayes, 433

Schilke, P., Benford, D. J., Hunter, T. R., Lis, D. C., & Phillips, T. G., A Line Survey of Orion-KL from 607 to 725 GHZ. 2001, ApJS, 132, 281

Schneider, N., Csengeri, T., Hennemann, M., et al., Cluster-formation in the Rosette molecular cloud at the junctions of filaments. 2012, A&A, 540, L11

Schuller, F., Menten, K. M., Contreras, Y., et al., ATLASGAL - The APEX telescope large area survey of the galaxy at 870 μm. 2009, A&A, 504, 415

Scott, D. W. 1992, Multivariate Density Estimation

Seifried, D., Sánchez-Monge, Á., Suri, S., & Walch, S., Modelling the chemistry of star-forming filaments - II. Testing filament characteristics with synthetic observations. 2017, MNRAS, 467, 4467

Shimajiri, Y., Kawabe, R., Takakuwa, S., et al., New Panoramic View of ^{12}CO and 1.1mm Continuum Emission in the Orion A Giant Molecular Cloud. I. Survey Overview and Possible External Triggers of Star Formation. 2011, PASJ, 63, 105

Shimajiri, Y., Kitamura, Y., Nakamura, F., et al., Catalog of Dense Cores in the Orion A Giant Molecular Cloud. 2015, ApJS, 217, 7

Shimajiri, Y., Kitamura, Y., Saito, M., et al., High abundance ratio of ^{13}CO to C^{18}O toward photon-dominated regions in the Orion-A giant molecular cloud. 2014, A&A, 564, A68

Shu, F. H., Adams, F. C., & Lizano, S., Star formation in molecular clouds - Observation and theory. 1987, ARA&A, 25, 23

Silverman, B. W. 1986, Density estimation for statistics and data analysis

Smith, R. J., Glover, S. C. O., Clark, P. C., Klessen, R. S., & Springel, V., CO-dark gas and molecular filaments in Milky Way-type galaxies. 2014, MNRAS

Smith, R. J., Glover, S. C. O., & Klessen, R. S., On the nature of star-forming filaments - I. Filament morphologies. 2014b, MNRAS, 445, 2900

Smith, R. J., Glover, S. C. O., Klessen, R. S., & Fuller, G. A., On the nature of star-forming filaments - II. Subfilaments and velocities. 2016, MNRAS, 455, 3640

Sodroski, T. J., Odegard, N., Arendt, R. G., et al., A Three-dimensional Decomposition of the Infrared Emission from Dust in the Milky Way. 1997, ApJ, 480, 173

Solomon, P. M., Rivolo, A. R., Barrett, J., & Yahil, A., Mass, luminosity, and line width relations of Galactic molecular clouds. 1987, ApJ, 319, 730

Sommerfeld, A. 1916, Atombau und Spektrallinien

Sorai, K., Sunada, K., Okumura, S. K., et al. 2000, in Proc. SPIE, Vol. 4015, Radio Telescopes, ed. H. R. Butcher, 86–95

Sousbie, T., The persistent cosmic web and its filamentary structure - I. Theory and implementation. 2011, MNRAS, 414, 350

Stutz, A. M. & Kainulainen, J., Evolution of column density distributions within Orion A⋆. 2015, A&A, 577, L6

Sunada, K., Yamaguchi, C., Nakai, N., et al. 2000, in Proc. SPIE, Vol. 4015, Radio Telescopes, ed. H. R. Butcher, 237–246

Suri, S. 2014, Master's thesis, Argelander Institute for Astronomy, University of Bonn

Suri, S., Sánchez-Monge, Á., Schilke, P., et al., The CARMA-NRO Orion Survey. Filamentary structure as seen in $C^{18}O$ emission. 2019, A&A, 623, A142

Tafalla, M. & Hacar, A., Chains of dense cores in the Taurus L1495/B213 complex. 2015, A&A, 574, A104

Takahashi, S., Saigo, K., Ho, P. T. P., & Tomida, K., Spatially Resolving Substructures within the Massive Envelope around an Intermediate-mass Protostar: MMS 6/OMC-3. 2012, ApJ, 752, 10

Takahashi, S., Saito, M., Ohashi, N., et al., Millimeter- and Submillimeter-Wave Observations of the OMC-2/3 Region. III. An Extensive Survey for Molecular Outflows. 2008, ApJ, 688, 344

van der Werf, P. P., Goss, W. M., & O'Dell, C. R., Tearing the Veil: Interaction of the Orion Nebula with its Neutral Environment. 2013, ApJ, 762, 101

Walch, S., Girichidis, P., Naab, T., et al., The SILCC (SImulating the LifeCycle of molecular Clouds) project - I. Chemical evolution of the supernova-driven ISM. 2015, MNRAS, 454, 238

Walker, C. K., Adams, F. C., & Lada, C. J., 1.3 millimeter continuum observations of cold molecular cloud cores. 1990, ApJ, 349, 515

Yamauchi, S., Koyama, K., Sakano, M., & Okada, K., Broad-Band X-Ray Observations of the Orion Region with ASCA. 1996, PASJ, 48, 719

LIST OF FIGURES

LIST OF TABLES

ACRONYMS

ALMA Atacama Large Millimeter/submillimeter Array

APEX Atacama Pathfinder Experiment

AsLS Asymmetric Least Squares Smoothing

BCGS Bonn-Cologne Graduate School

BEARS The 25-Beam Array Receiver System

BTS Behind The Spectra

CARMA Combined Array for Research in Millimeter-wave Astronomy

Caltech California Technology Institute

CMF Core Mass Function

CNM Cold Neutral Medium

DFG Deutsche Forschungsgesellschaft

DisPerSE Discrete Persistent Structures Extractor

FilChaP Filament Characterization Package

FIVE Friends in velocity

FOREST Four beam Receiver System on 45m-Telescope

GALEX Galaxy Evolution Explorer

GBT Green Bank Telescope

GILDAS Grenoble Image and Line Data Analysis Software

GREAT German Receiver for Astronomy at Terahertz Frequencies

HH Herbig-Haro

HIM Hot Ionized Medium

HMC Hot Molecular Core

HPBW Half Power Beam Width

HST Hubble Space Telescope

IMF Initial Mass Function

INTEGRAL International Gamma-Ray Astrophysics Laboratory

IRAM Institut de Radioastronomie Millimétrique

ISF integral shaped filament

ISM Interstellar Medium

JCMT James-Clerk-Maxwell Telescope

JPL Jet Propulsion Laboratory

KDE Kernel Density Estimation

miriad Multichannel Image Reconstruction, Image Analysis and Display

MSC Morse-Smale Complex

NRO Nobeyama Radio Observatory

PDR photo-dissociation region or photon-dominated region

ROSAT The Roentgen Satellite

SAM45 Spectral Analysis Machine for the 45m telescope

SED Spectral Energy Distribution

SN supernova

SOFIA Stratospheric Observatory for Infrared Astronomy

VISION Vienna Survey in OrionSpectral Analysis Machine for the 45m telescope

WIM Warm Ionized Medium

WNM Warm Neutral Medium

XMM-Newton The X-ray Multi-Mirror Mission

YSO Young Stellar Object

There's a point, around age twenty, when you have to choose
whether to be like everybody else the rest of your life,
or to make a virtue of your peculiarities.
Those who build walls are their own prisoners.
I'm going to go fulfil my proper function in the social organism.
I'm going to go unbuild walls.

— Ursula K. Le Guin, The Dispossessed

ACKNOWLEDGMENTS

This work was carried out within the framework of Sonderforschungsbereich SFB 956, the Conditions and Impact of Star Formation subproject A4, funded by the Deutsche Forschungsgesellschaft (DFG). I am also grateful to Bonn-Cologne Graduate School (BCGS) from which I have received a PhD honors-branch scholarship and a travel grant.

This is the closing of one of the biggest and most important chapters of my life and I am sure my words will fall short when I try to express my gratitude for all the support I have received. I will, nevertheless, try my best to acknowledge everyone who supported me throughout this journey. I would like to start by thanking my supervisor and mentor Prof. Dr. Peter Schilke. Thank you, Peter, for the constant support and encouragement, but most importantly for your confidence in my work. I would also like to thank Prof. Dr. Stefanie Walch-Gassner and Prof. Dr. Jürgen Stutzki for their support throughout this work. Many thanks to Dr. Álvaro Sánchez Monge, for always making time for discussions, calculations, plots and proof-reads. Many thanks to Dr. Seamus Clarke, I am grateful for your knowledge, your passion about science and your ability to pass it on. Thank you for helping me debug `FilChaP`.

I would like to thank the CARMA-NRO Orion Survey team, it has been and still is a pleasure to work with so many great scientist. I thank Dr. John Carpenter for inviting me to California Technology Institute (Caltech), and teaching me about `miriad` and interferometry. I have acquired most of my practical radio interferometry knowledge at CARMA, and therefore, I am beyond thankful for the experience. I would also like to thank the IRAM 30m crew and kitchen. Whenever I went observing, both at CARMA and the 30m, I had no shortage of gluten-free food. Thank you all for your effort to keep an observer happy and healthy. I also thank Prof. Dr. Paul Goldsmith and Dr. Umut Yildiz for kindly hosting me at the Jet Propulsion Laboratory (JPL). Seeing the Mars rovers is still one of the highlights of my life.

I would like to thank the entire Schilke Group; my academic family. My office mates: Álvaro, Andreas, Fanyi and Mahya, thank so much for your support. Also for listening to me complain about life, which is a big part of the life of a PhD student. Thanks for all the laugh, coffee, tea, occasional stupidity and mouse calls! I also want to thank my academic family *from the other building*. Thank you Annika, Daniel, Franta, Juan, Nassim, Prabesh, Seamus and Shash for your friendship and encouragement especially in the last few months of my PhD. Thank you Anna and Cristian for your friendship.

Many thanks to Dr. Volker Ossenkopf-Okada for very valuable discussions on filaments. I also would like to thank Dr. Amy Stutz, Dr. Jouni Kainulainen for the *Herschel* data. Thanks to Prof. Dr. John Bally for countless amounts of complementary datasets on Orion. Many thanks Dr. Daniel Seifried for sharing the Zoom-in simulations with me that provided a base for testing DisPerSE.

I cannot thank enough to Anika Schmiedeke, Álvaro Sanchez-Monge, Daniel Seifried and Sebastian Haid for their valuable comments on this manuscript and Andreas Schwörer for translating the abstract and finding the right German words.

Many many thanks to Dr. Petra Neubauer-Guenther for supporting me out throughout my graduate school life in Cologne. Thank you, Petra, for letting me give talks for the newcomers every year which made me feel like an actual rock star. Many thanks to Dr. Frank Schlöder for helping me with anything technical, debugging and compiling codes. Most importantly thank you for all the ice cream that the kitchen has now (I should also thank Moritz Wiegand here :-)), it made an entire summer in the office more bearable. Thank you Dr. Susanne Herbst, Mariia Soloviova, Bettina Krause and Steffi Simon for all your help throughout these years.

I want to take a moment to thank Anika and Gwendo for standing by my side through this 4,5,6 years. Thank you for being inspirational, thank you for making me laugh, think, appreciate, talk and listen. I love you both so much.

I am finding it very hard to leave Cologne and I would like to thank all the people who made this foreign city feel like home. Thank you Nassim and Seamus for all the Saturday cooking sessions, travels, science discussions, for convincing me to watch RuPaul, and endless good time. Many many thanks from the bottom of my heart to Daniel, Elaheh, Elena, Gerold, Madeleine, Moritz, Nastaran, Nicola and Pavol. Thank you guys all for everything, and yes my suggestion for us all to move to Heidelberg still stands.

My friends far far away; Cody, Özge, Steve, Yani. Thank you guys so much. I would like to believe life has plans for all of us and we will hang out again very very soon. I miss you all. Many thanks to my cat who tried to sit on my laptop whilst writing most of this thesis. You made it very hard for me to finish my PhD, Luna.

Finally, I would like to thank my family whom I terribly missed during these past few months. Thank you mama for raising me to be the woman I am today, I am proud of what I have achieved, and I hope you are too. Thank you to my not so little sister; I could not have accomplished anything without you in my life. Thank you for being my best friend since day 540. Thank you my dear Baschtl, I am looking forward to see what is next for us. I love you all with my whole heart and I cannot wait to spend more time with you soon. Sizi seviyorum.

ERKLÄRUNG

Ich versichere, dass ich die von mir vorgelegte Dissertation selbständig angefertigt, die benutzten Quellen und Hilfsmittel vollständig angegeben und die Stellen der Arbeit – einschließlich Tabellen, Karten und Abbildungen –, die anderen Werken im Wortlaut oder dem Sinn nach entnommen sind, in jedem Einzelfall als Entlehnung kenntlich gemacht habe; dass diese Dissertation noch keiner anderen Fakultät oder Universität zur Prüfung vorgelegen hat; dass sie – abgesehen von unten angegebenen Teilpublikationen – noch nicht veröffentlich worden ist, sowie, dass ich eine solche Veröffentlichung vor Abschluss des Promotionsverfahrens nicht vornehmen werde.

Die Bestimmungen der Promotionsordnung sind mir bekannt. Die von mir vorgelegte Dissertation ist von Prof. Dr. Peter Schilke betreut worden.

Teilpublikationen:

The CARMA-NRO Orion Survey: The Filamentary Structure as seen in $C^{18}O$ emission S. Suri, A. Sanchez-Monge, P. Schilke, S. Clarke, R. Smith, V. Ossenkopf-Okada, R. Klessen, P. Padoan, P. Goldsmith, H. Arce, J. Bally, J. Carpenter, A. Ginsburg, D. Johnstone, J. Kauffmann, S. Kong, D. Lis, S. Mairs, T. Pillai, J. Pineda, A. Duarte-Cabral
2019, A&A, 623, A142

Ich versichere, dass ich alle Angaben wahrheitsgemäss nach bestem Wissen und Gewissen gemacht habe und verpflichte mich, jedmögliche, die obigen Angaben betreffenden Veränderungen, dem Dekanat unverzüglich mitzuteilen.

Köln,

Sümeyye Suri